



IAHR
2017

37th IAHR
WORLD CONGRESS
13-18 August, 2017
Kuala Lumpur, Malaysia

COASTAL STRUCTURES
(PORTS AND HARBOURS)

STABILITY FORMULA FOR TETRAPODS USING MULTIGENE GENETIC PROGRAMMING (MGGP)

JAE SUNG LEE ⁽¹⁾ & KYUNG-DUCK SUH ⁽²⁾

⁽¹⁾Seoul National University, Republic of Korea,
wofmtjd@snu.ac.kr

⁽²⁾Seoul National University, Republic of Korea,
kdsuh@snu.ac.kr

ABSTRACT

Studies on the stability of Tetrapods have been conducted mainly through hydraulic model test. In this study, we propose the stability formula for Tetrapods by symbolic regression using multigene genetic programming (MGGP), a new technique of data mining. The main advantage of multigene symbolic regression is that it can find the form and coefficients of an equation without prior assumptions. The developed formula has no constraints on its application and is much more accurate than previous empirical formulas.

Keywords: Tetrapod; breakwater; data mining; multigene genetic programming (MGGP); stability.

1 INTRODUCTION

Recently, data-based machine learning methods (e.g. ANNs, fuzzy, SVM, GMDH, GP) have been used in various areas of civil engineering. Data mining techniques can be very useful when a large amount of experimental data or a lot of data measured in the field is available. Multigene genetic programming (MGGP) technique is a new regression tool that mimics Darwin's evolutionary theory as an extended method of genetic programming. The great advantage of symbolic regression using MGGP is that it can find a relationship without prior assumption of the form of the equation. In other words, not only the parameters of the equation but also the form of the equation can be obtained automatically. Tetrapod is an artificial sofa block placed on a rubble mound breakwater, which resists the incident waves. The stability number of Tetrapods is the value required to determine its proper weight. Hudson (1959) proposed a simple formula for calculating the stability number based on small-scale model test using regular waves. Van der Meer (1987) formula was developed for surging breaker on 1:1.5 slope using irregular wave tests. De Jong (1996) proposed an empirical formula for plunging breaker on 1:1.5 slope and took into account the influences of packing density and crest elevation. Suh and Kang (2012) developed a stability formula for various structure slope angles. Recently, Lee and Suh (2016) proposed the ANN (Artificial Neural Network) model for calculating the stability number of Tetrapods. In this study, we develop an equation that can calculate the stability number of Tetrapods through symbolic regression using MGGP. In addition, the accuracy of the developed formula is compared statistically with the existing empirical formulas.

2 THEORETICAL BACKGROUNDS

2.1 Stability number

The stability number is a dimensionless number that indicates the stability of the armor layer of a rubble mound structures. It is defined as

$$N_s = \frac{H_s}{\Delta D_n} \quad [1]$$

where H_s is the significant wave height, $\Delta = \rho_c / \rho_w - 1$ is the relative density, ρ_c and ρ_w are the densities of concrete armor unit and water, respectively and D_n is the nominal size of the armor unit. Figure 1 shows the definition of the nominal size. The nominal size is the length of one side of a cube with the same volume as the armor units. Therefore, if the stability number and the significant wave height are given, we can obtain the nominal size. Finally, we can calculate the weight of armor unit. From previous studies, it can be seen that the stability number is expressed as a function of the hydraulic and structural parameters.

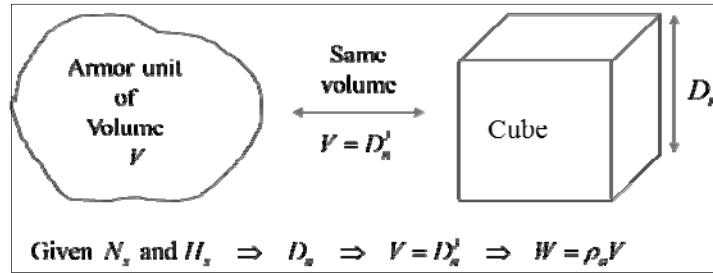


Figure 1. Definition of the nominal size.

2.2 Multigene symbolic regression

Multigene symbolic regression is a technique for finding the relationship between data through symbolic regression using MGGP. The genetic programming (GP) based technique, MGGP, finds the solution through *crossover* and *mutation*, which are the main operators of the GP. These operators are iterated until the solution can solve the given problem. Figure 2 and Figure 3 show an example of crossover and mutation, respectively.

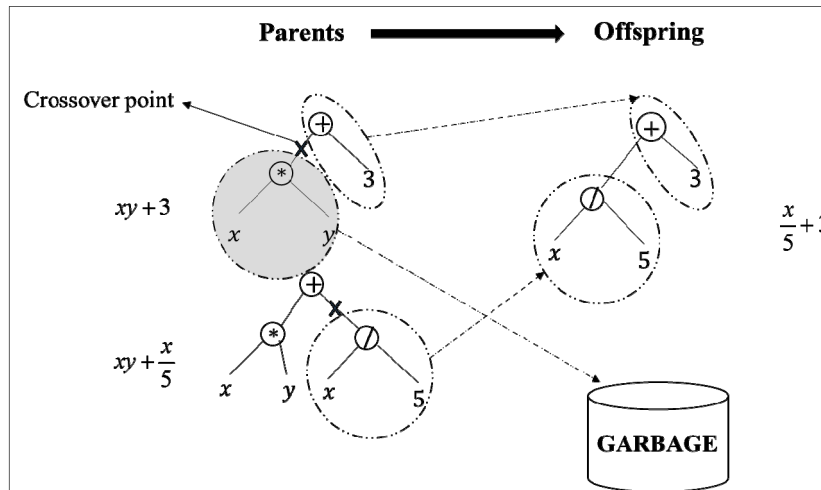


Figure 2. An example of crossover.

The process of crossover is the process by which two randomly generated genes (called parents) generate the next generation offspring from randomly selected crossover point.

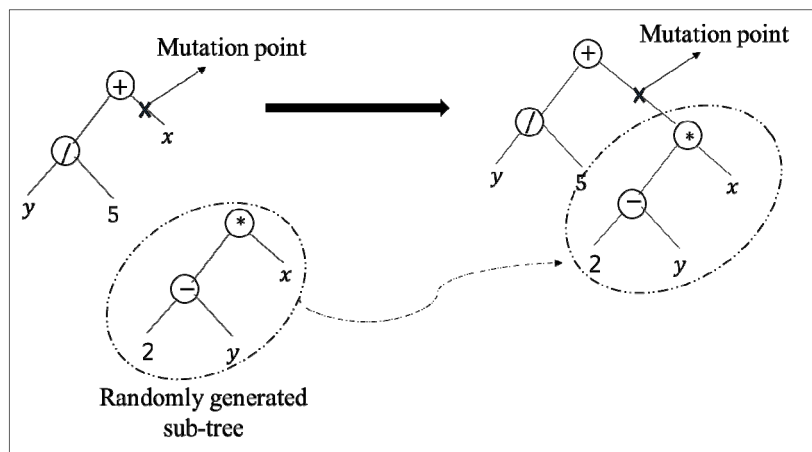


Figure 3. An example of mutation.

The process of mutation is the process of replacing newly generated genes at the mutation point with genes initially generated. Variables and constants are called *terminals* and mathematical operators are called *functions* in a solution expressed by the above tree structure. Terminals and functions can be selected by the user to perform the model.

In genetic programming, the solution is represented by a single tree structure, whereas in the MGGP, several tree structures of the solution are respectively weighted and represented by their linear combination. Figure 4 shows the structure of MGGP model.

Figure 4. The structure of MGGP model, where n is the number of genes (trees), d_0 is bias term and d_1, \dots, d_n are the scaling parameters (weights).

The prediction of the y training data is given by

$$\hat{y} = d_0 + d_1 \mathbf{t}_1 + \dots + d_G \mathbf{t}_G \quad [2]$$

where \mathbf{t}_i is the $(N \times 1)$ vector of the output from the i th gene constituting the multigene individual and \mathbf{G} is defined as $(N \times (G+1))$ gene response matrix as follows.

$$\mathbf{G} = [\mathbf{1} \ \mathbf{t}_1 \ \dots \ \mathbf{t}_G] \quad [3]$$

where the number $\mathbf{1}$ refers to a $(N \times 1)$ column of ones used as the offset input. The \mathbf{d} vector in the form of a $((G+1) \times 1)$ can be computed from the training data using the least square estimation.

$$\mathbf{d} = (\mathbf{G}^T \mathbf{G})^{-1} \mathbf{G}^T \mathbf{y} \quad [4]$$

3 METHODOLOGY

3.1 Experimental data and input variables

In this study, the experimental data of Van der Meer (1987), De Jong (1996) and Suh and Kang (2012) were used. The total number of data was 286 and the composition of the data is shown in Table 1. Here, the output value, N_s is the stability number of Tetrapod. In the training set of the model, 70% of the total data was extracted using the random sampling technique.

Table 1. Input and output parameters of MGGP model for Tetrapods.

Symbol	Notation	Mean	Maximum	Minimum
H_s (m)	Significant wave height	0.168	0.087	0.266
T_m (s)	Mean wave period	1.782	1.036	2.99
N_0	Relative damage	0.64	0	5.75
N	Number of waves	1642	427	3078
R_c / H_s	Relative crest elevation	1.4	3.07	-0.54
k_Δ	Packing density	1.01	0.88	1.02
$\cot \alpha$	α = slope angle of structure	1.55	1.333	2
N_s	Stability number	2.76	1.66	5.025

In this study, all of the input variables were used as dimensionless parameters so that the developed model can be used in the field. The dimensionless parameters used as the input variables of the MGGP model are shown in Table 2.

Table 2. Dimensionless input and target parameters of MGGP model.

Input parameters	Target parameter
$\xi_m, N_0, N, R_c / H_s, k_\Delta$	N_s

where ξ_m a dimensionless number is called a surf-similarity parameter and is computed as

$$\xi_m = \tan \alpha / \sqrt{2\pi H_s / g T_m^2}.$$

3.2 Complexity measurement for models

One of the most important thing in developing a data mining model is that the model should show reliable predictions not only for the trained data but also for the untrained data. However, if the model is overtraining the training data, it shows a large error (noise) in the new data, which is called *overfitting*. Overfitting errors occurs when the complexity of the model is large, such as when the number of parameters is too large compared to the number of observations. Fig. 3.1 shows how the error of training data and testing data varies with the complexity of the model. As shown in Figure 5, when the complexity of the model increases, it means that the model is overtrained for the training data, so there is only a small error for the training sample. However, for the test sample, the best result is obtained from a moderately complex model rather than overtrained model. Therefore, in this study, the complexity of the model is measured and its complexity is limited to some extent, which greatly reduces the possibility of overfitting.

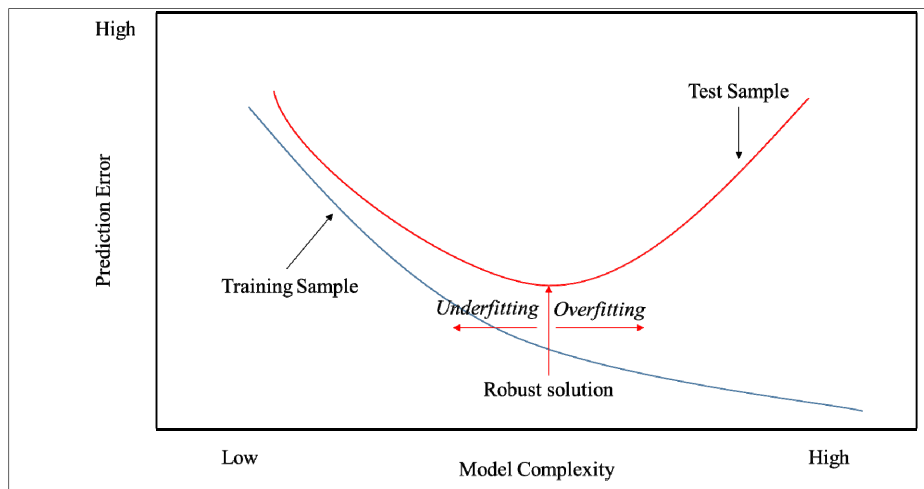


Figure 5. Prediction error according to model complexity.

The complexity of the MGGP model expressed in the tree structure can be calculated as shown in Figure 6. Finally, when the tree-shaped models were obtained, the complexity values were calculated in the same manner as the following figure, and the robust model was selected using the calculated values.

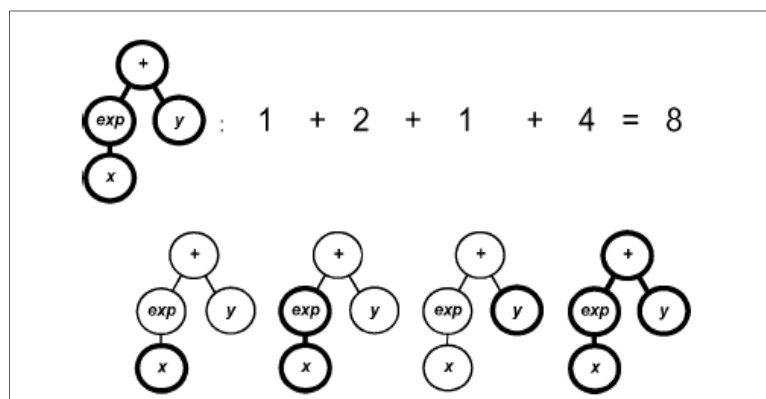


Figure 6. Expressional complexity of a tree model is the total number of nodes in all subtree models, (Vladislavleva, 2009).

Figure 7 shows the complexity and accuracy of the 1,500 models performed in this study. In the figure, R on the y-axis means the correlation coefficient, which means that the smaller the y-axis value, the higher the accuracy of the model. Since the accuracy of the model shown in Fig. 3.3 is related to training data, it can be seen that the best solution is very complex. In other words, the best model with the highest accuracy in Fig. 3.3 has a high probability of overfitting error because the complexity is very high.

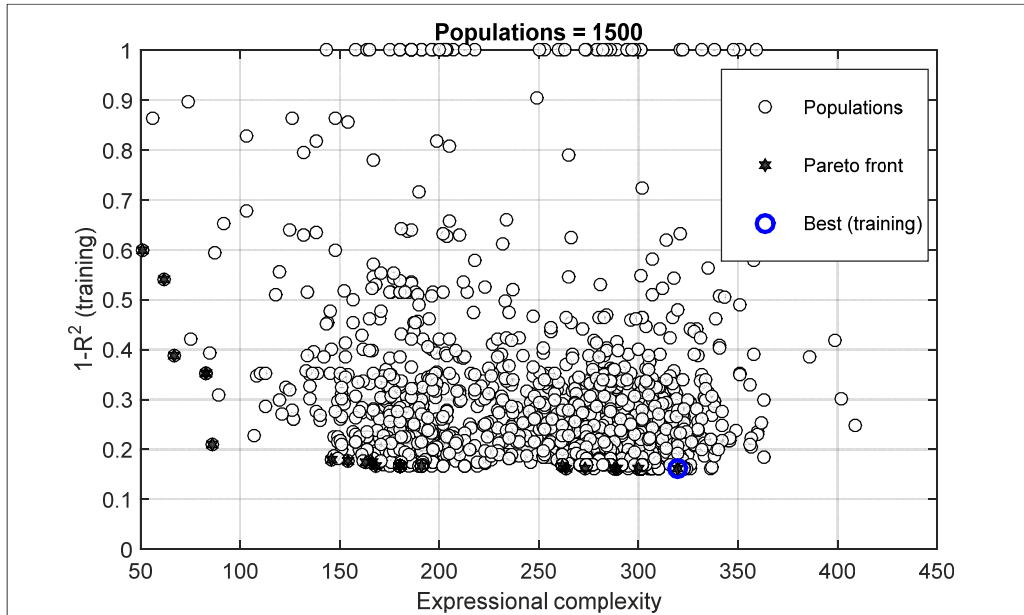


Figure 7. Pareto front of the models.

In this study, to reduce the possibility of overfitting, we selected a model with the best performance among models with a model complexity between 150 and 200.

3.3 Parameter settings for MGGP running

The parameters for running MGGP were all determined through trial and error, with reference to previous studies. The running parameters are shown in Table 3.

Table 3. Parameters setting for MGGP running.

Parameter	Setting
Function set	+, -, ×, tanh, exp
Population size	500
Number of generations	300
Maximum number of genes allowed in an individual	5
Maximum tree depth	6
Tournament size	2
Probability of GP tree crossover	0.85
Probability of GP tree direct copy	0.1
Probability of GP tree mutation	0.05
Elitism	0.1
Probability that a constant node	0.15

4 RESULTS AND DISCUSSIONS

In this study, the MGGP model was performed using the dimensionless input variables in Table 2 and the running parameters in Table 3. We also attempted to minimize the possibility of overfitting by limiting the complexity of the model. The stability formula for Tetrapods from the finally selected model is shown in Eq. (4.1). The calculated expressional complexity of the model is 191.

$$\begin{aligned}
 N_s = & -0.69 \exp \left[\exp(-N \times N_0) \exp \left(\frac{R_c}{H_s} \right) \right] + 2.16 \exp \left[-\exp(\exp(k_\Delta)) \right] \exp(-5,941N_0) \exp(-\xi_m) \\
 & - 0.24 \exp(-N_0) + 2.03 \exp \left[-\exp(5,941N_0) \right] + 0.24 \frac{R_c}{H_s} \left(k_\Delta^3 - \frac{R_c}{H_s} \right) \\
 & - 7.86 \exp \left[\exp \left(-\frac{R_c}{H_s} \right) \right] \exp(-\exp(k_\Delta)) \exp(-N_0) + 2.05
 \end{aligned} \tag{5}$$

Figure 8 shows the accuracy of the training set and the testing set, respectively.

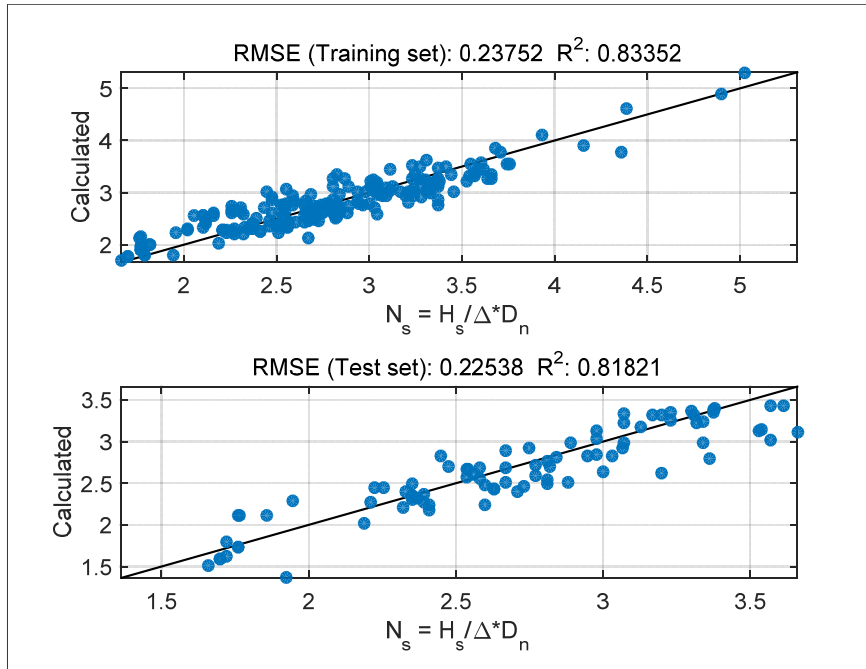


Figure 8. The N_s predictions made by MGGP

Figure 9 is the result of plotting the value of the stability number obtained by substituting all the 286 experimental data into Eq. (4.1). The x-axis represents the observed values from the experiment as a definition of a stability number.

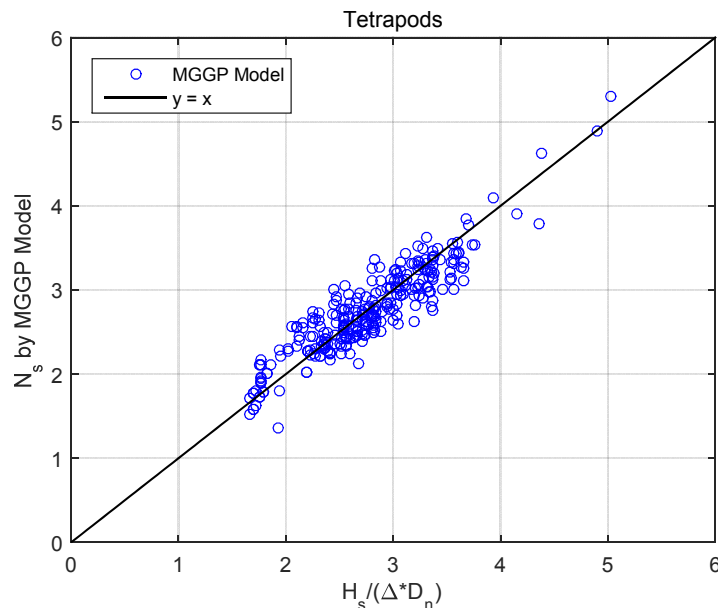


Figure 9. Scatter plot of total data

The correlation coefficient is 0.912, the root-mean-square-error (RMSE) is 0.234 and the index of agreement is 0.953. The index of agreement (I_a) is a statistical parameter that can be used to measure the performance of the prediction model. It varies between 0 and 1, where 1 indicates perfect agreement between the observations and predictions. Figure 10 shows the comparison of the MGGP model with the previous empirical formulas and ANN model.

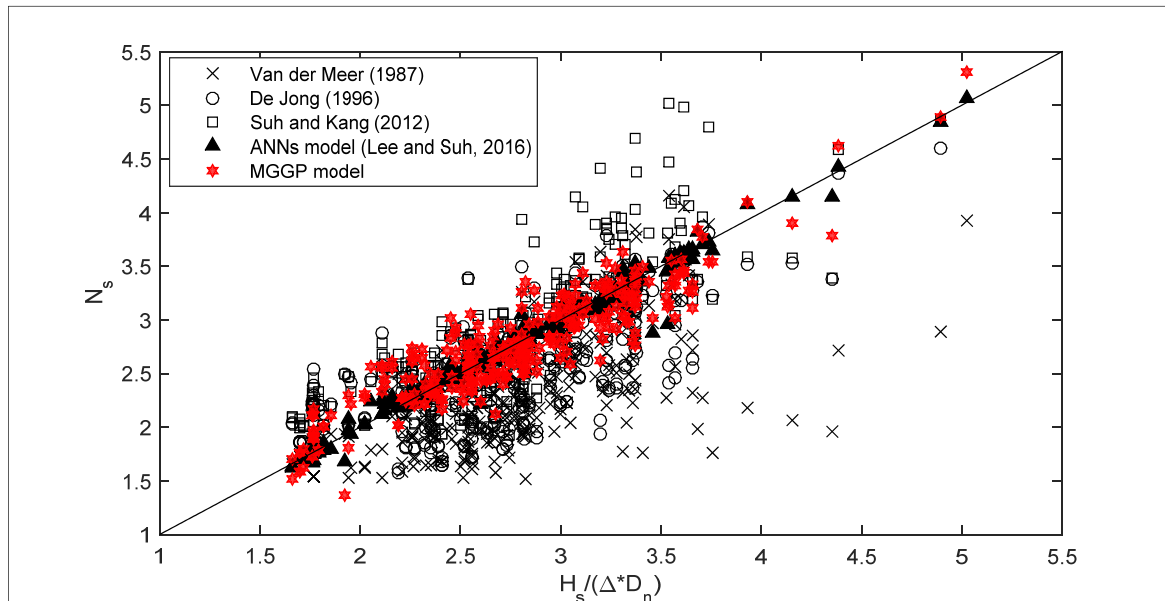


Figure 10. Comparison the developed formula with the previous methods

It can be seen that the MGGP model is much more accurate than the empirical formulas of Van der Meer (1987), De Jong (1996) and Suh and Kang (2011). Table 4 shows the comparison of statistical values.

Table 4. Statistical parameters of the results.

	R	RMSE	I_α
Van der Meer (1987)	0.666	0.417	0.707
De Jong (1996)	0.707	0.411	0.806
Suh and Kang (2012)	0.805	0.406	0.876
ANN model (2016)	0.990	0.080	0.995
MGGP model	0.912	0.230	0.953

From Table 4, it can be seen that the MGGP model has a much better performance than the empirical formulas, but has a lower predictive performance than the ANN model. However, the proposed ANN model was developed on the laboratory scale only, it is difficult to apply it to the field. The model developed in this study can be applied directly to the field because all of the input variables are used with a dimensionless parameters.

5 CONCLUSIONS

In this study, a formula was developed to calculate the stability number of Tetrapods using experimental data of Van der Meer (1987), De Jong (1996) and Suh and Kang (2012). The proposed formula is applicable to both surging breaker and plunging breaker and can be used regardless of the slope angle of the structure. It was also found that the developed formula was much more accurate than the previous empirical formulas. In summary, we developed the stability formula for Tetrapods with high accuracy through development of MGGP model using dimensionless parameters. Once the stability number is calculated, the nominal size (D_n) of the Tetrapod is obtained by substituting the significant wave height of the field into $N_s = H_s / (\Delta D_n)$.

ACKNOWLEDGEMENTS

This research was supported by Basic Science Research Program through the National Research Foundation of Korea (NRF) funded by the Ministry of Science, ICT and Future Planning (NRF-2014R1A2A2A01007921). This research was also supported by the BK21 PLUS research program of the NRF.

REFERENCES

De Jong, R. J. (1996). Wave Transmissions at Low-Crested Structures. Stability of Tetrapods at Front, Crest and Rear of a Low-Crested Breakwater *PhD Dissertation*, TU Delft, Delft University of Technology.

- Lee, J. S. & Suh, K. D. (2016). Calculation of Stability Number of Tetrapods using Weights and Biases of ANN model. *Journal of Korean Society of Coastal and Ocean Engineering*, 28(5), 277~283.
- Suh, K. D. & Kang, J. S. (2011). Stability Formula for Tetrapods. *Journal of Waterway, Port, Coastal and Ocean Engineering*, 138(3), 261-266.
- Van der Meer, J. W. (1987). *Stability of Rubble Mound Breakwaters, Stability Formula For Breakwaters Armoured with Tetrapods*, Report on Basic Research, H462, 2.
- Vladislavleva, E. J., Smits, G. F. & Den Hertog, D. (2009). Order of Nonlinearity as a Complexity Measure for Models Generated by Symbolic Regression via Pareto Genetic Programming. *IEEE Transactions on Evolutionary Computation*, 13(2), 333-349.

EXPERIMENTAL STUDY ON STABLE THICKNESS OF CONCRETE SLAB REVETMENT ON INNER SLOPE OF DIKES

CHEN WEI-QIU⁽¹⁾, WANG DENG-TING⁽²⁾, SUN TIAN-TING⁽³⁾ & KUAI YU⁽⁴⁾

⁽¹⁾ College of Harbor, Coastal and Offshore Engineering, Hohai University, Nanjing, China,
chenweiqiu@hhu.edu.cn

⁽²⁾ Department of River and Harbor Engineering, Nanjing Hydraulic Research Institute, Nanjing, China,
dtwang@nhri.cn

⁽³⁾ Department of River and Harbor Engineering, Nanjing Hydraulic Research Institute, Nanjing, China,
qdsfstt@126.com

⁽⁴⁾ College of Harbor, Coastal and Offshore Engineering, Hohai University, Nanjing, China,
kuaiyu@hhu.edu.cn

ABSTRACT

A series of physical model tests were conducted on stable thickness of concrete slab revetment on the inner slope. The objective of this study is to discuss the relationship among stable thickness of concrete slab, average overtopping discharge and inner slope gradient according to the damage process of different slopes and different thicknesses of revetments. The result shows that there is a linear correlation between stable relative thickness and dimensionless average overtopping discharge with the same slope. Relative thickness decreases as the slope gets gentler. Equations are presented for stable thickness of concrete slab revetment on the inner slope with different gradients. It can provide reference for dike design.

Keywords: Concrete slab; overtopping; inner slope; stable thickness.

1 INTRODUCTION

Dikes are used worldwide to protect infrastructure and populations from floods as a result of storm surges. Overtopping, which will occur during extreme events, possibly causes breaching of the protective structure. Destruction of dikes will result in major catastrophes in terms of loss of life and economic damages. Global warming leads to sea level rise and frequent occurrence of storm surge. The volume of overtopping over the crest of dikes increases significantly as a result of storm surge, which greatly influences the stability of back slope. The failure of inner slope will perhaps affect the overall stability of the defense system. Thus, back slope protection has become one of the main concerns of water managers in many nations.

Concrete slab is widely used in dike protection. Compared to dry masonry block stone, riprap and so forth, its stability is relatively good and anti-sinking capability is relatively strong. Besides that, it can withstand greater flow velocity. However, there are no relevant equations to calculate the stable thickness of concrete slab cover on the inner slope. Therefore, quantitative analysis of stable thickness is necessary for the dike design and protection of inner slope.

Concrete slabs are chosen as the back revetment during physical models tests in this study. Overtopping is the direct cause of landward slope destruction. And the back slope gradient is an important factor affecting the stability of inner slope. Based on the tests, the relationship between the thickness of concrete slabs and dimensionless overtopping discharge is investigated with different slope gradients; to produce new equation for calculating the stable thickness of concrete slabs in response to irregular waves.

2 PROTECTION OF BACK SLOPE

2.1 Overtopping flow parameters

Landward slope is very important to ensure the overall safety of sea dikes. Previous studies have shown that velocity and thickness of the overtopping flow were closely associated with the erosion, infiltration and landslide failure of the landward-side slope. Many researches had been carried out on the backward failure process and overflow parameters, such as velocity and thickness. At present, there are equations and methods for predicting wave run-up, average overtopping discharge, the overtopping volume distribution, overflow velocity and thickness. Pullen et al. (2007) had put forward systematic equations for estimating overtopping and overflow parameters. Schüttrumpf (2005) had conducted research on parameters of the overtopping water by performing physical model tests and theoretical analysis. Van Gent (2002) gave the equations for the thickness and velocity of overtopping flow along landward slope through model tests and mathematical modeling. More recently, equations for predicting instantaneous overtopping distribution, overtopping velocity and pressure had been proposed by Hughes (2008), comprehensively considering a combination of sea waves and storm surges by conducting two-dimensional model tests. Based on the achievements of Van Gent and other scholars, Trung (2014) proposed modified equations of the velocity and thickness of overtopping flow. The effects of friction coefficient on overflow velocity and thickness were discussed.

Empirical equations for overtopping flow thickness and velocity at the crest given by Van Gent are as below:

$$\frac{h_{2\%}}{H_s} = C_h' \left(\frac{R_{u2\%} - R_c}{\gamma H_s} \right) \quad [1]$$

$$\frac{u_{2\%}}{\sqrt{gH_s}} = C_u' (\gamma - c)^{0.5} \left(\frac{R_{u2\%} - R_c}{\gamma H_s} \right)^{0.5} / \left(1 + C_u'' \frac{B}{H_s} \right) \quad [2]$$

where $\gamma - c$ is roughness coefficient at the crest, C_h' , C_u' , C_u'' are empirical coefficients and 0.1, 1.7, 0.1 are chosen as their values respectively.

Expressions (Eq. [3] and Eq. [4]) for overflow water thickness and velocity along the back slope are shown as the following:

$$h = h_0 u_0 / \left[\frac{A}{B} + \mu \exp(-3AB^2 s) \right] \quad [3]$$

$$u = \frac{A}{B} + \mu \exp(-3AB^2 s) \quad [4]$$

where s is the abscissa along the back slope, the junction of the crest and back slope is zero. h_0, u_0 respectively represent thickness and velocity of overflow at the junction of dike crest and back slope, which can be calculated by Eq. [1] and Eq. [2]. The above equations only apply to dikes without seawalls.

Eq. [5] and Eq. [6] developed by Hughes respectively represent average overflow thickness and velocity on the back slope of seawall without walls.

$$h = 0.4 \left[\frac{1}{g \sin \theta} \right]^{1/3} (q_{ws})^{2/3} \quad [5]$$

$$u = 2.5 (q_{ws} \cdot g \cdot \sin \theta)^{1/3} \quad [6]$$

in Eq. [5] can be calculated by Eq. [7]:

$$\frac{q_{ws}}{\sqrt{gH_{m0}^3}} = 0.034 + 0.53 \left(\frac{-R_c}{H_{m0}} \right)^{1.58} \quad [7]$$

where q_{ws} is the average overtopping discharge under the effect of a combination of waves and storm surges; θ is the angle between the back slope and the horizontal plane.

2.2 Inner slope failure process

The process of overtopping dikes has been subject of a huge amount of research (Van der Meer, 2008). In contrast, dike failure mechanism as a result of landward slope instability during flood events was not known well. In order to study the breaching process of dikes, some scholars' had carried out a series of physical model tests and numerical researches. Through model tests, Möller (2002) analyzed the failure progress of landward-side slope resulting from overtopping flow. In order to understand the failure process of dikes due to wave overtopping, Tinney and Hsu (1961) conducted a series of physical models and results showed that the scour rate was related to the material properties of dikes. For larger particle size, the degradation rate was higher. Chinnarasri (2003) studied flow patterns and progressive damage of dike overtopping by performing physical model tests and using numerical models. The overtopping flow could be classified into four stages. Van der Meer (2007) invented the overtopping simulator that could simulate overtopping flow, which solved the difficult problem where the roughness of turf revetment in small-scale models was difficult to be accurately simulated.

Through physical model tests, Möller et al. (2003) researched the erosion process of inner slope of dikes without seawalls as a function of overtopping. The conclusions are as follows:

- (1) The crest of embankment was firstly penetrated and eroded;
- (2) The permeable damage dominated when the turf was not fully developed;
- (3) The permeable damage on inner slope was more obvious in response to sustained function of overtopping.

Li et al. (2014) studied the stability of artificial concrete block revetment with the action of wave overtopping and storm surges through large-scale two-dimensional model tests. The results indicated that the effective stress varied with the amount of overtopping, but the value of effective stress was always positive

throughout the test. No soil strain was detected, which might be caused by the small wave force and hydrodynamic pressure imposed on the slope. Artificial concrete block revetment maintained stability as a whole after the test.

Fan (2006) mainly discussed the influence of seawall height on parameters of overtopping flow. For the higher seawall, the pressure on the crest was larger and the flow velocity on the back slope was smaller. The main reason was that as the seawall height increased, the leaping height of the overtopping water became larger in front of seawall, resulting in increase of the force imposed on the crest. However, the initial velocity of overtopping flow reduced while the amount of overtopping decreased. As a result, the flow velocity on the back slope decreased as well.

Prior researches mainly focused on the erosion process of landward slope of dikes without seawalls which was caused by overtopping. However, dikes with parapet walls are widely used in some countries, for example China and the failure mechanisms were different from those without seawalls. Hence, it is necessary to systematically study the inner slope failure of this type of embankments.

3 MODEL DESIGN AND EXPERIMENT METHODS

3.1 Experimental setup

The model experiment was conducted in Basic Sediment Theory Experiment Hall of Nanjing Hydraulic Research Institute. The wave flume is 175m long, 1.2m wide, 1.5m deep. The flap type wave paddle is capable of generating regular and irregular waves with wave heights up to 0.35m and wave periods between 0.5 ~ 6.0 s. The active section of this flume is divided into two parts, one of which was taken as the test section. The function of the other part was to diffuse re-reflective waves. Flume was equipped with gentle slopes to absorb waves at both sides, so as to reduce the wave reflection. Computers automatically control the required wave elements and simultaneously collect and process water fluctuating signals measured by wave gages. The wave-making machine can generate irregular waves with different spectrums.

A water butt was adopted for water receiving and overtopping discharge measurement in this experiment. The water-receiving plate is 0.2m wide.

3.2 Experimental methods

A cross section of a simple single-slope dike with a 1:1.5 seaward slope and a vertical wave wall is adopted in this model experiment. Accropode blocks and concrete slabs, the size of which is 13 cm × 13 cm, were used respectively as the seaward slope and inner slope revetments. The water depth at the toe of the dike was 40cm. The tested dike cross section is demonstrated in Figure 1 in model-scale units. Seaward is on the left side of the figure.

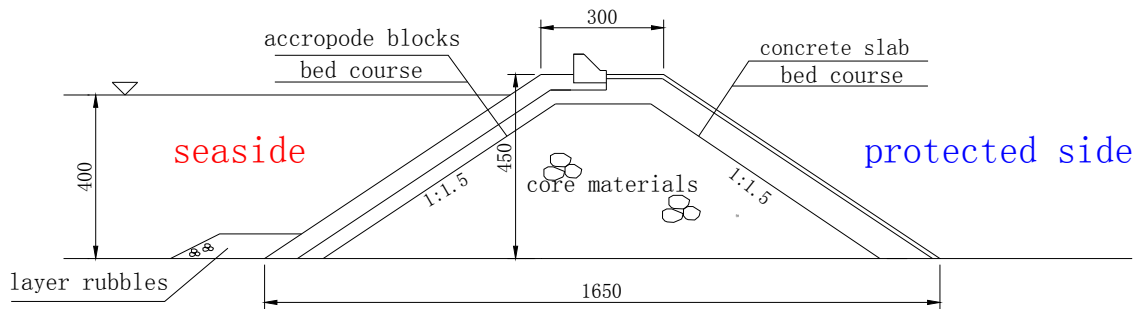


Figure 1. Tested cross section (unit: mm).

Different concrete slab thicknesses, inner slope gradients and different wave periods were combined for a series of model experiments. For each combination, a small wave height was firstly used to act on the experimental cross section. Overtopping occurs when wave run-up goes beyond the wave wall elevation, and then the overtopping impacts the concrete slab revetment of the inner slope. If the revetment was stable, the wave height will be further increased until the concrete slab loses stability, and the corresponding mean overtopping discharge is determined then. The failure process was observed. After each test, concrete slabs should be re-levelled. The experimental conditions include:

- (1) Wave periods were respectively 1.5s, 2s, and 3s.
- (2) Concrete slab thicknesses were respectively 1.0 cm, 1.5 cm, 2.0 cm, and 2.5 cm.
- (3) The slopes were 1:1, 1:1.5, 1:2, and 1:3, corresponding to $m = 1, 1.5, 2,$ and 3 respectively;
- (4) Irregular waves were simulated by JONSWAP spectrum;

Each test was repeated at least 3 times to avoid the effect of accidental factors and ensure the validity of the experiment results.

4 EXPERIMENT RESULTS AND ANALYSIS

4.1 Analysis of failure process of inner slope

In order to determine the relationship between the stable thickness of concrete slabs and the wave elements, a series of tests with different wave heights and wave periods were performed on revetments with different gradients and thicknesses. It was concluded that there were two main failure modes of concrete slabs after observing the destruction process of back slope: overturning damage and lifting damage.

When the wave run-up was higher than the elevation of dike crest, the overtopping occurs. With the same wave period, the overtopping discharge was less when the wave height is lower. The impact of overtopping was not strong enough to cause the slab instability. The volume of overtopping wave increases with increasing wave height. When the wave height reaches the critical value, some concrete slabs slightly rise due to overtopping smashing against the crest and inner slope. Small gaps developed around the slabs. The overtopping flow constantly scours small particles in the bedding under the concrete slabs. Flows with a certain velocity penetrate into the bottom of slabs and kinetic energy instantly converts to pressure energy imposing on the bottom of slabs. Consequently, the concrete plates were further elevated. Some overtopping water simultaneously scours the front edge of the elevated concrete slabs. Slabs will be suddenly lifted after a period of time. Ultimately, overturning damage at the dike crest or along the landward slope was caused. See Figure 2 for details.

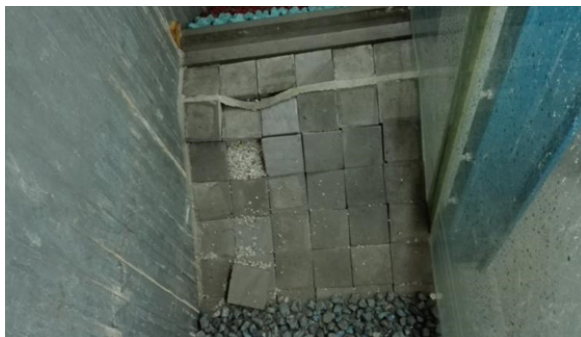


Figure 2. Concrete slab overturning damage



Figure 3. Lifting damage

Lifting damage is similar to overturning damage. After the upper part of the concrete slab was lifted slightly, the constraining force around the slab was weakened. Some overtopping water around the slab penetrates into the bottom of the slab from the slits to form strong jacking force underneath the slab, and the whole slab will enter a critical state of floating. Under the continuous action of overtopping, the water continues to penetrate into the bottom of the concrete slab. The revetment was gradually shifted by jacking force induced by penetration. Uplifts of concrete slabs can be observed from the vertical direction of the flume, as shown in Figure 3. When the displacement exceeds the thickness of one slab, the entire slab will eventually break away from the revetment and lose instability. In addition, when the period is rather short and the wave was very steep, damages mainly appear at the junction of dike crest and landward-side slope. When the period was long and the wave was barely steep the damages mainly occurs along the back slope.

4.2 Determination of stable thickness of concrete slabs on back slope

In order to avoid the influence of model scale, the relative thicknesses of the revetment were obtained by dividing the thickness of the concrete slab by significant wave height. It was found that the relative stable thickness of the concrete slabs was related to wave height with the same gradient and the same wave period. Therefore, the change of relative thickness with wave steepness is firstly analyzed. The relationship is shown in Figure 4.

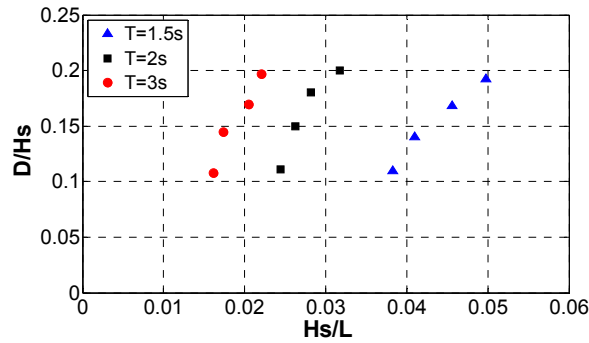
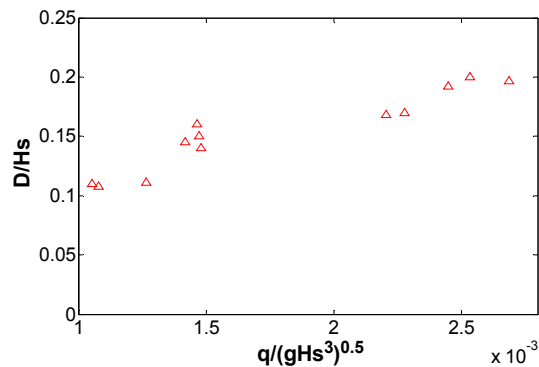


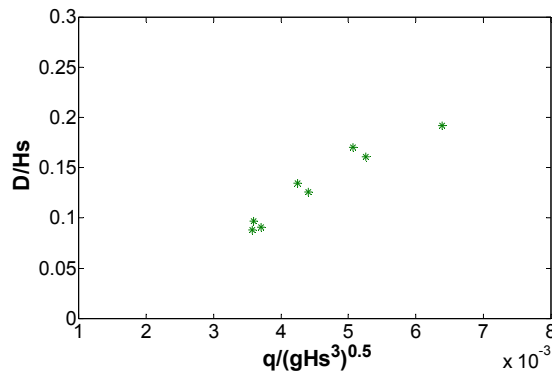
Figure 4. Relationship between relative thickness and wave steepness ($m=1.5$).

The following conclusions can be obtained by analyzing tested data in Figure 4. There is a significant influence of wave steepness on the relative thickness with the same slope and the same wave period. The greater the volume of overtopping was, the stronger the strength acting on back slope will be. Accordingly, the relative stable thickness was larger as well. It can be concluded that the relative thickness of the revetment was very sensitive to changes in wave height. For the same relative thickness, when the wave period is shorter, the wave steepness corresponding to the critical stability of the concrete slab was greater.

The above conclusions only present the qualitative relationship between the relative thickness of the revetment and the wave steepness, which can hardly be applied in practical engineering. Under the premise of certain period, the average overtopping discharge increases gradually with increasing wave steepness. Therefore, in order to determine the equation for calculating the thickness of concrete slab on back slope, the relative thickness of revetment was adopted and its relationship with the dimensionless volume of overtopping was further explored (Figure 5).



(a) $m=1.5$



(b) $m=3$

Figure 5. Relationship between relative thickness and dimensionless overtopping volume.

It can be seen from Figure 5 that the relative thickness has a linear relation with the dimensionless overtopping volume and the relative thickness increases with increasing volume of overtopping when $m=1.5$ and $m=3$. Overtopping was a direct factor for slope destruction and the gradient of inner slope was an important factor affecting the stability of concrete slab revetment. Therefore, it was necessary to figure out the influence of slope gradient on relative thickness. 1 cm concrete slab revetment was chosen in the model test. The tests combined by different wave periods and different significant wave heights were separately carried out by changing the gradient of the slope, which was, $m=1, 1.5, 2, 3$ respectively.

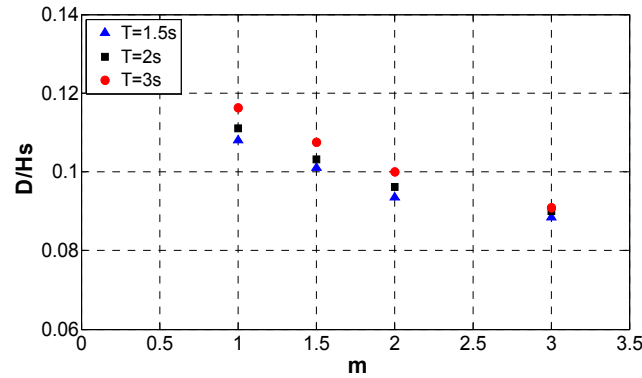


Figure 6. The relationship between relative thickness and slope gradient.

From Figure 6, the following conclusions can be drawn:

- (1) When revetment thickness was kept constant, the relative thickness decreases as the gradient slows down. This is because the gentler the slope was, the larger the wave height will be required to cause concrete slab instability. And the relative thickness was smaller accordingly. It can be concluded that the test results are reasonable and effective.
- (2) Under the same gradient, the relative thicknesses become smaller as the wave period decreases. For shorter wave period, overtopping water had less energy with the same slope. The wave height needs to be increased to make concrete slabs unstable. As a result, the relative thickness will be smaller.

After comprehensively analyzing the relationship among the relative thickness and dimensionless overtopping volume and slope gradients, the following relation fitting curve can be obtained

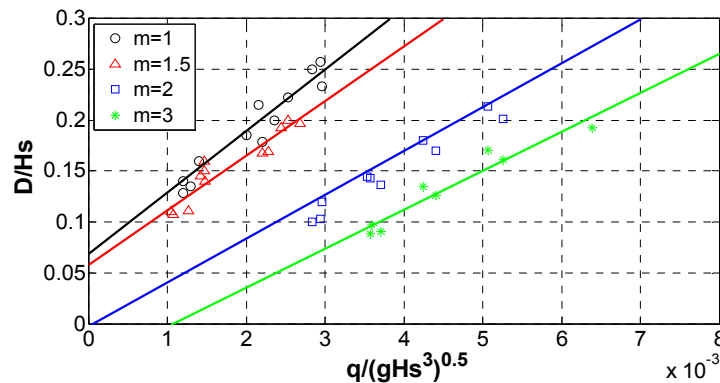


Figure 7. Calculation curves of relative thickness.

The above figure shows the relations of curve between the relative thickness and the dimensionless overtopping volume with different slope gradients. With the same dimensionless overtopping volume, the gentler the slope was, the smaller the stability thickness would be required. The empirical coefficients A and B were introduced, and the following formula is proposed to calculate the thickness of concrete slab revetment:

$$\frac{D}{H_s} = A \frac{q}{\sqrt{gH_s^3}} + B \quad [8]$$

is the average overtopping discharge per unit structure length and it can be calculated by using the overtopping equation given by Hebsgaard (1998). Calculated values of Eq. [9] were compared with practical values (Figure 8). Seen from Figure 8, a correlation coefficient between the calculated values and the practical values is 0.92. The calculated values by the Hebsgaard equation agree well with the practical values.

$$q = k_1 \sqrt{gH_s^3} \ln(S_{op}) \exp\left(\frac{k_2 (\cot \alpha)^{0.3} (2Rc + 0.35b)}{\gamma H_s}\right) \quad [9]$$

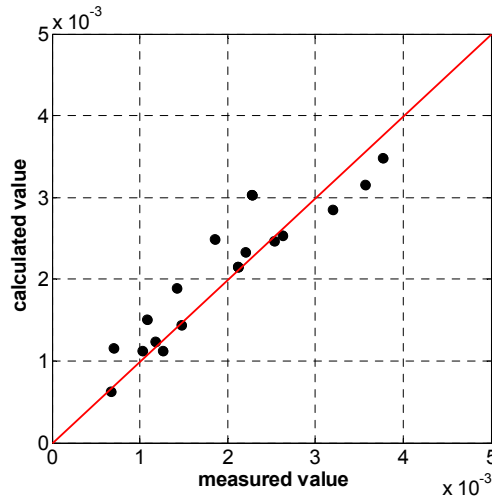


Figure 8. Verification of dimensionless average overtopping discharge.

Substituting Eq. [9] into Eq. [8] yields:

$$\frac{D}{H_s} = Ak_1 \ln(S_{op}) \exp\left(\frac{k_2(\cot \alpha)^{0.3} (2Rc + 0.35b)}{\gamma H_s}\right) + B \quad [10]$$

where D is the stable thickness of concrete slabs. H_s is the significant wave height. R_c is crest elevation.

S_{op} is deep water wave steepness obtained by the linear wave theory, $S_{op} = \frac{2\pi H_s}{gT_p^2}$. T_p is spectral peak period. γ is influence coefficient of concrete slab roughness. β is oblique angle, which is 90 degree when the wave incidence is normal to the dike axis. When a breast wall exists, k_1 equals to -0.01 and k_2 equals to -1.0. A and B are empirical coefficients, which were determined by Table 1.

Table 1. Empirical coefficient

m	1	1.5	2	3
A	60.5	53.7	43.1	38.33
B	0.069	0.058	-0.002	-0.041

The comparison between the values were measured by conducting tests and the values calculated by the Eq. [9] is shown in Figure 9.

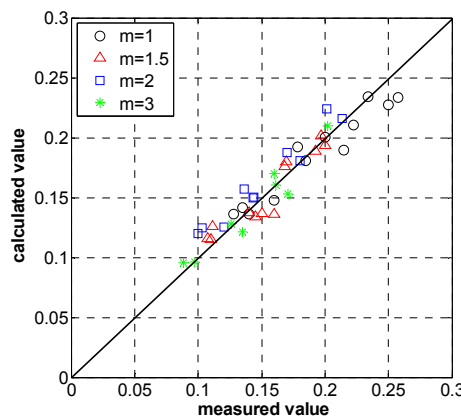


Figure 9. Verification of relative thickness.

Good agreement was found between the relative thicknesses calculated by the Eq. [9] and the measured values, and the correlation coefficient R was 0.96. The Equation proposed in this paper can effectively estimate the stable thickness of concrete slabs. For other inner slopes within the gradient from 1: 1 to 1: 3, stable thickness can be estimated by interpolating the calculation curves in Figure 7.

In summary, the Eq. [10] can be used to calculate stable thickness of concrete slabs on the backward slope. The equation proposed in this paper can provided as reference for inner slope protection of dikes.

5 CONCLUSIONS

- (1) A series of physical model tests are conducted on the concrete slab revetment of the back slope as a function of irregular waves. The main ways of concrete slab failure are due to overturning damage and lifting damage.
- (2) Based on a series of tests, the equation for calculating the stable thickness of concrete slabs on landward slope against overtopping is put forward. The results show that the effect of wave height is dominant and direct. The relative thickness is linear with dimensionless overtopping volume and sensitive to the wave height change. It increases with increasing wave steepness when the period is kept constant. As the gradient becomes slower the relative thickness decreases.
- (3) The equation for stable thickness of concrete slabs proposed in this paper only applies to the dike structure in this paper under the condition that the back slope gradient is from 1: 1 to 1: 3. For different gradients, stable thickness of concrete slabs can be estimated by interpolating the calculation curves in this paper.

ACKNOWLEDGEMENTS

The research is funded by National Natural Science Foundation of China (NSFC) (51579156), and Major Project of Nanjing Hydraulic Research Institute Funds (Y214009). It is also funded by Jiangsu Province Hydraulic Science and Technology Projects (2012001-8), Jiangsu Province Hydraulic Science and Technology Projects (2014048), and special funds targeting at industrial scientific researches for public welfare of Ministry of Water Resources (MWR) (201401004). The laboratory experiments are conducted in Nanjing Hydraulic Research Institute. Thanks are also extended to Dengting Wang, Tianting Sun, Yu Kuai, for their critical support of the experiments.

REFERENCES

- Chinnarasri, C., Tingsanchali, T., Weesakul, S. & Wongwiset, S. (2003). Flow Patterns and Damage of Dike Overtopping. *International Journal of Sediment Research*, 18(4), 301-309.
- Fan, H.X. (2006). Experimental Research on Overtopping Volume and Flow of Sloped Seadike, *MSc Thesis*. Hohai University.
- Van Gent, M.R.A. (2002). Low-exceedance wave overtopping events-measurements of velocities and the thickness of water-layers on the crest and inner slope of dikes. Final Report DC030202/H3803, Delft Cluster, Delft, Netherlands.
- Hebsgaard M., Sloth, P. & Juhl, J. (1998). Wave Overtopping of Rubble Mound Breakwaters. *Coastal Engineering*, ASCE, 1998:2235-2248.
- Schüttrumpf, H., Oumeraci H. (2005). Layer Thicknesses and Velocities of Wave Overtopping Flow at Seadikes. *Coastal Engineering*, 52(6):473-495.
- Hughes, S.A. (2008). *Combined Wave and Surge Overtopping of Levees: Flow Hydrodynamics and Articulated Concrete Mat Stability*. US Army Corps of Engineers.
- Li, L., Amini, F., Pan, Y. & Li, C. (2014). Stability Monitoring of Articulated Concrete Block Strengthened Levee in Combined Wave and Surge Overtopping Conditions. *Geo-Congress*. 2014, 262-271.
- Van der Meer, J.M. (2007). Design, Construction, Calibration and Use of The Wave Overtopping Simulator. *ComCoast, workpackage 3: Development of Alternative Overtopping-Resistance Sea Defences, Phase 3*. Final Report, Infram and Royal Haskoning, Delft, Netherlands.
- Van der Meer, J.M. (2008). Erosion Strength of Inner Slopes of Dikes Against Wave Overtopping: Preliminary Conclusions After Two Years of Testing with the Wave Overtopping Simulator. *Summary Report*.
- Möller, J., Weissmann, R., Schüttrumpf, H., Grüne, J., Oumeraci, H. & Richwien, W. (2003). Interaction of Wave Overtopping and Clay Properties for Seadikes. *Coastal Engineering Conference*. ASCE, 2003: 2105-2115.
- Pullen, T., Allsop, N.W.H., Bruce, T., Kortenhaus, A., Schüttrumpf H. & Van der Meer, J.W. (2007). *Eurotop: Wave Overtopping of Sea Defences and Related Structures: Assessment Manual*, HR Wallingford, Wallingford, U.K.
- Tinney, E.R. & Hsu, H.Y. (1961). Mechanics of Wash-Out of An Erodible Fuse Plug. *Journal of the Hydraulic Engineering*, ASCE, 97(3): 1-30.
- Trung, L.H. (2014). Velocity and Water-Layer Thickness of Overtopping Flows on Sea Dikes: Report of Measurements and Formulas Development. *Tu Delft Department Hydraulic Engineering*.

WAVE RUN-UP FORECASTING MODEL USING ARTIFICIAL NEURAL NETWORK BETWEEN OFFSHORE WAVE DATA AND WAVE RUN-UP SCALE

SEOK-BONG LEE⁽¹⁾ & KYUNG-DUCK SUH⁽²⁾

⁽¹⁾ Department of Civil and Environmental Engineering, Seoul National University,
playnow8902@snu.ac.kr

⁽²⁾ Department of Civil and Environmental Engineering, Seoul National University,
kdsuh@snu.ac.kr

ABSTRACT

Artificial neural network (ANN) is a statistical learning algorithm which is inspired by biological neural network. ANN has been widely used in various forecasting areas. Therefore, it can be applied to forecast wave run-up scale. The wave run-up scale which was introduced by Na et al. (2011), describes the degree of wave run-up on a breakwater. In a previous research, Na et al. (2011) developed a wave run-up forecasting model by performing multiple linear regressions between several offshore wave data and photographed wave run-up scale data. In this research, we use an artificial neural network model instead of multiple linear regression models. The target is the breakwaters of this research are the same as those of the previous research, i.e. four breakwaters (Aninjin, Ayajin, Jungja and Kyungjung breakwater) located on the east coast of Korea. The ANN model is trained by using almost 70% of total data, and the remaining 30% was used to test the model. Good results are observed except at the Kyungjung breakwater, where Na et al.'s (2011) regression model also gave a bad result, probably because the wave run-up scale is smaller than at other breakwaters.

Keywords: Coastal structures; artificial neural network (ANN); wave run-up; wave forecasting; wave overtopping.

1 INTRODUCTION

Recently, because of the global warming, rise of sea level is occurring around the world. For this reason, several hazardous phenomena such as large scale wave overtopping and wave run-up have been occurring at some breakwater in East Coast of Korean peninsula. Frequent wave overtopping can lead serious damages to humans and their properties. Actually, there are some cases that traveler visiting to breakwater at the East Sea passed away by sudden wave overtopping at the breakwater. Another accident example is the collision of coastal road, breakwater, and residential area near the coastal area near the East Sea. Therefore, development of wave run-up forecasting system is needed under the present circumstances.

Previous research by Na et al. (2011) is a part of a wave run-up forecasting model development. They classified wave run-up values into nine classes. Using these classified classes, they defined these classes which is called 'wave run-up scale'. Moreover, they suggested wave run-up scale forecast model using multiple linear regression method.

In previous research by Na et al., four breakwaters located at East Coast of Korea were used (Aninjin Port, Ayajin Port, Jungja Port, Kyungjung Port) to multiple linear regression. The offshore wave data from the above four breakwaters are used as independent (explanatory) variables, and the wave run-up scale data are used as dependent variable. The wave run-up scale data are observed in photographed form on January 2008 ~ September 2008. The length of data is from January to June for making a regression model, and from July to September for validation of the model.

In this research, wave run-up scales which are defined and observed by previous research are applied to Artificial Neural Network model. The form and length of data are the same as previous research for comparison of results. The accuracy criteria to compare two models are mean absolute error (MAE) and probability of detection (POD). Additionally, index of agreement was proposed to represent ANN model performance. The range of training data for ANN is from January 2008 to June 2008, and the range of test data for ANN is from July 2008 to September 2008. These are the same set of timelines used in previous research for comparison convenience. Lastly, comparison results between ANN and previous regression model are proposed using accuracy criteria values that are mentioned above.

2 COMPOSITION AND APPLICATION OF ANN MODEL

2.1 Composition of ANN model structure

The Artificial Neural Network (ANN) model is a kind of machine learning model that consist of input vector, output vector, weighted vector, bias vector, and transfer function. The Input variables were applied to ANN in a form of input vector. In the ANN model, input vector multiplies by weighted vector and results of multiplication were added with bias vector. Next, it was transferred to the transfer function and this function

releases final forecast results. This result is in the same form of dependent variables of regression model. These series of process are called 'Training'. If differences between final results by training procedure and observed values were bigger than critical error values, ANN would perform the above training process again until good training results were derived. After training ANN model, test step should be occurred for validation of ANN model. Input data in test range was applied to weight vector, bias vector, and transfer function which was constructed by training procedure. Following figure shows the schematic diagram of ANN model

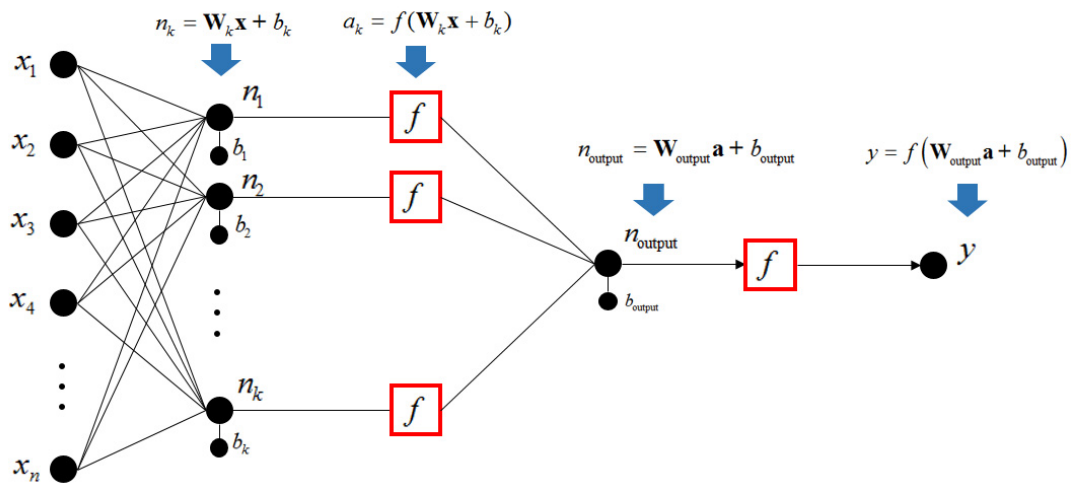


Figure 1. Schematic diagram of ANN.

where f = hyperbolic tangent sigmoid transfer function.

In this research, multilayer back-propagation ANN model was used. In this model, three neural layers (Input layer, Output layer, Hidden layer) exist. When input values which are a form of input vectors were applied to input layer, training process of ANN model was carried out in the hidden layer. In this training process, ANN model makes important vector and bias vector. Output layer releases some results by training process. Finally, validation process was carried out using the test data.

The main problem of applying ANN model is the 'Overfitting'. Overfitting occurs when training process makes ANN excessive fitting of previous data, so ANN model cannot predict expected wave run-up values of future. Excessive fitting in training procedure occurs from immoderate training number (epoch number). Following figure shows the error increase when the test data training number increase. Excessive large epoch number derives high mean absolute error in test procedure.

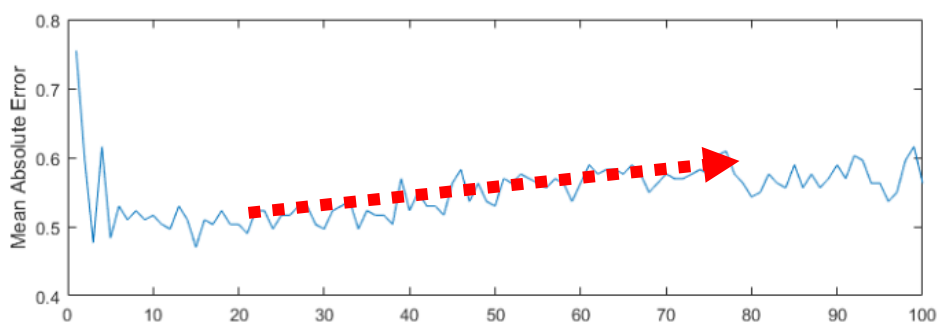


Figure 2. Forecasting error increase in test range by excessive training number.

For reduce overfitting, suitable epoch number should be selected at each forecasting place to ensure optimum epoch number at each forecasting point was decided to avoid overfitting. Increasing epoch number from 1 to 100, where epoch number derives minimum error of test data and this can be found in Figure 2.

Meanwhile, overfitting also can occur when the structure of ANN is highly complex. Hence, to avoid overfitting, appropriate structure of ANN model is being needed. Generally, structure complexity of ANN can be determined by number of neurons in hidden layer. Fletcher et al. (1993) proposed suitable number of neurons in hidden layer to avoid overfitting as follows. Minimum value in following range was used in this research.

$$2\sqrt{n} + m \leq k \leq 2n + 1 \quad [1]$$

where k is number of neurons in hidden layer, n is number of input variables and m is number of outputs.

Retraining ANN model was also a kind of method that can find good generalization results. The number of retraining selected was 400 according to the following figure. The iteration number which occurs with minimum error can derive most generalized test results.

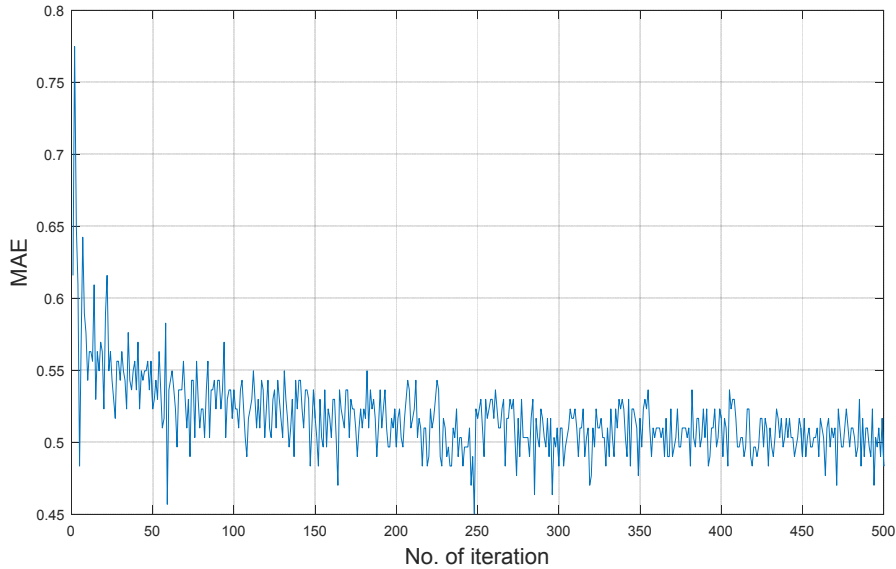


Figure 3. Mean absolute error by iteration number of ANN.

2.2 Data collection

Observation points for measuring wave run-up scale data are shown in Figure 3 from four breakwaters (Aninjin, Ayajin, Jungja, Kyungjung) at the East Sea. Observed wave run-up data were measured by photograph image analysis at each port.

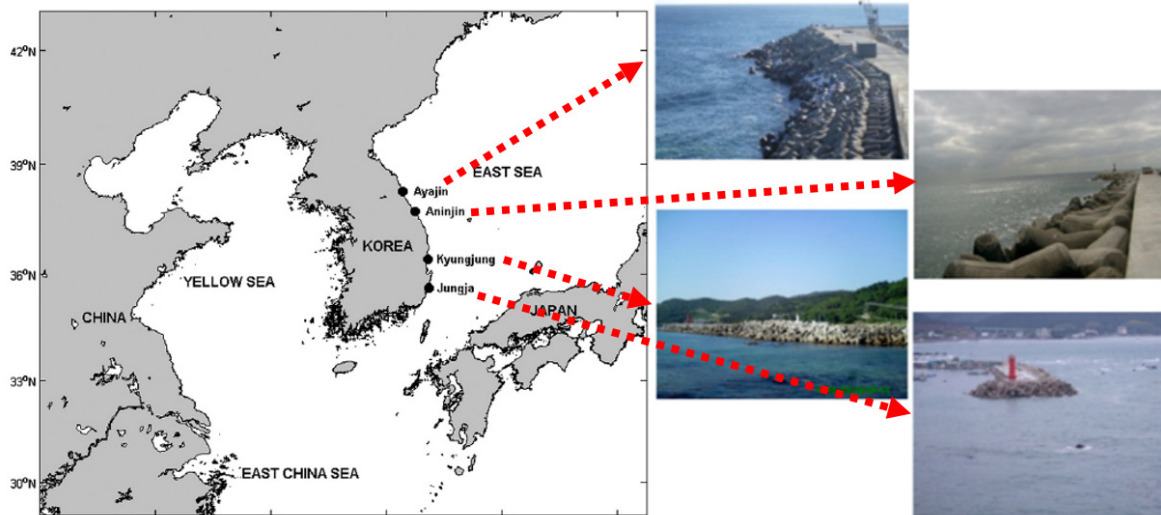


Figure 4. Observation point of wave run-up scale (source: Na et al., 2011).

Brief explanation of wave run-up scale (scale 1 ~ scale 8) are shown in Table 1. The wave run-up scale by Na et al. (2011) were similar to Beaufort Scale and Douglas Scale, which were defined according to various ranges of wave run-up values. The wave run-up scales, especially 4 to 7 in Table 1 would corresponds to significant wave run-up height, $R_s = (1/8 - 3/8)h_c$, $(3/8 - 5/8)h_c$, $(5/8 - 7/8)h_c$, and $(7/8 - 9/8)h_c$, respectively, where h_c is the crest elevation of the breakwater.

Table1. Summary of wave run-up scale (Na et al., 2011).

Scale	Sea conditions	Sea state photo	Scale	Sea conditions	Sea state photo
1	Flat or ripples without crests.		5	Wave run-up height is one half of the crest elevation of the breakwater.	
2	Small wavelets. Crests of glassy appearance, not breaking.		6	Wave run-up height is three quarter of the crest elevation of the breakwater.	
3	Moderate wavelets.		7	Wave run-up height is the same as the crest elevation of the breakwater.	
4	Large wavelets.		8	Most waves overtop the breakwater.	

Following that, input variables in Table 2 were used in this research. For comparison with previous research results, same offshore wave data were used in regression model which were applied to ANN model. All offshore wave data were provided by Japan Meteorological Agency (JMA) from January 2008 to September 2008.

Table 2. Offshore wave data for forecasting model (Na et al., 2011).

Input	Description of Input
x_1	Wave height (m) at the nearest grid point to the breakwater
x_2	Wave height (m) at the point 30 km offshore from the nearest grid point
x_3	Wave direction at the nearest grid point to the breakwater
x_4	Wave direction at the point 30 km offshore from the nearest grid point
x_5	Wind speed (m/s) at the nearest grid point to the breakwater
x_6	Wind speed (m/s) at the point 30 km offshore from the nearest grid point
x_7	Wind direction at the nearest grid point to the breakwater
x_8	Wind direction at the point 30 km offshore from the nearest grid point
x_9	Difference between x_1 and x_2
x_{10}	Product of x_1 and x_3
x_{11}	Product of x_5 and x_7

In this research, Pearson correlation test was applied between each variable and observation of wave run-up scale because usage of highly correlated input variable can produce good ANN model results. Low correlated data were not used to ANN model. For Pearson correlation test, assumption that the data follow normal distribution is needed, but generally, the number of data is more than 100. Normal distribution assumption can be applied. The data number in this research was more than 500, so normal distribution assumption can be used. Table 3 showed the definitive input variables which were selected by Pearson correlation test.

Table 3. Definitive Inputs for ANN model

Port	Input for ANN
Aninjin	$x_1, x_2, x_3, x_4, x_5, x_6, x_8, x_9, x_{10}$
Ayajin	$x_1, x_2, x_3, x_4, x_7, x_8, x_{10}$
Kyungjung	$x_1, x_2, x_3, x_4, x_5, x_6, x_7, x_8, x_9, x_{10}$
Jungja	$x_1, x_2, x_3, x_4, x_5, x_6, x_7, x_8, x_9, x_{10}$

3 CRITERIA FOR COMPARISON WITH PREVIOUS RESEARCH

3.1 Mean absolute error (MAE)

In previous research, mean absolute error (MAE) was used for criteria of model forecasting accuracy. MAE is a typical method for measuring accuracy of model. MAE can be calculated as follows:

$$MAE = \frac{1}{n} \sum_{i=1}^n |X_{obs} - X_{fct}| \quad [2]$$

In above formula, X_{obs} shows the observed wave run-up scale, and X_{fct} shows the forecasted wave run-up scales by ANN model. n shows the number of data in test range.

3.2 Probability of detection (POD)

Probability of detection (POD) is the probability that absolute errors between forecasting wave run-up results and observed wave run-up data are smaller than certain value. In this research and previous research, POD1 and POD2 were used. POD1 is the probability that absolute errors between forecasting wave run-up data and observed wave run-up data were smaller than 0.5. POD2 is the probability that above absolute errors were smaller than one. POD1 can be used for more detailed forecasting criteria than POD2. The definition of POD1 and POD2 can be expressed as follows:

$$POD1 = \Pr(|X_{obs} - X_{fct}| \leq 0.5), \quad POD2 = \Pr(|X_{obs} - X_{fct}| \leq 1) \quad [3]$$

3.3 Index of agreement (I_a)

Index of agreement (I_a) is the criteria that show the overall explanatory power of model. If the model has high index of agreement value, this model can explain relationship between two variables well. It assures good model performance. The definition of index of agreement is as follows:

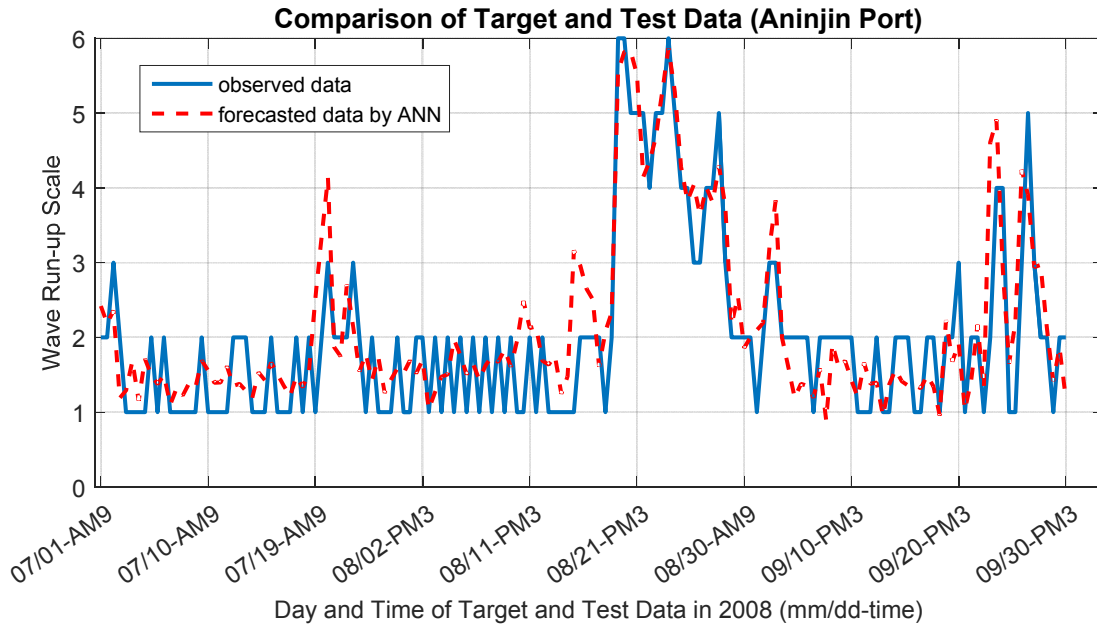
$$\text{Index of Agreement, } I_a = 1 - \frac{\sum_{i=1}^n (X_{obs} - X_{fct})^2}{\sum_{i=1}^n (|X_{fct} - \bar{X}_{obs}| + |X_{obs} - \bar{X}_{obs}|)^2} \quad [4]$$

As the value of index of agreement is nearer the one, a higher explanatory power of model can be guaranteed.

4 RESULTS AND DISCUSSIONS

4.1 Wave run-up scale forecasting results at Aninjin Port breakwater.

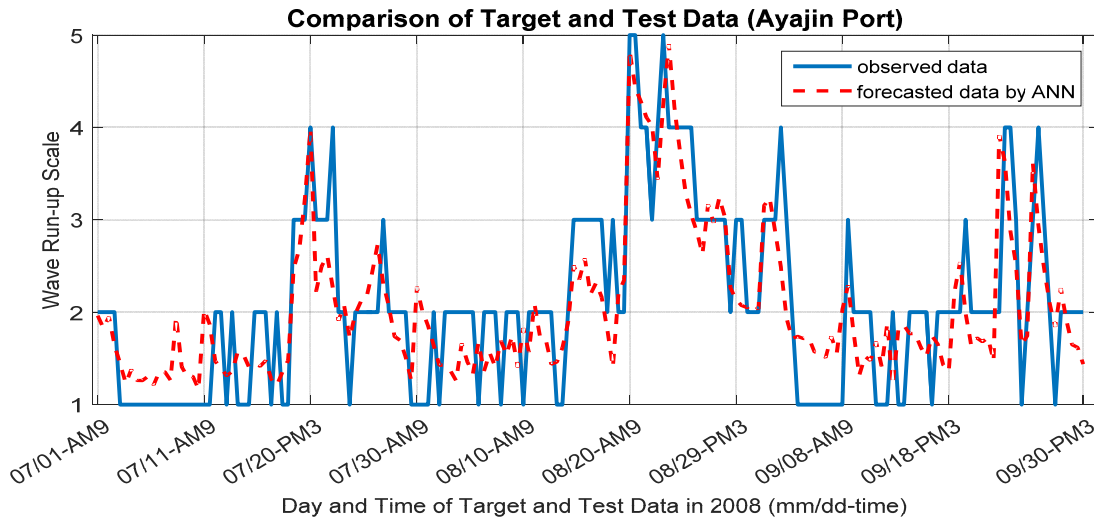
Figure 5 shows the results of forecasting at Aninjin Port breakwater. The figure shows that ANN model was forecasting well in case of high wave run-up scale events. Dashed line shows the forecasted data by ANN model, and straight line shows the observed data. x-axis shows the time sequence of test range (July 1, 2008 ~ September 30, 2008). Some missing observed wave run-up scale data existed in this dataset, so these data were excluded in this research. The number of missing wave run-up scale data in Aninjin Port was 30.



Day and Time of Target and Test Data in 2008 (mm/dd-time)
Figure 5. Forecasting results at Aninjin Port breakwater using ANN model.

4.2 Wave run-up scale forecasting results at Ayajin Port breakwater

Figure 6 showed the wave run-up scale forecasting results at Ayajin Port breakwater using ANN model. The range and type of data was the same as 4.1. The number of missing wave run-up scale data in Ayajin Port was 7.



Day and Time of Target and Test Data in 2008 (mm/dd-time)
Figure 6. Forecasting results at Ayajin Port breakwater using ANN model.

4.3 Wave run-up scale forecasting results at Jungja Port breakwater

Figure 7 shows the wave run-up scale forecasting results at Jungja Port breakwater using ANN model. The number of missing wave run-up scale data in Jungja Port was 15.

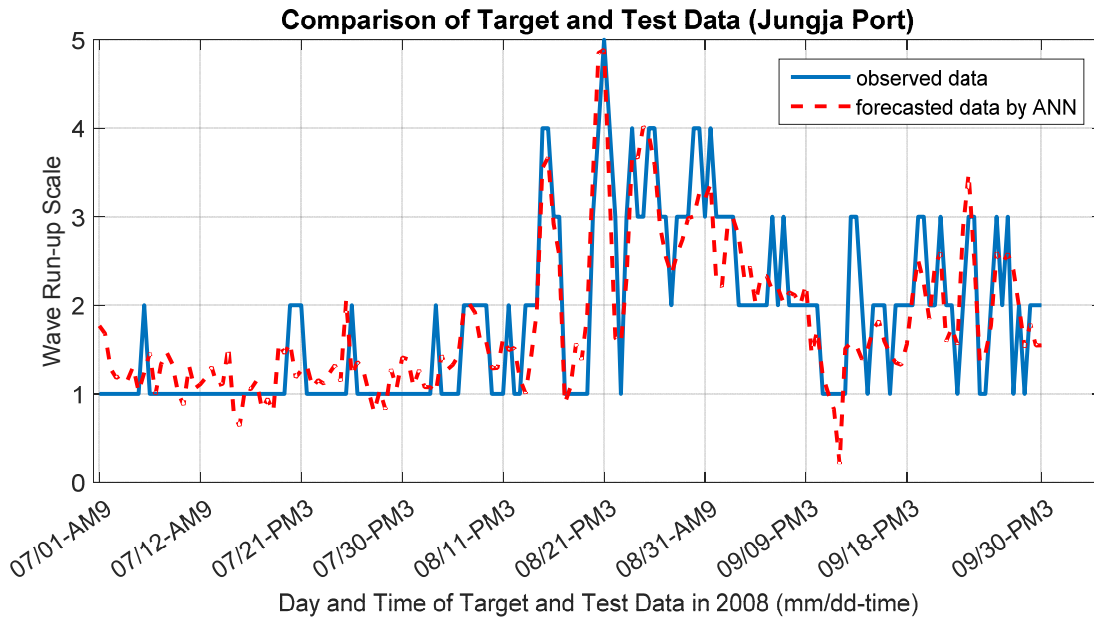


Figure 7. Forecasting results at Jungja Port breakwater using ANN model.

4.4 Wave run-up scale forecasting results at Kyungjung Port breakwater

Figure 8 shows the wave run-up scale forecasting results at Kyungjung Port breakwater using ANN model. The number of missing wave run-up scale data in Aninjin Port was 8.

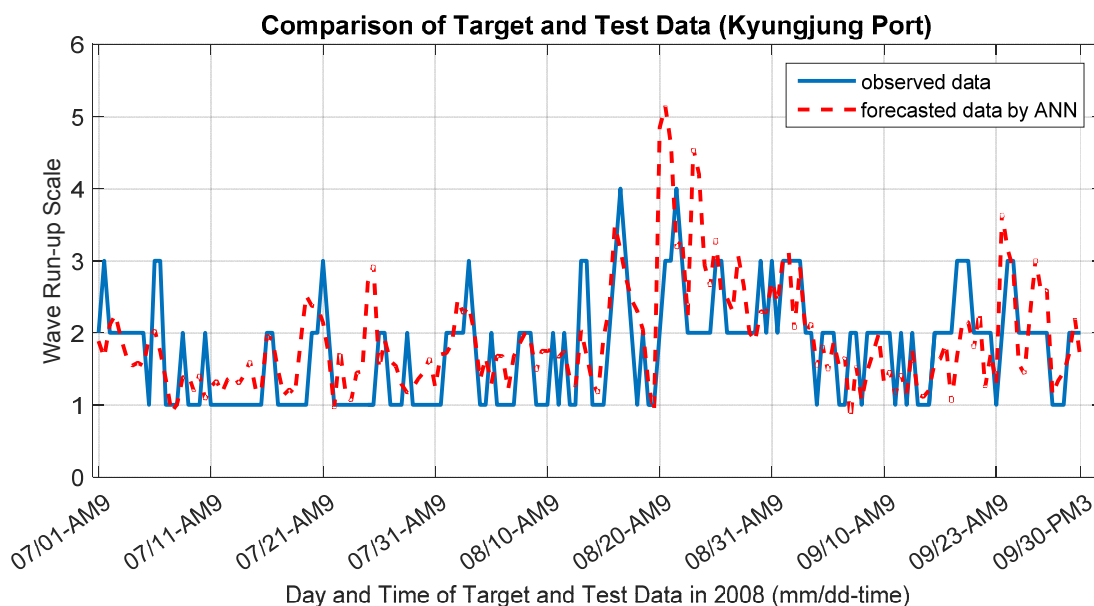


Figure 8. Forecasting results at Kyungjung Port breakwater using ANN model.

4.5 Discussion of results

Table 4 shows the comparison results of each port between ANN model and regression model during the test period. According to Table 4, forecasting accuracy and performance were generally improved when ANN model was applied to forecast wave run-up scale.

Table 4. Comparison of ANN results and regression results.

	Aninjin	Ayajin	Kyungjung	Jungja
MAE by ANN	0.5332	0.4996	0.5091	0.3910
MAE by regression	0.56	0.50	0.50	0.42
POD1 & POD2 by ANN (%)	53.90 / 89.61	53.67 / 92.66	63.64 / 90.34	72.78 / 96.45
POD1 & POD2 by regression (%)	48.40 / 88.40	52.80 / 90.90	50.60 / 90.30	71.40 / 96.40
Index of Agreement by ANN	0.9182	0.8723	0.7457	0.9196

In the case of Kyungjung and Ayajin, they are very little difference in MAE, but POD1 and POD2 were highly improved when ANN model is used. Especially, in case of Kyungjung, POD1 was increased by 13 percent. Also, in Aninjin, both MAE and POD were shown to have better results when ANN model is applied to wave run-up scale. In case of Jungja, significant improvement of MAE occurred that the value of MAE decreased by 0.03. Index of agreement of each breakwater is much higher than 0.9 in the case of Aninjin and Jungja. Ayajin also had comparatively high value of index of agreement. However, in case of Kyungjung, relatively low index of agreement was derived. This is mainly because of the effects of topographic characteristics near the Kyungjung Port. Figure 9 shows the topography near the Kyungjung Port breakwater.

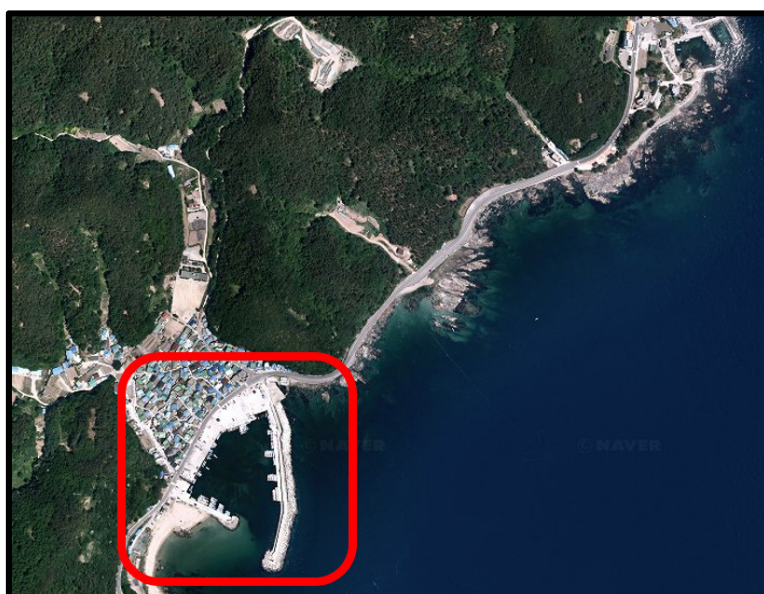


Figure 9. Topography near the Kyungjung Port breakwater.

Breakwater in the red line is Kyungjung Port breakwater. In this figure, Kyungjung Port is partially blocked by northeast land. This land can block the northeast wave, which is the major directional wave in the East Coast of Korea. This topography characteristic makes ANN performance insignificant at Kyungjung Port breakwater.

5 CONCLUSIONS

Through this research, it can be confirmed that performance of wave run-up scale forecasting model using ANN is better than using multiple regression. Especially, in terms of POD, POD1 at each port the value were increased when ANN model is used. So, ANN model is more suitable than regression model when detailed forecasting is needed. However, if topography around the breakwater is complex such as in Kyungjung Port case, the performance of ANN model is not as well as expected. In this case, some structural and topographical parameter should be added to the input vector of ANN. Also, for better performance of ANN model, another offshore wave data must be available to be used at such wave period. Wave period is generally correlated with wave run-up, so wave period data will be able give rise to better performance of ANN. However, in this research, wave period data could not be secured, so additional research concerning wave period will be needed. Additionally, seasonal characteristics will be able to be used in ANN model for better performance.

ACKNOWLEDGEMENTS

This study is performed as a part of the project of “Investigation of large swell waves and rip currents and development of the disaster response system (No. 20140057)” sponsored by the Ministry of Oceans and Fisheries of the Korean government. The Institute of Engineering Research and Entrepreneurship at Seoul National University provided the research facilities for this work. This research is also supported by the BK21 PLUS research program of the National Research Foundation of Korea.

REFERENCES

- de Waal, J.P. & van der Meer, J.W. (1992). Wave Run-Up and Overtopping on Coastal Structures. *Proceedings of 23rd International Conference on Coastal Engineering*, ASCE, Venice, 1758-1771.
- Fletcher, D. & Goss, E. (1993). Forecasting with Neural Networks – An Application Using Bankrupt Data. *Information & Management*, 24, 159-167.
- Goda, Y. (2010). Random Seas and Design of Maritime Structures (3rd Edition). *World Scientific*, Singapore.
- Hagan, M.T., Demuth, H.B. & Beale, M. (2002). *Neural Network Design* (2nd Edition).
- Hedges, T.S. & Reis, M.T. (1998). Random Wave Overtopping of Simple Sea Walls: A New Regression Model. *Proceedings of Institution of Civil Engineers: Water and Maritime Engineering*, 130, 1–10.
- Huang, W. & Foo, S. (2002). Neural Network Modeling of Salinity Variation in Apalachicola River. *Water Research*, 36, 356-362.
- Kobayashi, N., Otta, A.K. & Roy, I. (1987). Wave Reflection and Run-Up on Rough Slopes. *Journal of Waterway, Port, Coastal and Ocean Engineering*, 113, 282–298.
- Kottegoda, N.T. & Rosso, R. (1997). *Statistics, Probability, and Reliability for Civil and Environmental Engineers*. McGraw-Hill, New York.
- Mori, N. & Cox, D.T. (2003). Statistical Modeling of Overtopping for Extreme Waves on Fixed Deck. *Journal of Waterway, Port, Coastal and Ocean Engineering*, 127, 165–173.
- Na, S. J., Do, K. D. & Suh, K. D. (2011). Forecast of Wave Run-Up on Coastal Structure Using Offshore Wave Forecast Data. *Coastal Engineering*, 58, 739-748.
- Pullen, T., Allsop, N.W.H., Bruse, T., Kortenhaus, A., Schüttrumpf, H. & van der Meer, J.W. (2007). *Eurotop — Wave Overtopping of Sea Defences and Related Structures: Assessment Manual*. www.overtopping-manual.com 2007 Die Kuste. Heft 73.
- Sharma, S. & Isik, S. (2013). Deriving Spatially Distributed Precipitation Data Using the Artificial Neural Network and Multilinear Regression Models. *Journal of Hydrologic Engineering*, 18(2), 194-205.
- Sorensen, R.M. (2006). *Basic Coastal Engineering* (3rd Edition). Springer, New York.
- Willmott, C. J. (1981). On the Validation of Models. *Physical Geography*, 2, 184-194.
- Xu, S. & Huang, W. (2010). ANN Applications to Storm Surge Predictions in Apalachicola, Florida. *Proceedings of Computational Intelligence and Software Engineering*, 2010.

EFFECT OF DENSITY DIFFERENCES ON THE FORCES ACTING ON A VESSEL DURING LOCKING OPERATIONS

HELENA I. S. NOGUEIRA⁽¹⁾, TOM O'MAHONEY⁽²⁾, ARNE VAN DER HOUT⁽³⁾ & WIM KORTLEVER⁽⁴⁾

^(1,2,3) Department of Harbour, Coastal and Offshore, Hydraulic Engineering Unit, Deltares, Delft, The Netherlands,
Helena.Nogueira@deltares.nl; Tom.OMahoney@deltares.nl; Arne.vanderHout@deltares.nl

⁽⁴⁾ Rijkswaterstaat, Ministry of Infrastructure and the Environment, Utrecht, The Netherlands,
Wim.Kortlever@rws.nl

ABSTRACT

This paper focuses on the effect of density differences on the forces acting on a moored vessel during locking operations. Based on hydraulic scale model, research performed for the new sea lock in IJmuiden at the entrance to the Port of Amsterdam, it is shown that in the presence of density differences with asymmetric mooring of the ship in the lock chamber, the hydrodynamic forces generated during levelling, and after opening the lock gate, can largely exceed the allowable force limit. In particular, forces in the transversal direction of the ship, which are often not considered in hydraulic research of lock operations, can be significantly larger in these conditions. The forces due to density differences are the dominant forces in the performed tests and the performance of the levelling system cannot be assessed without taking this into consideration.

Keywords: Navigation lock; hydraulic structures; density currents; mooring forces.

1 INTRODUCTION

The new world's largest sea lock is being built in the Dutch coast at the entrance of the North Sea Canal in IJmuiden, connecting the North Sea with the Port of Amsterdam. The new lock will replace the northern lock of the existing lock complex, which was nearing the end of its useful life, ensuring accessibility to the Port of Amsterdam for new generation of sea-going vessels and stimulating the economy in the region while protecting the hinterland from storm surges. The main challenge in the hydraulic design of a navigation lock is to ensure that filling and emptying of the lock chamber occur as fast as possible with a minimum delay for navigation, provided that the hydrodynamic forces acting on the vessels remain acceptable. The magnitude of the forces depends strongly on the type and design of the filling system. In Netherlands, for practical and economic reasons, a hydraulic system through the lock heads is typically preferred to a longitudinal filling system. However, this design leads to a concentration of currents and waves at one end of the lock chamber and, as a consequence, higher forces on the vessel. In order to ensure fast and safe locking operations, force criteria are defined during the design phase of the lock to limit the hydrodynamic forces on the ship due to levelling. For the larger vessels envisaged for the new sea lock of IJmuiden, force criteria are stricter than for smaller vessels since mooring line strengths do not proportionally increase with increasing vessel masses. In addition to the larger expected forces associated with larger vessels and stricter force criteria, the presence of density differences makes the design process even more challenging: the interaction between the salt water on the sea side and fresh water on the canal side leads to the generation of density currents during locking operations that contribute to additional force of component that the mooring lines have to resist.

The forces generated during levelling can be attributed to the combined effect of translatory waves, momentum variation, skin friction, filling jets and density currents (Vrijburcht, 1991). Translatory waves are surface waves caused by the non-constant flow rate through the levelling openings and propagate into the lock chamber, being reflected at the ship and at the gates, resulting in water level oscillations. The filling jet and momentum decrease in the longitudinal direction of the lock, when lower water level in front of the bow of the ship, which contributes to the water level difference between bow and stern. Longitudinal water level differences lead to forces in the longitudinal direction. The effect of the filling jet and skin friction are usually limited, provided that the ship is at a considerable distance from the area of influence of the filling jets and the blockage of the lock chamber cross section by the ship is not very large, which is the situation in the new sea lock in IJmuiden.

In the absence of density differences, the translatory waves and momentum variation are typically the main force components and the resulting force acts in the longitudinal direction of the ship. In the presence of density differences, however, the propagation of the density currents in the lock chamber change the flow patterns and contribute with an additional force component that can be significant. Additionally, if the ship is placed at an asymmetric position relative to the lock centreline, i.e., with one side placed closer to one of the lock walls, which is typically needed for mooring operations, then forces may also build up in the transversal direction due to different vertical density distributions along the sides of the vessel. When the gate opens after

levelling, there is an exchange flow between the water in the lock and the water in the approach harbour, owing to residual density differences after levelling. This can lead to even higher forces on the ship. The ship is usually still moored for a short while after the gate has opened so the forces arising at the beginning of the lock-exchange may still need to be absorbed by the mooring lines. The longitudinal forces can be accurately predicted by numerical tools, provided that they are well calibrated (LOCKFILL, De Looer et al., 2013). As for the transversal forces, at the moment there are no numerical models that can accurately predict their magnitude. Consequently, the transversal force component is usually not taken into account during the design phase of new locks (Roumieu et al., 2008; USACE, 2006; Philpott, 1961) and at the present there is no way of accurately estimating its magnitude without performing physical scale model research or field measurements.

In the context of the new sea lock in IJmuiden, Deltares was commissioned by Rijkswaterstaat (Part of the Ministry of Infrastructure and the Environment) to perform a scale model research in order to test the reference designs for the levelling system of the new lock. More than 200 tests were performed where the complete levelling process was simulated, including the lock-exchange process after opening of the lock gate. This paper focuses on locking operations at the outer head (sea side) since this is the situation leading to the most critical situations in terms of forces due to the relatively high lockage levels at this head. The measured force signals show that in the presence of a density difference, besides the longitudinal force component, a force in the transversal direction builds up pushing the vessel away from the lock chamber wall, during levelling and after opening the lock gate, thus having a direct effect on the tension that the mooring lines have to resist. The position of the vessel in the lock plays a crucial role on the magnitude of the transversal forces: the closer the centre of the ship is to the centreline of the lock the lower the transverse forces are. This scale model research provided unique insight into the hydraulic functioning of the considered levelling systems where density driven currents have a key influence on the forces acting on the vessel.

2 EXPERIMENTAL DETAILS

2.1 Scale model

The experiments were performed in the physical scale model built in the experimental facilities at Deltares. The scale model was constructed geometrically similar at a scale 40 to 1, with the main dimensions of the lock chamber being 70 m × 545 m, with floor at level NAP -17.75 m (NAP: Amsterdam Ordnance Datum), see Figure 1. Froude scaling was used to translate the values from model to prototype scale. The values presented throughout this manuscript are in prototype scale (unless otherwise mentioned).

The main parameters measured over time are water levels, forces on the ship, density and position of the levelling valves and gates. Figure 1 presents the locations where water levels (red circles) and density (blue circles) are measured. The water levels in the model were adjusted by labyrinth weirs placed at the beginning of each approach harbour. To avoid reflections of the translatory waves during tests a constant flow rate was maintained over the weirs by using a suitable pumping system. The water levels were measured by 12 water level sensors (MTS Temposonic®): two sensors were placed in each approach harbour, 6 sensors were placed in the lock chamber and one sensor was placed in each large gate recess. The accuracy of the sensors is 0.05 mm (model scale).

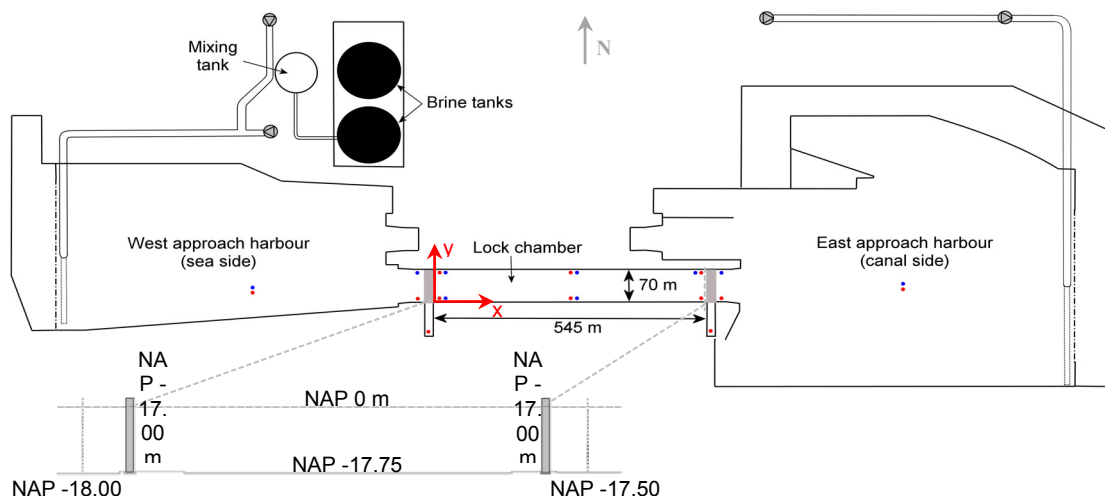


Figure 1. Schematic representation of the physical scale model and location of the water levels sensors (red dots) and density measurement locations (blue dots). Coordinate system (red arrows). Values presented in prototype scale.

Two underground reservoirs supply water to the model: a salt water reservoir supplies salt water to the outer (west) approach harbour and the fresh water reservoir supplies fresh water to the inner (east) approach harbour. A mixing tank (see Figure 1) is used to mix brine and fresh water homogeneously until the aimed density of the saline mixture is obtained. The density was obtained at 9 locations in the model by measuring temperature and conductivity simultaneously at several points in the vertical: 12 points in the conductivity sensors located in the approach harbours and 8 points in the vertical of the sensors placed in the lock chamber. The conductivity gauges have an accuracy of 5 % of the full measurement range and the temperature gauges an accuracy of 0.2 °C. The conversion from conductivity and temperature to density was obtained through the expressions presented in Godefroy (1981), presented below. First a conversion from conductivity to salinity was performed, followed by a conversion from salinity to density according to the “standard equation” for solutions prepared with NaCl (Labrique, 1964). In the expressions below, S is salinity (-) σ is conductivity (mS/cm), T is temperature (°C) and ρ density (kg/m³).

$$S(T, \sigma) = \left(\frac{\sigma}{2.134 \times \left((8.018 \times 10^{-3} T + 1.0609)^2 - 0.5911 \right)} \right)^{\frac{1}{0.92}} \quad [1]$$

$$\rho(T, S) = 999.904 + 4.8292 \times 10^{-2} T - 7.2312 \times 10^{-3} T^2 + 2.9963 \times 10^{-5} T^3 + 0.76427 S - 3.1490 \times 10^{-3} S T + 3.1273 \times 10^{-5} S T^2 \quad [2]$$

A model of a bulk carrier was used as a design vessel (Figure 2), with the main characteristics presented in Table 1. Two force sensors were used to measure the forces acting on a ship. Each sensor was attached to a supporting frame that holds the ship in place in the horizontal plane. The ship was free to move in the vertical direction (heave), so it could follow changes in water level, and it was free to roll and pitch. The connection points (ship- to force sensor) were located in the centreline of the ship at the level of its center of gravity (see Figure 2). The measuring range of the sensors was 50 N (model scale). Three force components were measured (x , y and z directions) in each sensor.

Table 1. Main characteristics of the model vessel. Values presented in prototype scale.

Vessel characteristics	
Length overall L_{oa} (m)	330
Length between perpendiculars L_{pp} (m)	320.75
Breadth (m)	52
Design draft (m)	19.00
Draft in the scale model (m), $\rho = 1000 \text{ kg/m}^3$	14.05
Position center of gravity x_{COG} (m)	146.05
Weight (N)	1.870×10^9
Displacement volume (m ³)	1.906×10^5
Displacement mass (kg)	1.906×10^8
Block coefficient	0.813

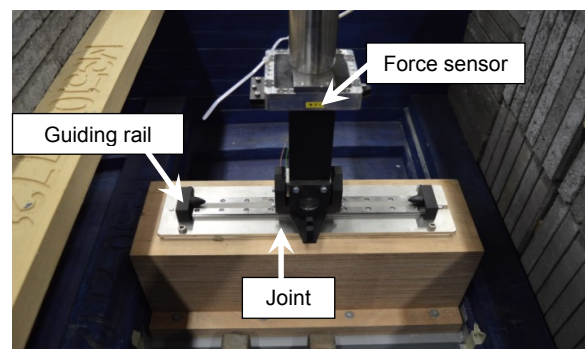


Figure 2. Model bulk carrier viewed from the stern (left) and detail of the joint with the force sensor, seen from the side of the ship (right).

2.2 Levelling systems

Two levelling systems through the lock heads were tested (see Figure 3):

- i. a system of openings in the gate;
- ii. a system of short lateral culverts.

These two types of levelling systems were considered by Rijkswaterstaat as reference designs during the tender phase for the construction of the new lock in IJmuiden. The system of openings in the gate consists of 16 rectangular openings, 2.24 m × 3.04 m each; with the center axis at level NAP –8.50 m. Energy dissipation bars were mounted on the eastern gate plate in each gate. The system of culverts consists of a northern and southern culvert circuit for each lock head. In the outer head, both north and south systems contact directly with the lock chamber, whereas in the inner head the northern culverts contact directly with the lock chamber and the southern culvert connects via the large gate recess. Each culvert circuit consists of two bends: inner bend and outer bend. The flow in each bend is regulated by a vertical sliding valve. The cross-section of each culvert bend is 4 m × 5 m. The hydraulic design of the levelling system has been done on the basis of numerical flow models (CFD), using STAR-CCM+ (O'Mahoney and De Loo, 2015).

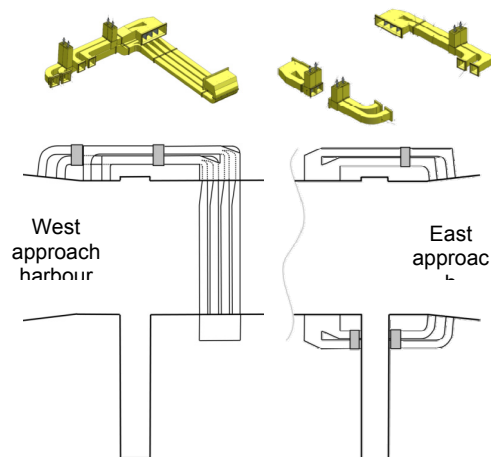


Figure 3. Levelling systems: gate openings (left top, view of the outer gate from the lock chamber) and culverts (left bottom, view of the northern culvert at the outer head; right, schematization of the culverts).

2.3 Force criteria

The maximum hydrodynamic force allowed on the ship during levelling and after opening the gate is fixed at 0.20% in the longitudinal direction (x -direction) and 0.12% in the transversal direction (y -direction), at the position of both forward and aft perpendiculars, expressed as a permillage of the weight of the volume displaced by the ship. This corresponds to the following force limits:

$$F_{x,lim} = 1.906 \times 10^8 \times 9.81 \times 0.20 / 1000 = 374 \text{ kN}$$

$$F_{y,lim} = 1.906 \times 10^8 \times 9.81 \times 0.12 / 1000 = 224 \text{ kN}$$

The force criteria were defined in an earlier stage of the project, initially based on a static equilibrium approach, following the method described by Vrijer (1977). In a later stage of the project the applicability of these criteria had been verified using the dynamic mooring model SCHAT (Van Kleef, 1990), in which the vessel movements and tension in the mooring lines were simulated in time, including dynamic effects and handling of the winches.

2.4 Experiments

An extensive data set was obtained during this research by varying the levelling system, active head, levelling scenarios, water level conditions, density differences, type of vessel, and position of the vessel in the lock. A series of 7 filling tests at the outer head were selected for discussion in this paper. The parameters of the selected tests are summarized in Table 2. The parameters that had been varied in the selected tests were the initial density difference, $\Delta\rho_0$, and the transversal position of the ship in the lock chamber, Δy . The selected tests can be roughly divided in two subseries:

- i. three tests with increasing density difference, using culverts;
- ii. four tests with a ship positioned at different transversal distances from the quay wall, using gate openings.

In both subseries, the ship was kept at 50 m in the longitudinal direction from the active gate and moored at the northern quay wall. The water levels in the selected tests (Table 2) correspond to the levels leading to the maximum water level difference expected at the outer head. The water level in the lock chamber, $h_{lock,0}$, is the initial mean value measured by the 6 water level sensors in the lock chamber. Similarly, $h_{ah,0}$ is the initial mean value measured by the two water level sensors in the approach harbour. The initial water level difference over the active lock head, Δh_0 , is given by $\Delta h_0 = h_{ah,0} - h_{lock,0}$. The transversal position of the ship, Δy , is measured between the ship side and the (northern) quay wall. At a distance of $\Delta y = 9$ m, the ship is

positioned at the centreline of the lock, resulting in a symmetrical situation in the transversal direction. A smaller value of Δy means that the ship was positioned closer to the quay wall, leading to more asymmetry. The ship was kept at a fixed position for the duration of a test, notwithstanding the vertical displacement with the rising water level.

Table 2. List of levelling tests performed at the outer head. Abbreviations used: G gate openings, C culverts, Y yes and N no. Values presented in prototype scale.

Subseries	Test	Levelling	$h_{lock,0}$	$h_{ah,0}$	Δh_0	$\Delta \rho_{0,3}$	Δy	Gate	Lifting speed
i	1.1	C	-0.73	+4.00	4.73	0.0	1.5	N	3.5; 4.4 /2.4
	1.2	C	-0.66	+4.05	4.72	10.6	1.5	Y	3.5; 4.4 /2.4
	1.3	C	-0.59	+4.04	4.62	19.2	1.5	Y	3.5; 4.4 /2.4
ii	2.1	G	-0.76	+4.01	4.77	19.6	1.5	Y	0.82
	2.2	G	-0.75	+4.00	4.75	20.1	3.0	Y	0.82
	2.3	G	-0.74	+4.01	4.75	21.2	6.0	Y	0.82
	2.4	G	-0.75	+4.01	4.74	20.8	9.0	Y	0.82

The acquisition frequency of the measurement signals is 15 Hz (model scale). The water level signals were filtered with a moving average filter with 32 s width in order to attenuate the short period oscillations from the signal. The water level difference in the lock in the longitudinal direction is given by:

$$\Delta h_{LN} = h_s - h_b \quad [3]$$

where h_s and h_b are the instantaneous mean values measured by the two water level sensors at the downstream end of the lock, after the stern, and by the two water level sensors at the upstream end, in front of the bow, respectively. This variable can be compared with the explicit force measurements because a first-order approximation of the hydrodynamic forces on a vessel is given by the water level slope multiplied by the weight of the vessel. The discharge entering the lock chamber, Q , is determined by the variation of the water level in the lock chamber in time:

$$Q = A \times \frac{dh_{lock}}{dt} \quad [4]$$

where A is the wetted area (545 m × 70 m). The resulting discharge is also filtered using a moving average filter with 32 s width.

The speed of the denser current was estimated by tracking the instant front passed by the density measurement locations. The interface was defined by a threshold corresponding to 5 % of the initial density difference. The interface height, h_{int} , is defined as the vertical distance between the interface level and the lock floor and is normalized by the local water depth in the lock: $h_{int}^* = h_{int}/H$.

Two force sensors were used to measure forces in the longitudinal and transversal directions of the ship. The ship is free to rotate and move in the vertical direction. Also, at the rear measurement point (closer to the stern) the ship was free to move along the guiding rail in the longitudinal direction. Thus, at the foremost measurement point forces in the longitudinal and transversal directions (surge and sway) were measured and at the rear point only forces in the transversal direction (sway) were measured. The forces in the longitudinal and transversal directions and the moment about the vertical axis are determined by:

$$F_x = F_{x,1} + F_{x,2} \quad [5]$$

$$F_y = F_{y,1} + F_{y,2} \quad [6]$$

$$M_z = d_1 \times F_{y,1} - d_2 \times F_{y,2} \quad [7]$$

where F_x is the total longitudinal force, F_y is the total transversal force, and the subscripts “1” and “2” represent the contributions of both force sensors (“1” closer to the bow and “2” closer to the stern), M_z is the moment about the vertical axis, mid ship ($L_{pp}/2$), d_1 and d_2 are the distances from mid ship to the force sensors. For the movement along the guiding rail in the rear measurement point (see Figure 2) a static friction force must be overcome (in the range 2 - 4 N, model scale), for this reason, the total longitudinal force F_x also includes the measured force $F_{x,2}$. The forces applied on the forward and aft perpendiculars are obtained by:

$$F_{fp} = 0.5F_y + M_z/L_{pp} \quad [8]$$

$$F_{ap} = 0.5F_y - M_z/L_{pp} \quad [9]$$

The forward and aft perpendiculars are at a distance $L_{pp}/2$ from mid ship; the forces are given at the height of the center of gravity. The forces presented here are related to a ship-fixed coordinate system, in which the positive longitudinal force points towards the bow and the positive transversal forces were directed away from the lock wall at which the vessel was moored. The longitudinal force signal was filtered by applying a low-pass filter with cut-off frequency of 0.08 Hz, in prototype scale (periods longer than 12 s are not filtered). This frequency was based on the natural frequency of the measuring system, which is approximately 0.11 Hz (9 s) in the longitudinal direction. In the transversal direction, the natural roll oscillation of the ship can lead to transversal forces, even though the ship is free to roll. The relatively high frequency roll oscillation is a relevant physical phenomenon but it is also partly a result of the measuring method in the scale model (i.e. a model effect), since, as a result of the coupling between roll and sway, roll motions will always also lead to transversal forces in the sway-captive measurement setup. To help interpretation of the measured transversal forces frequencies larger than 0.04 Hz (periods shorter than 25 s) were filtered out.

3 RESULTS

3.1 Levelling process

Figure 4 represents an overview of the entire lockage process for one of the performed filling tests (test 2.1, see Table 2). The exact instant of start levelling (SL) is determined at the instant the valves start to move. The levelling process ends (EL) when the water level difference over the active lock head reaches the pre-defined value for which the gate was allowed to be opened. In the presented plots the instant the gate was open (GO) corresponds to the instant the gate reached the fully opened position.

In the beginning of levelling, as the water level at the bow increases faster than at the stern, a (negative) force develops pushing the ship away from the active lock head (Figure 4c). The maximum longitudinal negative force occurs at the beginning of levelling and was related to the initial translatory waves. Its magnitude depends mainly on the type of vessel (blockage) and variation of the flow rate, this being a function of the initial water level difference, levelling system and initial discharge. The maximum longitudinal force (positive force) during levelling occurs close to the moment of maximum discharge and is due to the effect of density pushing the ship towards the (saltier) active lock head. After the dense current had passed the stern ($t \sim 1200$ s, Figure 4e), the longitudinal forces started to decrease.

The forces in the transversal direction (Figure 4d) start to rise as the current passes along the ship. The force direction is towards the saltier side of the lock, i.e., towards the wider part of the lock, pushing the ship away from the northern quay wall. A second force peak appears ($t \sim 1700$ s, Figure 4d) and was related to the internal wave generated by the dense current reaching the ship after being reflected at the downstream gate. This peak was also observed in tests where the gate does not open after end levelling (not shown here). When the gate opens, the oncoming denser flow will interact with the reflected wave. However, it is not yet clear how this interaction affects the forces.

Figure 4e shows that the propagation of the density current was asymmetric with the ship placed at an asymmetric position in the lock ($\Delta y = 1.5$ m), travelling faster in the wider part of the lock than in the narrow part (and under the ship). The interface height is substantially different between the two sides of the ship: in the narrow part the denser current had a limited vertical development, the interface remaining at about 30 % of water depth during levelling, whereas in the wider part the interface reaches about 60 %.

As the gate opens after levelling, salt water with higher density than the mixed fluid in the lock enters the lock chamber and, at the same time, the upper fresher layer flows out of the chamber. Due to the exchange flow, the zone at the entrance of the lock was dominated by high flow velocities in both directions (in, at the bottom, and out at the surface) and the interface rises due to the entrance of denser fluid into the lock chamber (note: the location of the interface could not be determined accurately above the highest – wet – density measurement point. This is the reason why in Figure 4e the interface height seems initially not to reach the free surface but eventually does so after some time). When reflecting off the gate at the downstream end of the lock, the interface height increases significantly and thereby mixing saline and fresh water, resulting in a lower average density in the reflected denser current than in the incoming denser current. These differences in flow velocity and density distribution contributed to a greater water level difference in the longitudinal direction ($t > 1800$ s, Figure 4b) and as a consequence the ship was subjected to a force of about $2.5 \cdot F_{x,lim}$ pushing it towards the open gate ($t \sim 2200$ s, Figure 4c).

3.2 Effect of increasing $\Delta\rho$

Figure 5 represents the measured forces and interface heights for the tests in subseries i, performed with increasing initial density difference (see Table 2).

The initial levelling phase was dominated by the translatory waves and since the tests were performed under similar initial water level conditions and using the same levelling system with same valves lifting speed, a similar longitudinal force evolution was expected for the three tests. After the denser current had propagated a certain distance in the lock chamber, its effect becomes noticeable by the attenuation of the oscillations in the longitudinal force signal with an increase of the force magnitude in the longitudinal direction. The

oscillations in the force signal generated at the beginning of levelling due to the transitory waves were slightly attenuated in the presence of a density difference. This density effect might be explained by internal flow dynamics, where energy from the main flow was being transferred to feed internal phenomena occurring at the interface between fresh and denser currents (for instance, used in the generation of Kelvin-Helmholtz billows).

The increase of the longitudinal forces due to the arrival of the density current occurs earlier at the test with higher density difference (test 1.3, blue line in Figure 5) because the front propagates with higher speed, reaching the bow of the ship earlier. After the dense current had passed the stern ($t \sim 1100$ s, Figure 5g), the longitudinal forces decrease. The maximum longitudinal and transversal forces were clearly due to the effect of density, as can be seen by comparing the maximum positive forces between the tests without a density difference with those including a density difference. The maxima were reduced only slightly, about 10 % during levelling, when the initial density difference was reduced by half (test 1.2, grey line in Figure 5). After opening the gate the difference in extreme forces was more noticeable between tests, where the maximum F_x is reduced about 30 % in test 1.2.

The current speed is a function of the density difference, increasing with it (Benjamin 1968). The mean speed of the denser current was 0.56 m/s in test 1.3 ($\Delta\rho_0 = 19.2 \text{ kg/m}^3$) and 0.46 m/s in test 1.2 ($\Delta\rho_0 = 10.6 \text{ kg/m}^3$). The density difference also affects the interface height, where a lower density difference leads to a higher interface height in front of the bow (Figure 5d), slightly lower interface height after the stern (Figure 5g) on the sides of the ship (Figure 5e,f). This was related to the lower propagation speed of the denser current. The lower discharge of salt water towards the downstream end of the lock results in accumulation of more salt water in front of the bow, given the same discharge of salt water into the lock. Because of these phenomena, the hydrodynamic forces on the ship do not scale linearly with the density difference. The interface heights tend to match between tests towards the end of levelling and towards the end of the test, after opening the gate.

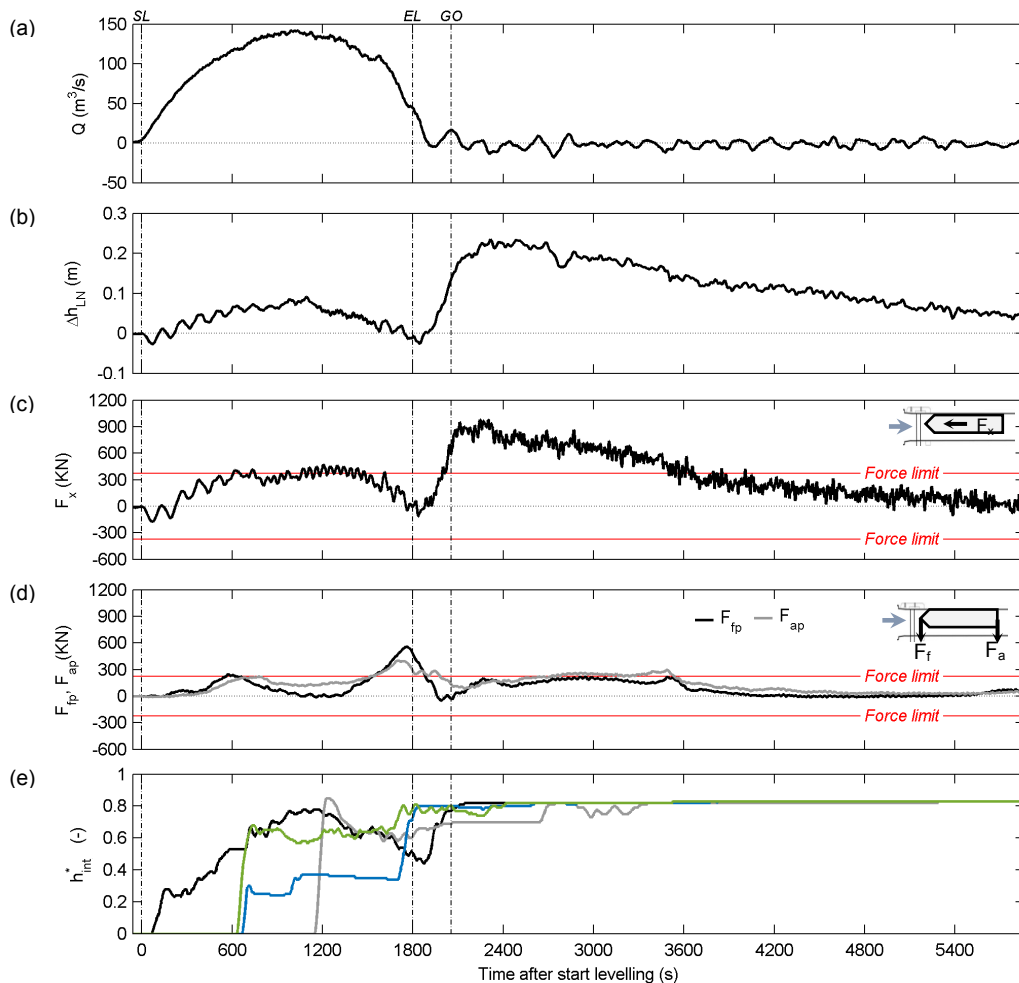


Figure 4. Levelling results for test 2.1 (see Table 2); (a) discharge through the levelling system; (b) water level difference in the longitudinal direction; (c) force measured in the longitudinal direction and longitudinal force criterion (374 kN, red lines); (d) transversal force components and transversal force criterion (224 kN, red lines) and (e) normalized interface height measured in front of the bow (black line), in the wider part of the lock (green line), in the narrow part of the lock (blue line) and after the stern (grey line).

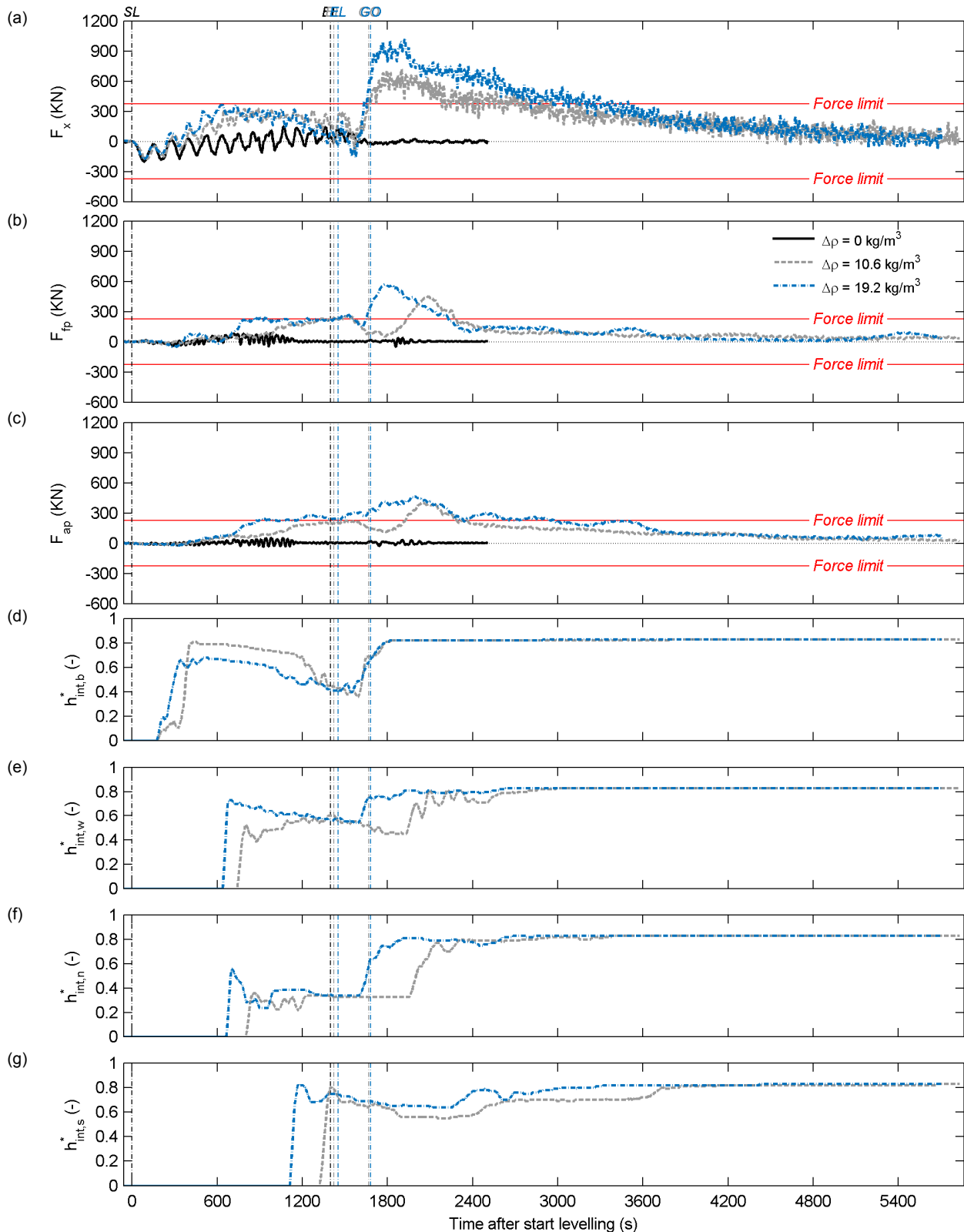


Figure 5. Levelling results for tests in subseries i, with increasing initial density difference (see Table 2); (a) force measured in the longitudinal direction and longitudinal force criterion (374 kN, red lines); transversal force components F_{tp} (b) and F_{ap} (c) and transversal force criterion (224 kN, red lines); normalized interface height measured in front of the bow (d), in the wider part of the lock (e); in the narrow part of the lock (f) and after the stern (g).

3.3 Effect of increasing $\Delta\rho$

Figure 6 represents the measured forces and interface heights for the tests in subseries ii, performed with a density difference of approximately 20 kg/m^3 with the ship kept at the same longitudinal distance from

the gate (50 m), and at consecutively greater distances from the northern quay wall (see Table 2). The distance $\Delta y = 9.0$ m corresponds to the ship aligned with the centreline of the lock chamber.

The forces in the longitudinal direction (Figure 6a) show that there were no significant differences between tests when placing the ship at different transversal distances from the quay wall. This plot also shows good reproducibility of results for tests performed under the same initial conditions. In the transversal direction, however, the effect of the distance Δy was obvious: the magnitude of the first transversal force peak (Figure 6b, c $t \sim 600$ s) seems to be directly related to the distance Δy since it decreases proportionally as the distance increases. When the ship was placed symmetrically in the lock chamber at $\Delta y = 9.0$ m the transversal forces were reduced to nearly zero. The second transversal force peak originated from the reflected dense current reaching the stern of the ship ($t \sim 1800$ s, Figure 6b,c) was also affected by the transversal location of the ship but it seems to be less sensitive for distances of $\Delta y \geq 6.0$ m. The differences in the interface height in the transversal direction are shown in Figure 6d, e. The interface height on both sides of the ship becomes more symmetric as the ship was placed closer to the centreline of the lock chamber. The density current develops higher in the vertical when there was more space available between the ship and the quay wall. These results show that the magnitude of the transversal forces was directly related to the difference in density distribution between the sides of the ship.

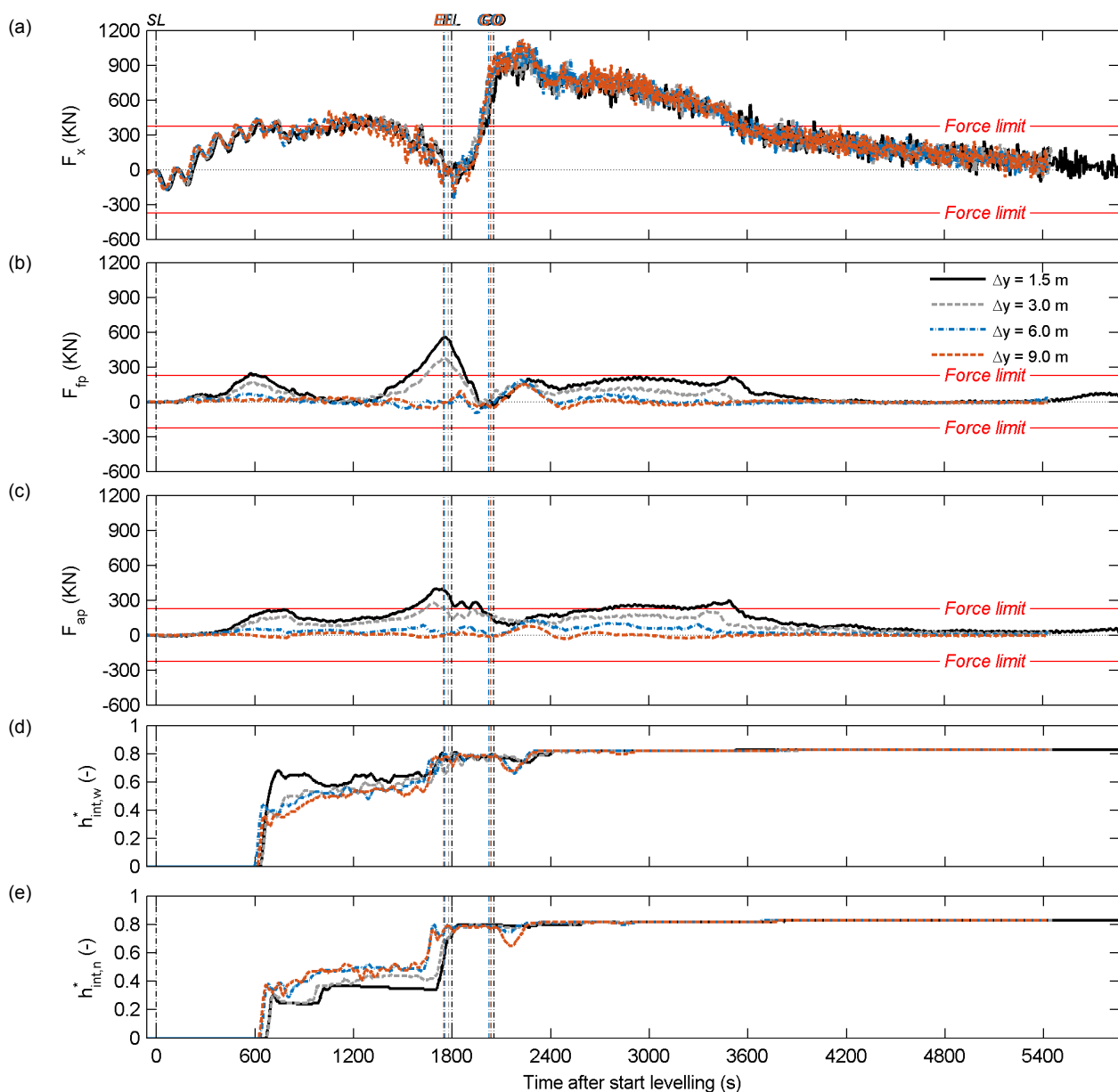


Figure 6. Levelling results for tests in subseries ii, with increasing distance in the transversal direction to the northern quay wall (see Table 2); (a) force measured in the longitudinal direction and longitudinal force criterion (374 kN, red lines); transversal force components F_{fp} (b) and F_{ap} (c) and transversal force criterion (224 kN, red lines); normalized interface height measured in the wider part of the lock (d) and in the narrow part of the lock (e).

4 CONCLUSIONS

The presence of density currents during locking operations increase the forces acting on the ship in the longitudinal direction and in the transversal direction, if the ship is moored asymmetrically in the lock chamber. The mooring lines used to restrict the motions of the ship where it has to resist the combined effect of the hydrodynamic forces. The hydraulic behaviour of a levelling system of a sea lock depends to a large extent on the operational conditions, where the resulting force magnitude depends on the initial water level difference, levelling system, flow discharge into the lock, density difference, and type of vessel and its location in the lock chamber. The hydrodynamic forces generated during filling in the presence of a density difference can be very significant but these can be accurately predicted by numerical models, in the longitudinal direction, provided that the models are well calibrated. As for the forces in the transversal direction, at the moment there are no numerical models that can accurately predict their magnitude.

Based on extensive scale model research, the results presented here show that the maximum forces during levelling are due to density currents, where the maximum measured force can largely exceed the allowable force limit. Decreasing the initial density difference also decreases the maximum force but not in a directly proportional way, i.e., half the initial density difference does not lead to half the maximum forces. This is because the density, speed and interface height of the current, all play a role on the resulting force and these parameters do not vary linearly with density. Placing the ship at a location as close as possible to the lock centreline, although this may be practically less feasible, is the measure tested here that leads to lower forces in the transversal direction. For the longitudinal forces, the reported variations did not lead to significant force reduction. Only by regulating the flow discharge into the lock by using a variable lifting programme and extending the levelling times, it is possible to bring the longitudinal forces to acceptable levels (not presented here).

This scale model research provided unique insight into the hydraulic functioning of the considered levelling systems where density driven currents have a key influence on the forces acting on the vessel. The results obtained in the physical model were also used for validation of numerical models (not presented here) that are valuable tools for the design of future locks. Other future large sea locks (e.g. the New Lock in Terneuzen, The Netherlands) will benefit from this scale model research and the optimized calculations developed through this project.

ACKNOWLEDGEMENTS

The authors wish to acknowledge Rijkswaterstaat for giving permission to use the measurement data obtained during model tests performed for the new large sea lock in IJmuiden.

REFERENCES

- Benjamin, T.J. (1968). Gravity Currents and Related Phenomenon. *Journal of Fluid Mechanics*, 31(2), 209-248.
- De Loor, A., Weiler, O. & Kortlever, W. (2013). LOCKFILL: A Mathematical Model for Calculating Forces on a Ship While Levelling Through the Lock Head. *Proc. PIANC SMART Rivers Conference*, Liège & Maastricht, Paper 93.
- Godefroy, H.W.H.E. (1981). Nieuwe nauwkeurige dichtheidsformules voor zuiver water en zoutoplossingen: dichtheid als functie van temperatuur en zoutconcentratie (New accurate density formula for pure salt solutions). *Delft Hydraulics*, Report S0215-1 (in Dutch), Delft, The Netherlands.
- Labrique, J. P. (1964). Portable Conductivity Meters for Low or Medium Salinity Measurements. *Bull. Int. Ass. Scient. Hydrological Sciences Journal*, IX, 4, 59.
- O'Mahoney, T.S.D. & De Loor, A. (2015). Computational Fluid Dynamics Simulations of The Effects of Density Differences During The Filling Process In A Sea. *Proc. 7th PIANC Smart Rivers Conference*, Buenos Aires, Paper 55.
- Philpott, K.L. (1961). Progress Report on The Terneuzen Lock Investigation, *Delft Hydraulics*, Report 667, Delft, The Netherlands.
- Roumieu, P., Roux, S., De Regge, J., Wong, J. & De Mulder, T. (2008). Physical Model for The Filling and Emptying System of The Third Set of Panama Locks. *Int. Navigation Seminar PIANC AGA*, Beijing, Paper 119.
- USACE (2006). *Hydraulic Design of Navigation Locks*, U.S. Army Corps of Engineers, Engineer Manual 1110-2-1604, Washington, D.C.
- Van Kleef, E.A. (1990). Troskrachtcriteria in sluizen: rekenmodel voor scheepsbewegingen en troskrachten (Force Criteria in Locks: Mathematical Model for Ship Movement and Mooring Forces), Part 3 (in Dutch). *Delft Hydraulics*. Report Q0225, Delft, The Netherlands
- Vrijer, A. (1977). Criteria for The Mooring Forces of Ocean-Going Ships in Locks. *17th IAHR Congress*, Baden-Baden (Delft Hydraulics publication no. 189).
- Vrijburcht, A. (1991). Forces On Ships in A Navigation Lock Induced by Stratified Flows. *PhD thesis*, TU Delft, The Netherlands.

SPANISH BREAKWATER DEVELOPMENT IN THE XXI CENTURY

RAMON M. GUTIERREZ⁽¹⁾ & JOSE M. GRASSA⁽²⁾

^(1,2) Centre for Ports and Coastal Studies, Centre of Studies and Experimentation of Public Works (CEDEX), Ministry of Fomento, Spain, ramon.m.gutierrez@cedex.es; jose.m.grassa@cedex.es

ABSTRACT

The purpose of this paper is to present an overview of the important port development which has taken place in Spain in this century, in the ports belonging to the Central Government (Spanish State Port System). It is regarding the design, construction and performance of its breakwaters, including a general summary of its main characteristics and the detail of those of the ports of: Gijón, Ferrol, Coruña, Algeciras and Barcelona, as examples of the most significant structures. A total of 34.46km of breakwaters has been constructed from the year 2000, most of them with depths ranging between -20 and -40m. The paper also includes references to the physical models tests conducted at CEDEX for its design and construction and a brief historical mention of the most relevant breakwaters built in Spain, particularly in the last third of the 20th century.

Keywords: Breakwater; port; Spain; development.

1 INTRODUCTION

It must be mentioned that, along the Spanish economic growth and with the impact of globalization, handling of goods in Spanish Ports increased by 57% in the period 1997-2007, against an average percentage for the 15 EU countries of 26%, according to EUROSTAT, and this explain in part the need for extension of the Spanish port infrastructures.

The most significant breakwaters constructed in the 21th century, most of them in the first decade, were in the State Port System -28. Port Authorities manages them and 44 ports- were under the coordination of the Public Body Puertos del Estado are used in this study. It is clear that it is not possible to include details from all the breakwaters carried out in the State Port System and the Autonomous Regions (10 regions) with coastline, which also manage many smaller ports for fishing and marinas.

An attempt had been made to include certain examples which best illustrate the major problems that Spanish port engineering has been facing with and at same time present the innovative solutions that it has found to overcome them. The problems were such as great depths, strong waves or singular geotechnical problems, which were determined by the need to build new ports or their enlargements with no or few natural protection. This was not only because of the general lack of natural shelter along the Spanish coast, but also for environmental reasons, which make it very difficult to construct along bays, estuaries or river mouths, where the major world ports use for their developments.

In this circumstance, the lack of natural sheltered waters, was not new for the Spanish ports. Although, as it was mentioned, ports were traditionally located in bays and estuaries or in rivers, the aforementioned nature of the Spanish coast, led to a need for breakwaters being built along the history. In this respect, the following can be mentioned (CEHOPU, 1994); the Roman breakwater of Bares Port in the NW of the Iberian Peninsula; the breakwaters of Santander (1575), Gijón (1635) and in the 18th Century those of Málaga, Valencia and Barcelona Ports (Figure 1). Breakwater construction sharply increased in the 19th Century, a trend which continued into the 20th Century.

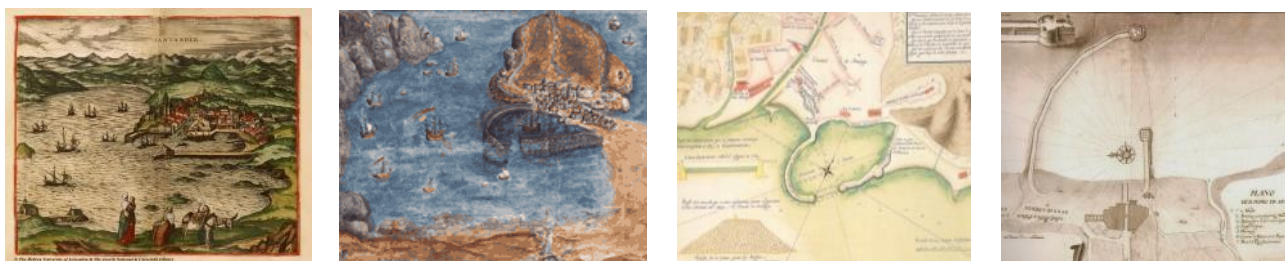


Figure 1. Breakwaters of the Ports of Santander (1575), Gijón (1635), Málaga (1784) and Valencia (1800).

In the last few decades of the 20th Century, the following breakwaters were among the most outstanding (MOPU, 1988): Bilbao (Punta Lucero, 1985), Las Palmas (Reina Sofía, 1972 and subsequent ones), Gijón (Príncipe de Asturias, 1976) and Tenerife (Los Llanos, 1980 and previous ones).

On the contrary, one question that has been a new and major challenge to Spanish port engineering over this century and in the last years, is the sheer scale and singularity of the port enlargements that have taken place and the problems that these circumstances had caused.

In this sense, and only within the scope of the State Port System, a special mention must be made of the following: the magnitude of the breakwaters that have been provided for the new outer ports of Gijón, Ferrol and Coruña, in the Atlantic Ocean, which are 3.8, 1 and 3.4km long, have maximum heights of 48, 49 and 64m and designed according significant waves height (Hs) of 9.5; 7.6 and 15m, respectively, being of rubble mound and caissons typologies; the enlargement to the Algeciras port, with a 2km. Low reflection vertical breakwater were with drafts ranging from 30 to 40m where the geotechnical problems were caused by the mud foundation of the two breakwaters of the Barcelona port enlargement.

Apart from those referred to above, other smaller, but in any case huge breakwaters have been constructed such as in Málaga, Motril, Escombreras, Alicante, Valencia, Sagunto, Castellón, Tarragona, Barcelona (North Mouth), Ibiza and Las Palmas (Reina Sofía and Esfinge). In this century, about 34.46m of large breakwaters have been constructed, where 17.24km were rubble mound type and 17.22km were vertical type. Table 1 provides a summary of the characteristics of all the breakwaters mentioned, and Figure 2 of their nomenclature and some locations.

Table 1. Breakwaters constructed in Spain in the 21th century. State Port System (Puertos del Estado, 2012).

RUBBLE MOUND BREAKWATER CONSTRUCTED IN 21th CENTURY										
Name	L (m)	D _{max} (m)	B (m)	C (m)	h (m)	W (t)	S (H/V)	H _{Sdesign} (m)	t (m)	
Torres. Gijón.	1,416	-22	-	22	44	145*	2:1	9.5	4.6	
Outer Port. Ferrol	1,100	-33	-15	18	51	90*	3.5:2	7.60	4.5	
Outer Port. Main breakwater Coruña.	4,000	-42	-28	25	67	150*	2:1	15.1	4.5	
Outer Port. West breakwater Coruña.	1,500	-34	-10	17	22	15+45**	1.5:1	8,75	5,0	
Enlargement North Valencia.	1,123	-16	-9	12	28	35*	3:2	6.3	1	
East. Barcelona.	2,165	-20	-10	12	32	50*	3.5:2	7.3	0	
South. 1 & 2. Barcelona	3,100	-23/-27	-14	11	33/38	40*	1.75:1	7.3		
North mouth. Barcelona	1,000	-25.2	-10	11	35.2	40*	3:2	6.4	0	
Alicante	1,200	-16	-8	7.5	23.5	20*	3:2	4.4	0	
Esfinge. Las Palmas	302	-39	-10	15	54	56*	3:2	7,3	3.0	
Punta Sollana. Bilbao (construction)	330	-25	-14	15	40	75*	1.5:1	8,5	4.5	
						Total length: 17,236 m				
VERTICAL BREAKWATER CONSTRUCTED IN 21th CENTURY										
Name	L (m)	D _{max} (m)	B (m)	C (m)	W (m)	h (m)	H _{Sdesign} (m)	t (m)		
North. Gijón	1,566	-30	-24.75	24	32.01	48.75	9.5	4.6		
Isla Verde. Algeciras	1,750	-43	32.5	7.5	21.4	40	4.8	1.3		
Levante. Málaga	1,200	-20	-20	10	21.1	30	6.3	0.8		
Motril	550	-20	-12	7.5	21.1	91.5	6.3			
Enlargement Escombreras. Cartagena	1.955	-52	-28	8	24	32	8.1	0.6		
Enlargement North. Valencia	2,271	-16	-	13	19.17	29	6.3	1		
Sagunto	1,204	-15	-	9	19.6	24	6.4	0		
East. Castellón	440	-12	-13	12	19.6	25	7.3	0.5		
East extension. Castellón	358	-15	-13	12	19.6	25	7.3	0.5		
South. Castellón	819	-16	-12.5	12	15	5.20	7.3	0.5		
Enlargement. Tarragona	736	-30	-21.5	8	24	29.5	7	0		
South 2. Barcelona	1,700	-20	-15	11	24.4	26	7,6	0		
North mouth. Barcelona	450	-29	-17.5	6	19.6	25.5	6.4	0		
Botafoc. Ibiza	615	-25	-20	7	21.1	27	6.3	0		
Reina Sofía. Las Palmas	490	-40	-26	12.2	24	38.2	7.3	3.0		
Esfinge. Las Palmas	664	-55	-26	12.2	24.6	38.2	7,3	3.0		
West. Phase 1. Almería	417	-26	-24	7	21	31	5,7	1,4		
						Total length: 17,225				

The investment in the port development during this period had been about 13,000 million euros; having carried out by equal parts of EU FEDER funds, own resources and indebtedness of Port Authorities.

Some outstanding breakwaters have also been constructed in the Autonomous Regions, mainly along the North Coast, highlighting those of the ports of Bermeo, Laredo, Llanes or San Esteban de Pravia and in Canary Island Tazacorte Port. Although it was not in Spain, reference must also be made to the floating breakwater (352 x 28 x 19m) for the La Condamine Port [2] (Hormigón y Acero, 2002 and www.monaco.gouv.mc), which was constructed by two Spanish companies in the Algeciras port and towed to its destination, where it was joined to the mainland with an abutment caisson with a 2.60m diameter knuckle joint, secured by eight chains to steel piles driven into the seabed at depths ranging from 50 to 80m (Figure 3).

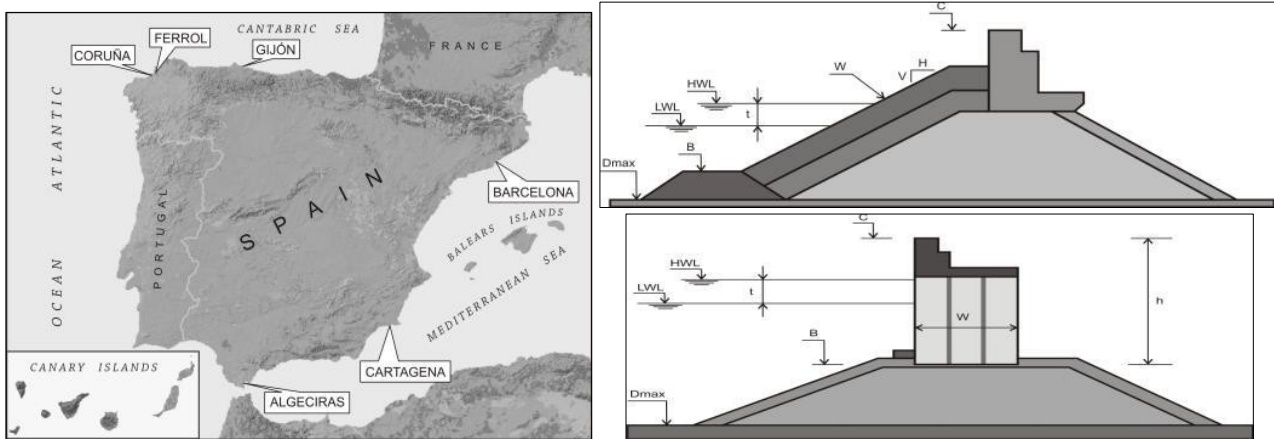


Figure 2. Breakwaters nomenclature and location of main breakwaters included in this paper.



Figure 3. Floating Breakwater. Port of La Condamine (Monaco).

The following are among the most outstanding aspects of these breakwater developments: increased size of the vertical structures; construction of very large rubble mound solutions with blocks of 150, 90 and 200t; innovative construction procedures e.g. caissons laying; introduction of low-reflection vertical breakwaters and breakthroughs made in the geotechnical and structural instrumentation and in wave prediction systems. One circumstance that had been useful in this development is the State Ports Measurement Observation Network (www.puertos.es/oceanografia_y_meteorologia), thanks to which information had been made available about storms. This has been of great help in designing and constructing these breakwaters. Another factor that had been of considerable assistance was the concerns of the Maritime Works Recommendations (ROM).

2 BREAKWATER FOR THE ENLARGEMENT TO THE PORT OF GIJÓN

In view of the fact that the existing port was accommodating more traffic than it had been designed for and there were draught restrictions on vessels, the Port Authority decided to enlarge the port by constructing an outer port close to the current one, to the west zone of previous port (east of Cape Torres). The new port (Figure 4) consists of a 3,834m long breakwater and a 1,250m wharf with draughts from 23 to 27m, which enables three 230,000 DWT bulk carriers to berth at the same time. It will provide shelter for a water surface area of 145ha and will have 145ha of esplanades.

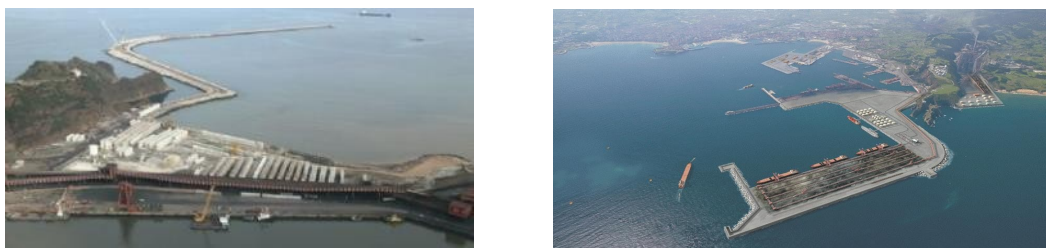


Figure 4. Gijón enlargement. Site of the new port and aerial view of its layout and the previous port.

The breakwater leads off from Cape Torres and is composed of 3 alignments: Torres Breakwater, North Breakwater and the Secondary Breakwater. The Torres Breakwater which is 1,488m long, is a rubble mound structure, lying at depths from 10 to 22m, with a main armour layer of blocks from 10 to 145t, and the crown between elevations were +14 and +24m. Figure 5 shows a cross section of the final section of the breakwater.



Figure 8. State of the works: October 2006 and summer 2007 and 2008.

The entire construction and safety process had been planned on the basis of a wave prediction system (SAPO) developed specifically for these works. This forecasting system furnishes information about exceeding the thresholds of criterias such as significant wave height (HS), peak period (TP) and wind speed. The progress on land works was being determined by $HS > 1.5m$. The works has withstood many storms with significant waves $H_s > 5m$, and in three such storms $H_s > 7m$ was reached, one of which lasted for no less than 3 days. H_s was $\sim 6,6m$ y $H_{maximum} \sim 11.2m$, $TP \sim 18s$ and tide level was $5.5m$. The damage was kept under control in all of these storms, and it only affects the sections under construction and the temporary protect.

3 BREAKWATER FOR THE NEW FERROL OUTER

The traffic growth predictions, together with the diversification strategy, played a decisive part in the Port Authority's decision to opt for new facilities, which have now taken the form of the current outer port, located at the entrance to the Ferrol estuary in the Cape Prioriño zone.

The new port is composed of: a 1,040m long rubble mound breakwater with a 172m long vertical spur breakwater close to its head, and a 1,515m wharf, with 857.8m constructed at the first stage, with a draught of 20m. The facilities include 90m of esplanade. Figure 9 shows the site of the new port and an overview it.



Figure 9. Ferrol Outer Port. Location, layout and overview of the new outer port (2004).

The breakwater is a rubble mound structure sloping $1.75H/1V$, with one alignment of a main armour layer of 90t blocks, the crown being at elevation of $+18m$. The head is also a rubble mound type of 90 t blocks, sloping $2H/1V$ and reaching a maximum depth of 32m. There is also a 172m spur breakwater close to the head at right angles to the breakwater; composed of caissons sunk at $-15m$. Figure 10 shows cross section.

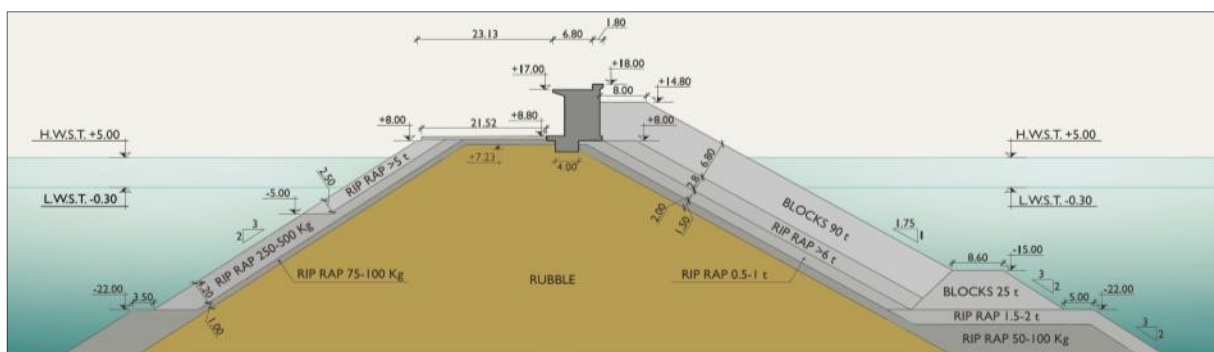


Figure 10. Cross sections of the breakwater.

The shelter afforded by Cape Prioriño ensures that the design waves were from the W, with a significant wave height of 7.6m and a peak period of 18s, for a 280-year return period. A series of 2D and 3D physical model tests were conducted as part of the design process (2D E: 1/43 and 1/15; 3D E: 1/38.5). Figure 11 shows the 2D test in the Large Wave Flume and the 3D test in the Multidirectional Wave Tank, conducted at the CEDEX.



Figure 11. 2D and 3D physical model tests. CEDEX.

The works started in 2001 and were completed in 2004. Before the breakwater construction an auxiliary port was constructed with a 6t. rubble mound breakwater and a 150m wharf for the maritime activities, which made it possible for the breakwater progress to an elevation of -8m, after which the land works began with dumpers, bulldozers and cranes for laying the blocks in place. The breakwater had already withstood several storms with negligible damage. Figure 12 shows the block manufacturing yard and the crane laying the blocks in place and a close-up of the crown construction work.



Figure 12. Block manufacturing yard and crane laying blocks.

4 BREAKWATER FOR THE NEW CORUÑA OUTER PORT

A lack of sea and land space in the current port site, which encroaches upon the urban area coupled with environmental problems and the need to remove the petroleum products at pipelines between the port and the refinery (3km from the city), which cross at underground, meant that in the 1990s, the Port Authority considered to enlarge the port beyond the confines of the city. After a series of studies, a decision was taken to locate the new port at Punta Langosteira, 8km to the southwest of the existing port. The new facilities were to be composed of: a 3,354m long rubble mound breakwater with a vertical spur breakwater lying at 391m to its head, a 921.5m transverse wharf with a draft of 22m and a 579m of secondary breakwater, also rubble mound type. The new port will provide 230.5ha of shelter waters and 143.5ha of esplanades, mooring facilities on the breakwater for 9 200,000 DWT oil tankers and berthing facilities on the wharf for other goods. The mooring line could be extended with others to 3,000m wharf and 230ha of esplanades. Figure 13, shows the site and a simulation of its layout.



Figure 13. Coruña Outer Port. Site, layout and aerial view.

The breakwater has 3 alignments, the first section and two on its main stretch. It will be a maximum of 40m. deep and the crown is at elevation +25m along the main section and at +19m where it leads off. The breakwater head is vertical type at 144m long, composed of 5 caissons, founded of -29m, running at right angles to the centerline of the final stretch. A spur breakwater will be constructed along this stretch, composing of caissons founded of -26m. Figure 14 shows the cross sections of the breakwater main stretch. The contact between the main armour layer and the head is one peculiar area, where 200t blocks were being used in this zone. Another singular zone was the armour layer for the sheltered area, where 150t blocks with holes have been arranged between the head and the spur breakwater and 50t blocks being used for the rest.

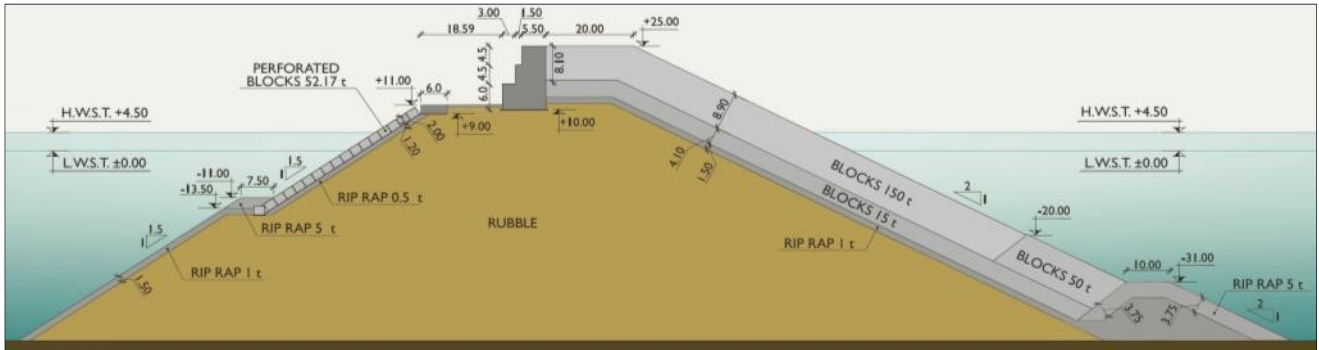


Figure 14. Main Cross sections of the breakwater.

The maritime climate conditions for which the breakwater had been designed were for a return period of 140 years, resulting in a significant wave height (HS) of 15.1m. The way it was distributed throughout the length of the breakwater can be seen in Figure 15.

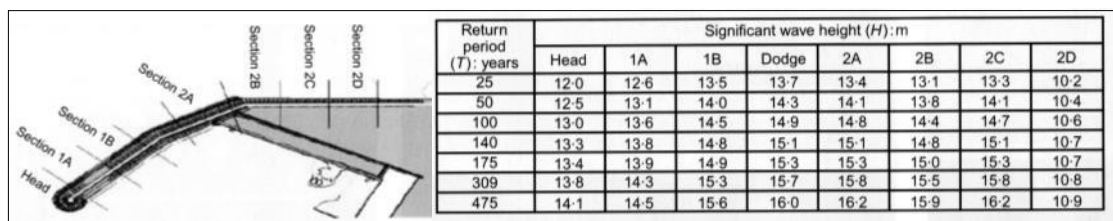


Figure 15. Extreme wave regime throughout the breakwater.

A series of physical model tests were conducted in several laboratories before the design was finally perfected. When the CEDEX was concerned, 2D tests were carried out on the initial section (E: 1/45) and on the main section (E: 1/25 y 1/30), as well as 3D tests on the main section and the head (E: 1/60). Figure 21 shows the tests on the main section in the large flume and the 3D tests in the multidirectional wave tank. The works were initiated in March 2005 and they finished it in September 2011. The first two years were spent carrying out the groundwork: access, quarries, aggregate and concrete plants, block manufacturing yard and the construction of an auxiliary port, consisting of a rubble mound breakwater 503m long with 50t blocks and a 350m wharf. Figure 16 shows the block yard for the main armour layer and the auxiliary port.



Figure 16. Physical model tests, 2D and 3D. CEDEX.

The breakwater construction process (Figure 17) advanced from the sea, the core material being poured in was guided by two retaining side moats, before being protected with 1t quarry stones and 15t blocks, over which the two layers of 150t blocks for the main armour were laid. The aforementioned process was carried out with the use of two of the largest cranes in the world, which are able to lay 150t blocks at a distance of 115m.



Figure 17. Main block yard, cranes and auxiliary port.

The general advance of the breakwater was halted during the winter months. During this period only the barge carries on working, pouring in the core material and the quarry stones. Figure 18 shows how the works had progressed at different dates (2007, July 2008 and May 2009).



Figure 18. State of the Works: final campaign 2007, July 2008 and May 2009.

One aspect concerning the construction process that must be stressed is the safety conditions under which it was taking place, to the extent that for significant wave heights greater than 1.3m, the activities on the breakwater work platform were halted. A specific wave prediction system (SPOL) had been developed for improving the security during the works.

So far, the breakwater has fulfilled expectations where performance is concerned. The 1,600m constructed in 2007 and 2008, have withstood several storms, particularly the ones that happened on 10th March 2008 and 20th January 2009, and January and February 2014, the first one reached the design wave level, without damages being detected. Figure 19 shows the breakwater during these storms.



Figure 19. Storms of 10. 03.2008 and 20.01.2009. Winter head protection.

5 BREAKWATER FOR THE ENLARGEMENT TO THE ALGECIRAS PORT ON ISLA VERDE

By 1990, the Algeciras port, in the south of Spain, overlooking the Straits of Gibraltar, and leading Mediterranean container port, was finding it difficult to cope with the amount of traffic. To overcome this, a decision was taken to carry out the biggest enlargement plan in the port's history, and this was in the zone known as "Isla Verde" (Figure 20). This enlargement consists of a 2,060m long vertical detached breakwater, which provides shelter for two wharves: The North Wharf -680m long with a draught of 17.5m- and the East Wharf -1,540m long with a draught of 18.5m-. There was also a rubble mound breakwater on the south side, with 890m long, which has a 100Ha esplanade. The detached breakwater is a vertical structure comprising 43 anti-reflective caissons with one single alignment, separated 413m from the East Wharf, laid on an armour stone foundation at -35m and crowned at +7.5m, with the seabed at depths from -43m to -28m.



Figure 20. Enlargement to the Port of Algeciras at Isla Verde. Layout and general views.

The top of the caisson cells and the crown cells serve to reduce the reflection level, the first row of these cells were being open, in order to dissipate the incident wave energy, thereby reducing the wave reflected. A cross section can be seen in Figure 21.

A return period of 275 years was taken into consideration when designing the breakwater, which yielded a significant wave height of 4.8m and a peak period of 9s and SSE direction. Several physical model tests were developed at the CEDEX when designing this type of ant-reflective typology (Figure 22). Reductions of 60% being obtained for the reflection coefficient for short periods (< 8s.) and wave heights ranging from 0.5 m to 1 m where reductions of 40 to 20% was being obtained for more severe waves.

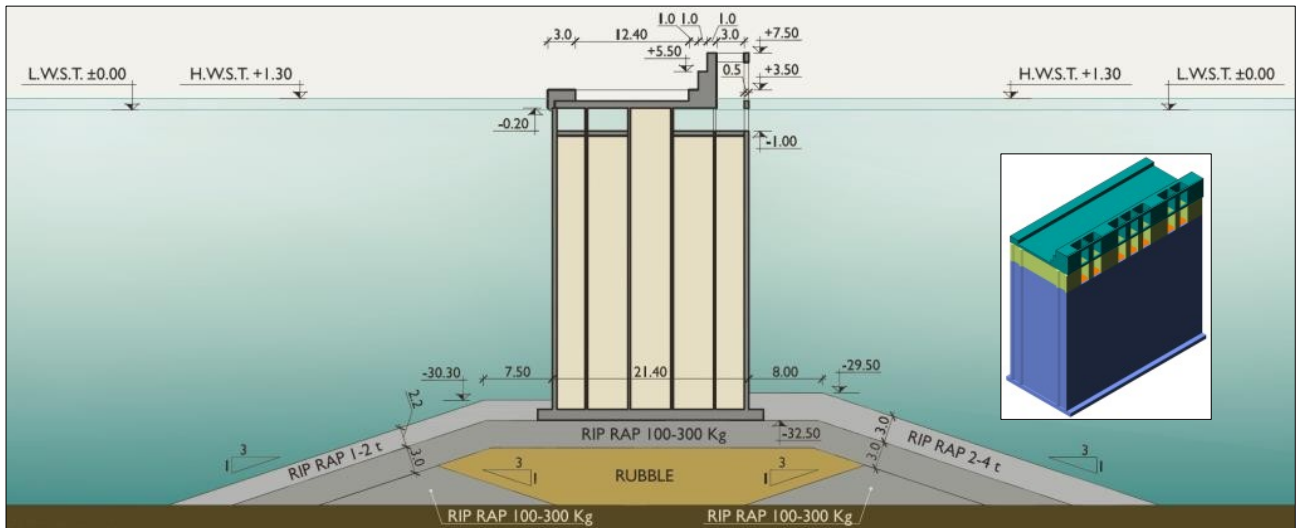


Figure 21. Cross section



Figure 22. 2D Physical Model Tests. CEDEX.

The works commenced in 2006 and have been completed in 2009. It had withstood a storm from the east, on 11th October 2008, causing a deep-water wave height of 7m reaching the breakwater at 3m. The only damage to the structure being slight settlement (less than 10cm) affecting the caissons.

6 BREAKWATERS FOR THE ENLARGEMENT TO THE PORT OF BARCELONA

Towards the end of the 1980s, the Port Authority in order to overcome the following problems: to cater for the increasing growth in traffic, the growing number of vessels and their greater draught, to meet the demand for new land surface areas and to find an acceptable solution for the port-city relationship, devised the “Delta Plan” for the port development. Apart from enlarging the Port, the main activities also included diverting the River Llobregat, enlarging the airport (both lying to the south of the port), increasing the logistics activities area and creating new road and rail infrastructures. The port enlargement works, which began in December 2001, involved the construction of two breakwaters: the 4,800m long Southern Breakwater and the 2,170m long Eastern Breakwater; a container terminal with 1,500m of mooring facilities and a minimum draught of 16m, as well as other mooring facilities, thereby increasing the land surface area by 208ha. Figure 23 shows the enlargement.



Figure 23. Barcelona enlargement Port. General view and final layout.

The breakwaters lie in maximum depths ranging from 23 to 27m. However, it was necessary to take into account the important fact that the seabed has a low bearing capacity with 50 to 70m layer of soft silt and soft silty clay overlying the rock stratum (Puertos del Estado, 2012).

The Southern Breakwater (4,800m) has been split into three Stretches:

- Stretch 1 (2,000m): it is of the rubble mound type, with a main block armour layer from 8 to 60t, depending on the direction of the storm and its angle of incidence, the crown being at elevation +12m. Extensive armour stone foundations have been positioned on either side to guarantee stability against the risk of sliding (Figure 24);

- Stretch 2 (1,700m): is vertical type, 47 caissons at 33m wide and 21.5m depth, founded on an extensive 73m wide armour stone, whose crown is at elevation of +12m (Figure 25);
- Stretch 3 (1,100m): is of the rubble mound type, with a main armour layer composed of 40t blocks at its trunk and the head being formed with two caissons.

The Eastern Breakwater (2,165m) is a rubble mound structure whose foundation was laid in direct contact with the seabed, after a 3m thick trench had been dredged. The main armour layer was composed of 50t blocks (Figure 26).

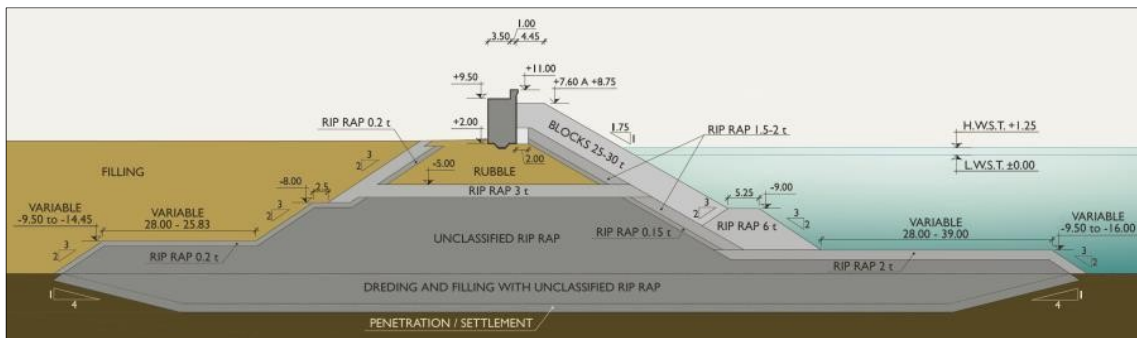


Figure 24. Southern Breakwater, stretches 1 Eastern Breakwater. Cross section.

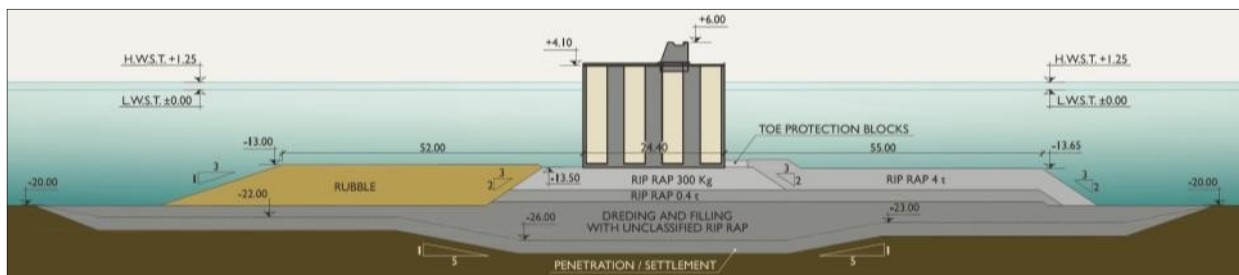


Figure 25. Southern Breakwater. Stretch 2. Cross section.

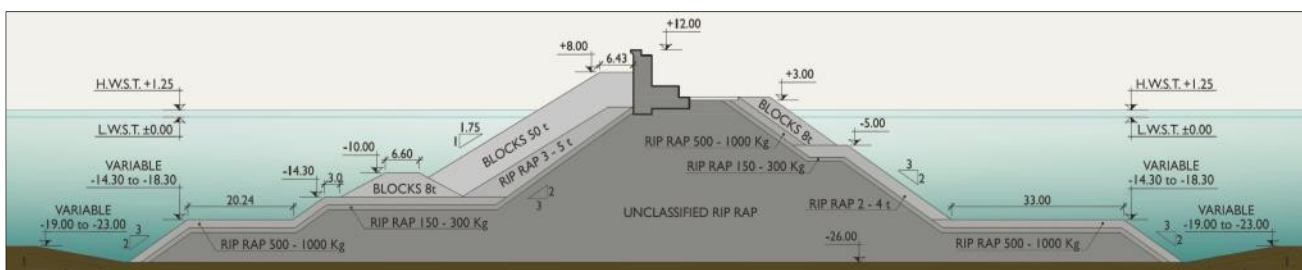


Figure 26. Eastern Breakwater. Cross section.

The maritime climate conditions for which the breakwaters were designed were for a significant wave height of 7.6m along Stretch 2 (vertical) of the Southern Breakwater and 7.3m along Stretch 3 (rubble mound) and for the Eastern Breakwater, a peak period of 13sec. being adopted. A large number of 2D and 3D physical model tests were conducted in CEDEX for the design of both breakwaters and for the construction stages (Figure 27).



Figure 27. Physical models. Eastern & Southern Breakwaters and Eastern construction stage.

The low bearing capacity of the seabed foundation (Puertos del Estado, 1999) -silts and clays- (Figure 28), meant that it was only possible to increase its strength, to make feasible to construct the breakwaters, by consolidating the seabed and dissipating the pore pressures, which was brought about by loads transmitted

as the breakwaters were gradually being constructed. Instruments were placed in 8 sections, 4 for each breakwater [10] (Figure 28) to ensure that construction was consistent with design. The parameters measured were: settlement, lateral deformation and pore pressure.

The construction stages, as it were mentioned, was conditioned by the poor quality of the soil foundation, in such a way that it was necessary to accomplish it in several stages for the soil consolidation. Figure 29 show several construction operations.

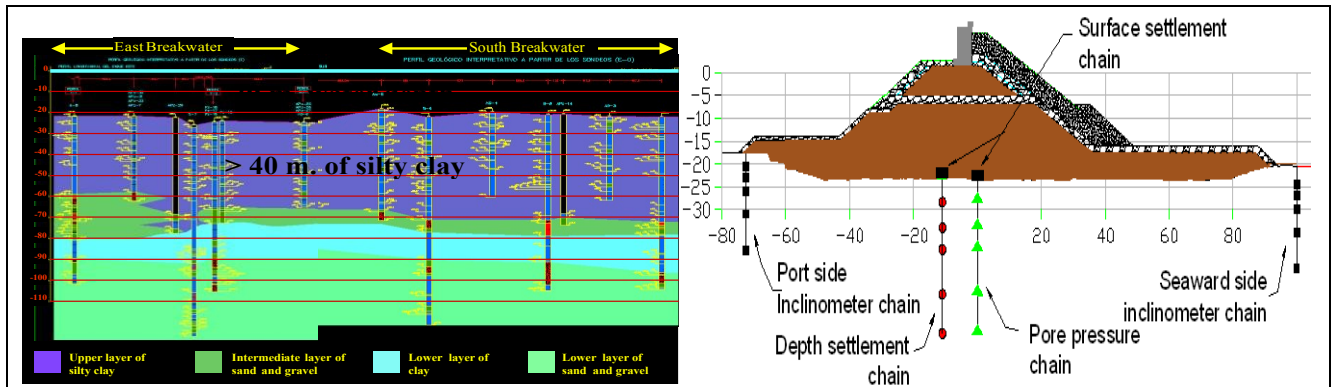


Figure 28. Seabed foundation profile and instrumentation for the rubble mound breakwaters.



Figure 29. Construction stages. Dumping barge, crane blocks placement and caisson sinking.

ACKNOWLEDGEMENTS

We thank the organizers of this Conference for invitation to present this paper. Likewise, we thank the Public Body Público Puertos del Estado and the Port Authorities referred to in the text, for the information received to enable us to prepare this paper and for thrusting CEDEX for the physical model tests developed.

REFERENCES

- CEHOPU (1994). *Puertos Españoles en la Historia*. Centro de Estudios Históricos de Obras Públicas y Urbanismo, CEDEX, Spain.
- Díaz, J.L., et al. (2008). Extension to the Port of Gijón, Spain. In *Proceedings of the Institution of Civil Engineers-Maritime Engineering*, 161(4), 153-174.
- del Estado, P. (2012). *Diques de Abrigo en Los Puertos de Interés General, Años 1986-2011*, Spain.
- del Estado, P. (1999). *Atlas Geotécnico del Puerto de Barcelona*, Ministerio de Fomento, Spain.
- del Estado, P. (1999). *Maritime Works Recommendations*, CEDEX, Spain.
- Grassa, J.M., et al. (2009). Ferrol Outer Port: Experimental and In Situ Design Studies. In *Proceedings of the Institution of Civil Engineers-Maritime Engineering*, 162(2), 57-72.
- MOPU (1988). *Diques de Abrigo en España, Vol. 1 and 2*. Ministerio de Obras Públicas y Urbanismo. Spain.
- Noya, F. (2008). New Port Facilities at Punta Langosteira, Spain. In *Proceedings of the Institution of Civil Engineers-Maritime Engineering*, 161(3), 101-106.
- Uzcanga, J., et al. (2007). *Instrumentation of Barcelona Harbour Breakwaters*, PIANC, issue 127, May 2007.
- y Acero, H. (2002). El Dique Flotante de Mónaco. *Journal "Hormigón y Acero"*, (223-226), Spain.

EXPERIMENTAL INVESTIGATION OF TSUNAMI BORE IMPACT FORCE AND PRESSURE ON A BRIDGE STRUCTURE WITH WING WALL ABUTMENTS

FARZAD FARVIZI⁽¹⁾, BRUCE W. MELVILLE⁽²⁾ ASAAD Y. SHAMSELDIN⁽³⁾ & STUART E. NORRIS⁽⁴⁾

^(1,3) Department of Civil and Environmental Engineering, the University of Auckland, Auckland, New Zealand,
ffar897@aucklanduni.ac.nz; b.melville@auckland.ac.nz; a.shamseldin@auckland.ac.nz

⁽⁴⁾ Department of Mechanical Engineering, the University of Auckland, Auckland, New Zealand
s.norris@auckland.ac.nz

ABSTRACT

Over the last two decades, tsunamis in Indonesia (2004), Chile (2010), and Japan (2011) have caused hundreds of thousands of deaths and billions of dollars of damage to many kinds of infrastructure such as ports, roads, bridges, and coastal dwellings. Failure of the transportation infrastructure in these regions of isolated communities hindered emergency services, delayed emergency repairs, and significantly impacted the recovery of local economies. Many of the bridges, which lie within possible tsunami inundation zones, are critical links in transport networks. Therefore, it is necessary to investigate the effects of tsunamis on bridges. To investigate the tsunami effect, physical modeling experiments have been carried out to measure the characteristics of hydrodynamic forces on bridge structures with varying abutment lengths, for various bore strengths. The experiments are conducted in a 14 m long, 1.2 m wide and 0.8 m deep wave flume equipped with an automatic gate designed to generate a tsunami bore. Forces and pressures exerted on the bridge model are measured, and a relation between bore velocity and bore height is presented. The results show that horizontal and uplift forces increase with increasing bore height. The vertical reactions increase with increasing abutment length, except the 300mm length, which is due to the significant amount of water accumulation on the seaside of the bridge structure while the horizontal pressures were slightly sensitive to the variation of the abutment length.

Keywords: Tsunami forces; horizontal pressures; wing wall abutment; bridge structure.

1 INTRODUCTION

The recent tsunami events of Tōhoku earthquake (magnitude 9.0) on March 11, 2011, and Sumatra Island in Indonesia on December 26, 2004, shocked the whole world, especially South-East Asia. The subsequent huge loss of human lives in these disasters has reminded the international scientific community to investigate tsunami interaction with coastal structures. Such investigations provide useful information for designing tsunami resilient structures and useful information to plan the mitigation of tsunami effects on the coastal communities especially bridge structures. Flow depth and velocity as the main tsunami flow characteristics are highly variable. For instance, the maximum runup height of 38.2 m and 28.7 m were recorded for the 1896 Meiji and 1933 Showa tsunamis, respectively (Suppasri et al., 2013). During the 2011 Tōhoku tsunami, the flow depth reached 8 m at Kamaishi City (Fraser et al., 2012), and 6 m at Arahama Town (Suppasri et al., 2012). The tsunami waves traveled with an average velocity estimated to be between 3 and 4 m/s at Kamala beach and 6 to 8 m/s at Khao Lak (Rossetto et al., 2007). The tsunami flow velocity reached between 10 to 13 m/s on a coastal plain close to the Sendai Airport (Jaffe et al., 2012). It was estimated about 8 m/s at 1 km inland of the shoreline in Sendai (Hayashi and Koshimura, 2013). Figures 1 and 2, show washed away concrete and steel girder bridges, respectively, during the Japan Tsunami.



Figure 1. Washed away concrete girder bridge (Mazinani et al., 2014).



Figure 2. Washed away girder bridge and truss bridge (Mazinani et al., 2014).

The extensive bridge failure caused by the recent tsunamis, particularly the unprecedented 2004 Indian Ocean tsunami and tsunami of Tōhoku, indicates an urgent need for an efficient tsunami load estimation method for bridges. In the Tōhoku tsunami, more than 300 bridges were washed away by the tsunami. It was observed that either high or low bridge did not suffer damage by the tsunami because their decks were deeply submerged or above the tsunami height, respectively (Kawashima et al., 2011). Numerous studies have been carried out to evaluate the tsunami forces on bridge structures (Azadbakht and Yim, 2014; Kataoka et al., 2006; Kosa et al., 2010; Lau, 2009; Lukkunaprasit et al., 2011b; Sugimoto and Unjoh, 2007; Zhang et al., 2010). Scour, and fluid loadings are clear examples of damages to bridge structures presented by Ghobarah, Yeh, and Robertson (Ghobarah et al., 2006; Wei et al., 2015). The wave action on a girder bridge superstructure located on a dry bed was investigated by Lemura (2007). Box type bridge decks which were placed on a wet bed at certain heights of still-water, were modeled by Kataoka et al. (2006) and (Shoji and Mori, 2006). Shoji and Mori (2006) located the bridge deck on idealized abutments while Kataoka et al. (2006) and Lemura (2007) conducted their experiments on a simplified model by neglecting the bridge piers. No attempt was done by Shoji and Mori (2006) to measure induced pressures (Lukkunaprasit et al., 2011a). Hydraulic experiments were conducted by Sugimoto and Unjoh (2007) to evaluate the bridge failure mechanism. Shoji et al. (2011; 2008) conducted experiments in a wave flume to study the tsunami wave generated fluid forces acting on a bridge deck. Lukkunaprasit et al. (2011b) undertook experimental modeling of tsunami forces on bridge decks to investigate the effect of perforations on the girders and parapets on the horizontal tsunami loads. Tsunami loads on five California coastal bridges were estimated by (Azadbakht and Yim, 2014) to quantify the horizontal and vertical forces and overturning moments. A shallow-water flow simulation using the Delft-3D model was carried out to evaluate tsunami behavior near a highway bridge in Japan by (Bricker and Nakayama, 2014) to find out the bridge deck failure mechanisms. Bridge deck inclination, trapped air, and the presence of nearby structures such as seawalls were identified as the main bridge failure mechanisms.

Although there have been many research studies about tsunami forces on bridges, few of them have focused on a complete pier-deck model (Mazinani et al., 2014) with different lengths of abutments. Araki et al. (2011) carried out experiments in which tsunami waves were modeled as solitary waves using a wavemaker. The instantaneous dam break, using the rapid release of a sluice gate or a radial gate, creates a positive wave propagating downstream a flume, which is similar to a tsunami bore (Chanson, 2006; Cross, 1967; Yeh, 2006). This bore generation method was used by various researchers (Árnason, 2005; Nistor et al., 2011; Nouri, 2008; Rahman et al., 2014a; Rahman et al., 2014b). This method was used to simulate the tsunami-like waves in the current study.

The above studies have not lead to a unified tsunami design code for bridge structures. Furthermore, there have been few studies relating to complete pier-deck bridge models with abutments. Other shortcomings of previous research include omission of the piers, which is reduced the applied uplift force magnitude on the bridge model. In some of the previous studies, tsunami-induced pressures were not measured. This paper reports the effects of bore strength, and abutment length, on the tsunami-induced forces and pressures on an on-shore complete pier-deck bridge structure.

2 EXPERIMENTS

A 14 m long, 1.2 m wide and 0.8 m deep wave flume, connected to a reservoir 11 m long, 7.3 m wide and 0.6 m deep, was used (Figure 3). The flume is equipped with an automatic gate to generate a tsunami bore. The flume has concrete block side walls and a horizontal bottom of moderately smooth concrete to enable simulation of tsunami bore propagation over a plane dry bed. The flume is emptied using the drain gate and drain channel. The 1.2 m wide and 0.9 m high automatic gate consists of a sliding gate and a shutter gate, both of which open rapidly, providing near-instantaneous water release (Figure 4).

Four capacitance-type wave gauges were placed 15 mm above the flume floor at the centre of the flume along its length to measure the depth of the flow and observe the bore propagation. The first wave gauge (WG1) was placed 4.25 m downstream from the gate, with the remaining gauges (numbered WG2 to WG4) equally spaced 1.75 m apart over a total distance of 9.5 m downstream from the gate. The approaching bore

featured a sloping front, as is typical for such experiments. The recorded time at which the bore struck each wave gauge was used to calculate average velocity. The water depths behind the sloping front of the approaching bore were used to measure the bore heights.

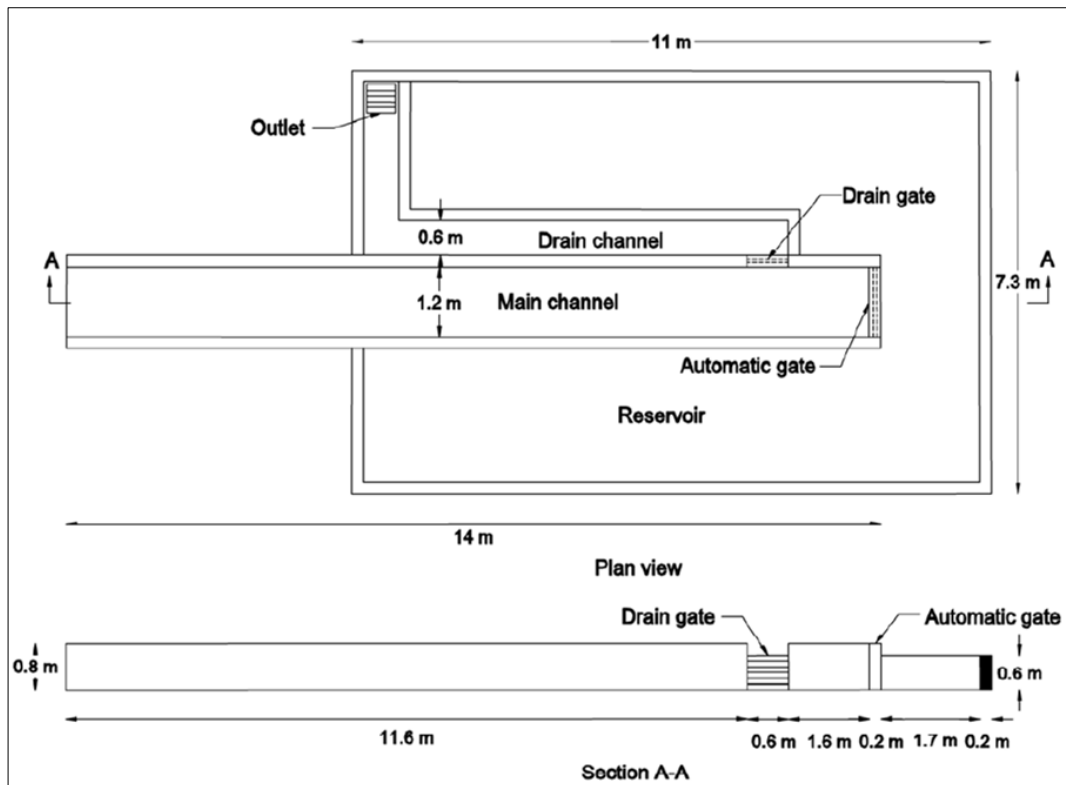


Figure 3. Experimental set-up.

The 1:40 model is a representative bridge model which is widely constructed in New Zealand. The dimensions of the "average" bridge were obtained as simple averages of the values from five actual bridges. The representative bridge, spanning 24 m, consists of a deck 9.6 m wide supported by 1.4 m deep girders. The bridge model was placed 10 m downstream from the sliding gate with varying abutment length at both sides to investigate the effect of this parameter on the tsunami hydrodynamic forces on the bridge structure.

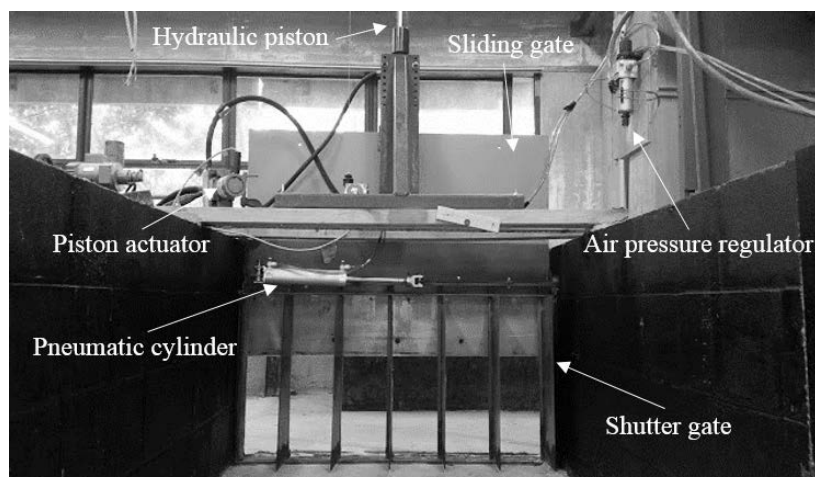


Figure 4. Details of gate.

To increase the reliability of the results, a simplified superstructure (i.e. a box as a common geometrical shape rather than girders) was used. The pier-deck bridge model was constructed from 5 mm thick clear acrylic sheets mounted on a base plate installed flush with the surrounding semi-dry bed located downstream of the gates. Figure 5 (a) illustrates the typical cross section geometry of the bridge model. The bridge model was installed across the width of the flume and perpendicular to the flow direction. The superstructure was instrumented with pressure sensors (Honeywell 26PC series) to measure the applied pressures. Also, shown

in Figure 5 (b) are the positions of pressure sensors on the model. P_1 , P_2 , and P_3 designate the pressure sensor locations at the seaward side of the bridge model, used for horizontal pressure measurements.

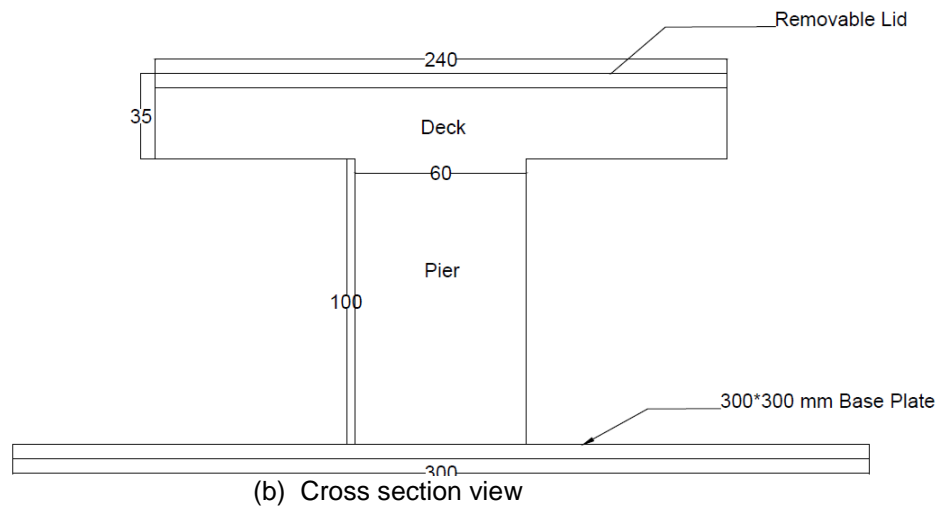
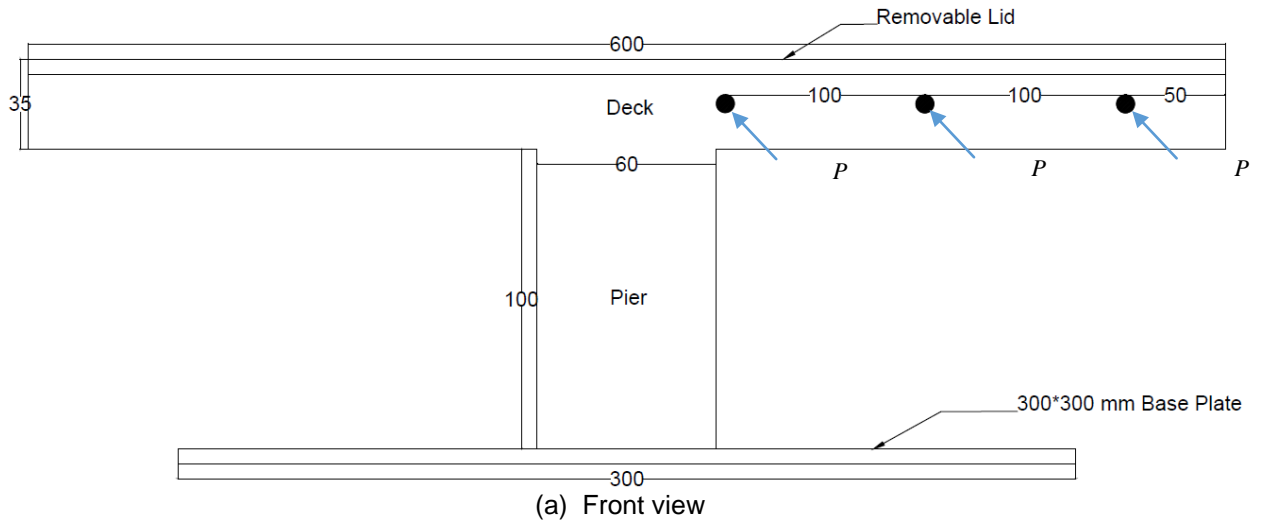


Figure 5. Model dimensions.

Each pressure sensor was fitted with two flexible transparent plastic tubes and the pressure difference between these tubes was measured (Figure 6 (a)).



Figure 6. Pressure sensors and load cell installation.

A JR3 multi-axis waterproof load cell, model 75E20A4, was used to measure the force and moment acting on the structure in three dimensions with the positive x-axis aligned with the flow direction (Figure 6 (b)).

3 RESULTS

For the experiments, the reservoir was filled to a depth of 400 mm, 500 mm, or 600 mm and the sliding gate was lifted to a constant height of either 200 mm, 300 mm, or 400 mm. Table 1 lists combinations of gate opening height (GO), reservoir water depth (WL), and abutment length, which were used to conduct 16 test

cases (4 bore heights × 4 abutment lengths). For each case, the bore height and the bore velocity were taken as the mean values from five repetitions. It was found that the velocity variation along the length of the flume was not significant, showing that in this study the force and pressure measurements were independent of the structure position along the flume. As expected, increasing depth of water in the reservoir and gate opening height, both resulted in higher bore velocities and heights. The generated bore took about 3.6 to 5.1 s, depending on each case velocity, to travel the 10m length of the flume to reach the structure, with bore velocities in individual experiments ranging from 1.95 to 2.75 m/s, corresponding to prototype velocities ranging from 12.33 to 17.39 m/s. For the 2004 Indian Ocean tsunami, most structures experienced 2 to 5 m bore height (Dias et al., 2006) and tsunami flow velocities were estimated at between 3 to 4 m/s at Kamala beach and 6 to 8 m/s at Khao Lak (Rossetto et al., 2007).

Table 1. Different cases of the bore height and velocity combinations.

Case	WL (mm)	GO (mm)	h_b (mm)	U_b (m/s)	Abutment length (mm)
Case 1	600	400	220	2.75	0
Case 2	600	300	200	2.65	0
Case 3	500	300	170	2.35	0
Case 4	400	200	120	1.95	0
Case 5	600	400	220	2.75	100
Case 6	600	300	200	2.65	100
Case 7	500	300	170	2.35	100
Case 8	400	200	120	1.95	100
Case 9	600	400	220	2.75	200
Case 10	600	300	200	2.65	200
Case 11	500	300	170	2.35	200
Case 12	400	200	120	1.95	200
Case 13	600	400	220	2.75	300
Case 14	600	300	200	2.65	300
Case 15	500	300	170	2.35	300
Case 16	400	200	120	1.95	300

Based on the measured bore velocities and heights from this study, averaged over the five runs for each combination, an empirical equation in standard format is suggested for calculating the bore propagation velocity;

$$u_b = 2.1(gh_b)^{0.5} \quad [1]$$

in which u_b is the bore velocity, h_b is the bore height, and g is the gravitational acceleration. Figure 7 shows the results of this study. The least square fit to the results for an equation with the form of Eq. [1] gives a α_u value of 2.1. The range of velocities is within 5% and 15% of those predicted by the equations of Murty (1977) and Heintz and Mahoney (2012), respectively.

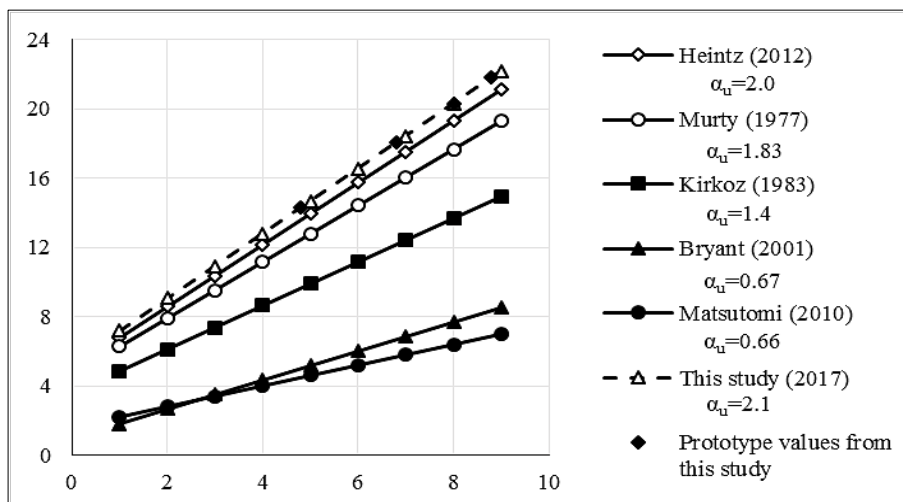


Figure 7. Relationship between average tsunami bore velocity and bore height for different studies, prototype scale.

Figure 8 shows the time histories of (a) the stream-wise force (F_x), and (b) the uplift force (F_z), respectively. The magnitudes of the forces increase with increasing bore strength (i.e. bore height and

velocity). Figure 8 (a) shows that as the sloping bore front impacts the bottom of the piers, the first peak value of approximately 10 N is observable. This force may be regarded as the peak force due to the piers, and after that, there is an initial rapid rise in the stream-wise force (F_x) as the tsunami bore impacts the bridge deck.

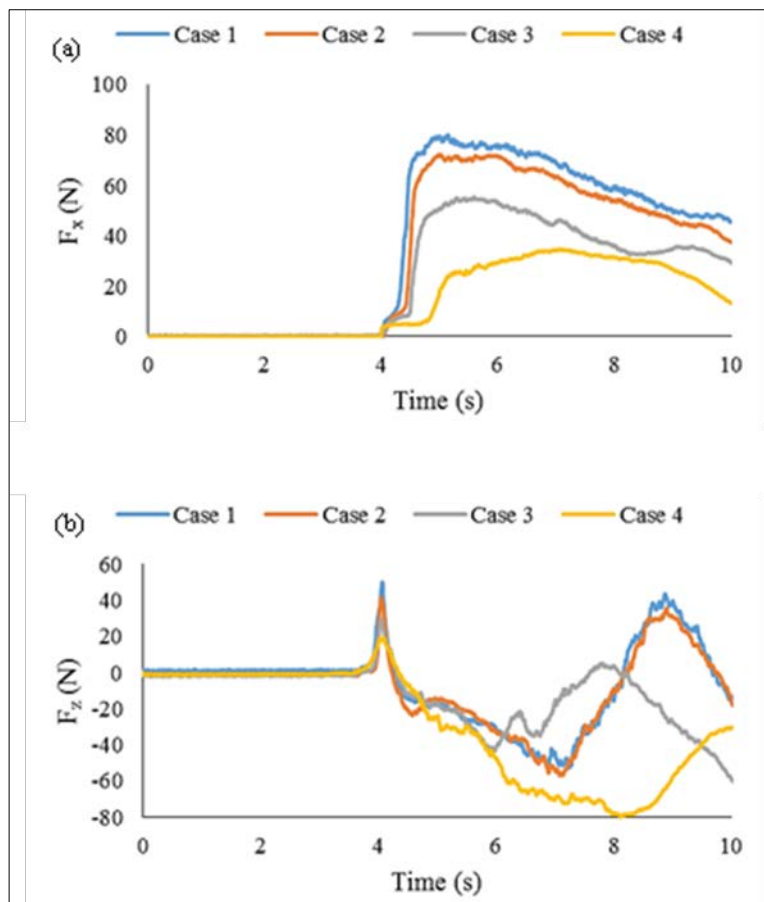


Figure 8. Time histories of the induced (a) horizontal force (F_x), and (b) vertical force (F_z) (Case 1).

The initial rapid rise in the applied force is due to the initial bore impact which suddenly pushes the structure in the flow direction, but does not exceed the total hydrodynamic force exerted on the structure. This force is sustained for the duration of the flow past the structure until backflow from the end of flume arrives back at the structure. The hydrodynamic force is a combination of a hydrostatic force caused by the accumulation of water on the seaside of the bridge structure and a drag force due to the resistance of the bridge structure against the tsunami flow.

As shown in Figure 8 (b), soon after the first arrival of a tsunami bore at the structure, the bridge superstructure will experience an upward vertical impulsive force resulting from an increase in pressure under the bridge. This impulsive force is sometimes identified as a hydrodynamic uplift force (Livermore, 2014). The upward impulsive force rapidly changes to a downward force as free-surface elevation reaches the top of the bridge deck and starts to flow onto the bridge deck, leading to ponding on the deck until the bridge is totally inundated. At this time, the horizontal force reaches a relatively steady state (i.e. the hydrodynamic part). It is observed that the time interval representing the initial impact of the tsunami on the bridge structure leads to the maximum horizontal and uplift force.

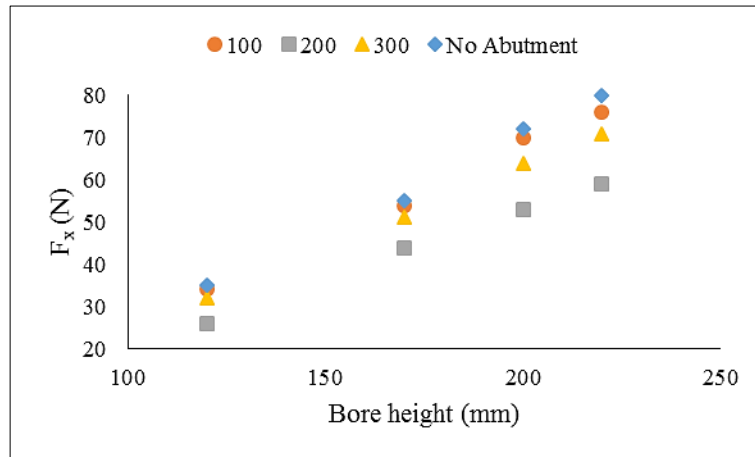


Figure 9. Relation between bore height and maximum horizontal force.

Figure 9 shows the relationship between bore height and maximum horizontal force with three different abutment lengths used to conduct the test cases. The result shows an increasing trend in the maximum horizontal force, as the bore height increases. Figure 9 also shows that the maximum loading occurs for Cases 1 to 4 (i.e. no abutment cases). As the abutment length increases, the maximum horizontal force decreases because of the flow constriction caused by the abutments. This trend is different for the 300mm abutment length (Cases 13 to 16) because, for those cases, the accumulated water upstream of the structure is much more than the other test cases. The accumulation of water leads to a greater horizontal force on the bridge structure compared with the cases with 200 mm abutment length.

Figure 10 shows the relationship between bore height and maximum uplift force. The maximum uplift force increases, as the bore height increases. This increasing trend is due to the higher flow velocity for higher bore heights. The results also show that the maximum loading occurs for Cases 9 to 12 (i.e. 200 mm abutment length). As the abutment length increases, the flow exerted a greater uplift force on the bridge superstructure. There is an exception for Cases 13 to 16 (i.e. 300 mm abutment length), which is caused by flow deceleration as a result of a very large amount of water accumulation upstream of the structure. The accumulation of water leads to a lower exerted uplift force on the bridge structure for these test cases. The results also revealed that there is not a significant difference between maximum uplift forces at lower bore heights for different abutment lengths.

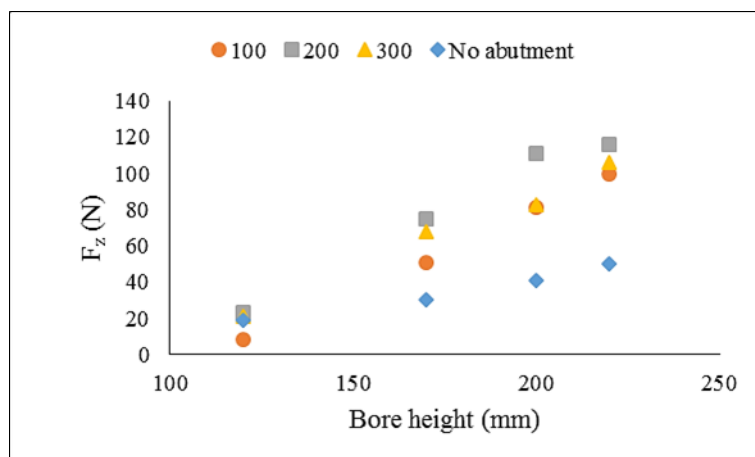


Figure 10. Relation between bore height and maximum uplift force.

As shown in Figure 11 (a), the pressure time histories can be separated into two main phases. The first phase is the impulsive part, where high values are reached for a short time (of the order of milliseconds) and is associated with the initial impact of the bore. The second phase is a longer quasi-steady state with lower values over a longer period (of the order of seconds).

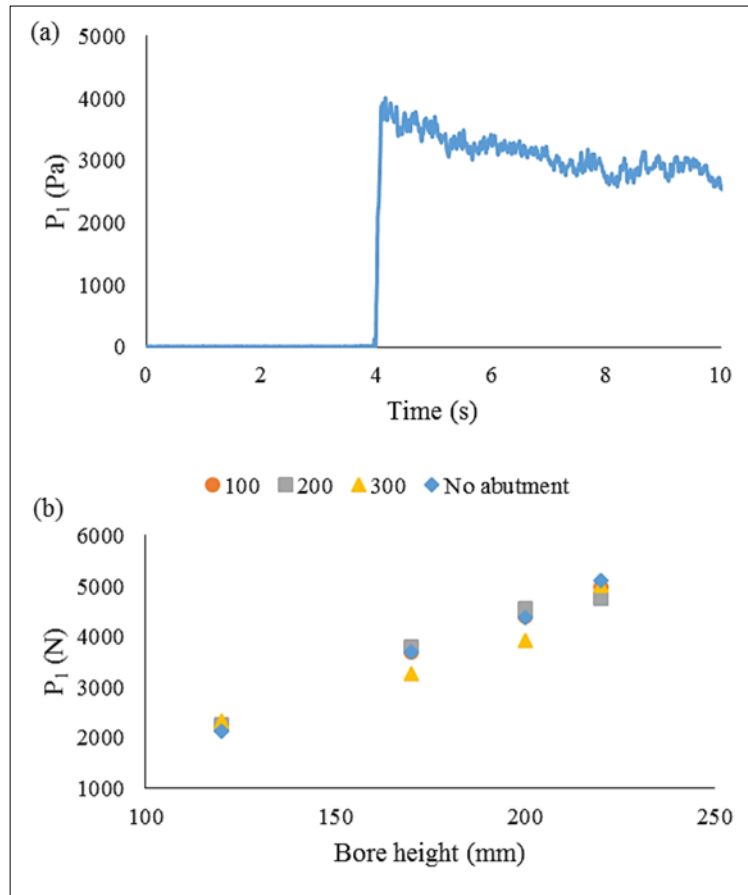


Figure 11. (a) Time history of the pressure for sensor 1 (Case 1), and (b) relation between bore height and maximum horizontal pressure.

The pressure fluctuations in the second phase are probably due to the variations of the trapped air between the bore and the structure, or vibration of the structure, while the bore is flowing past the structure (Nouri et al., 2010). Figure 11 (a) is the average pressure profile from five repetitions. The magnitudes of the three horizontal pressure sensor readings were quite similar, such that only one of them is presented (i.e. P_1). Figure 11 (b) shows the relationship between bore height and horizontal pressure. The result shows an increasing trend in the horizontal pressure, as the bore height increases. Note that the maximum horizontal pressure does not change significantly for the different abutment lengths.

4 CONCLUSIONS

The impingement of a tsunami bore on a complete pier-deck bridge model with different wing wall abutment lengths was investigated. Measurements of the applied horizontal and vertical forces and horizontal pressure on the seaward side of the bridge deck were made. A range of bore heights and velocities were created by varying the depth of water in the reservoir and the height to which the sluice gate was raised. As expected, the bore height and the bore velocity increased with increasing depth of water in the reservoir and increased the height of the gate opening. The bore velocity u_b was determined to be equal to about 2.1 $(gh_b)^{0.5}$, where h_b is the bore height. The coefficient of 2.1 is within 5% and 15% of the values proposed by Murty (1977) and Heintz and Mahoney (2012), respectively.

It was observed that varying abutment length affects the magnitude of the applied forces and pressures. The front face of the structure (i.e. facing the oncoming bore) received an impulsive horizontal force, which was followed by hydrodynamic loading. The hydrodynamic force is a combination of a hydrostatic force caused by the accumulation of water on the seaside of the bridge structure, and a drag force due to the resistance of the bridge structure against the tsunami flow. The maximum uplift force during the initial impact time interval is found to occur when the tsunami free-surface elevation reaches the top of the bridge superstructure; this occurs just before water overtops the bridge and starts to flow over the bridge superstructure. After that, the uplift force acting on the partially inundated bridge is counterbalanced by the weight of water ponding on the deck and the downward vertical force caused by the tsunami hitting the upper surface of the bridge deck. The resultant vertical force is downward and increases in magnitude as the tsunami free surface elevation and flow velocity increase.

Overall, as the bore height and associated bore velocity increase, the horizontal and uplift forces and horizontal pressure also increase.

ACKNOWLEDGEMENTS

The authors would like to thank the New Zealand Transport Agency (NZTA) for financial support of the project.

REFERENCES

- Araki, S., Ishino, K. & Deguchi, I. (2011). Stability of Girder Bridge against Tsunami Fluid Force. *Coastal Engineering Proceedings*, 1(32), 56.
- Árnason, H. (2005). Interactions between an incident bore and a free-standing coastal structure, UMI Dissertation Services.
- Azadbakht, M. & Yim, S.C. (2014). Simulation and Estimation of Tsunami Loads on Bridge Superstructures. *Journal of waterway, port, coastal, and ocean engineering*, 141(2), 04014031.
- Bricker, J.D. & Nakayama, A. (2014). Contribution of Trapped Air, Deck Superelevation, and Nearby Structures to Bridge Deck Failure during a Tsunami. *Journal of Hydraulic Engineering*, 140(5), 1-7.
- Chanson, H. (2006). Tsunami Surges on Dry Coastal Plains: Application of Dam Break Wave Equations. *Coastal Engineering Journal*, 48(04), 355-370.
- Cross, R.H. (1967). Tsunami Surge Forces. *Journal of the waterways and harbors division*, 93(4), 201-234.
- Dias, P., Dissanayake, R. & Chandratilake, R. (2006). *Lessons Learned from Tsunami Damage in Sri Lanka*. In *Proceedings of the Institution of Civil Engineers-Civil Engineering*, 159(2), 74-81.
- Fraser, S., Leonard, G.S., Matsuo, I. & Murakami, H. (2012). *Tsunami Evacuation: Lessons from the Great East Japan Earthquake and Tsunami of March 11th 2011*, GNS Science Report, 17, 89.
- Ghobarah, A., Saatcioglu, M. & Nistor, I. (2006). The Impact of the 26 December 2004 Earthquake and Tsunami on Structures and Infrastructure. *Engineering structures*, 28(2), 312-326.
- Hayashi, S. & Koshimura, S. (2013). The 2011 Tohoku Tsunami Flow Velocity Estimation by the Aerial Video Analysis and Numerical Modeling. *Journal of Disaster Research*, 8(4), 561-572.
- Heintz, J. & Mahoney, M. (2012). *Guidelines for Design of Structures for Vertical Evacuation from Tsunamis*, FEMA.
- Iemura, H., Pradono, M.H., YASUDA, T. & TADA, T. (2007). Experiments of Tsunami Force Acting on Bridge Models. In *Proceedings of the JSCE Earthquake Engineering Symposium*, 29(1), 902-911.
- Jaffe, B.E., Goto, K., Sugawara, D., Richmond, B.M., Fujino, S. & Nishimura, Y. (2012). Flow Speed Estimated by Inverse Modeling of Sandy Tsunami Deposits: Results from the 11 March 2011 Tsunami on the Coastal Plain near the Sendai Airport, Honshu, Japan. *Sedimentary Geology*, 282, 90-109.
- Kataoka, S., Kusakabe, T. & Nagaya, K. (2006). Wave Forces Acting on Bridge Girders Struck by Tsunami. In *Proceedings of the 12th Japan Earthquake Engineering Symposium*, 154-157.
- Kawashima, K., Kosa, K., Takahashi, Y., Akiyama, M., Nishioka, T., Watanabe, G., Koga, H. & Matsuzaki, H. (2011). Damages of Bridges during 2011 Great East Japan Earthquake. In *Proceedings of the 43rd joint meeting, US-Japan panel on wind and seismic effects*, 1-14.
- Kosa, K., Nii, S., Miyahara, K. & Shoji, M. (2010). *Experimental study for estimating tsunami forces acting on bridge girders*. In *Proceedings of the 26th US-Japan Bridge Engineering Workshop* 1-14. Tsukuba, Japan: Public Works Research Institute.
- Lau, T.L. (2009). *Tsunami Force Estimation on Inland Bridges Considering Complete Pier-Deck Configurations*. Chulalongkorn University, Thailand.
- Livermore, S.N. (2014). Evaluation of Tsunami Design Codes and Recommendations for Bridges Susceptible to Tsunami Inundation, Doctoral dissertation. University of Washington.
- Lukkunaprasit, P., Lau, T., Ruangrassamee, A. & Ohmachi, T. (2011a). Journal of Tsunami Society International. *Science of Tsunami Hazards*, 30(4), 244.
- Lukkunaprasit, P., Lau, T., Ruangrassamee, A. & Ohmachi, T. (2011b). Tsunami Wave Loading on a Bridge Deck with Perforations. *The 14th World Conference of Earthquake Engineering*, 14-19.
- Mazinani, I., Ismail, Z., Hashim, A.M. & Saba, A. (2014). Experimental investigation on tsunami acting on bridges. *International Journal of the Civil Architectural Structural Construction Engineering*, 8(10), 1040-1043.
- Murty, T.S. (1977). *Seismic Sea Waves—Tsunamis*. Canada Fisheries Research Board Bulletin 198, 337.
- Nistor, I., Palermo, D., Cornett, A. & Al-Faesly, T. (2011). Experimental and Numerical Modeling of Tsunami Loading on Structures. *Coastal Engineering Proceedings*, 1(32), 2.
- Nouri, Y. (2008). The Impact of Hydraulic Bores and Debris on Free Standing Structures, Doctoral dissertation. University of Ottawa (Canada).
- Nouri, Y., Nistor, I., Palermo, D. & Cornett, A. (2010). Experimental Investigation of Tsunami Impact on Free Standing Structures. *Coastal Engineering Journal*, 52(1), 43-70.
- Rahman, S., Akib, S., Khan, M.T.R. & Shirazi, S.M. (2014a). Experimental Study on Tsunami Risk Reduction on Coastal Building Fronted by Sea Wall. *The Scientific World Journal*, 2014(2014), 1-7.

- Rahman, S., Akib, S. & Shirazi, S.M. (2014b). Experimental Investigation on the Stability of Bride Girder Against Tsunami Forces. *Science China Technological Sciences*, 57(10), 2028-2036.
- Rossetto, T., Peiris, N., Pomonis, A., Wilkinson, S., Del Re, D., Koo, R. & Gallocher, S. (2007). The Indian Ocean Tsunami of December 26, 2004: Observations in Sri Lanka and Thailand. *Natural Hazards*, 42(1), 105-124.
- Shoji, G., Hiraki, Y., Fujima, K. & Shigihara, Y. (2011). Evaluation of Tsunami Fluid Force Acting on a Bridge Deck Subjected to Breaker Bores. *Procedia Engineering*, 14, 1079-1088.
- Shoji, G. & Mori, Y. (2006). Hydraulic Model Experiment to Simulate the Damage of a Bridge Deck Subjected to Tsunamis. *Annual Journal of Coastal Engineering*, 53(2), 801-805.
- Shoji, G. & Moriyama, T. (2008). *Evaluation of a Tsunami Wave Load Acting to a Deck of a Road Bridge*. In *The 14th World Conference on Earthquake Engineering*, 12-17.
- Sugimoto, T., & Unjoh, S. (2007, November). Hydraulic Model Tests on the Bridge Structures Damaged by Tsunami and Tidal Wave. In *Proceedings of the 23th US–Japan Bridge Engineering Workshop*, 1-10. Tsukuba, Japan: Public Works Research Institute.
- Suppasri, A., Koshimura, S., Imai, K., Mas, E., Gokon, H., Muhari, A. & Imamura, F. (2012). Damage Characteristic and Field Survey of the 2011 Great East Japan Tsunami in Miyagi Prefecture. *Coastal Engineering Journal*, 54(01), 1-30.
- Suppasri, A., Shuto, N., Imamura, F., Koshimura, S., Mas, E. & Yalciner, A.C. (2013). Lessons Learned from the 2011 Great East Japan Tsunami: Performance of Tsunami Countermeasures, Coastal Buildings, and Tsunami Evacuation in Japan. *Pure and Applied Geophysics*, 170(6), 993-1018.
- Wei, Z., Dalrymple, R.A., Héroult, A., Bilotta, G., Rustico, E. & Yeh, H. (2015). SPH Modeling of Dynamic Impact of Tsunami Bore on Bridge Piers. *Coastal Engineering*, 104, 26-42.
- Yeh, H. (2006). Maximum Fluid Forces in the Tsunami Runup Zone. *Journal of waterway, port, coastal, and ocean engineering*, 132(6), 496-500.
- Zhang, G., Hoshikuma, J. & Usui, T. (2010). *A Study on Countermeasure for Reducing the Effect of Tsunami on Highway Bridges*. In *Proceedings of the 26th US-Japan Bridge Engineering Workshop*, 175-183.

SCATTERING OF OBLIQUE WAVES BY A FLOATING ELASTIC PLATE OVER A POROUS BED

HAREKRUSHNA BEHERA⁽¹⁾, CHIU-ON NG⁽²⁾ & TRILOCHAN SAHOO⁽³⁾

⁽¹⁾ SRM Research Institute & Department of Mathematics, SRM University, Kattankulathur, Tamil Nadu, India, hkb.math@gmail.com

⁽²⁾ Department of Mechanical Engineering, The University of Hong Kong, Pokfulam Road, Hong Kong, China, cong@hku.hk

⁽³⁾ Department of Ocean Engineering and Naval Architecture, Indian Institute of Technology Kharagpur, India, tsahoo@naval.iitkgp.ernet.in

ABSTRACT

An analytical study is presented for oblique wave scattering by a floating elastic plate in a body of water over a porous seabed. The problem is solved using the eigenfunction expansion method under the assumption of small-amplitude surface waves and structural response. The study aims to look into the interaction between oblique waves and a floating elastic plate that serves as an effective breakwater. Numerical results for the plate having free edge, simply-supported edge and clamped edge are compared where most of the results are analysed for plate having clamped edge. Numerical results for the reflection and transmission coefficients are computed and examined for various values of the wave, porous bed and structural parameters.

Keywords: Wave scattering; porous seabed; floating elastic plate; eigenfunction expansion.

1 INTRODUCTION

Over the past few decades, wave interaction with floating structures have been extensively investigated, by researchers as well as practicing engineers, for a wide range of applications in ocean and coastal engineering. The main advantage of floating structures is that they allow free passage of currents, thereby avoiding undesirable problems such as sediment deposition around the structures. In particular, there has been an increasing interest in the use of flexible floating structures as breakwaters, as flexible structures may enhance wave attenuation through wave-structure interaction, and most importantly, these structures are light in weight, cost-effective, reusable and environmental friendly. In order to study the hydroelastic response of floating elastic plate, various analytical and numerical methods are proposed by researchers. Sahoo et al. (2001) studied the wave scattering by semi-infinite floating elastic plate using eigenfunction expansion method and orthogonal mode coupling relation. Kohout et al. (2007) investigated the problem of linear water wave propagation with a set of floating elastic plates of variable properties. Karmakar and Soares (2012) studied scattering of gravity waves by a moored finite floating elastic. The effect of compression on wave diffraction by a floating elastic plate was studied by Mohapatra et al. (2013). Unlike the case of attenuation of surface waves with the help of floating elastic plate, submerged elastic plate can be used as an effective breakwater. Because, submerged horizontal breakwater does not block the incoming waves and these structures do not hamper the sea scape. Hassan et al. (2009) developed an analytic method to study wave scattering by submerged horizontal flexible plate of different configurations. Recently, Behera and Sahoo (2015) investigated the surface gravity wave interaction with submerged elastic porous plate. The aforementioned studies are based on the assumption that the sea bed is rigid and impermeable.

On the other hand, natural seabed is usually composed of permeable beds that enable mass and momentum transfer across the interface. When waves propagate over a porous seabed, the water seabed interface will experience a positive dynamic pressure under a wave crest and negative dynamic pressure under a wave trough. Further, as the waves propagate over permeable bed, wave energy dissipation due to flow resistances inside the porous bed results in the decrease of wave heights. Zhu (2001) studied water waves within a porous medium on an undulating bed. The study of wave damping over porous seabed can be found in Karunarathna and Lin (2006). A numerical model was presented by Tsai et al. (2006) to investigate the wave transformation over a submerged permeable breakwater on a porous slope seabed. Martha et al. (2007) studied oblique water-wave scattering by small undulations on a porous bed. Wave characteristics within the porous structures in two-layer fluid were analyzed by Behera and Sahoo (2014). Recently, Das et al. (2016) investigated wave interaction with floating elastic plate over a poro-elastic bed. Several aspects of wave interaction with porous structure of finite width can be found in Losada et al. (1996), Behera et al. (2015) and the literature cited therein.

In the present work, oblique wave scattering by floating elastic plate over a porous bed is studied. For simplicity, small-amplitude surface waves and structural response are assumed. It is also assumed that the flexible plate is under the action of a uniform compressive force. Euler-Bernoulli's beam equation is used to model the floating flexible plane. The effect of wave run up and overtopping is not considered in the present

study. The plate is under the action of hydrodynamic pressure and the atmospheric pressure is being assumed to be constant on the plate surface. Thus, in the present model, the wave will not ride above the structure. On the other hand, the porous bed condition as used by Maiti and Mandal (2014) is adopted in the formulation of the associated mathematical boundary value problem, which is solved by the eigenfunction expansion method. In the present study, a special type of porous bed is considered and the motion of the fluid inside the porous bed is not analyzed. The seabed boundary condition depends on a known parameter of dimension (length)⁻¹ which is said to be porosity parameter. Further, the flow resistance is considered by neglecting inertial term. Thus, the value of G is considered as real. Three different types of edge conditions, namely, clamped edge, simply-supported edge, and free edge are considered. Numerical results are computed for the reflection and transmission coefficients to understand the effects due to the flexural rigidity, compressive force, length of the plate, porous-effect parameter of the porous bed and angle of incidence on wave scattering by the plate.

2 MATHEMATICAL FORMULATION

Three-dimensional Cartesian coordinates are chosen wherein the z -axis is taken vertically downward into the fluid region with ($z=0$) being the undisturbed free surface, and the x - y plane being the horizontal plane. It is assumed that a thin elastic plate of length b and uniform thickness d floats on the mean free surface $z=0$ of a fluid medium of uniform density ρ and water of finite depth H . The seabed is considered as a semi-infinite porous medium with a porous-effect parameter G as in Martha et al. (2007) and Maiti and Mandal (2014). The whole fluid domain is divided into three sub-domains as shown in Figure 1, namely, the open-water region ($x < 0$) as region 1, the region below the flexible plate ($0 < x < b$) as region 2, and the open-water region ($x > b$) as region 3. The fluid is assumed to be inviscid, incompressible, and the fluid motion is considered not rotational and simple harmonic in time with an angular frequency ω , which ensures the existence of velocity potentials $\Phi_j(x, y, z, t)$ for $j=1,2,3$ in the three regions.

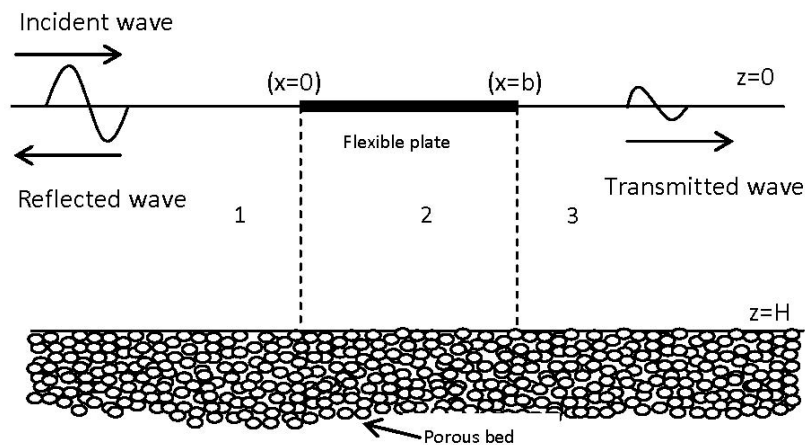


Figure 1. Schematic diagram of wave scattering by a floating elastic plate over a porous seabed.

The velocity potentials Φ_j for $j=1,2,3$ satisfy the three-dimensional Laplace equation given by:

$$\left(\frac{\partial^2}{\partial x^2} + \frac{\partial^2}{\partial y^2} + \frac{\partial^2}{\partial z^2} \right) \Phi_j = 0. \quad [1]$$

The bottom boundary condition is given by :

$$\frac{\partial \Phi_j}{\partial z} - G \Phi_j = 0 \quad \text{on } z = H, \quad \text{for } j = 1, 2, 3, \quad [2]$$

where G is the porous-effect parameter characterizing the seabed as in Martha et al. (2012). The linearized kinematic condition on the mean free surface is given by:

$$\frac{\partial \Phi_j}{\partial z} = \frac{\partial \eta_j}{\partial t} \quad \text{on } z = 0, \quad \text{for } j = 1, 2, 3, \quad [3]$$

where η_1 and η_3 are the free surface elevations in the open-water regions 1 and 3, and η_2 is the deflection of the floating plate. The linearized dynamic condition on the mean free surface in regions 1 and 3 yield:

$$\frac{\partial \Phi_j}{\partial t} = g\eta_j \text{ on } z=0, \text{ for } j=1,3. \quad [4]$$

Eliminating η_j for $j=1,3$ from the kinematic and dynamic conditions as in Eq. [3] and [4], the linearized free-surface boundary conditions in the open-water regions 1 and 3 are obtained as follows:

$$\frac{\partial \Phi_j}{\partial z} = \frac{\partial^2 \Phi_j}{\partial t^2} \text{ on } z=0, \text{ for } j=1,3, \quad [5]$$

where g is the acceleration due to gravity. The hydrodynamic pressure $P_h(x, y, z, t)$ acting on the floating plate is given by:

$$P_h = -\rho \frac{\partial \Phi_2}{\partial t} + \rho g \eta_2 \text{ on } z=0. \quad [6]$$

In the presence of a uniform compressive force N along the $x-y$ plane, the thin plate equation is given by:

$$\left(EI \nabla_{xy}^4 + N \nabla_{xy}^2 + \rho_e d \frac{\partial^2}{\partial t^2} \right) \eta_2 = -P_d, \quad [7]$$

where E , ρ_e and P_d are Young's modulus, density of the elastic plate and dynamic pressure exerted on the elastic plate, respectively, with $I = d^3 / \{12(1-\nu^2)\}$ and ν being the Poisson ratio of the elastic plate. It is assumed that there is no gap between the fluid and the floating elastic plate. Thus, the hydrodynamic pressure is equal to the pressure exerted on the elastic plate. It may be noted that, in the present work, the floating plate is assumed to be elastic in nature which does not have a mechanism for energy dissipation. When gravity waves will propagate below the floating structure, flexural gravity waves will be generated below the structure. Thus, there will not be any energy dissipation by the flexible plate, and details have been well studied (see Sahoo et al., 2001). Further, using Eq. [5–7], the linearized plate-covered boundary condition on $z=0$ is obtained as follows:

$$\left(EI \nabla_{xy}^4 + N \nabla_{xy}^2 + \rho_e d \frac{\partial^2}{\partial t^2} + \rho g \right) \frac{\partial \Phi_2}{\partial z} = \rho \frac{\partial^2 \Phi_2}{\partial t^2}. \quad [8]$$

Assuming that the incident wave is propagating at an angle θ with respect to the x -axis and the motion is simple harmonic in time with angular frequency ω , the velocity potentials and free surface elevations in each region are of the form $\Phi_j(x, y, z, t) = \text{Re} \left\{ \phi_j(x, z) e^{i(\mu_y y - \omega t)} \right\}$ and $\eta_j(x, y, t) = \text{Re} \left\{ \bar{\eta}(x) e^{i(\mu_y y - \omega t)} \right\}$, respectively, for $j=1,2,3$, where $\mu_y = k_0 \sin \theta$ with k_0 being the wave number of the plane gravity wave. Thus, the spatial velocity potential $\phi_j(x, z)$ for $j=1,2,3$ will satisfy the Helmholtz equation given by:

$$\left(\frac{\partial^2}{\partial x^2} + \frac{\partial^2}{\partial z^2} - \mu_y^2 \right) \phi_j = 0, \text{ for } j=1,2,3, \quad [9]$$

along with the boundary conditions as in Eq. [2–5]. Further, the dynamic boundary condition as in Eq. [8] can be rewritten as:

$$\left(D \frac{\partial^4}{\partial z^4} - Q \frac{\partial^2}{\partial z^2} - MK + 1 \right) \frac{\partial \phi_2}{\partial z} + K \phi_2 = 0, \quad [10]$$

where $D = EI / \rho g$, $Q = N / \rho g$, $K = \omega^2 / g$ and $M = \rho_p d / \rho$. The continuity of pressure and velocity at $x=0$ and $x=b$ yield:

$$\phi_j(x, z) = \phi_2(x, z), \quad \frac{\partial \phi_j(x, z)}{\partial x} = \frac{\partial \phi_2(x, z)}{\partial x}, \quad [11]$$

where $j=1$ at $x=0$ and $j=3$ at $x=b$. It is assumed that the edges of the floating plate are free, simply-supported, or clamped. In the case of free edges, the bending moment and shear force are zero on the edges and the conditions are given by:

$$EI \left(\frac{\partial^2}{\partial x^2} - \nu k_y^2 \right) \frac{\partial \phi_2}{\partial z} = 0, \quad \left[EI \left\{ \frac{\partial^2}{\partial x^2} - (2-\nu)k_y^2 \right\} \frac{\partial}{\partial x} + Q \frac{\partial}{\partial x} \right] \frac{\partial \phi_2}{\partial z} = 0 \quad \text{at } (0,0) \text{ and } (b,0). \quad [12]$$

In the case of simply-supported edges, the deflection and bending moment are zero near the edges and the conditions are given by:

$$\frac{\partial \phi_2}{\partial z} = 0, \quad EI \left(\frac{\partial^2}{\partial x^2} - \nu k_y^2 \right) \frac{\partial \phi_2}{\partial z} = 0 \quad \text{at } (0,0) \text{ and } (b,0), \quad [13]$$

whilst plate deflection and slope of the plate deflection are zero in the case of clamped edges, and the conditions are given by:

$$\frac{\partial \phi_2}{\partial z} = 0, \quad \frac{\partial^2 \phi_2}{\partial x \partial z} = 0 \quad \text{at } (0,0) \text{ and } (b,0). \quad [14]$$

Finally, the radiation condition for oblique wave scattering by a floating elastic plate over a porous bed yields:

$$\phi_j(x, z) = \begin{cases} (I_0 e^{iq_0 x} + R_0 e^{-iq_0 x}) f_0(k_0, z), & \text{for } j=1, x \rightarrow -\infty, \\ T_0 e^{iq_0 x} f_0(k_0, z), & \text{for } j=3, x \rightarrow \infty, \end{cases} \quad [15]$$

where I_0 , R_0 and T_0 are constants associated with the incident, reflected and transmitted wave amplitudes, respectively, with $q_0 = \sqrt{k_0^2 - \mu_y^2}$ and $f_0(k_0, z)$ being the associated eigenfunctions.

3 METHOD OF SOLUTION

The spatial velocity potentials in regions 1, 2 and 3 satisfying the governing equation Eq. [9] along with the boundary conditions is prescribed in Eq. [2] and [5] are written as:

$$\phi_j(x, z) = \begin{cases} I_0 e^{iq_0 x} f_0(k_0, z) + \sum_{n=0}^{\infty} R_n e^{-iq_n x} f_n(k_n, z), & \text{for } x < 0, j=1, \\ \sum_{n=0}^{\infty} \{ A_n e^{iQ_n x} + B_n e^{-iQ_n(x-b)} \} g_n(p_n, z), & \text{for } 0 < x < b, j=2, \\ \sum_{n=0}^{\infty} T_n e^{iq_n(x-b)} f_n(k_n, z), & \text{for } x > b, j=3, \end{cases} \quad [16]$$

where I_n , A_n , B_n and T_n for $n=0,1,2,\dots$ are unknown expansion coefficients to be determined with $q_n = \sqrt{k_n^2 - \mu_y^2}$ and $Q_n = \sqrt{p_n^2 - \mu_y^2}$, and the eigenfunctions $f_n(k_n, z)$ and $g_n(p_n, z)$ are given by:

$$f_n(k_n, z) = \left(\frac{ig}{\omega} \right) \frac{k_n \cosh k_n(H-z) - G \sinh k_n(H-z)}{\cosh k_n H - G \sinh k_n H}, \quad [17]$$

$$g_n(p_n, z) = \left(\frac{ig}{\omega} \right) \frac{p_n \cosh p_n(H-z) - G \sinh p_n(H-z)}{\cosh p_n H - G \sinh p_n H}. \quad [18]$$

In the open-water regions 1 and 3, the eigenvalues k_n satisfy the dispersion relation:

$$k_n(k_n \tanh k_n H - G) = K(k_n - G \tanh k_n H). \quad [19]$$

On the other hand, in the plate-covered region 2, the eigenvalues p_n satisfy the dispersion relation:

$$(Dp_n^4 - Qp_n^2 - MK + 1)(p_n^2 \tanh p_n H - p_n G) = K(p_n - G \tanh p_n H). \quad [20]$$

The vertical eigenfunctions in the open-water regions $f_n(k_n, z)$ are orthogonal, i.e.:

$$\int_0^H f_n(k_n, z) f_m(k_m, z) dz = \delta_{nm}, \quad [21]$$

where δ_{nm} is the Kronecker delta. However, the vertical eigenfunctions in the plate-covered region are not orthogonal as had been discussed by Sahoo et al. (2001). In the present study, the orthogonality of the eigenfunction in the open-water regions is used to solve the boundary-value problem. Next, using the matching conditions at $x=0$ and $x=b$ as in Eq. [11], and the orthogonality of the eigenfunctions as defined in Eq. [21] and truncating the infinite sums after N terms, a system of $4N+4$ equations for the determination of the unknowns associated with the velocity potentials in Eq. [16] are obtained as follows:

$$\left. \begin{aligned} \sum_{n=0}^N R_n X_{nm} - \sum_{n=0}^N (A_n + B_n e^{-iQ_n b}) Y_{nm} &= -\delta_{0m} I_0 X_{0m}, \\ \sum_{n=0}^N q_n R_n X_{nm} - \sum_{n=0}^N Q_n (-A_n + B_n e^{-iQ_n b}) Y_{nm} &= \delta_{0m} q_0 I_0 X_{0m}, \\ \sum_{n=0}^N T_n X_{nm} - \sum_{n=0}^N (A_n e^{-iQ_n b} + B_n) Y_{nm} &= 0, \\ \sum_{n=0}^N q_n T_n X_{nm} - \sum_{n=0}^N Q_n (A_n e^{-iQ_n b} - B_n) Y_{nm} &= 0, \end{aligned} \right\} \quad [22]$$

where:

$$X_{nm} = \int_0^H f_n(k_n, z) f_m(k_m, z) dz \quad \text{and} \quad Y_{nm} = \int_0^H g_n(p_n, z) f_m(k_m, z) dz. \quad [23]$$

Further, it was assumed that the edges of the floating elastic plate are simple-supported. Thus, using Eq. [13], four additional equations are obtained as follows:

$$\left. \begin{aligned} \sum_{n=0}^N E_n p_n (A_n + B_n e^{iQ_n b}) &= 0, \\ \sum_{n=0}^N E_n p_n (A_n e^{iQ_n b} + B_n) &= 0, \\ \sum_{n=0}^N EI(Q_n^2 - \nu \mu_y^2) E_n p_n (A_n + B_n e^{iQ_n b}) &= 0, \\ \sum_{n=0}^N EI(Q_n^2 - \nu \mu_y^2) E_n p_n (A_n e^{iQ_n b} + B_n) &= 0, \end{aligned} \right\} \quad [24]$$

where:

$$E_n = \frac{p_n \sinh p_n H - G \cosh p_n H}{p_n \cosh p_n H - G \sinh p_n H}. \quad [25]$$

Solving the system of equations as given in Eq. [22] and [24] will determine the unknown constants I_0, R_n, A_n, B_n and T_n . Similarly, Eq. [12] and [14] are used in the case of the floating plate having free or clamped edges, respectively.

4 RESULTS AND DISCUSSIONS

In this section, the effects due to various wave and structural parameters on the reflection and transmission coefficients are investigated. Numerical results were generated using MATLAB programs. Unless stated otherwise, the following values of physical parameters were considered: $H = 5$ m, $T = 5$ sec, $b/H = 6$, $GH = 0.5$, $g = 9.81$ m/sec², $\theta = 20^\circ$, $\nu = 0.3$, $E = 5$ GPa, $d = 0.1$ m, and $N = \sqrt{EI\rho g}$. Once the unknowns were determined, the reflection and transmission coefficients can be easily computed using the formulae:

$$K_r = |R_0/I_0| \quad \text{and} \quad K_t = |T_0/I_0|. \quad [26]$$

In Figure 2(a), the reflection and transmission coefficients versus k_0b are plotted for different edge conditions, namely, clamped edge, simply-supported and free edges. From this figure, it is observed that the plate having clamped edges exhibits larger reflection and smaller transmission which indicates that a clamped plate allows less incident wave energy to be transmitted below the plate and in turn the reflection becomes larger. However, the plate having free edges exhibits smaller reflection and larger transmission compared to the other two types of edge conditions. Further, in the case of clamped edge, zero reflection and full transmission occur for a larger value of k_0b compared to the other two types of edge conditions. Hereafter, all the numerical results in the manuscript were discussed for a floating plate having clamped edges.

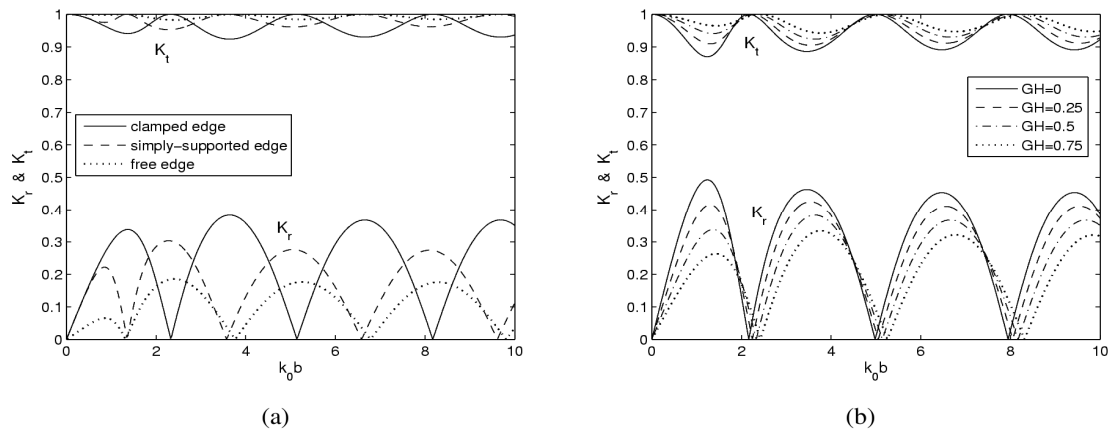


Figure 2. Variation of the reflection and transmission coefficients versus k_0b for different (a) edge conditions with $GH = 0.5$, and (b) values of GH with clamped edge condition, and $E = 1$ GPa, $N = \sqrt{EI\rho g}$ and $\theta = 20^\circ$.

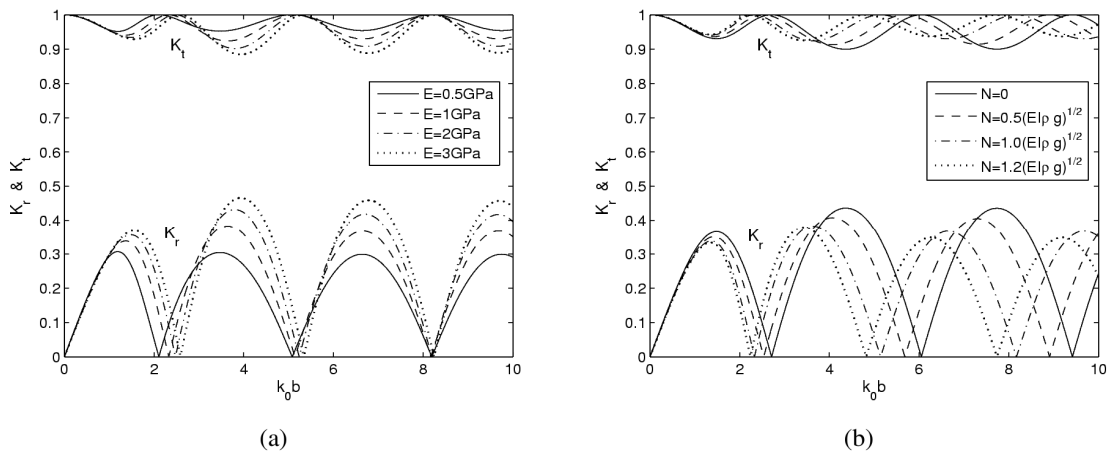


Figure 3. Variation of the reflection and transmission coefficients versus k_0b for different values of (a) E with $N = \sqrt{EI\rho g}$, and (b) N with $E = 1$ GPa, and $GH = 0.5$ and $\theta = 20^\circ$.

The reflection and transmission coefficients versus k_0b were plotted for different values of the non-dimensional porous-effect parameter GH in Figure 2(b). From both figures, it was observed that the reflection

and transmission coefficients follow certain oscillatory pattern with an increase in the structural length, k_0b . Furthermore, the amplitude of oscillation in the reflection coefficient decreases while the transmission coefficient increases with an increase in the plate length, k_0b in the case of a porous bed, unlike the amplitude of oscillation that follows certain uniform periodic pattern in the case of a non-porous bed. Figure 2(b) depicts that with an increase in porous-effect parameter GH of the porous bed, the reflection coefficient decreases while the transmission coefficient increases. The observations were similar to that of Maiti and Mandal (2014) in the case of wave scattering by a semi-infinite floating elastic plate over a porous bed. Further, with an increase in GH , zero reflection and full transmission occurs for smaller values of k_0b . It may be noted that for an impermeable bed, it was seen that the reflection and transmission coefficients satisfy energy relation $K_r^2 + K_t^2 = 1$.

In Figure 3(a, b), the reflection and transmission coefficients versus k_0b were plotted for different values of Young's modulus of the floating plate E and compressive force N respectively. Figure 3(a) depicts that the increase in Young's modulus of the plate E results in an increase in the wave reflection but a decrease in the wave transmission. The plate becomes more rigid with larger E , and therefore most of the waves which concentrate near the free surface are reflected back and in the process. Less wave energy was transmitted below the plate. Similar observations were made by Sahoo et al. (2001) and Maiti and Mandal (2014) in the case of wave scattering by a semi-infinite plate over a porous/non-porous bed. Furthermore, zero reflection and full transmission occur for lower values of k_0b with an increase in E . On the other hand, the wave reflection decreases and transmission increases with an increase in compressive force N as shown Figure 3(b). Further, there was a left shift of the zero reflection and full transmission with an increase in N .

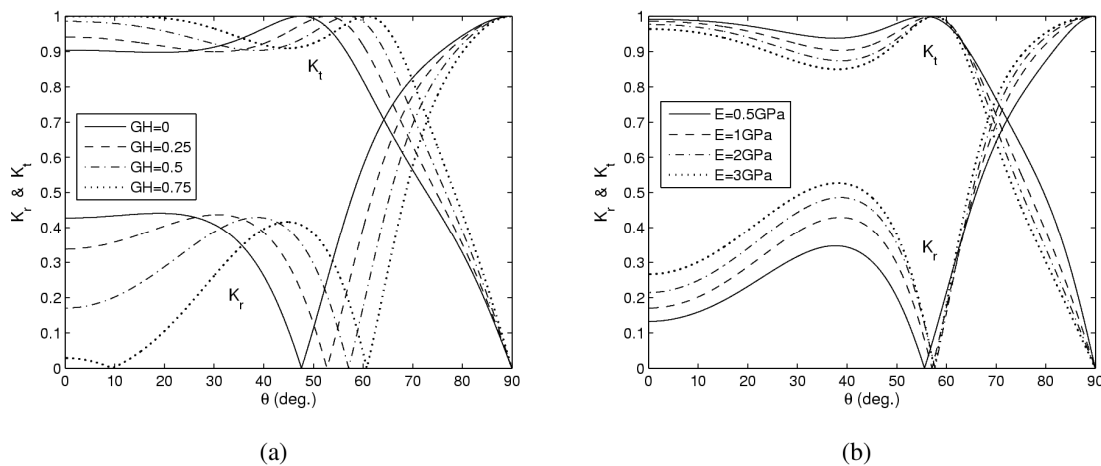


Figure 4. Variation of the reflection and transmission coefficients versus θ for different values of (a) GH with $E = 1$ GPa and (b) E with $GH = 0.5$, and $N = \sqrt{EI\rho g}$ and $b/H = 6$.

In Figure 4(a, b), the reflection and transmission coefficients versus oblique angle θ were plotted for different values of the porous-effect parameter GH and Young's modulus of the floating plate E , respectively. From these figures, it was observed that zero reflection and full transmission occur for certain values of the angle of incidence. This angle of incidence is said to be critical angle and symbolised by θ^c . Figure 4(a) depicts that multiple critical angle can be found for higher GH . From Figure 4(b), it was found that for $0 < \theta < 58^\circ$ and $64^\circ < \theta < 90^\circ$ the reflection coefficient keeps increasing with the increase in Young's modulus E , whereas in the case of transmission coefficient, an opposite pattern was observed. However, for $58^\circ < \theta < 64^\circ$, there was a negligible change in wave reflection and transmission with an increase in Young's modulus E .

5 CONCLUSIONS

The present study deals with the problem of oblique wave scattering by a floating elastic plate over a porous bed in a single-layer fluid system. The mathematical problem is formulated under the assumption of small-amplitude waves and structural response, and is solved using the eigenfunction expansion method. Numerical results are computed and discussed for the reflection and transmission coefficients to reveal effects due to the wave and structural parameters. The present study reveals that under particular conditions for some combinations of the wave and structural parameters, zero reflection and full transmission may occur. It is observed that with an increase in the porous-effect parameter of the porous bed, wave reflection decreases and the wave transmission increases. These findings will be of immense importance in the design of floating

offshore breakwaters that serve to reduce wave load on coastal/marine structures in the marine environment having located on porous bed like a sandy bed.

ACKNOWLEDGEMENTS

The research reported herein was carried out when the first author was appointed as a Research Associate at the University of Hong Kong during August 2015 – August 2016.

REFERENCES

- Behera, H., Koley, S. & Sahoo, T. (2015). Wave Transmission by Partial Porous Structures in Two-Layer Fluid. *Engineering Analysis with Boundary Elements*, 58, 58–78.
- Behera, H. & Sahoo, T. (2014). Gravity Wave Interaction with Porous Structures in Two-Layer Fluid. *Journal of Engineering Mathematics*, 87, 73–97.
- Behera, H. & Sahoo, T. (2015). Hydroelastic Analysis of Gravity Wave Interaction with Submerged Horizontal Flexible Porous Plate. *Journal of Fluids and Structures*, 54, 643–660.
- Das, S., Behera, H. & Sahoo, T. (2016). Flexural Gravity Wave Motion Over Poroelastic Bed. *Wave Motion*, 63, 135–148.
- Hassan, U.L.M., Meylan, M.H. & Peter, M. (2009). Water-Wave Scattering by Submerged Elastic Plates. *Quarterly Journal of Mechanics and Applied Mathematics*, 62, 321–344.
- Karmakar, D. & Soares, C.G. (2012). Scattering of Gravity Waves by a Moored Finite Floating Elastic Plate. *Applied Ocean Research*, 34, 135–149.
- Karunaratna, S. & Lin, P. (2006). Numerical Simulation of Wave Damping Over Porous Seabeds. *Coastal Engineering*, 53, 845–855.
- Kohout, A., Meylan, M., Sakai, S., Hanai, K., Leman, P. & Brossard, D. (2007). Linear Water Wave Propagation Through Multiple Floating Elastic Plates of Variable Properties. *Journal of Fluids and Structures*, 23, 649–663.
- Losada, I., Silva, R. & Losada, M. (1996). 3-D Non-Breaking Regular Wave Interaction with Submerged Breakwaters. *Coastal Engineering*, 28, 229–248.
- Maiti, P. & Mandal, B. (2014). Water Wave Scattering by An Elastic Plate Floating in an Ocean with A Porous Bed. *Applied Ocean Research*, 47, 73–84.
- Martha, S., Bora, S. & Chakrabarti, A. (2007). Oblique Water-Wave Scattering by Small Undulation on A Porous Sea-Bed. *Applied Ocean Research*, 29, 86–90.
- Mohapatra, S., Ghoshal, R. & Sahoo, T. (2013). Effect of Compression on Wave Diffraction by A Floating Elastic Plate. *Journal of Fluids and Structures*, 36, 124–135.
- Sahoo, T., Yip, T.L. & Chwang, A.T. (2001). Scattering of Surface Waves by A Semi-Infinite Floating Elastic Plate. *Physics of Fluids*, 13, 3215–3222.
- Tsai, C.P., Chen, H.B. & Lee, F.C. (2006). Wave Transformation Over Submerged Permeable Breakwater on Porous Bottom. *Ocean Engineering*, 33, 1623–1643.
- Zhu, S. (2001). Water Waves Within a Porous Medium on An Undulating Bed. *Coastal Engineering*, 42, 87–101.

OVERTOPPING EVENTS IN BREAKWATERS: COMPARISON OF 2D PHYSICAL EXPERIMENTS AND EMPIRICAL FORMULAE

ANA MENDONÇA⁽¹⁾, RUTE LEMOS⁽²⁾, MARIA TERESA REIS⁽³⁾, JUANA FORTES⁽⁴⁾, MARIA GRAÇA NEVES⁽⁵⁾, ANDRÉ RAMOS⁽⁶⁾ & RUI CAPITÃO⁽⁷⁾

⁽¹⁾ Laboratório Nacional de Engenharia Civil, Lisbon, Portugal
amendonca@lnec.pt, rlemos@lnec.pt, treis@lnec.pt, jfortes@lnec.pt, gneves@lnec.pt, aramos@lnec.pt, rcapitao@lnec.pt

ABSTRACT

Reliable prediction of wave run-up/overtopping and structure damage is a key task in the design and safety assessment of coastal and harbor structures. Run-up/overtopping and damage must be below acceptable limits, both in extreme and in normal operating conditions, to guarantee the stability of the structure as well as the safety of people and assets on and behind the structure. The mean-sea-level rise caused by climate change and its effects on wave climate may increase run-up/overtopping events and make the existing coastal/harbour structures more vulnerable to damage. Accurate estimates, through physical modelling, of the statistics of overtopping waves for a set of climate change conditions, are needed. Project HYDRALAB+ (H2020-INFRAIA-2014-2015) gathers an advanced network of environmental hydraulic institutes in Europe, which provides access to a suite of environmental hydraulic facilities. They play a vital role in the development of climate change adaptation strategies, by allowing the direct testing of adaptation measures and by providing data for numerical model calibration and validation. The use of physical (scale) models allows the simulation of extreme events as they are now, and as they are projected to be under different climate change scenarios. The experimental work developed at LNEC within HYDRALAB+, TASK 8.2 of RECIPE, entitled "Damage characterization under variable and unsteady test conditions", considers 2D damage and overtopping tests for a rock armor slope, with four different approaches to represent storms: a standard cumulative storm build-up (with increasing wave heights) with increasing water level; a standard cumulative storm build-up with a constant water level; a constant wave period; and a standard storm build-up, with a constant water level and with rebuilding. This paper presents a comparison of measured (physical model tests) and predicted (empirical formulae) mean overtopping discharges and individual overtopping volumes at a cross-section of a rubble mound breakwater.

Keywords: Overtopping; breakwaters; physical experiments; empirical formulae; Hydralab.

1 INTRODUCTION

Understanding future changes in flood risk from waves overtopping seawalls or other structures is a key prerequisite for effective management of coastal defenses. Occurrences of economic damage or loss of life due to the hazardous nature of wave overtopping are more likely than ever, and coastal managers and users are more aware of health and safety risks. Reduction of overtopping risk is therefore a key requirement for the design, management and adaptation of coastal structures, particularly as existing coastal infrastructure is assessed for future conditions. There are also needs to warn or safeguard individuals potentially to overtopping waves on coastal defenses or seaside promenades.

Seawalls range from simple earth banks through to vertical concrete walls and more complex composite structures. Each of these calls for different methods to assess overtopping. This paper presents a comparison of mean overtopping discharges and individual overtopping volumes at a cross-section of a rubble mound breakwater obtained through physical model tests and empirical formulae (EurOtop, 2016).

2 PHYSICAL EXPERIMENTS

2.1 Model setup

LNEC's experiments were performed at the Ports and Maritime Structures Unit (NPE) of the Hydraulics and Environment Department of LNEC, in a wave flume (COI 1) approximately 50 m long, with an operating width and an operating water depth of 80 cm.

The flume is equipped with a piston-type wave-maker that combines both irregular wave generation and dynamic absorption of reflected waves through the use of two wave gauges located in front of the paddle (Figure 1). Ten additional resistive-type wave gauges were deployed along the flume (Figure 1) and an extra gauge was placed on the model armor layer slope to measure run-up levels. A computer was used to collect and store the measured data, in digital format, at a frequency of 25Hz.

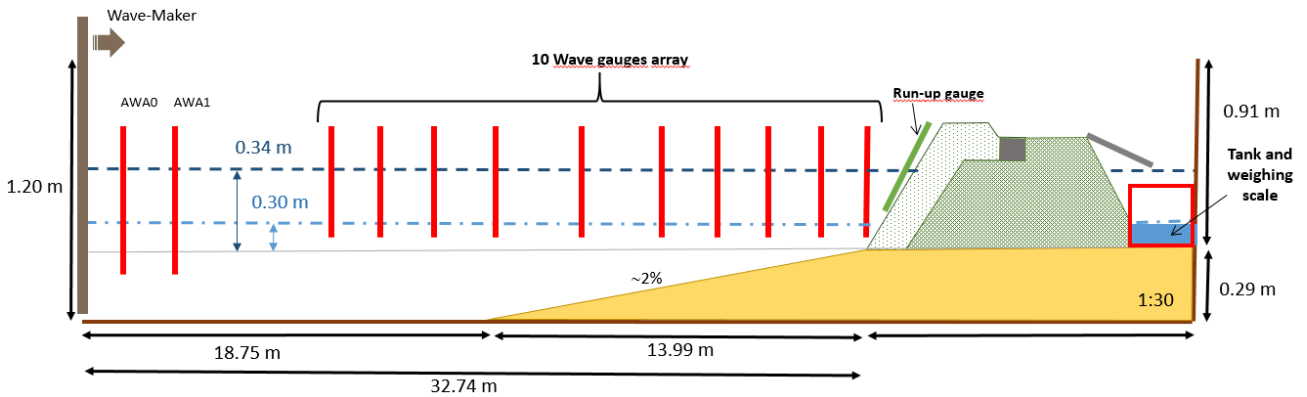


Figure 1. Sketch of the experimental setup in the wave flume (dimensions for a 1:30 scale and for the minimum and maximum water levels).

The equipment used to collect the overtopping water consisted of a tank, located at the back of the structure. The water was directed to the tank by means of a chute, 40 cm wide. The overtopping tank was placed over a weighing scale (KERN KXS-TM), which also allowed the measurement of the overtopping variation in time. The measured data were collected and stored, in digital format, at a frequency of 1Hz (Figure 2).

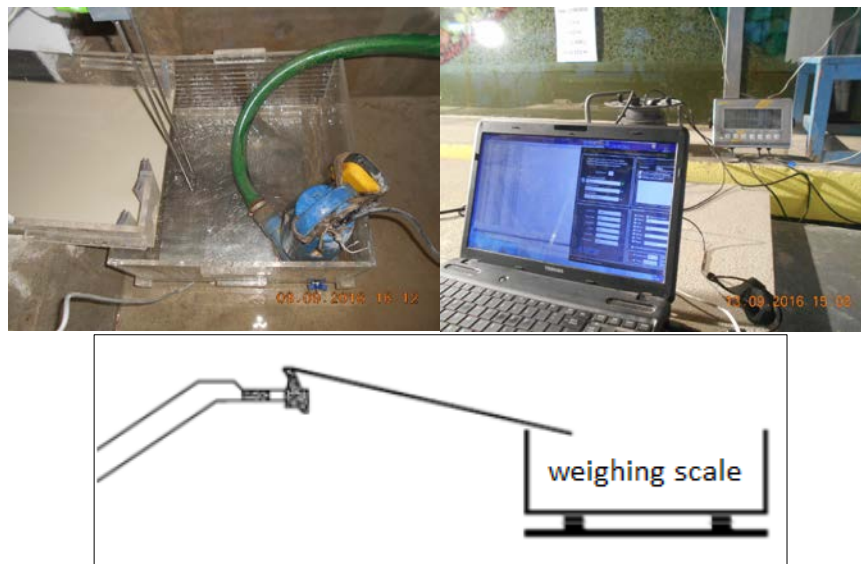


Figure 2. Setup for overtopping measurement.

The breakwater model was built and operated according to Froude's similarity law, with a geometrical scale of 1:30, to ensure reduced scale effects (wave heights should lead to values of the Reynolds number $Re > 3 \times 10^4$). The breakwater cross-section at prototype scale is presented in Figure 3.

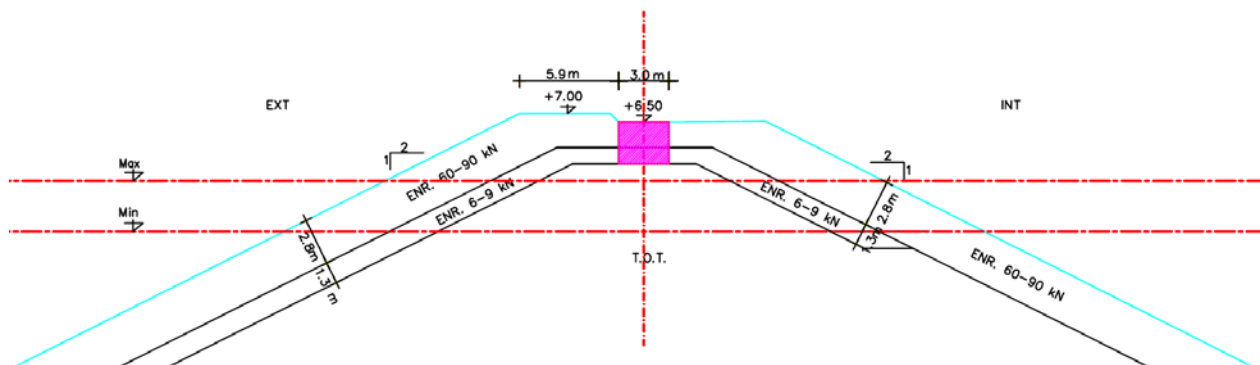


Figure 3. Breakwater cross-section at prototype scale (natural seabed at -8.1 m (CD)).

2.2 Test approaches and conditions

Two-dimensional damage and overtopping tests for a rock armor slope were performed to represent four approaches: A) a standard cumulative storm build-up (with increasing wave heights) with increasing water level; B) a standard cumulative storm build-up with a constant water level; C) a constant wave period; and D) a standard storm build-up, with a constant water level and with rebuilding.

Irregular wave tests conformed to a JONSWAP spectrum, with a peak enhancement factor of 3.3. Test durations were 1980 s, 2160 s and 2400 s for peak periods of 10 s, 11 s and 12 s, respectively (approximately 1000 waves). All tests were repeated at least three times.

The nominal test conditions are presented in Table 1, in which H_s represents the significant wave height at the toe of the structure and T_p represents the peak wave period. Tests 1-7 represent approach A; tests 1-3 and 4-7 represent approach B; tests 1-3, 4-7 and 8-15 represent approach C; and tests 4-7, with rebuilding, represent approach D.

Table 1. Nominal test conditions at structure toe.

Test	Prototype			Model		
	Water Depth, d (m)	T_p (s)	H_s (m)	Water Depth, d (m)	T_p (s)	H_s (m)
1	9.1	10	3.2	0.30	1.826	0.107
2	9.1	10	3.7	0.30	1.826	0.123
3	9.1	10	4.2	0.30	1.826	0.140
4	10.1	11	3.7	0.34	2.008	0.123
5	10.1	11	4.2	0.34	2.008	0.140
6	10.1	11	4.7	0.34	2.008	0.157
7	10.1	11	5.2	0.34	2.008	0.173
Rebuilding						
8	11.1	12	3.7	0.37	2.191	0.123
9	8.1	12	3.7	0.27	2.191	0.123
10	11.1	12	4.2	0.37	2.191	0.14
11	8.1	12	4.2	0.27	2.191	0.14
12	11.1	12	4.7	0.37	2.191	0.157
13	8.1	12	4.7	0.27	2.191	0.157
14	11.1	12	5.2	0.37	2.191	0.173
15	8.1	12	5.2	0.27	2.191	0.173

3 EMPIRICAL FORMULAE

The prediction of wave overtopping for seawalls and coastal structures can be carried out using empirical formulae to describe mean overtopping discharges, or peak volumes, using results gained from physical models for defined wave and structure parameters.

EurOtop (2016) described the methods to predict wave overtopping of sea defenses and related coastal or shoreline structures, recommending approaches for calculating mean overtopping discharges, overtopping wave volumes and the proportion of waves overtopping a seawall. These prediction methods are then used to confirm that the established tolerable discharges or overtopping wave volumes for design wave conditions are not exceeded.

The mean overtopping discharge is often used to judge allowable overtopping. It is easy to measure and an extensive database on mean overtopping discharge were gathered for the CLASH project (Van der Meer et al., 2009). This mean discharge does not fully describe the real behavior of wave overtopping, where only large waves will reach the top of the structure and give overtopping. Random individual wave overtopping means random in time and each wave gives a different overtopping volume. However, the description of individual overtopping is based on the mean overtopping, as the duration of overtopping multiplied with this mean overtopping discharge gives the total volume of water overtopped by a certain number of overtopping waves.

The physical model overtopping data collected at LNEC for the 15 test conditions shown in Table 1 have also been used to check the applicability of the methodologies/tools recommended in EurOtop (2016) to estimate mean overtopping discharges and individual overtopping volumes for a structure like the tested breakwater.

For rubble mound slopes of 1:2 to 1:4/3, subject to perpendicular wave attack, the mean discharge, q , may be evaluated as follows (EurOtop, 2016):

$$\frac{q}{\sqrt{g \cdot H_{m0}^3}} = 0.09 \cdot \exp \left[- \left(1.5 \frac{R_c}{H_{m0} \cdot \gamma_f} \right)^{1.3} \right] \quad [1]$$

where

g : acceleration due to gravity ($=9.81 \text{ m/s}^2$),

H_{m0} : spectral significant wave height at the toe of the structure,

R_c : crest freeboard of the structure, crest height of a structure relative to the water level,

γ_f : influence factor to account for dissipation induced by structure slope roughness and permeability.

EurOtop (2016) tabulates values of γ_f for permeable rubble mound structures with slope of 1:1.5, for breaker parameters, $\xi_{m-1,0}$ in the range 2.8 to 4.5 (with $\xi_{m-1,0} = \tan \alpha / \sqrt{H_{m0} / L_{m-1,0}}$, α the angle between structure slope and horizontal and $L_{m-1,0} = gT_{m-1,0}^2 / 2\pi$ the spectral wave length in deep water obtained using the spectral mean wave period, $T_{m-1,0}$). For a rock slope in two layers with a permeable core, a value of $\gamma_f = 0.4$ is recommended. However, for $\xi_{m-1,0} > 5$, meaning a large wave period, it is suggested to increase the influence factor as follows:

$$\gamma_{f \text{ mod}} = \gamma_f + (\xi_{m-1,0} - 5) \cdot (1 - \gamma_f) / 5.0 \quad [2]$$

With a maximum $\gamma_{f \text{ mod}} = 0.6$ for rubble mound structures with a permeable core.

The distribution of individual overtopping wave volumes can be represented by the two parameter Weibull probability distribution, given by the percent exceedance distribution in Eq.3 (EurOtop, 2016):

$$P_{V\%} = P(V_i \geq V) = \exp\left[-\left(\frac{V}{a}\right)^b\right] \cdot (100\%) \text{ and} \quad [3]$$

$$P_{V\%} = P_V \cdot (100\%)$$

Where

V_i : individual wave volume of overtopping,

V : specified volume of overtopping water,

P_V : probability (between 0 and 1) that an individual wave volume (V_i) will be less than a specified volume (V),

$P_{V\%}$: percentage of wave volumes that will exceed the specified volume (V),

a : parameter of the Weibull distribution; dimensional scale factor that normalizes the distribution (Eq. 4),

b : parameter of the Weibull distribution; non-dimensional shape factor for rubble mound structures that helps define the extreme tail of the distribution Eq. 5 (Zanuttigh et al., 2013),

$$a = \left(\frac{1}{\Gamma\left(1 + \frac{1}{b}\right)} \right) \left(\frac{qT_m}{P_{ov}} \right) \quad [4]$$

$$b = 0.85 + 1500 \left(\frac{q}{gH_{m0}T_{m-1,0}} \right)^{1.3} \quad [5]$$

Where Γ is the mathematical gamma function. The scale parameter, a , depends on the mean overtopping discharge, q , but also on the mean period, T_m , and the probability of overtopping, P_{ov} , or, which is similar, on the storm duration and the actual number of overtopping waves (EurOtop, 2016).

To predict the number or percentage of overtopping waves, Eq. 6 may be used:

$$P_{ov} = N_{ow} / N_w = \exp\left[-\left(\frac{A_c D_n}{0.19H_{m0}^2}\right)^{1.4}\right] \quad [6]$$

Where

N_{ow} : number of overtopping waves,

N_w : number of incident waves,
 A_c : armor crest freeboard of the structure, crest height of a structure armor relative to the water level,
 D_n : nominal diameter of armor units (D_{n50} for rock units).

4 RESULTS

4.1 Spectral and wave-by-wave analysis of the free surface elevation

Prior to determining individual overtopping volumes and mean overtopping discharges of the tested structure, spectral and wave-by-wave analyses of the free surface elevation were performed for specific locations along the flume.

For each test, the elevation of the free surface was measured and analyzed with a time-domain wave-by-wave analysis, using the zero up-crossing method, and with a spectral-domain analysis (Ramos et al., 2015), using classical Fast Fourier Transform (FFT) method. The wave-by-wave analysis allowed the determination of H_s , the significant wave period, T_s (relative to H_s), and the 1/10th of the wave height, $H_{1/10}$. The spectral analysis allowed the determination of the spectral significant wave height, H_{m0} , T_p , and $T_{m-1,0}$.

Figure 4 shows the values of H_{m0} obtained for test conditions 1 to 6 (Table 1) at the wave gauge placed at the toe of the structure. It also shows the mean, μ and the standard deviation, σ of H_{m0} obtained for the repetitions performed for each test condition. The obtained results present some variability, as usually expected in test repetitions. However, this variability may also be due to the fact that, after some tests (but not all), the structure had to be rebuilt and, in practice, this procedure may have introduced slightly different starting conditions for the different repetitions. In order to illustrate this point, Figure 5 shows H_{m0} for test condition 3, where the blue lines indicate the days when the model was rebuilt.

The same type of conclusions can be drawn from Figure 6, which shows the values of $T_{m-1,0}$ obtained for test conditions 1 to 6 at the wave gauge placed at the toe of the structure. Again, the obtained results showed some variability, which is within the expectation in this type of tests, and one can confirm that the tests conducted after a reconstruction (repetitions 2 and 3) present, generally, a higher variability than when rebuilding is not made.

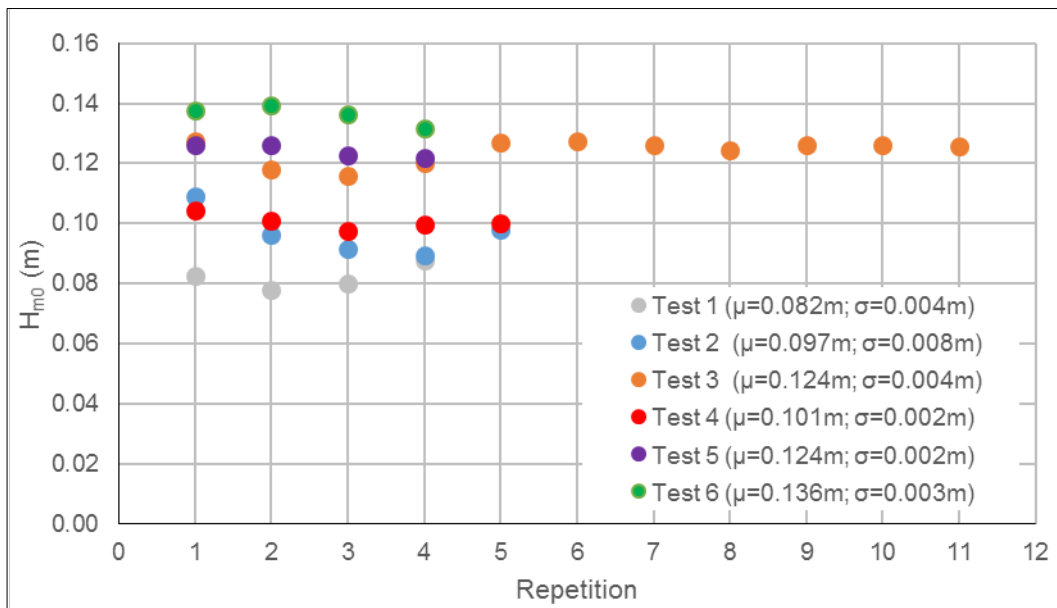


Figure 4. Computed spectral significant wave heights, H_{m0} , for test conditions 1 to 6.

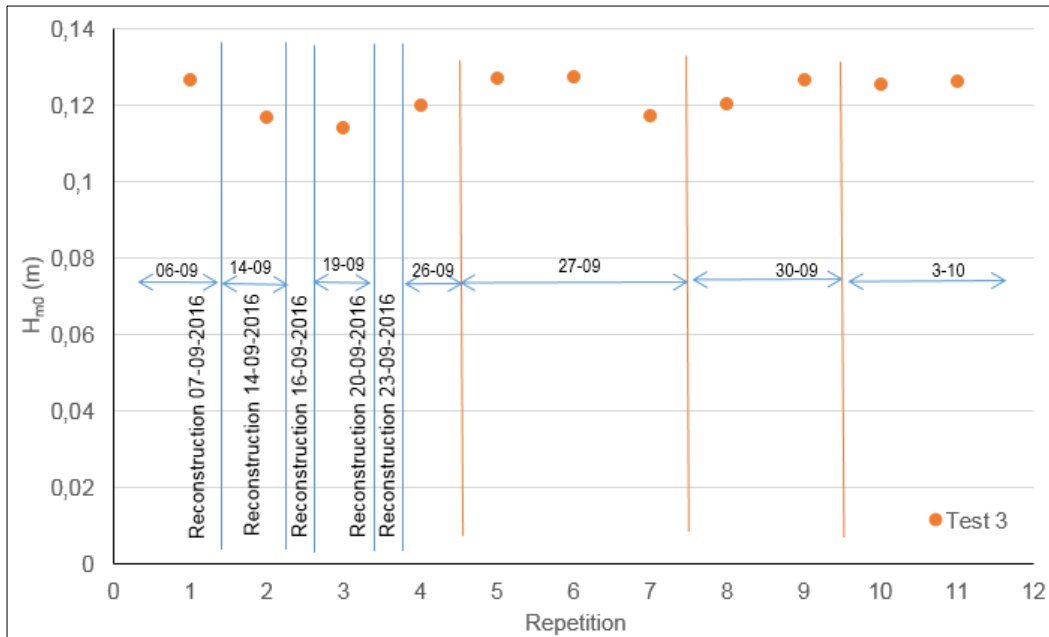


Figure 5. Computed spectral significant wave heights, H_{m0} , for test condition 3.

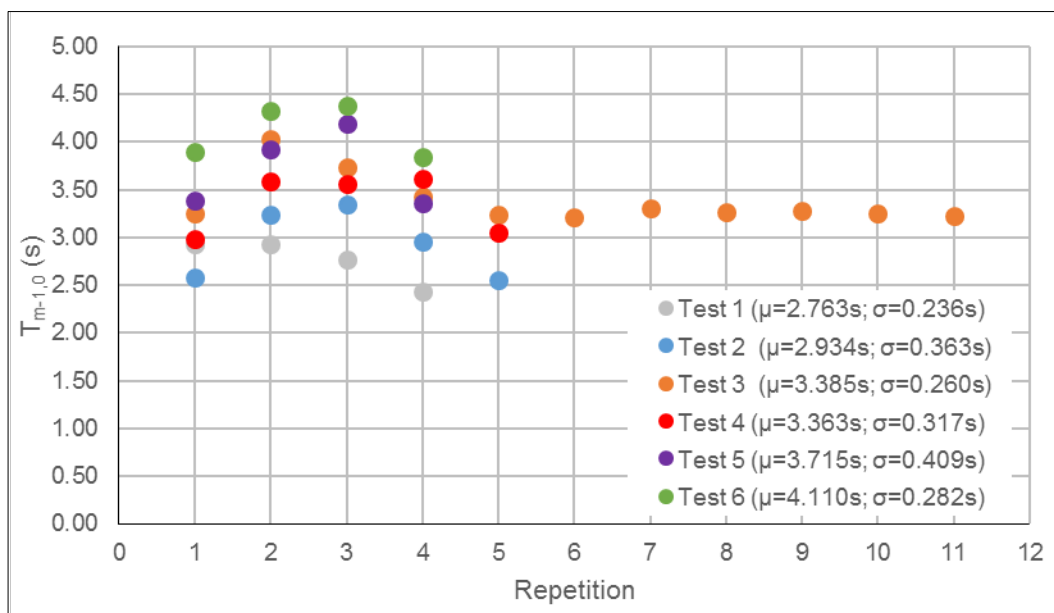


Figure 6. Computed spectral mean wave periods, $T_{m-1,0}$, for test conditions 1 to 6.

4.2 Mean overtopping discharge

The physical experiments presented in section 2 resulted in a data set with mean overtopping discharges for around 80 experiments. Different wave conditions were assessed and the total and individual overtopping volumes were analyzed and compared with existing empirical prediction methods (EurOtop, 2016). The overtopping results of test conditions 1 to 6 (32 tests) were analyzed in this section.

Figure 7 presents mean overtopping discharges per meter length of structure, q , as a function of H_{m0} , for test conditions 1 to 6. As expected, for the same water depth (tests 1 to 3 and tests 4 to 6), q increases with H_{m0} .

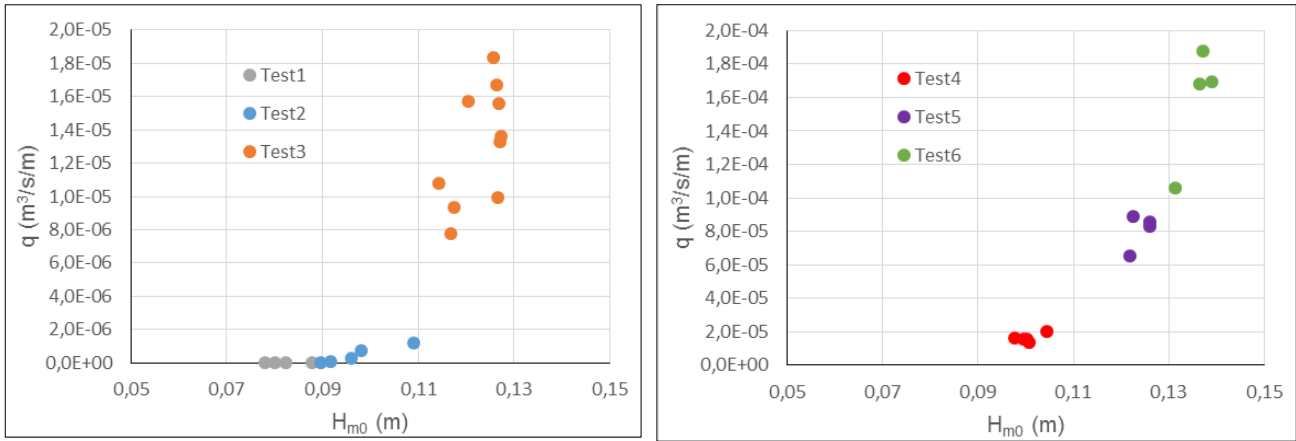


Figure 7. Measured mean overtopping discharges, q , versus H_{m0} for test conditions 1 to 6.

Figure 8 shows the computed and the measured non-dimensional mean overtopping discharges, $q/(gH_{m0}^3)^{0.5}$, versus the non-dimensional freeboards, R_c/H_{m0} , for test conditions 2 to 6 (note that for test 1, there were no overtopping events). The computed values were obtained both using Eq. 1 (with the mean of the roughness factors of the tests, $\gamma_{f\text{mod}} = 0.544$; continuous line) and the 90%-confidence band (dotted lines) suggested in EurOtop (2016). The figure shows that the empirical formula provides good predictions of the mean overtopping discharges measured in the experiments, with all data points falling within the 90% confidence band of Eq. 1. For values of $q/(gH_{m0}^3)^{0.5} < 10^{-5}$, the predictions are less reliable and correspond to mean overtopping discharges less than 0.5 l/s/m (test 2), for which some scale effects are usually expected.

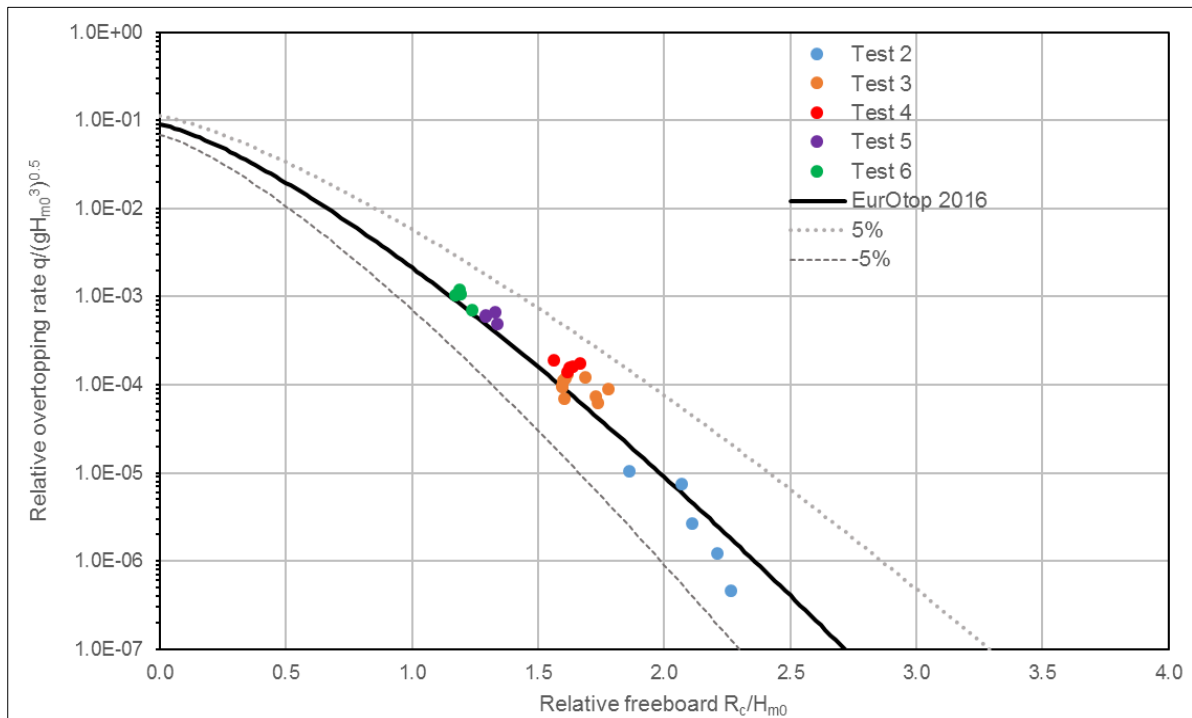


Figure 8. Computed (Eq. 1 obtained with $\gamma_{f\text{mod}} = 0.544$ and 90%-confidence band; EurOtop, 2016) and measured non-dimensional mean overtopping discharges, $q/(gH_{m0}^3)^{0.5}$, versus non-dimensional freeboards, R_c/H_{m0} , for test conditions 2 to 6.

4.3 Individual overtopping volumes

The individual overtopping volumes, V_i , measured for each test are shown in Figure 9, Non-dimensional overtopping volume (individual volume divided by the average of the individual volumes of the test), V_i/V_{average} , is plotted against probability of non-exceedance of each individual volume in the test (relative to the number of waves), P_{ov} . Figure 9 shows that the probability where the maximum individual volume is not larger than approximately eight times the average of the test volumes is 100%.

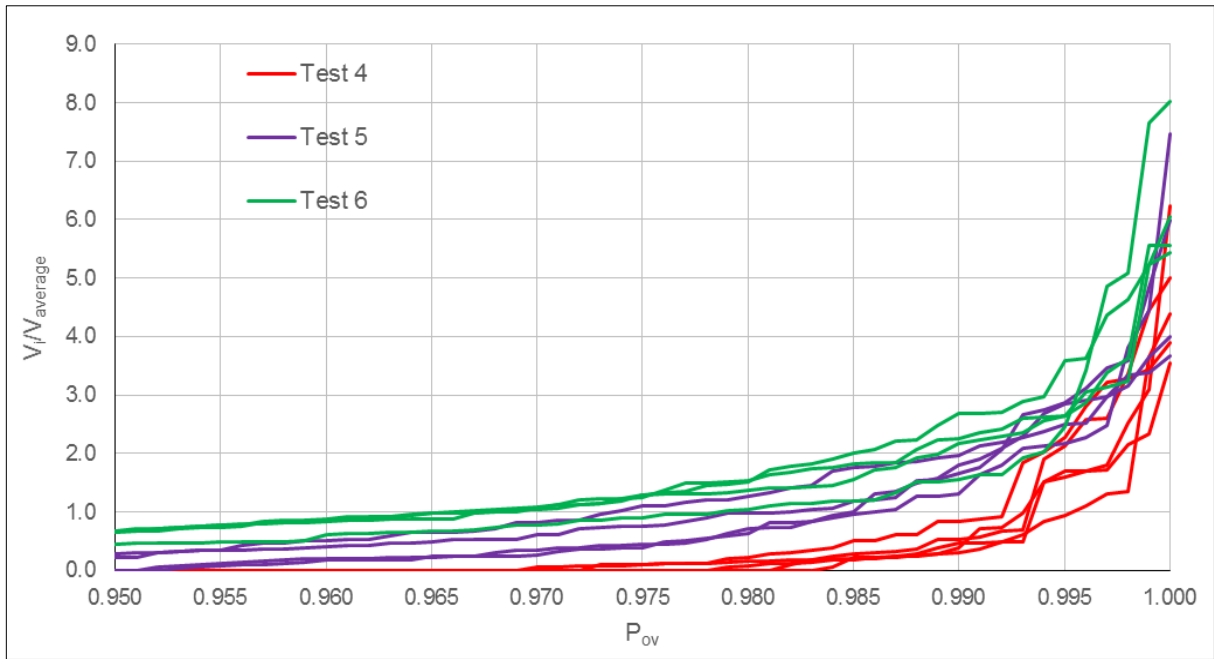


Figure 9. Measured non-dimensional individual overtopping volumes, $V_i/V_{average}$, versus the probability of non-exceedance, P_{ov} , for test conditions 4 to 6.

Figure 10 shows computed (Eq. 5) and measured Weibull shape factors, b , for rubble mound structures versus non-dimensional mean overtopping discharges, $q/(gH_{m0}T_{m-1,0})$. It shows that for a relative discharge $q/(gH_{m0}T_{m-1,0}) < 5 \times 10^{-5}$, the average value of b is about 0.85, with almost no scatter in the data, suggesting that $b=0.85$ can be used to describe overtopping of individual wave volumes. Data are in close agreement with the computed values of b .

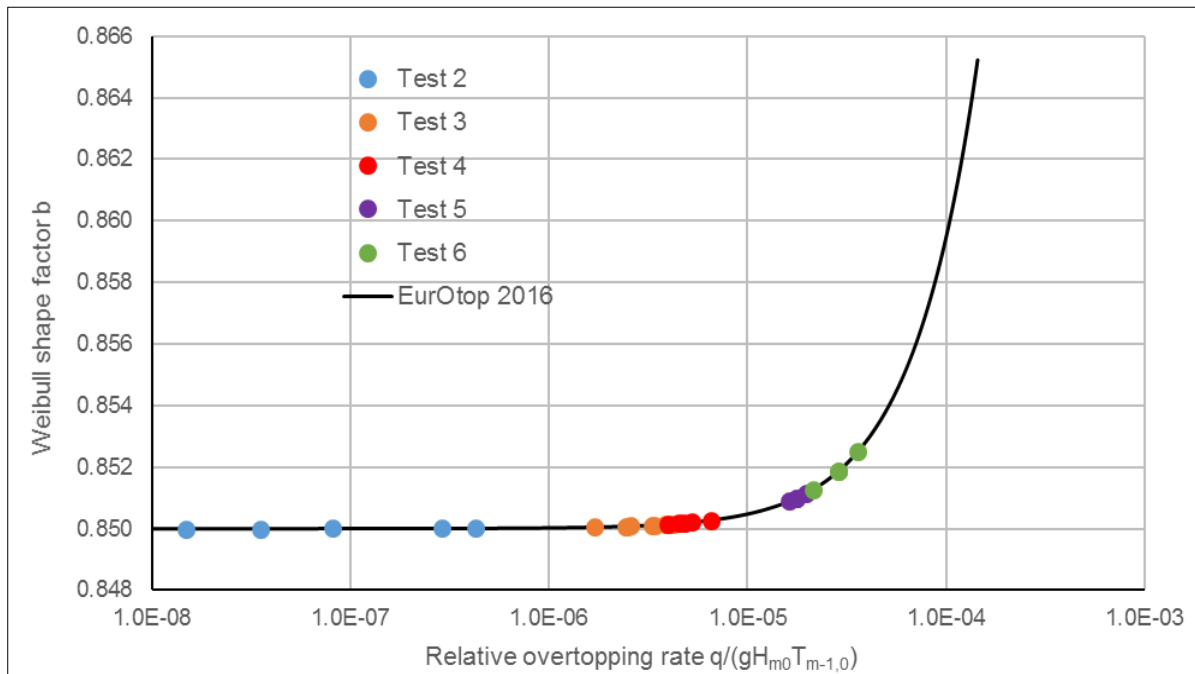


Figure 10. Computed (Eq. 5; EurOtop, 2016) and measured Weibull shape factors, b , for rubble mound structures versus non-dimensional mean overtopping discharges, $q/(gH_{m0}T_{m-1,0})$.

Figure 11 gives computed (Eq. 6) and measured percentage of overtopping waves versus the non-dimensional crest height, $A_c * D_n / H_{m0}^2$. The test data are in good agreement with the empirical prediction given by the EurOtop Manual (EurOtop, 2016). However, the presented tests (Tests 4, 5 and 6) cover a limited range of overtopping percentages, with maximum values of about 9%.

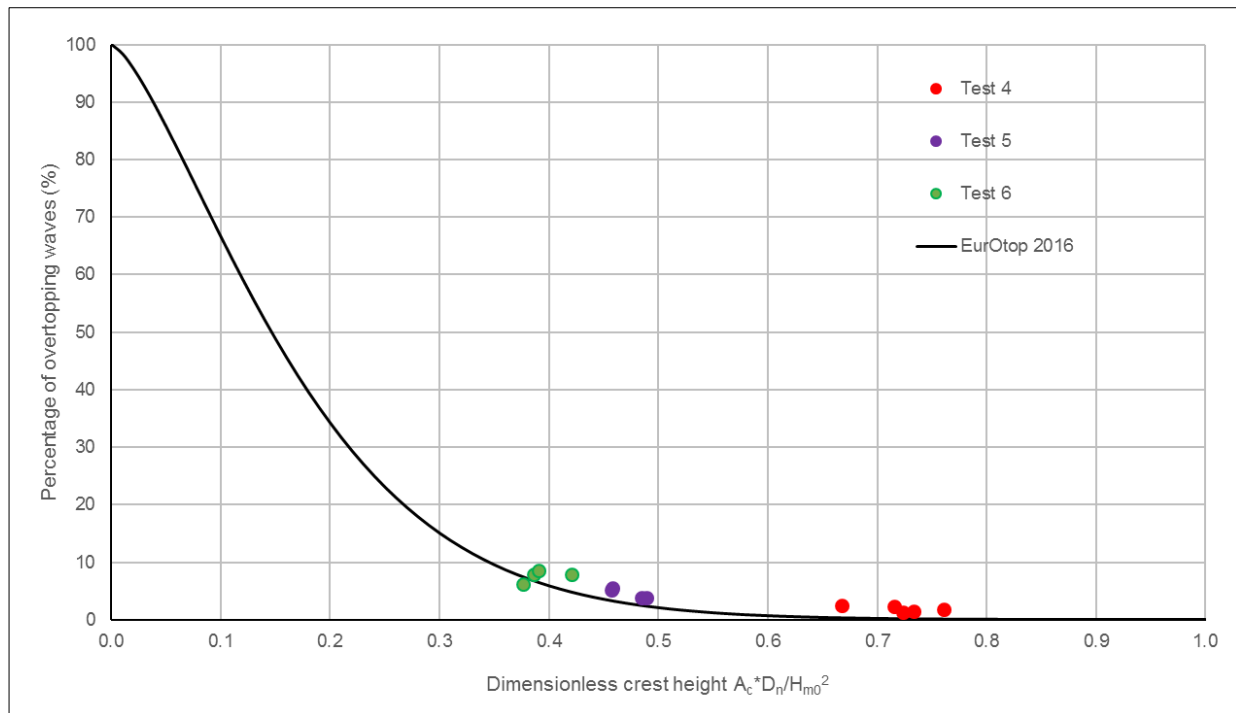


Figure 11. Computed (Eq. 6; EurOtop, 2016) and measured percentage of overtopping waves, P_{ov} , for rubble mound breakwaters versus relative (armor) crest height and armor size ($R_c \leq A_c$).

5 CONCLUSIONS

Two-dimensional physical model tests were carried out at LNEC measured wave overtopping on a rubble mound structure, with a 1:2 armor layer and a lower wall behind. A comparison of both mean overtopping discharges and individual overtopping volumes was performed between measured and computed values, with the latter obtained from EurOtop (2016) empirical formulae. Generally speaking, it was concluded that the overtopping experimental data were well explained by the standard EurOtop (2016) empirical methods.

Physical model data on mean overtopping discharges, q , were within the 90% confidence interval of the EurOtop (2016) empirical formula. As expected, for values of $q / (gH_{m0}^3)^{0.5} < 10^{-5}$ the predictions were less reliable.

Concerning the individual overtopping volumes measured during testing, the probability where the maximum individual volume is not larger than eight times the average of the test volumes was 100%. The theoretical probability distribution of overtopping wave volumes was assumed to be a two-parameter Weibull. Computed and measured Weibull shape factors, b , were compared. For a relative mean discharge $q / (gH_{m0} T_{m-1,0}) < 5 \times 10^{-5}$ the average value of b was about 0.85, with almost no scatter in the data, suggesting that $b=0.85$ can be used to describe overtopping of individual wave volumes. Data were in close agreement with the EurOtop (2016) values of b for rubble mound structures.

Computed (EurOtop, 2016) and measured percentage of overtopping waves were analyzed as a function of the non-dimensional crest height, $A_c * D_n / H_{m0}^2$. The test data were in good agreement with the empirical prediction given by the EurOtop Manual.

ACKNOWLEDGEMENTS

The authors acknowledge the financial support of the European project H2020-INFRAIA-2014-2015, N.654110 - Hydralab+ Adapting to Climate.

REFERENCES

- EurOtop, (2016). *Manual on Wave Overtopping of Sea Defences and Related Structures, An Overtopping Manual Largely Based on European Research*. EurOtop Overtopping Manual.
- Ramos, A. & Fortes, C.J.E.M. (2015). *Programa De Análise Espectral Utilizando A Função Wavelet*, Rel. LNEC 374/2015.
- Van Der Meer, J.W., Verhaeghe, H. & Steendam, G.J. (2009). The New Wave Overtopping Database for Coastal Structures. *Coastal Engineering*, 56, 108–120.
- Zanuttigh, B., Van Der Meer, J.W., Bruce, T. & Hughes, S. (2013). Statistical Characterization of Extreme Overtopping Wave Volumes. *Proc. ICE, Coasts, Marine Structures and Breakwaters 2013*, Edinburgh, UK.

NUMERICAL STUDY ON THE SILTATION IN THE MAIN CHANNEL OF ZHUHAI GAOLAN HARBOR CAUSED BY DREDGING AND ENGINEERING

SULAN LU⁽¹⁾, YU JIANG⁽²⁾, XINFENG ZHANG⁽³⁾ & YUE LI⁽⁴⁾

^(1,2,3,4) Pearl River Hydraulic Research Institute, Guangzhou, China,
esula2002@163.com; jiangyu-jy@163.com; zksxfj@vip.163.com; ly-hou@163.com

ABSTRACT

Zhuhai Gaolan harbor lies in Huangmao Bay. Severe siltation done irregularly in the main channel is a puzzling problem faced by the harbor recently. Variation characteristics of underwater bottom topography in the main channel during several years are analyzed. Large projects implemented nearby including upgrade of dredging in the main channel, dredger filling engineering, and Tieluwan breakwater construction are also of concern. Choosing the typical hydrological condition, with a 2d numerical models of wave, tidal flow and sediment, the paper simulates and analyzes the normal siltation in the main channel of Zhuhai Gaolan port, and the siltation changes caused by large projects mentioned above. In the simulation, the source intensity of different dredging boat and their position in the construction site are fully considered and represented. The result indicates that, the siltation rate in the main channel is 1.015m/a normally. Yet, under the upgrade of dredging condition, the siltation in the main channel can increase from 0.098m per month to 0.450m per month. The siltation in the area is using grab dredger which increases less sediment comparatively due to the less sediment source. According to the simulation, the dredger filling project, 2km away which is located in the east of the channel with cutter-suction dredger, mainly increases the siltation about 10% in the sub channel nearby. The main channel retains its siltation rate with the increase of 0.17% only. In addition, the effect of the Tieluwan breakwater construction is also studied. It concludes that, the siltation increases obviously in the south of Tieluwan breakwater. Yet the siltation of main channel decreases about 5.37% because of the less sediment source and the stronger currents due to the narrower cross-section. To sum up, the upgrade dredging work is the key factor of the severe siltation in the main channel of Zhuhai Gaolan harbor.

Keywords: Numerical study; siltation; main channel; dredging; engineering.

1 INTRODUCTION

Gaolan harbor which is the main harbor of Zhuhai port with fine deepwater condition lies in the east-north of Huangmao Bay in the Pearl River estuary. In recent years, however, the harbor has been troubled by serious siltation in some segments of the main approach channel. In the meantime, the Gaolan Harbor has been busy with engineering activities, wharf construction and channel upgrade dredging. To identify the key factors that cause abnormal siltation in some segments of the main channel is very urgent and important to the normal operation of the main channel. Whether the serious siltation in the main channel is caused by engineering activities in the surrounding areas, or improper dredging or sediment disposal, or sudden siltation due to typhoon, or incoming sediment carried by flood currents from the sea and water and sediment discharged from adjacent gates needs to be further studied.

The Huangmao Bay waters, affected by the discharge of water and sediment via the outlets in the upstream and affected by the incoming sediment from the sea carried by the South China Sea tides and shoal sediment movement by waves in the downstream, have a complicated water and sediment dynamic environment. For a long time, the study on the water and sediment movement characteristics, sea-bed evolution, channel development and harnessing, and harbor siltation of the Huangmao Bay (Yang et al., 2016; Guo et al., 2015; Zhang, 2015; Hou et al., 2012; Zhang et al., 2006; Wu et al., 1999; Wu, 1995; Yang, 1993) has been continuously conducted based on measured data analysis or mathematical model calculation. This helps in providing a scientific basis for the management, protection, development and utilization of the Huangmao Bay. However, in recent years, as the number of construction activities grows and the regional water and sediment environment changes greatly, the main approach channel of the Gaolan harbor is challenged by abnormal siltation in some areas. Regarding this specific problem, there isn't any other relevant analysis and research yet. Based on the analysis of underwater topography variation of the main channel of Gaolan harbor in recent years and the construction data during dredging, the purpose of this study is to simulate the influence of dredging on the siltation in the main channel and surrounding wharfs as well as the influence of major engineering activities in the surrounding area on the siltation in the main channel, to identify the main influencing factors of abnormal siltation in the main channel of the Gaolan harbor.

2 INFLUENCE OF DREDGING DURING CONSTRUCTION

The main channel of the Gaolan harbor, as shown in Figure 1, is 16km long. The topographic changes and siltation of the main channel during construction are studied based on the analysis of the underwater topography data measured every three months from March 2014 to June 2015 as well as the dredging workload data during the period. According to the construction data collected, from April to September 2014, the main channel underwent a 100,000 DWT maintenance dredging, with a total dredging volume of 4.5 million m³. Starting from November 2014, 150,000 DWT upgrade was carried out on the main channel. The dredging volume up to June 2015 totaled 12.91 million m³. Based on the underwater topography data measured in 7 rounds from March 2014 to June 2015 as well as the dredging volume in the same period, the siltation status in the main channel during construction was analyzed statistically. The calculation results are shown in Table 1.

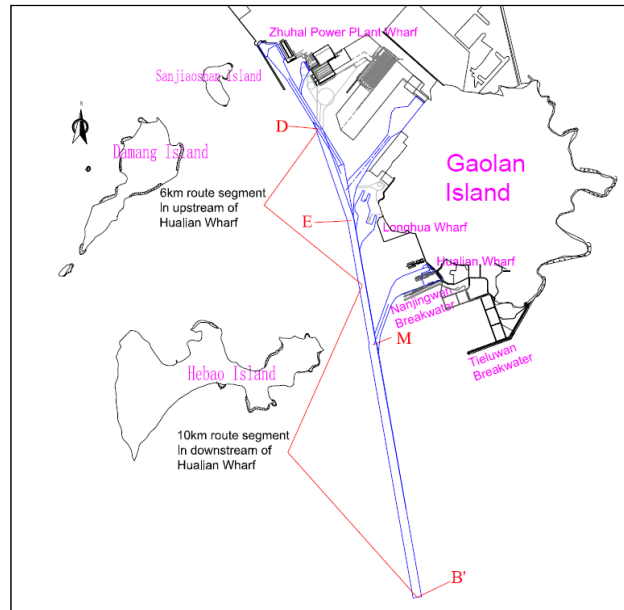


Figure 1. Segmentation of the main channel and distribution of surrounding wharfs.

Table 1. Statistical analysis of scouring and silting in the main channel during construction.

Measurement period	Measured statistics		Collected data		Total	
	Scouring or silting volume (10 ⁴ m ³)	Scouring or silting thickness (m)	Dredging volume (10 ⁴ m ³)	Net siltation volume (10 ⁴ m ³)	Net scouring or silting thickness (m)	Net scouring and silting thickness (m/month)
2014.3-2014.8	-268.92	-0.948	450.06	181.14	0.638	0.128
2014.8-2014.12	-320.77	-0.655	587.90	267.12	0.545	0.136
2014.12-2015.3	-224.54	-0.312	535.80	311.26	0.432	0.144
2015.3-2015.6	-334.93	-0.407	755.20	420.27	0.510	0.170

NOTE: A negative value indicates sea-bed deepening and growing sea-bed volume; a positive value indicates sea-bed siltation.

The table showed that, due to the presence of dredging engineering, the entire main channel was characterized by sea-bed deepening. In the measurement period, the sea-bed volume increment was 2.689 million m³ to 3.349 million m³, and the average deepening was 0.312m to 0.948m. The sea-bed volume increment was subtracted from the dredging volume during the period to get the siltation volume of the main channel during the measurement period; the bottom width of the main channel was divided by the siltation volume to get the siltation thickness of the main channel. The results show that, with the dredging volume fully considered, the average siltation thickness of the main channel in all measured rounds during construction was 0.432m to 0.638m where the average monthly siltation thickness was 0.128m to 0.170m. It averaged 0.144m, and when the dredging volume was large the siltation volume was also large, as shown in Figure 2.

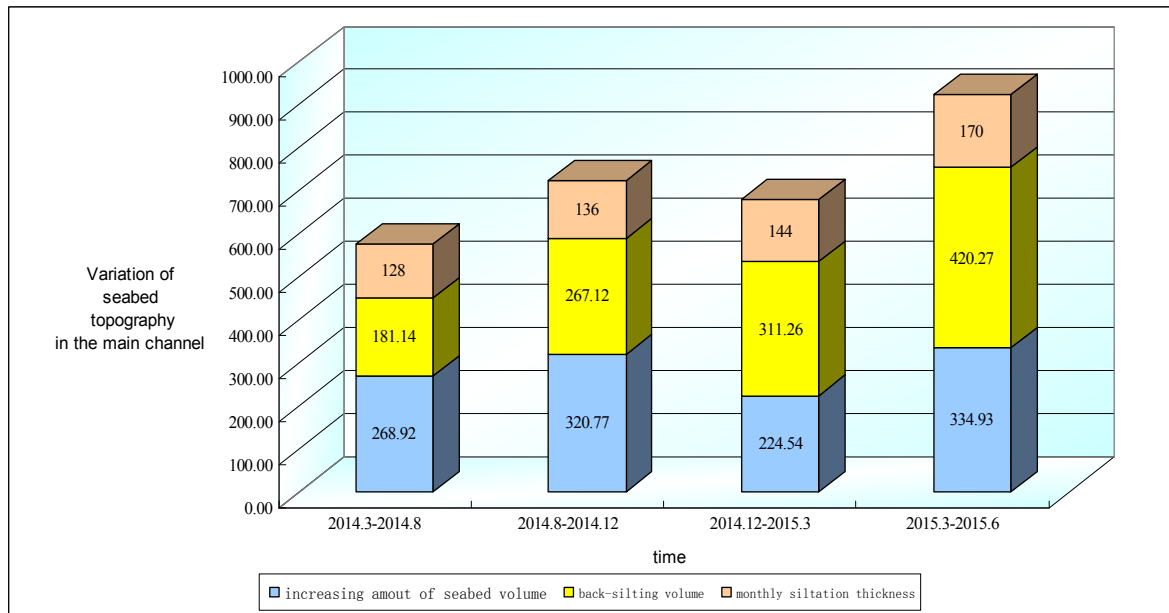


Figure 2. Topography and siltation of the main approach channel during construction (volume: 104m³; thickness: -mm).

According to the analysis of topographic data from December 2011 to March 2014, the average monthly siltation thickness in the main channel was about 0.101m. During recovery dredging and upgrade dredging of the main channel from March 2014 to June 2015, the siltation thickness increased to 0.144m, while there wasn't any sudden siltation increase caused by typhoon. Therefore, it's preliminarily believed that, since there wasn't any obvious difference in the water and sediment environment, the siltation increase of 43% during recovery dredging and upgrade dredging of the main channel was mainly caused by dredging construction. Figure 2 also showed that, the greater the dredging intensity was, namely, the greater the dredging volume in the same period of time was, the greater the influence on siltation was.

3 NUMERICAL MODEL OF WAVE-CURRENT-SEDIMENT

3.1 Model construction

The main approach channel of the Gaolan harbor, located at the south bay mouth of the Huangmao Bay, is significantly affected by waves from the open sea, so the sediment model must consider the combined impact of tidal currents, wind and waves on the sediment concentration and river-bed scouring and siltation.

Flow continuity equation:

$$\frac{\partial h}{\partial t} + \frac{1}{C_{\xi} C_{\eta}} \left[\frac{\partial}{\partial \xi} (Hu C_{\eta}) + \frac{\partial}{\partial \eta} (Hv C_{\xi}) \right] = \frac{q}{C_{\xi} C_{\eta}} \quad [1]$$

Flow momentum equations:

$$\frac{\partial u}{\partial t} + \frac{u}{C_{\xi}} \frac{\partial u}{\partial \xi} + \frac{v}{C_{\eta}} \frac{\partial u}{\partial \eta} + \frac{uv}{C_{\xi} C_{\eta}} \frac{\partial C_{\xi}}{\partial \eta} - \frac{v^2}{C_{\xi} C_{\eta}} \frac{\partial C_{\eta}}{\partial \xi} = fv - \frac{g}{C_{\xi}} \frac{\partial h}{\partial \xi} + E_{\xi} \left(\frac{1}{C_{\xi}} \frac{\partial A}{\partial \xi} - \frac{1}{C_{\eta}} \frac{\partial B}{\partial \eta} \right) - \frac{gu}{C^2 H} \sqrt{u^2 + v^2} \quad [2]$$

$$\frac{\partial v}{\partial t} + \frac{u}{C_{\xi}} \frac{\partial v}{\partial \xi} + \frac{v}{C_{\eta}} \frac{\partial v}{\partial \eta} + \frac{uv}{C_{\xi} C_{\eta}} \frac{\partial C_{\eta}}{\partial \xi} - \frac{u^2}{C_{\xi} C_{\eta}} \frac{\partial C_{\xi}}{\partial \eta} = -fu - \frac{g}{C_{\eta}} \frac{\partial h}{\partial \eta} + E_{\eta} \left(\frac{1}{C_{\xi}} \frac{\partial B}{\partial \xi} + \frac{1}{C_{\eta}} \frac{\partial A}{\partial \eta} \right) - \frac{gv}{C^2 H} \sqrt{u^2 + v^2} \quad [3]$$

Wave equation:

$$\frac{\partial}{\partial t} N + \frac{\partial}{\partial x} c_x N + \frac{\partial}{\partial y} c_y N + \frac{\partial}{\partial \sigma} c_{\sigma} N + \frac{\partial}{\partial \theta} c_{\theta} N = \frac{S}{\sigma} \quad [4]$$

Sediment transport equation:

$$\frac{\partial(HS)}{\partial t} + \frac{1}{C_\xi C_\eta} \left[\frac{\partial}{\partial \xi} (C_\eta H u S) + \frac{\partial}{\partial \eta} (C_\xi H v S) \right] = \frac{1}{C_\xi C_\eta} \left[\frac{\partial}{\partial \xi} \left(H \varepsilon_\xi \frac{C_\eta}{C_\xi} \frac{\partial S}{\partial \xi} \right) + \frac{\partial}{\partial \eta} \left(H \varepsilon_\eta \frac{C_\xi}{C_\eta} \frac{\partial S}{\partial \eta} \right) \right] - \alpha \omega (S - S_*^2) + S_0 \quad [5]$$

Seabed deformation equation:

$$\gamma_0 \frac{\partial \eta}{\partial t} = \alpha \omega (S - S_*^2) \quad [6]$$

In the formula, $A = \frac{1}{C_\xi C_\eta} \left[\frac{\partial}{\partial \xi} (C_\eta u) + \frac{\partial}{\partial \eta} (C_\xi v) \right]$; $B = \frac{1}{C_\xi C_\eta} \left[\frac{\partial}{\partial \xi} (C_\eta v) - \frac{\partial}{\partial \eta} (C_\xi u) \right]$; u and v represent the velocity

components in ξ and η directions respectively, h is water level, q is flow source of per unit area, H is water depth, g is gravity acceleration, f is coriolis coefficient, E_ξ and E_η represent the turbulent viscosity coefficient. Lami coefficient C_ξ and C_η are indicated as follows: $C_\xi = \sqrt{x_\xi^2 + y_\xi^2}$; $C_\eta = \sqrt{x_\eta^2 + y_\eta^2}$. N is wave spectrum; c_x , c_y , c_σ , c_θ represent the transmission speed in the direction of X , Y , σ , θ respectively; ε_ξ and ε_η are sediment diffusion coefficient; S_*^2 is the sediment carrying capacity of 2d module

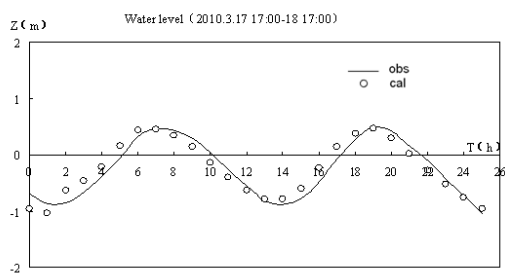
including both current and wave action, $S_*^2 = k_1 \frac{V^3}{\omega \sqrt{gH}} + k_2 \frac{H_w}{H^2 \omega}$, k_1 and k_2 are the sediment carrying capacity coefficients, V is depth averaged velocity; H_w is wave height; S_0 is sediment source, γ_0 is the dry specific gravity of the sand, η is the variation of seabed elevation.

The paper uses orthogonal curve grid to fit the complex boundary configuration of Huangmao Bay which presents trumpet shape with so many islands in it. In the 2d model, the governing equations were discretized by finite difference method. And the equations were solved with an alternative directional implicit method.

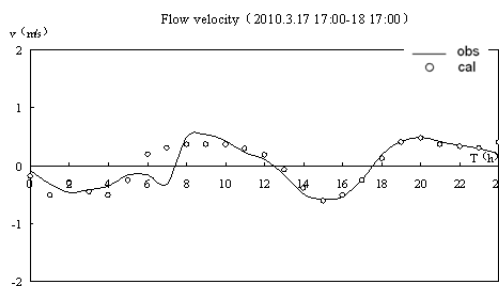
The research scope of the model: the control of hydrological stations at the exit of the four gates in the west of the Pearl River Estuary, namely Yamen Outlet Guanchong Station, Hutiao Outlet Xipaotai Station, Jiti Outlet Huangjin Station and Modao Outlet Denglongshan Station were considered as the upper boundary where else the open sea -30m contour line as the lower boundary with research scope covering Huangmao Bay neritic area, Jiti Outlet neritic area, and Modao Outlet neritic area. The research area is about 98km wide and about 102km long, and the controlled water area is about 9,996km². Generated grids total about 843×624. In the open sea area, the maximum grid size is about 293m×1,588m; in the gate area, the minimum grid size is about 10m×20m; and in the Gaolan harbor water area, the grid size is about 30m×40m.

3.2 Model validation

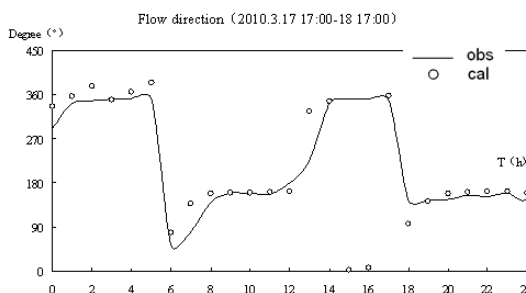
For estuarine flow validation, the selected hydrological combination is: "1992.7" (flood season), "1992.11" (dry season) and "2010.3" (tide combination). Validation cases included water level, flow velocity, flow direction and etc. Here a brief introduction on relevant validation is shown in Figure 3, with water level sample point locating in the southwest of Gaolan Island and flow sample point locating in the main channel near Longhua Wharf. The calculation of hydrological conditions for the validation of sediment concentration and the validation of scouring and siltation are: "1992.7" (flood season) and "1992.11" (dry season). This paper mainly discusses the results of scouring and silting validation. The measured statistics show that the average annual siltation intensity of the 100,000 DWT main channels was about 1.216m, while the model-based calculation result was 1.015m, with a discrepancy of about 16.5%. Scouring and siltation validation considers the impact of waves. Measured results were basically in line with the measured results, which largely reflected the north-to-south siltation along the main channel where it meets the accuracy requirements of the relevant specifications as shown in Figure 4.



(a) water level



(b) flow velocity



(c) flow direction

Figure 3. Validation of estuarine flow.

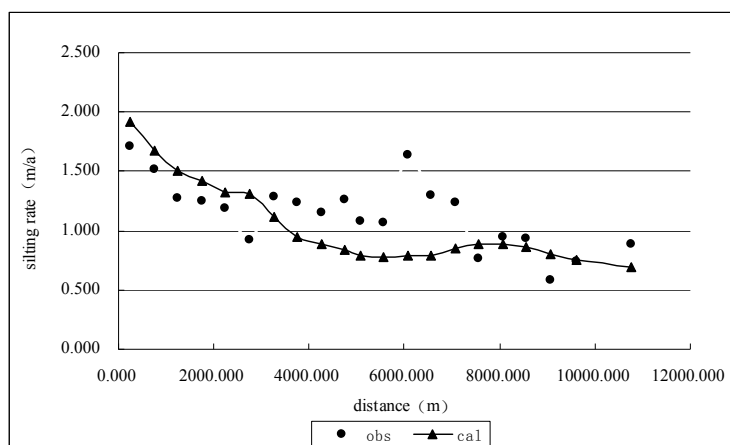


Figure 4. Validation of annual siltation thickness of the main inbound channel.

4 SIMULATION ON THE SILTATION OF MAIN CHANNEL CAUSED BY ENGINEERING

4.1 Engineering introduction and model processing

The engineering activities considered include: 150,000 DWT upgrade of the main channel, secondary transport of storage pit sediment in the Nanshui operation area of the Gaolan harbor, and Tieluwan breakwater.

(1) Upgrade of the main channel

The 150,000 DWT upgrade of the main channel, namely widening and deepening on the basis of the previous 100,000 DWT main channel, was started in November 2014. According to the data collected through site survey of constructor, the workboat type and working time during construction for the main channel were as follows: for the segment in the upstream (6km) of the Hualian wharf, 12m³ grab dredgers were used and two workboats were placed within 1km; for the segment in the downstream (10km) of the Hualian wharf, trail suction dredgers, with a tank volume of 5,000m³, 7,000m³ and 10,000m³, were used, generally 2 or 3 trail suction dredgers were used, and a maximum of 5 trail suction dredgers were used at the same time; the duration from full-tank overflow to return voyage after outbound shipment and sediment disposal was about 2-2.5h. All workboats work 24h a day.

In this simulation calculation, the workboat arrangement in the upstream of the Hualian wharf is consistent with that according to the site survey. In the downstream, with the most adverse effects considered, 5 trail suction dredgers were arranged to work at the same time. The tank volume from north to south is $5,000\text{m}^3$, $5,000\text{m}^3$, $7,000\text{m}^3$, $10,000\text{m}^3$ and $10,000\text{m}^3$ respectively. Each construction cycle was set to 2h: 1h from loading to full-tank overflow, and 1h for outbound shipment and empty-trunk return, namely 1h for emission of sand source.

(2) Secondary transport of sediment storage pit

The storage pit, located in the southern basin of the Nanshui operation zone of the Gaolan harbor and 2km to the east of the main channel, is designed for the temporary storage of dredged spoil of harbor basins, branch channels and the main channel within the harbor. Two cutter suction dredgers are conventionally arranged for secondary transport of sediment in the storage pit, which was used to hydraulically fill the beach land within the nearby jetty to form a land area. The productivity of cutter suction dredgers is $2,300\text{m}^3/\text{h}$ and $3,000\text{m}^3/\text{h}$ respectively, and the working time within a month was about 450-500h. The location of the storage pit is as shown in Figure 5.

(3) Tieluwan breakwater

Tieluwan breakwater, located at the control section of the southern outlet of the Huangmao Bay, between Gaolan Island and Damang Island and about 2.5km in the downstream of the Nanjingwan breakwater, is built along the southwest coastline of Gaolan Island. The breakwater, with a total length of 2,803.6m, reduces the cross-flow area of the inter-island control section by about 34%. According to the feedback from relevant company, abnormal siltation frequently occurs to the segment between the Nanjingwan breakwater and the Tieluwan breakwater, not conducive to navigation of passing vessels. Regarding whether abnormal siltation was related to the change of the water and sediment environment in some areas caused by the construction of the Tieluwan breakwater, the siltation in the main channel before and after the construction of the Tieluwan breakwater and the siltation around the breakwater were calculated. The statistical area around the Tieluwan breakwater is as shown in Figure 5.

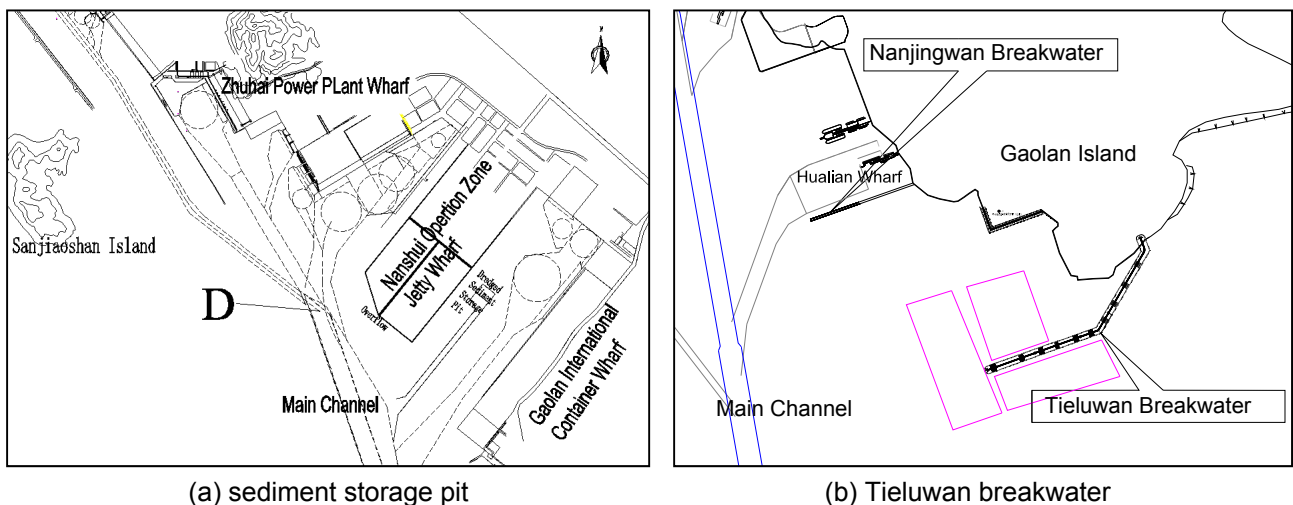


Figure 5. Location of the storage pit and statistical range of siltation around Tieluwan breakwater.

4.2 Determination of construction source intensity

Based on the results of the similar study (South China Sea Institute of Oceanology, CAS, 2010) (8m^3 grab dredgers, 2.08kg/s source intensity), this project uses 12m^3 grab dredgers (3.12kg/s source intensity by analogy). For trail suction dredgers, the scientific achievements of the Tianjin Research Institute for Water Transport Engineering (TIWTE), MOT will apply: tank volume of $4,500\text{m}^3/\text{h}$ and suspended matter (from dredging) source intensity of 7.5kg/s . The tank volume of trail suction dredgers for the main channel is $5,000\text{m}^3$, $7,000\text{m}^3$ and $10,000\text{m}^3$, with a source intensity of 8.3kg/s , 11.7kg/s and 16.7kg/s by analogy.

According to TIWTE's actual observation of SS diffusion when the test segment of the Tonggu channel of the Pearl River Estuary was dredged in 2000, the SS source intensity generated by the $1,500\text{m}^3/\text{h}$ vessel type when operating in the sea area of the Pearl River Estuary is about 2.15kg/s . For the storage pit in the Nanshui operation zone, $2,300\text{m}^3/\text{h}$ and $3,000\text{m}^3/\text{h}$ cutter-suction dredgers are used, with a source intensity of 3.30kg/s and 4.30kg/s respectively by analogy. The source intensity of the overflow port is set to 1.22kg/s based on our previous research on dredger filling project in the Qianhai land area, Western Shenzhen Port, in Lingding Bay of the Pearl River Estuary.

4.3 Simulation results and analysis

4.3.1 Influence of dredging

The statistics of siltation before and after upgrade construction of the main channel are as shown in Table 2. According to the calculation results, under the present construction condition, the siltation in the main channel increases obviously. When construction was not under way, the average siltation thickness and volume of the entire channel were about 0.098m and 419,500 m³ respectively; when construction was under way, the average siltation increases by 3.6 times, with a monthly siltation thickness of about 0.450m and a siltation volume of about 1.929 million m³.

Regarding the influence of different workboats on siltation, since trail suction dredgers have far greater source intensity than grab dredgers and bring non-point source pollution compared to point source pollution of grab dredgers, the suspended sediment concentration caused by trail suction dredgers was far greater than that caused by grab dredgers, resulting in much greater influence on siltation. According to the comparison of tidal sediment concentration at the sampling points of the channel when construction was and was not under way (see Figure 6), the sediment concentration increase caused by grab dredgers operating in the upstream (6km) is small, only 0.015kg/m³ in the upstream end, while the sediment concentration increase at the junction with the downstream trail suction dredger construction area is greater and up to 0.06kg/m³. In the downstream of Hualian wharf, the sediment concentration without dredging was less than 0.10kg/m³, which however increases to about 0.10-0.20kg/m³ during construction, with a maximum increase of 0.12kg/m³.

Table 2. Statistics of siltation changes in the main channel during dredging.

Range	Area (m ²)	Without Dredging		Grab + trail suction		Variation (%)
		Siltation volume (m ³)	Siltation thickness (m/month)	Siltation volume (m ³)	Siltation thickness (m/month)	
DE	778,400	144,278	0.185	194,089	0.249	34.52
EM	984,500	103,444	0.105	353,793	0.359	242.01
MB'	2,522,200	171,821	0.068	1,381,350	0.548	703.95
Total	4,285,100	419,543	0.098	1,929,232	0.450	359.84

According to the longitudinal siltation distribution of the channel (see Figure 5), for the MB' segment in the downstream of Hualian wharf, the monthly siltation thickness without dredging was about 0.068m, compared to the siltation thickness of up to 0.548m when construction was under way, an increase of 0.48m. For the DE segment in the upstream of Longhua wharf, the monthly siltation thickness under present situation is 0.185m, compared to the thickness of 0.249m when grab dredgers were used for construction, a slight increase up to 0.064m. Finally, for the EM segment between Longhua wharf and Hualian wharf where grab dredgers are used, since it's very close to the downstream MB' segment where trail suction dredgers were used, the segment had a large siltation increase as well, with a monthly thickness increase of 0.254m. The siltation difference before and after construction, when represented in percentage, is more obvious. Therefore, it can be concluded that, construction will cause not only the increase of siltation in the main channel but also the variation of siltation distribution along the channel. Namely, siltation under present situation basically decreases from north to south, which however changes when construction is under way: the siltation in the downstream segments increases significantly and is even greater than in the upper segments.

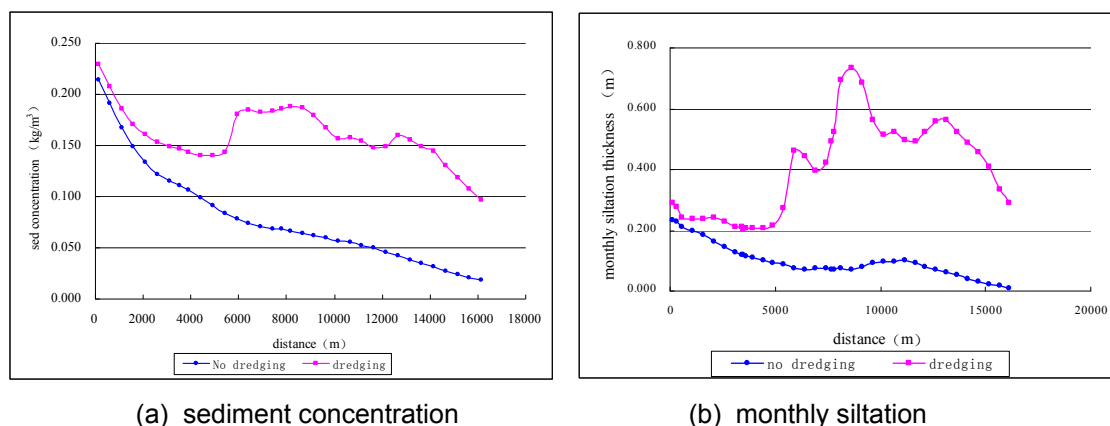


Figure 6. Comparative analysis of sediment concentration and monthly siltation along the main channel.

4.3.2 Influence of secondary transport of sediment storage pit

The calculation results show that, due to the small construction source intensity of cutter suction dredgers and the weak hydrodynamic force in the southern concave basin of Nanshui operation zone, the secondary transport of storage pit sediment brings limited increase of siltation in the harbor. The increase in some parts, mainly some segments of the branch channel of the Gaolan international container wharf near the storage pit, is significant, while the increase of siltation in other parts is slight.

Specifically, the hydraulic fill activity of the storage pit in the southern basin only causes an average siltation increase of 0.17% in the main channel. The maximum increase occurs to the DE segment which was nearest to the overflow port and storage pit and is only 0.38%. The siltation increase in the branch channel of Gaolan international container wharf is relatively obvious, with an overall increase of about 10%. Some segments of the branch channel nearest to the storage pit have an increase of up to 45% and the siltation thickness increases by about 0.06m (see Figure 7). The farther the other wharfs are away from the storage pit, the smaller the siltation increase is which was not greater than 0.59%.

Therefore, the secondary transport of storage pit sediment in the Nanshui operation zone only causes significant siltation increase in some segments of the branch channel of the Gaolan international container wharfs and has little influence on siltation in the main channel and other wharf areas.

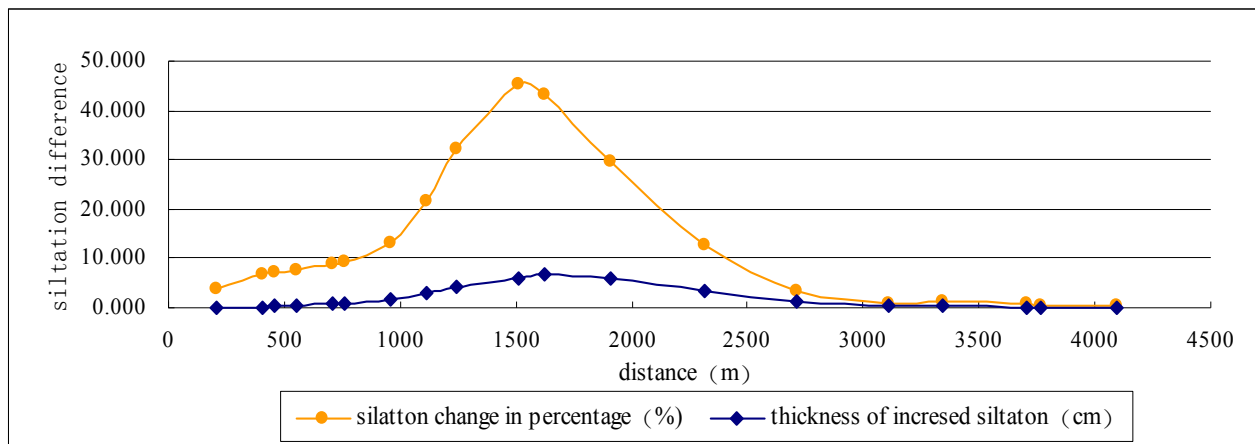


Figure 7. Variation of siltation in the Gaolan international container wharf basin and branch channel.

4.3.3 Influence of the Tieluwan Breakwater

The changes of siltation in various segments of the main channel and surrounding areas before and after the construction of the Tieluwan breakwater are as shown in Figure 8.

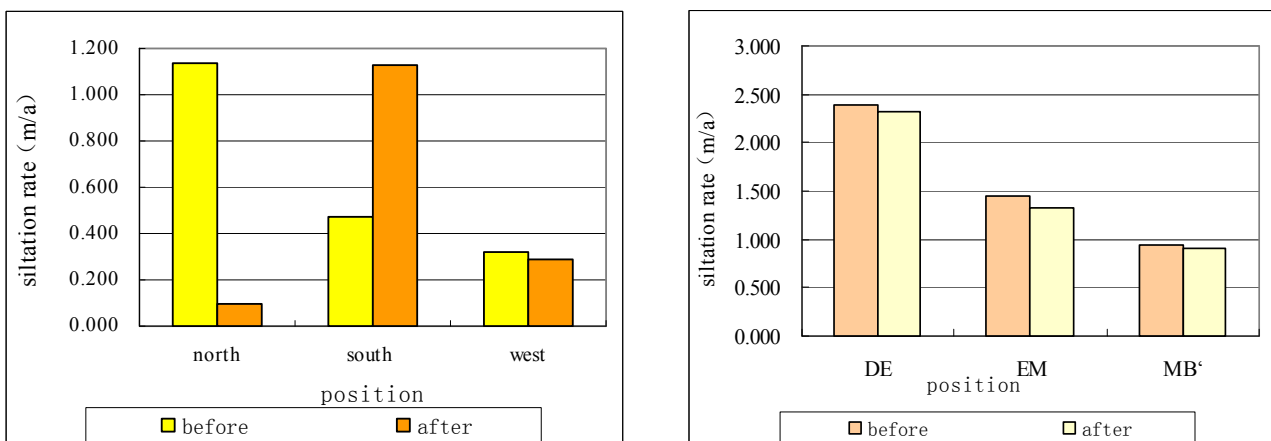


Figure 8. Variation of silting in the surrounding sea-bed of breakwater and in the main channel.

Before the construction of the Tieluwan breakwater, sediment discharged from the adjacent Jiti Outlet and nearshore shoal sediment in the south of the Gaolan Island were carried inward by tidal currents along the Gaolan Island shoreline. A siltation zone of 1.138m/a occurs on the north side of the Tieluwan breakwater, while the siltation intensity on the south and west side of the breakwater was relatively small, ranging from 0.316m/a to 0.475m/a. After the construction of the Tieluwan breakwater, the transport from the sea is

interrupted, and the siltation on the north side of the breakwater decreases significantly, leading to significantly reduced siltation intensity on the south side of the breakwater, due to the sediment trapping effect of the breakwater. The siltation increases dramatically and the siltation intensity increases from 0.475m/a before the construction of the breakwater to 1.124m/a on the west side, due to reduced cross-section area and strengthened current. Due to this the siltation decreases and the siltation density drops by 9.37% to 0.287m/a.

The variation of siltation along the main channel caused by the construction of the Tieluwan breakwater was consistent with that on the west side of the breakwater. Prior to the construction of the Tieluwan breakwater, the average siltation intensity of the main channel was 1.327m/a; after the construction of the breakwater, the average siltation intensity drops by 5.37% to 1.256m/a. The decrease by segment was ranged from 2.88% to 8.88%. Therefore, it can be concluded that, after the construction of the Tieluwan breakwater, the cross-section area decreases, the tidal dynamic increases, the sources of sand become less, and the siltation in the main channel reduces slightly.

5 CONCLUSIONS

The above research results show that, during construction, the influence on the siltation in the main channel is significant. The siltation in the entire channel increases by 3.6 times on average (the difference in increase is closely related to the workboat type) and the influence of grab dredger construction on siltation is far less than that of trail suction dredger construction. The influence of secondary transport of sediment storage pit in the southern basin of the Nanshui operation area on the siltation in the harbor is limited. Some segments of the branch channel of the Gaolan international container wharf near the storage pit reflects significant siltation growth, while the main channel and other wharf areas have an average growth of less than 0.59%. The construction of the Tieluwan breakwater mainly causes the formation of a siltation zone on the south side, and the siltation intensity increases from 0.475m/a to 1.124m/a; while on the west side of the breakwater and in the main channel, due to reduced cross-section area and strengthened hydrodynamic force, the siltation is slight. Therefore, abnormal siltation in the main channel of the Gaolan Harbor is closely related to construction. In the absence of effective regulation, unreasonable sediment disposal will cause more serious siltation.

ACKNOWLEDGEMENTS

The research reported is funded by the National Science Foundation of China (Grant No. 51409286), the Special Commonweal Research Foundation of the Ministry of Water Conservancy of China (Grant No. 201501010).

REFERENCES

- Guo, M.X., Wang, H., Liu, J.Y., et al. (2015). Study on mathematical model for siltation calculation of 150,000 DWT channel in Gaolan Harbor of Zhuhai Port. *Pearl River Water Transport*, 3, 60-61.
- Hou, J.Y., He, J. & Xin, W.J. (2012). Analysis of Sudden Sediment Siltation in Yamen Seaward Channel on Windy Days. *Hydro-Science and Engineering*, 2, 55-61.
- Jia, L.W., Luo, J. & Ren, J. (2012). Evolution and Causes Analysis of Sandbar in Huangmao Bay of Pearl River Estuary. *Acta Oceanologica Sinica*, 34(5), 120-127.
- South China Sea Institute of Oceanology, CAS, (2010). Special Report on the Environmental Impact of Marine Engineering of Sino-Kuwait Joint-venture Guangdong Refining and Chemical Integration Project.
- Wu, C.Y. (1995). Small-Scale Dynamic Structure of Huangmao Bay and Its Sedimentation Effect. *Journal of Sun Yat-sen University (Natural Science)*, 34(2), 86-94.
- Wu, J.X., et al. (1999). Study on Sediment Transport in Huangmao Bay - Application of McLaren Model In Estuarine Environments. *Journal of Sediment Research*, 3, 26-32.
- Yang, M.M., Wu, J.X., Zhang, Q.J., et al. (2016). Lateral residual circulation and sediment transport during flood season at Huangmao Bay of Pearl River. *Acta Oceanologica Sinica*, 38 (1), 31-45.
- Yang, X.W. (1993). Analysis of Sediment Source and Transport Process in Huangmao Bay of Pearl River Estuary. *Marine Science Bulletin*, 12 (6), 53-62.
- Zhang, X.F. (2015). Mode of Response Relationship Between Estuarine Suspended Sediment Concentrations and Multi-Factors. *Port & Waterway Engineering*, 4, 29-36.
- Zhang, X.F., Jiang X.K. & Xu, F.J. (2006). Study on Mathematic Model for Siltation Calculation in Gaolan Harbor. *Guangdong Water Resources and Hydropower*, 1, 7-10.

STUDY ON MAINTENANCE DREDGING SCHEME FOR CHANNEL WITH A NUMERICAL MODEL

XINFENG ZHANG ⁽¹⁾, SULAN LU ⁽²⁾, YU JIANG ⁽³⁾ & YAJU WU ⁽⁴⁾

^(1,2,3,4) Pearl River Hydraulic Research Institute, Guangzhou, China,
zksxfj@vip.163.com; esula2002@163.com; jiangyu-jy@163.com; rememberju@sina.com

ABSTRACT

Zhuhai Gaolan harbor is the largest harbor in Huangmao Bay. It shows that upgrade dredging work is the key factor which causes the local serious siltation in the main channel of Gaolan harbor and harms the normal running of channel frequently. Based on a verified numerical model with wave, tidal current and sediment, using the typical hydrological conditions, the paper carries out research on the maintenance dredging scheme for the main channel of Zhuhai Gaolan port. In the paper, compared with no dredging, the effects of dredging in flood season, in dry season, in flood tide, in ebb tide are discussed. It indicates that, with the same dredging boat and the same work hours, dredging in dry season causes higher siltation increase than in flood season. In flood season, the normal siltation rate in the main channel without dredging work is 0.125 m per month. And it rises to 0.331 m per month during maintenance dredging, about $88.4 \times 10^4 \text{ m}^3$ silting amount more in the main channel. And in dry season, the normal siltation rate in the main channel without dredging work is 0.083 m per month. It rises to 0.302 m per month during maintenance dredging, about $94.1 \times 10^4 \text{ m}^3$ silting amount more in the main channel. The differences on siltation between dredging in flood tide and in ebb tide are simulated both in flood season and in dry season. The conclusions reach an agreement. Dredging in flood tide causes higher rising rate of siltation whatever the season. In flood season, the amount of additional siltation in the main channel during dredging in ebb tide is 59% less than dredging in flood tide. And in dry season the discrepancy is about 65%. It concludes that dredging during ebb tide in flood season is an optimal maintenance scheme for the main channel of Zhuhai Gaolan harbor.

Keywords: Maintenance dredging scheme; numerical model; siltation; seasonal dredging; tidal dredging.

1 INTRODUCTION

The Huangmao Bay is located in the west of the Pearl River Estuary, and the Zhuhai Gaolan Harbor is its biggest harbor. Related research (Pearl River Hydraulic Research Institute of PRWRC, 2015) shows that, dredging is the main influencing factor that causes serious siltation in some segments of the main channel and damages the normal operation of the channel in recent years. Therefore, it is necessary and beneficial to make an optimal maintenance dredging scheme for the main channel after upgrading in order to minimize siltation increase caused by dredging activities and reduce maintenance costs.

As people's environmental awareness grows, the research on the influence of dredging activities focuses on environmental impact assessment or post-assessment, namely, the influence of construction source intensity on the distribution and turbidity of suspended sediment fields in waters (Lei et al., 2016; Xin et al., 2011), but the influence on sea-bed variation is not further discussed. A study (Wang et al., 2016), analyzes the influence of dredging on channel siltation and proposes the siltation depth to be reserved during construction, but does not compare and optimize different construction schemes in the model. Some studies focuses on the dredging optimization (Zou et al., 2014; Qian, 2012; Tang et al., 2008), however focusing on the improvement and operation parameter regulation of dredgers is important for productivity maximization. There's little research on dredging scheme formulation and optimization based on actual workload for the purpose of minimized siltation.

The 150,000 ton-grade approach channel of the Gaolan Harbor, upgraded from 100,000 ton-grade, starts from the open sea -20.532 m contour point (B' point), travels through E and M nodes, and ends at the turning point connecting the Zhuhai power plant branch channel (D point), with a total length of 16,250 m. Specifically, the DE segment is 3,300 m long and has a bottom width of 230 m; the EM segment is 4,263 m long and has a bottom width of 230 m; the MB' segment is 8,687 m long and has a bottom width of 290 m; the entire channel has a bottom elevation of -20.532 m and an excavation slope of 1:7. The parameters by segment are shown in Table 1, and the distribution and geographic location as well as the distribution of surrounding waters are shown in Figure 1. This paper uses the two-dimensional wave, tidal current and sediment mathematical model to predict the annual maintenance workload of the 150,000 ton-grade main approach channel, and carries out research on the optimization of the dredging scheme in terms of construction time sequence, region sequence, excavation slope, construction duration and channel grade for reduced impact on siltation. In the

paper, the research results of construction time sequence, namely optimal construction timing in different seasons (flood season, dry season) and different tides (ebb tide, flood tide), are mainly introduced to illustrate the significance and importance of dredging scheme optimization based on minimized siltation.

Table 1. Engineering parameters of the 150,000 ton-grade main channel of Zhuhai Gaolan Harbor.

Position	DE segment	EM segment	MB' segment
Grade	150,000 ton-grade	150,000 ton-grade	150,000DWT ton-grade
Effective bottom width	230 m	230 m	290 m
Mileage	0+000~3+330	3+330~7+563	7+563~16+250
Design bottom elevation	-20.532 m	-20.532 m	-20.532 m
Excavation slope	1:7	1:7	1:7

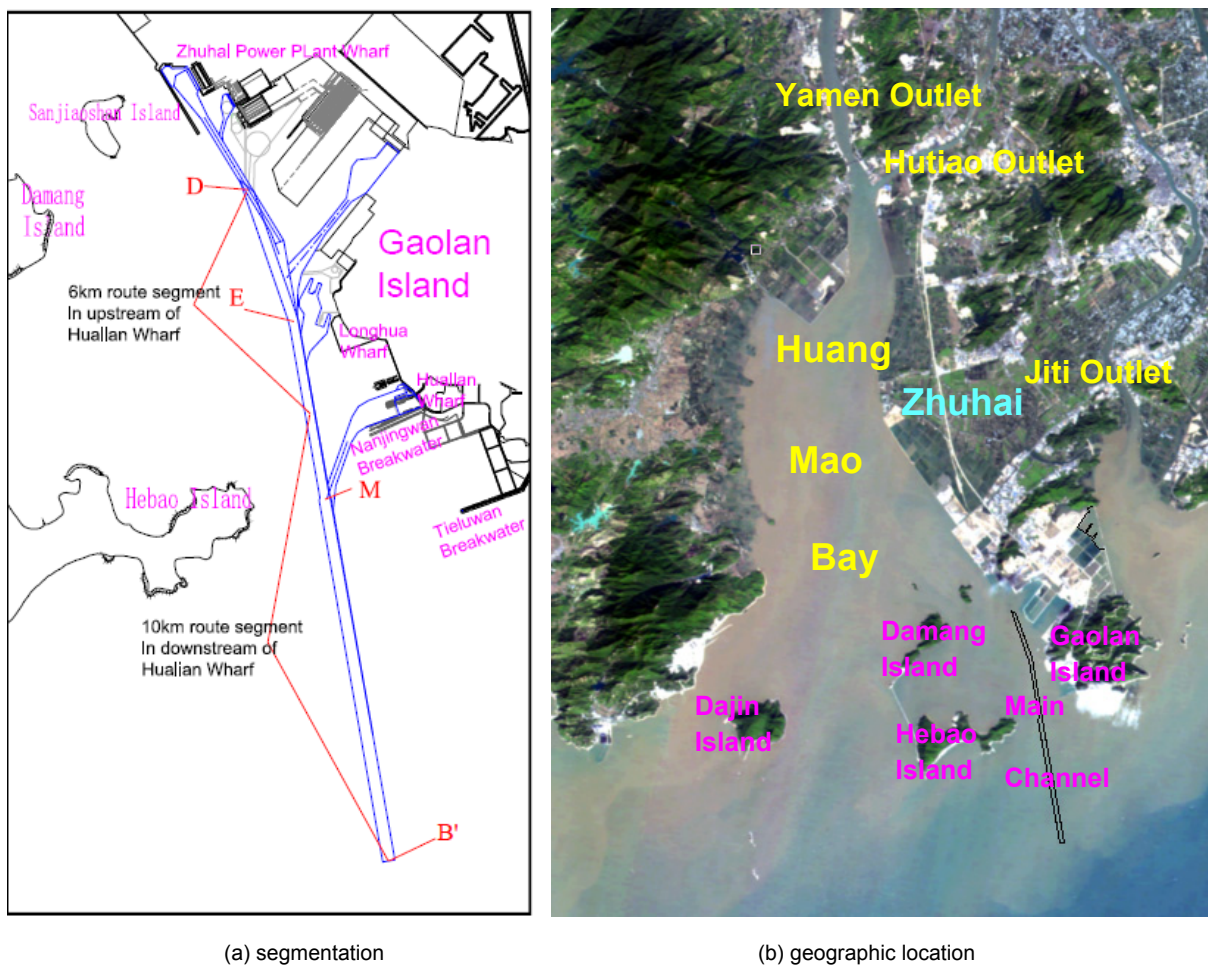


Figure 1. Segmentation and geographic location of the 150,000 ton-grade main channel.

2 MODEL OVERVIEW AND CONSTRUCTION ARRANGEMENT

2.1 Model establishment and validation

(1) Model establishment

The Huangmao Bay faces the open sea in the south, and the wave dynamic in the southern mouth is strong. The secondary transport of shoal sediment under wave action is one of the main sources of sediment in the area. Therefore, the influence of wave dynamic on the sediment concentration and scouring and siltation in the harbor area must be considered in the water and sediment model. The research scope of the model: the control hydrological stations at the four outlets in the west of the Pearl River Estuary (some are shown in Figure 1), namely Yamen outlet Guanchong Station, Hutiao outlet Xipaotai Station, Jiti outlet Huangjin Station and Modao outlet Denglongshan Station, as the upper boundary; the open sea -30m contour line as the lower boundary. The construction, calculation and validation of the model have been introduced in the author's previous papers (Zhang, 2015; Zhang et al., 2006) and are briefly discussed here.

The basic equations include flow continuity equation, flow momentum equations, wave equation, sediment transport equation and seabed deformation equation. The model uses orthogonal curve grid to fit the complex boundary configuration of Huangmao Bay. In the 2D model, the governing equations are discretized by finite difference method. And the equations are solved with an alternative directional implicit method. Generated grids are about 843×624 with the maximum grid size about 293m×1,588m and minimum grid size is about 10m×20m.

Flow continuity equation:

$$\frac{\partial h}{\partial t} + \frac{1}{C_\xi C_\eta} \left[\frac{\partial}{\partial \xi} (HuC_\eta) + \frac{\partial}{\partial \eta} (HvC_\xi) \right] = \frac{q}{C_\xi C_\eta} \quad [1]$$

Flow momentum equations:

$$\frac{\partial u}{\partial t} + \frac{u}{C_\xi} \frac{\partial u}{\partial \xi} + \frac{v}{C_\eta} \frac{\partial u}{\partial \eta} + \frac{uv}{C_\xi C_\eta} \frac{\partial C_\xi}{\partial \eta} - \frac{v^2}{C_\xi C_\eta} \frac{\partial C_\eta}{\partial \xi} = fv - \frac{g}{C_\xi} \frac{\partial h}{\partial \xi} + E_\xi \left(\frac{1}{C_\xi} \frac{\partial A}{\partial \xi} - \frac{1}{C_\eta} \frac{\partial B}{\partial \eta} \right) - \frac{gu}{C^2 H} \sqrt{u^2 + v^2} \quad [2]$$

$$\frac{\partial v}{\partial t} + \frac{u}{C_\xi} \frac{\partial v}{\partial \xi} + \frac{v}{C_\eta} \frac{\partial v}{\partial \eta} + \frac{uv}{C_\xi C_\eta} \frac{\partial C_\eta}{\partial \xi} - \frac{u^2}{C_\xi C_\eta} \frac{\partial C_\xi}{\partial \eta} = -fv - \frac{g}{C_\eta} \frac{\partial h}{\partial \eta} + E_\eta \left(\frac{1}{C_\xi} \frac{\partial B}{\partial \xi} + \frac{1}{C_\eta} \frac{\partial A}{\partial \eta} \right) - \frac{gv}{C^2 H} \sqrt{u^2 + v^2} \quad [3]$$

Wave equation:

$$\frac{\partial}{\partial t} N + \frac{\partial}{\partial x} c_x N + \frac{\partial}{\partial y} c_y N + \frac{\partial}{\partial \sigma} c_\sigma N + \frac{\partial}{\partial \theta} c_\theta N = \frac{S}{\sigma} \quad [4]$$

Sediment transport equation:

$$\frac{\partial (HS)}{\partial t} + \frac{1}{C_\xi C_\eta} \left[\frac{\partial}{\partial \xi} (C_\eta H u S) + \frac{\partial}{\partial \eta} (C_\xi H v S) \right] = \frac{1}{C_\xi C_\eta} \left[\frac{\partial}{\partial \xi} \left(H \varepsilon_\xi \frac{C_\eta}{C_\xi} \frac{\partial S}{\partial \xi} \right) + \frac{\partial}{\partial \eta} \left(H \varepsilon_\eta \frac{C_\xi}{C_\eta} \frac{\partial S}{\partial \eta} \right) \right] - \alpha \omega (S - S_*^2) + S_0 \quad [5]$$

Seabed deformation equation:

$$\gamma_0 \frac{\partial \eta}{\partial t} = \alpha \omega (S - S_*^2) \quad [6]$$

In the formula, $A = \frac{1}{C_\xi C_\eta} \left[\frac{\partial}{\partial \xi} (C_\eta u) + \frac{\partial}{\partial \eta} (C_\xi v) \right]$; $B = \frac{1}{C_\xi C_\eta} \left[\frac{\partial}{\partial \xi} (C_\eta v) - \frac{\partial}{\partial \eta} (C_\xi u) \right]$; u and v represent the velocity components in ξ and η directions respectively, h is water level, q is flow source of per unit area, H is water depth, g is gravity acceleration, f is coriolis coefficient, E_ξ and E_η represent the turbulent viscosity coefficient, Lami coefficient C_ξ and C_η are indicated as follows: $C_\xi = \sqrt{x_\xi^2 + y_\xi^2}$; $C_\eta = \sqrt{x_\eta^2 + y_\eta^2}$. N is wave spectrum; c_x , c_y , c_σ , c_θ represent the transmission speed in the direction of X , Y , σ , θ respectively; ε_ξ and ε_η are sediment diffusion coefficient; S_*^2 is the sediment

carrying capacity of 2d module including both current and wave action, $S_*^2 = k_1 \frac{V^3}{\omega \sqrt{gH}} + k_2 \frac{H_w}{H^2 \omega}$, k_1 and k_2

are the sediment carrying capacity coefficients, V is depth averaged velocity; H_w is wave height; S_0 is sediment source, γ_0 is the dry specific gravity of the sand, η is the variation of seabed elevation.

(2) Model validation

The model validation cases include: water level, flow velocity, flow direction and seabed deformation. Some results of validation are shown in Figure 2 with water level sample point locating in the southwest of Gaolan island and flow sample point locating in the main channel near Longhua Wharf. And the area of scouring and silting validation is the 100,000 ton-grade main channel of Gaolan harbor. It can be seen that the simulation results are basically consistent with the observation. And the average annual siltation

intensity of the main channel is about 1.216 m, while the simulation result is 1.015 m, with a discrepancy of about 16.5 %. It concludes that the model and the parameters are appropriate for further research.

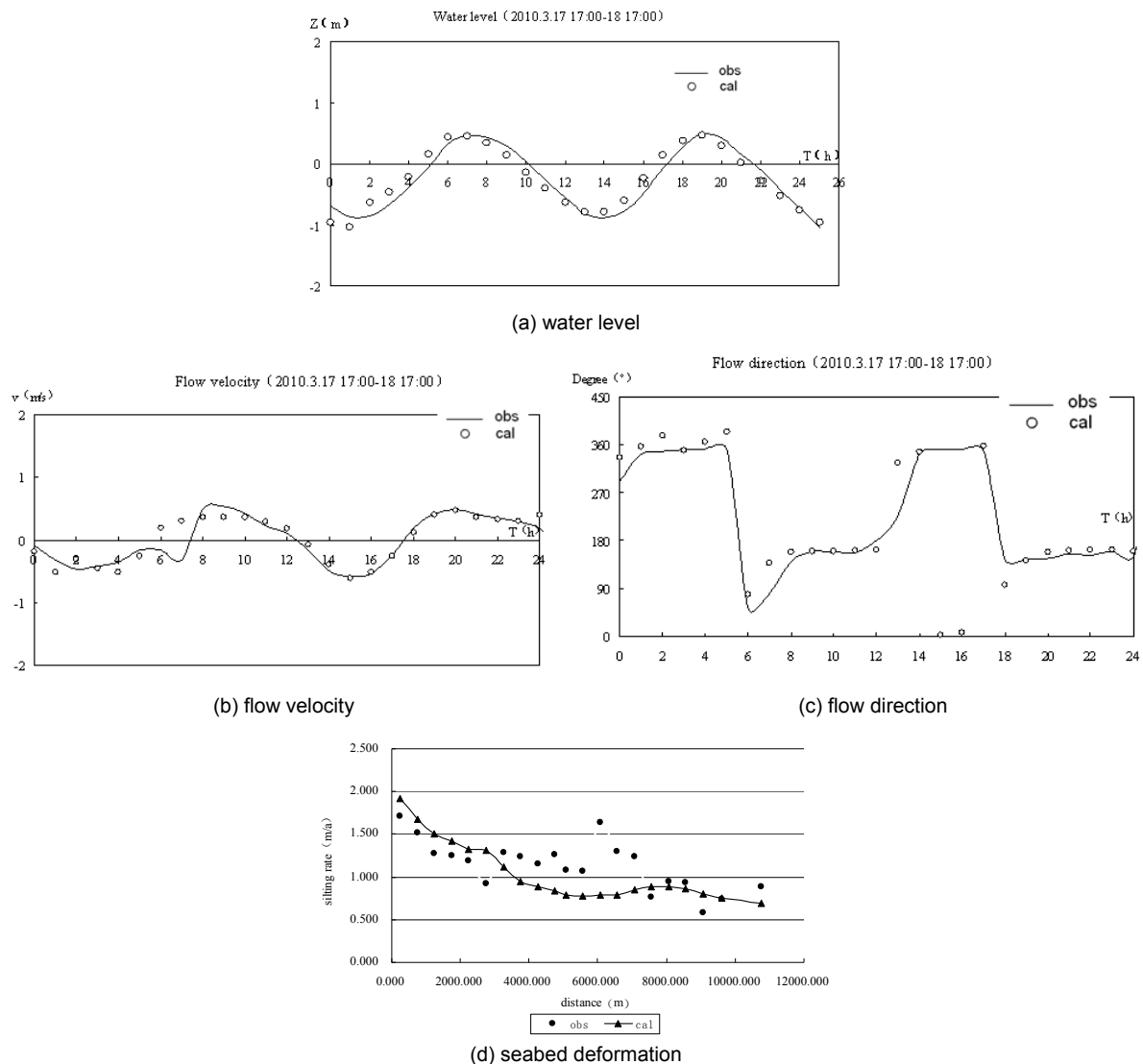


Figure 2. Comparison of model simulation result and observation.

2.2 Construction arrangement

The model calculation results show that, the annual siltation intensity and volume of the 150,000 ton-grade main channel are 1.256 m/a and 5.4 million m³/a respectively. According to the construction files collected during upgrade dredging, due to a combination of factors including size distribution of local bed materials conditions and navigation requirements, grab dredgers are arranged to work 24h a day in the upstream of the Hualian Wharf; in the downstream, trail suction dredgers are arranged to work for a period of 2h, 1h from loading to full-tank overflow and 1h for outbound shipment and empty-tank return, namely 1h for sediment source emission.

Based on the past construction experience, for the segment in the upstream (6 km) of the Hualian Wharf, 12* 12 m³ grab dredgers are used; for the segment in the downstream (10 km), 2* 5,000m³ trail suction dredgers are used to work continuously for 1 month, to complete maintenance dredging of the 150,000 ton-grade main channel. The types and quantities of dredger boats are mainly based on the size of local bed sand and construction experience. And the optimization on dredging is mainly focused on the hydraulic condition instead of dredgers themselves in this paper. For easy calculation and analysis of the difference in the influence of different construction schemes on the siltation in the main channel, workboats are generally so arranged. The construction source intensity can be obtained by analogy based on the similar research results (South China Sea Institute of Oceanology, CAS, 2010).

3 OPTIMIZATION CALCULATION OF CONSTRUCTION SCHEME

This paper presents the research results of construction time sequence optimization and briefs on scheme optimization from other perspectives. Construction time sequence focuses on construction in different seasons, namely under different hydrological conditions (runoff in flood season and tide in dry season), and in different tides, namely under different tidal current conditions (ebb tide and flood tide).

3.1 Difference caused by construction in different seasons

The comparison of siltation in the main channel caused by construction in flood and dry seasons is as shown in Table 2.

Table 2. Influence of construction in different seasons on the siltation in the main channel.

Range	Area (10 ⁴ m ²)	Flood season					
		Without dredging		grab + trail suction		Siltation increase	
		Siltation volume (10 ⁴ m ³)	Siltation thickness (m/month)	Siltation volume (10 ⁴ m ³)	Siltation thickness (m/month)	Increment (10 ⁴ m ³)	Percentage (%)
DE	77.84	18.70	0.240	21.15	0.272	2.45	13.09
EM	98.45	13.02	0.132	29.57	0.300	16.55	127.11
MB'	252.22	21.76	0.086	91.23	0.362	69.47	319.24
total(avg)	428.51	53.48	0.125(avg)	141.95	0.331(avg)	88.47	165.43(avg)
Range	Area (10 ⁴ m ²)	Dry season					
		Without dredging		grab + trail suction		Siltation increase	
		Siltation volume (10 ⁴ m ³)	Siltation thickness (m/month)	Siltation volume (10 ⁴ m ³)	Siltation thickness (m/month)	Increment (10 ⁴ m ³)	Percentage (%)
DE	77.84	10.99	0.141	13.51	0.173	2.51	22.88
EM	98.45	8.47	0.086	29.19	0.296	20.72	244.74
MB'	252.22	15.96	0.063	86.86	0.344	70.90	444.36
total(avg)	428.51	35.41	0.083(avg)	129.55	0.302(avg)	94.14	265.83(avg)

The calculation results show that the increase of siltation in the main channel caused by construction in dry season is greater: In flood season, the siltation increase of the segments is ranged from 13.09% to 319.24%, and the siltation in the entire channel increases by 1.65 times on average; in dry season, the siltation increase of the segments is ranged from 22.88 % to 444.36 %, and the siltation in the entire channel increases by 2.65 times on average. Specifically, the siltation increment caused by construction in dry season is 941,400 m³, 6.4% higher than the siltation increment of 884,700 m³ caused by construction in flood season.

The difference of siltation caused by construction in flood season and in dry season is mainly due to the seasonal difference of water and sediment dynamic conditions. According to the statistical results of the flow velocity along the main channel and the variation of sediment concentration (see Figure 3, D point in the north end as the starting point), in flood season, the tidal mean velocity is basically greater than in dry season. At the same time, the sediment from runoff is greater, and the sediment concentration is generally higher than in dry season. When the added source strength is the same, currents in flood season are more likely to carry high-concentration suspended sediment into the surrounding waters, and the sediment increment is relatively small, resulting in small siltation increment. In dry season, the flow velocity is small while on one hand, the sediment-carrying capacity is limited, so the sediment concentration in the waters can easily become saturated and cause siltation. On the other hand, the diffusion capacity of suspended sediment is lower than in flood season, so the sediment concentration increment is greater than in flood season (see Figure 3), resulting in a higher total siltation increment than in flood season.

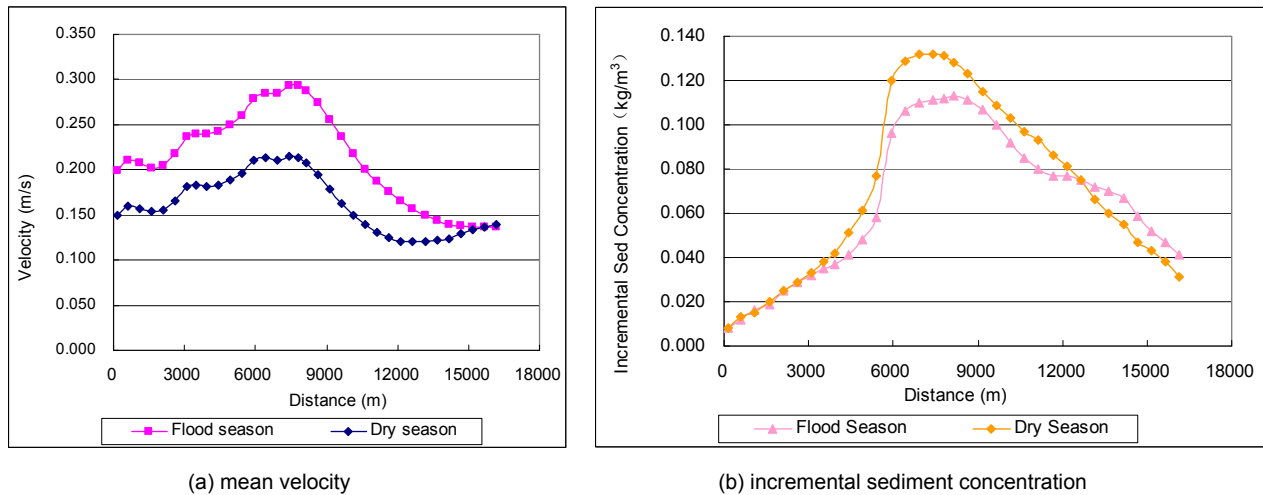


Figure 3. Mean velocity and incremental sediment concentration along the main channel.

3.2 Difference caused by construction in different tides

Regarding construction in different tides, it's necessary to identify the flood tide period and the ebb tide period under typical hydrological conditions, and then add source intensity into the grid where workboats are located in different periods. Therefore, for easy addition of source strength, in the simulation of construction in different tides, $3 \times 5,000 \text{ m}^3$ trail suction dredgers are arranged for the entire main channel while the use of different dredger types is not considered. Under hydrological conditions of flood season and dry season, within a same calculation period, the time for source strength addition in different tides is the same. Since the time scale of one cycle under hydrological calculation conditions in dry season is longer than in flood season, when the total calculation time is one month, the source strength added in dry season will be actually lower than in flood season.

The influence of dredging in different tides on the siltation in the main channel is shown in Table 3. Regardless of the season, the siltation increment in the main channel caused by dredging in flood tide is greater. In the case of dredging in flood season and flood tide, the siltation volume in the main channel is $1.784 \text{ million m}^3$, and the average siltation thickness is 0.416 m , 0.291 m higher compared to the case where dredging is not under way. In the case of dredging in ebb tide, the siltation volume in the main channel is $1.471 \text{ million m}^3$, and the average siltation thickness increases by 0.218 m to 0.343 m . The siltation increment caused by dredging in ebb tide is 25.08% lower than in flood tide, and the siltation increase (in percentage) caused by dredging in ebb tide is 59% lower than in flood tide.

In the case of dredging in dry season and in flood tide, the siltation volume in the main channel is $1.273 \text{ million m}^3$, and the average siltation thickness is 0.297 m , 0.214 m higher compared to the case where dredging is not under way. In the case of dredging in ebb tide, the siltation volume in the main channel is $1.042 \text{ million m}^3$, and the average siltation thickness increases by 0.160 m to 0.243 m . The siltation increment caused by dredging in ebb tide is 25.17% lower than in flood tide, and the siltation increase (in percentage) caused by dredging in ebb tide is 65% lower than in flood tide.

The siltation caused by dredging in flood tide is greater than in ebb tide, which is related to the difference of the water and sediment environment in different tides. In ebb tide, tidal currents are more likely to carry high-concentration suspended sediment into low-concentration areas of the open sea. In flood tide, an opposite situation occurs. The sediment concentration in the upstream bay is higher than in the open sea, the concentration gradient caused by dredging is lower than in ebb tide, the flood strength in some waters is lower than the ebb strength, and the sediment transport capacity is also weak, creating higher-concentration suspended sediment area in flood tide at the same source strength (see Figure 4), and resulting in a more significant influence on siltation.

Table 3. Influence of dredging in different tides on the siltation in the main channel.

Flood season								
Range	Without dredging		Ebb tide			Flood tide		
	Siltation volume (m ³)	Siltation thickness (m/month)	Siltation volume (m ³)	Siltation thickness (m/month)	Variation (%)	Siltation volume (m ³)	Siltation thickness (m/month)	Variation (%)
DE	18.70	0.240	44.05	0.566	135.60	50.28	0.646	168.92
EM	13.02	0.132	36.90	0.375	183.46	44.65	0.454	242.96
MB'	21.76	0.086	66.15	0.262	203.96	83.51	0.331	283.75
avg(total)	53.48(total)	0.125	147.10(total)	0.343	175.07	178.44(total)	0.416	233.67
Dry season								
Range	Without dredging		Ebb tide			Flood tide		
	Siltation volume (m ³)	Siltation thickness (m/month)	Siltation volume (m ³)	Siltation thickness (m/month)	Variation (%)	Siltation volume (m ³)	Siltation thickness (m/month)	Variation (%)
DE	10.99	0.141	29.88	0.384	171.88	36.68	0.471	233.71
EM	8.47	0.086	27.41	0.278	223.77	34.06	0.346	302.23
MB'	15.96	0.063	46.87	0.186	193.72	56.55	0.224	254.41
avg(total)	35.41(total)	0.083	104.16(total)	0.243	194.13	127.28(total)	0.297	259.42

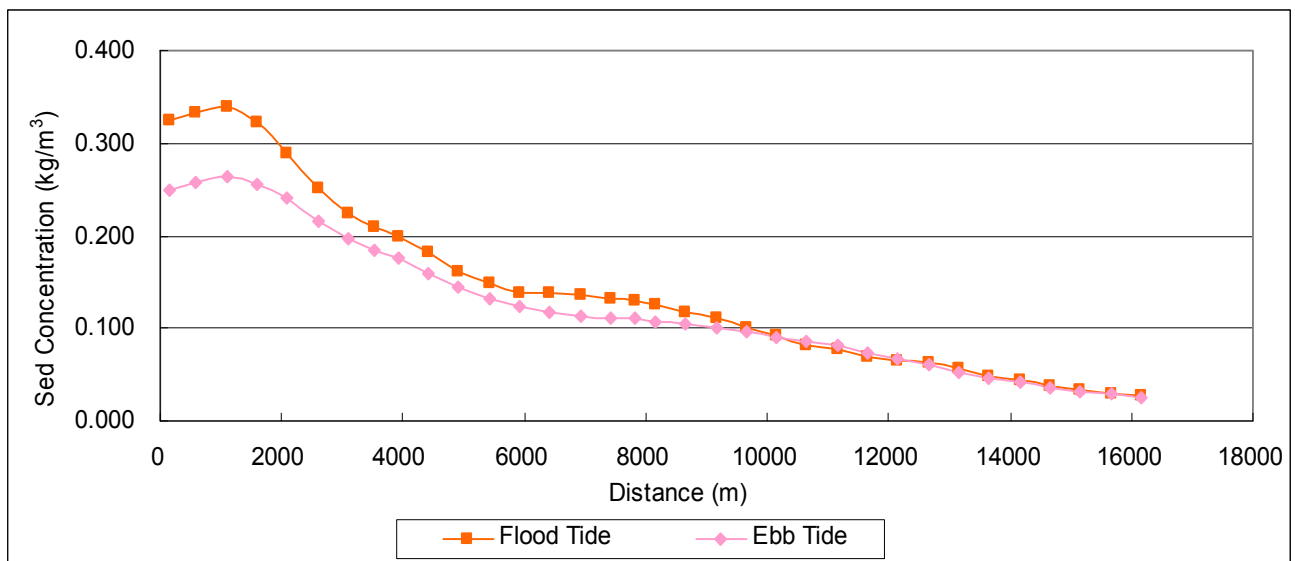


Figure 4. Comparison of sediment concentration caused by dredging in different tide in dry season.

An ebb tide further consists of early, medium and late stages. The above calculation and analysis results show that, ebb currents carry sediment into low-concentration areas in the open sea, which can help reduce the siltation in the harbor. Therefore, in the medium stage of an ebb tide, the currents are strongest and the velocity is greatest, being capable of carrying more suspended sediment from dredging into the open sea and resulting in small siltation increment in the main channel. To sum up, when the construction period is sufficient, it's advisable to carry out dredging in the medium stage of the ebb tide, which can further minimize the influence on the siltation in the main channel.

3.3 Introduction to other optimization schemes

This study also discusses the design of construction schemes based on regional sequence, construction slope, construction duration, channel grade and other factors. According to the calculation results, after the segmentation of the main channel, when different construction area sequences (south-to-north or north-to-south) are used, the difference of siltation in the main channel is lower than 0.5%, which is preliminarily attributed to the unavailability of factors in the upstream and downstream of the main channel that can cause sudden changes in regional water and sediment conditions. In the study on different construction durations, if the introduced total source intensity is the same, one-time emergency construction, due to the short term,

great number of workboats, and high concentration of source intensity, can cause a more significant increase in siltation. For phased construction with scattered source strength, the total siltation increase caused thereby is inversely proportional to the construction duration. In addition, the higher the channel grade is, the greater the design water depth is, the more the siltation will be, and the higher the maintenance dredging costs will be. The study also calculates the annual siltation intensity and volume by channel grade, and based on the siltation distribution along the channel calculates the annual dredging frequency and the corresponding dredging costs, to provide a technical basis for channel administration to scientifically determine the channel grade after taking a combination of factors including arriving vessel type and maintenance costs into consideration.

And other types of dredgers are rarely discussed in the paper. Doubtlessly, dredgers with higher efficiency will complete the construction work in less time. The siltation influence of their dredging work also can be simulated while sand source intensity is defined. We can make the optimization of dredging scheme on hydraulic conditions which causes less siltation increase as introduced before.

4 CONCLUSIONS

It's very necessary to develop optimized channel dredging schemes. The research on construction time sequence shows that, dredging in dry season can cause a greater increase (percentage) and increment (an average of 6.4% higher than in flood season) of siltation in the main channel. The comparisons in flood and ebb tides show that, regardless of the season, the siltation increment in the main channel caused by dredging in flood tide is 25% higher than in ebb tide. Therefore, dredging in flood season and in ebb tide can reduce siltation increase in the main channel and reduce the corresponding maintenance costs, making it a better way of dredging. In addition, optimization measures in other aspects such as construction duration and channel grade can be taken to further reduce the influence on the siltation in the main channel and lower the dredging maintenance costs.

ACKNOWLEDGEMENTS

The research reported herein is funded by the National Science Foundation of China (Grant No. 51409286).

REFERENCES

- Lei, X.L., Yuan, T., Yang, C., et al. (2016). Study on Numerical Simulation of Water Quality in Three Gorges Channel Environmental Dredging based on Delft3d Model. *Industrial Safety and Environmental Protection*, 42(3), 65-68.
- PRWRC. (2015). *Study on the Dredging Scheme for the Main Channel of the Zhuhai Gaolan Harbor*. Pearl River Hydraulic Research Institute of PRWRC
- Qian, G.T. (2012). Study on Loading Optimization during Dredging by Trail Suction Dredgers. *Science Technology and Engineering*, 12(5), 1065-1068.
- CAS. (2010). *Special Report on the Environmental Impact of Marine Engineering of Sino-Kuwait Joint-venture Guangdong Refining and Chemical Integration Project*. South China Sea Institute of Oceanology,
- Tang, J.Z., Wang, Q.F. & Bi, Z.Y. (2008). Model and Optimization of Dredging Operations. *Journal of Zhejiang University (Engineering Science)*, 42(5), 850-857.
- Wang, X.B., Zhang, Z.G., Sun, Y.K., et al. (2016). Study on Siltation Depth Reserved for the Tianjin Nangang channel project. *Port and Waterway Engineering*, 5, 162-166.
- Xin, X.K., Ye, M. & Wang, F. (2011). Prediction Model for the Impact of River Dredging on Suspended Substances. *Advances in Science and Technology of Water Resources*, 31(1), 8-10, 49.
- Zhang, X.F. (2015). Mode of Response Relationship between Estuarine Suspended Sediment Concentrations and Multi-Factors. *Port and Waterway Engineering*, 4, 29-36.
- Zhang, X.F., Jiang, X.K. & Xu, F.J. (2006). Study on Mathematic Model for Siltation Calculation in Gaolan Harbor. *Guangdong Water Resources and Hydropower*, (1), 7-10.
- Zou, S., Li, Z.S., Xiao, H.B., et al. (2014). Research and Design of Dredging Process of Grab Dredgers. *Journal of Wuhan University of Technology (Transportation Science & Engineering)*, 38(2), 379-383.

IMPACT OF A DRY BED SURGE AGAINST STRUCTURES WITH AND WITHOUT OPENINGS

DAVIDE WÜTHRICH⁽¹⁾

⁽¹⁾ Laboratoire de Constructions Hydrauliques (LCH), Ecole Polytechnique Fédérale de Lausanne (EPFL), Lausanne, Switzerland, davide.wuthrich@epfl.ch

ABSTRACT

Tsunamis, Impulse waves and the sudden collapse of dams are rare phenomena, but highly destructive. Nevertheless recent events showed that structures with openings can effectively reduce impact forces, ensuring people's safety and limiting reconstruction costs. The present experimental study systematically investigates the impact of a dry bed surge against a free standing structure with various degrees of porosity, measuring forces and moments in all directions. For the impervious scenario, results showed the absence of an initial overshoot and a good agreement with the classical hydrodynamic force computed as a function of the momentum flux. Structures with openings showed lower upstream water levels resulting in a reduced horizontal load. This was proved to be linearly proportional to the porosity value and the application point of the force was between 75 and 100 % of the maximum wave height, independently from the geometry. Vertical forces are given as the sum of buoyancy and the weight of water, presenting the highest values for porosities between 17 and 34 %.

Keywords: Tsunami; impulse wave; dam-break wave; impact forces; openings.

1 INTRODUCTION

Extreme natural events such as tsunamis, floods and storms are occurring more often, exposing human to severe hazardous consequences. Tsunamis and impulse waves, induced by landslides into water reservoirs, can generate extreme damage to buildings and infrastructures located near the shore along with often catastrophic loss of human lives. A strong similarity was proven between tsunami induced bores and hydrodynamic waves produced by the sudden collapse of a dam (Chanson, 2006). Some previous tragic events took place in Sumatra Island (Indonesia, 2004) and in Tōhoku (Japan, 2011). According to the World Bank, these events combined produced over 300'000 deaths and damages for over 240 billion USD. Nevertheless, these events showed that engineering and coastal planning measures can be effective to ensure people's safety and reduce reconstruction costs. Furthermore a properly designed building can represent a vertical shelter which can save people's lives (Figure 1a). The role of engineers and researchers is therefore to develop and design infrastructures able to withstand natural disasters and protect human lives.



Figure 1. (a) Example of tsunami-structure interaction during the Indian Ocean tsunami (2004) [MThompson];
(b) Example of porous structure: Port building in Ofunato Chock et al. (2013) [Robertson].

In the past the impact of hydrodynamic waves on structures was considered too rare and the resulting impact forces were typically neglected in the design process. A few studies on the impact of waves against structures were carried out to characterize and estimate this extreme hydrodynamic loading. However, the large amount of empirical or semi-empirical formulas available and their significant scattering suggested that the behavior of structures under such extreme loading is not yet fully understood. Post-tsunami forensic engineering surveys have shown that some structures behave better than others; moreover, buildings with openings seem to resist better under hydrodynamic impact (Figure 1b). Previous studies proved that a specific design can significantly decrease the load on the free-standing structure. The investigation of a tsunami

resistant house in Sri Lanka designed by the Harvard School of Architecture in collaboration with MIT showed that the allowance of a flow through the building resulted into a better performance of the structure compared to the conventional design (Thusyanthan and Madabhushi, 2008). Van de Lindt et al. (2009) proved that just by opening windows and doors the load was reduced by 60%. Furthermore, structures with opening configurations of 25 and 50% reduced the hydrodynamic force by 15-25% and 30-40% respectively (Lukkunaprasit et al., 2009a; Chinnarasri et al., 2013). Hartana and Murakami (2015) compared some experimental tests to numerical simulations for porosity values of 40 %. Nevertheless, the influence of porosity and openings on the resulting hydrodynamic force remains mostly unknown and forces it to be difficult to estimate.

2 EXPERIMENTAL SET-UP

The present study is based on an experimental approach. Tests were carried out in a large-scale facility at the Laboratory of Hydraulic Constructions (LCH) at the Ecole Polytechnique Fédérale de Lausanne (EPFL), in Switzerland. Wave formation was achieved through the vertical release of a known water volume from an upper reservoir, through multiple pipes into a lower tank linked to a horizontal channel (Figure 2). A similar technique was previously used by Chanson et al. (2002), Lukkunaprasit et al. (2009b), Meile et al. (2013) and Wüthrich et al. (2017). The wave propagated on a horizontal smooth channel with a total length of 15.5 m and a width (W) of 1.4 m. The roughness of the channel bottom was calculated through steady state experiments to a Darcy-Weissbach friction coefficient of $f = 0.021$. The produced bores were similar to classical dam-break waves where nowadays it is considered a more appropriate technique to reproduce bores and surges propagating inland, as tsunamis hardly produce a solitary wave (Yeh et al., 1996; Chanson, 2006; Madsen et al., 2008; Nistor et al., 2009; Nouri et al., 2010). The flexibility of the experimental set-up allowed to produce dry bed surges with various equivalent impoundment depths (d_0), representing the first incoming wave. Different surges with different hydrodynamic properties were produced, mainly in terms of wave height (h) and wave front celerity (U). The time-histories of the wave height in different locations of the channel were measured using 7 Ultrasonic Distance Sensors (US) located at $x = 2.00, 10.10, 12.10, 13.10, 13.35, 13.60$ and 13.85 m, sampled with an acquisition frequency of 12.5 Hz. Signal post-processing allowed to compute the wave front celerity (U) of the propagating wave averaged on the entire channel.

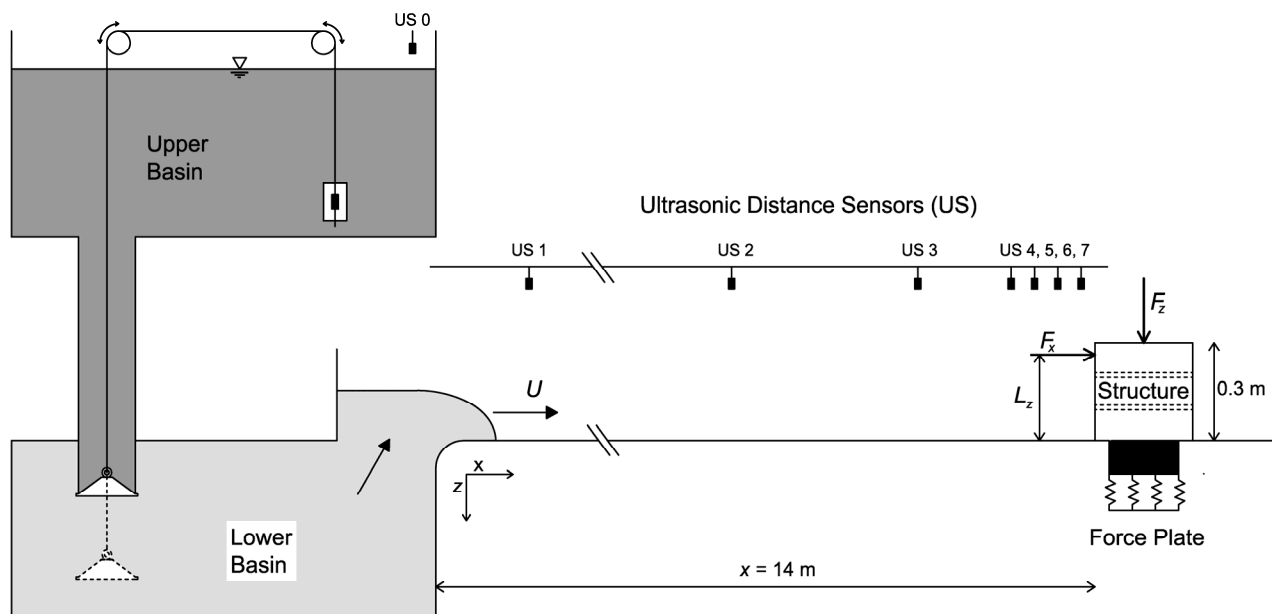


Figure 2. Experimental set-up used to produce dry bed surges through a vertical release technique.

The tested structures were located at a distance of 14 m from the channel inlet and had a width (B) of 0.3m, resulting into a blockage ratio $\beta = W/B = 4.7$. This value was sufficiently high to limit major side effects. The structures were made of aluminum cubes with a thickness of 10 mm and they were designed to be completely rigid, ensuring that the structure's response could be neglected. Numerical simulations of push-over tests allowed to calculate a stiffness values ranging between $k = 2.2 - 1.8 \cdot 10^8$ N/m for all tested structures. These structures corresponded to buildings with height and width of 9 m if a Froude scaling ratio of 1:30 is assumed. This corresponded to residential houses commonly observed in coastal zones exposed to tsunami hazard. As shown in Figure 2, the structures were installed on a dynamometer force plate (AMTI MC6-1000) which recorded the time-history of the impact forces and moments, including surge and drag components, with an acquisition frequency of 1 kHz. The installation of two floors inside the buildings allowed to measure the vertical component of the force induced by buoyancy and the weight of the water flowing

through the structure. The spatial and temporal development of the phenomenon was captured by means of a high speed cameras.

3 METHODOLOGY

The objective of this research project was to systematically evaluate the effect of building openings on the resulting hydrodynamic load via laboratory experiments. A list of the tests performed for the present study is presented in Table 1 along with the main characteristics of each experiment. A test without structure was also performed to characterize the hydrodynamic behavior of the wave. This corresponded to the $P = 100\%$ scenario. In this paper, H corresponds to flow height with the structure, whereas h is the wave height without the structure; F_x is the total horizontal force applied by the incoming wave against the structure, measured at the foundation. The surface porosity P is defined as the ration between the openings (A_o) and the building surface (Eq. [1]):

$$P = \frac{A_o}{B^2} \quad [1]$$

Table 1. Experimental program.

Test	Porosity	Bed condition	Impoundment depth	Wave front celerity	Height		Force
	P [%]		d_0 [m]	U [m/s]	h_{max} [m]	H_{max} [m]	$F_{x,max}$ [N]
1	0	dry	0.63	3.07	0.178	0.519	196.6
2	17	dry	0.63	3.08	0.178	0.543	166.9
3	34	dry	0.63	3.08	0.178	0.548	140.7
4	60	dry	0.63	3.08	0.178	0.507	84.3
5	100 (no structure)	dry	0.63	3.07	0.178	-	-

A good repeatability for all tests was observed, but herein not showed. The structures were not submerged for any incoming wave; however some initial run-up splashes were higher than the building rooftop (Figure 3). The wave front celerity U was in the range predicted by FEMA 55 (2000) and CCH (2000) for the given impoundment depths.

4 VISUAL OBSERVATIONS

The impacts of the propagating waves on the free standing structure were recorded through high speed cameras and GoPro videos. The impact mechanism on impervious structures for waves with different hydrodynamic properties was previously discussed by Wüthrich et al. (2016). Herein all tested scenarios showed crown-shaped splashes and run-up heights higher than the structure, as shown in Figure 3, however this was only limited to the first seconds. After the impact no overflow was observed for any configuration. For structures with openings the water was able to flow through the structure resulting into an interaction between the incoming surge and the building. Initially the water flowing through the structure only affected the first floor, however with the increase of the upstream height, the second and third floors were also eventually inundated. Being the sides open, a portion of the water entering from the front side left the building through these openings, resulting into an interaction with the flow around the structure (Figure 3b).

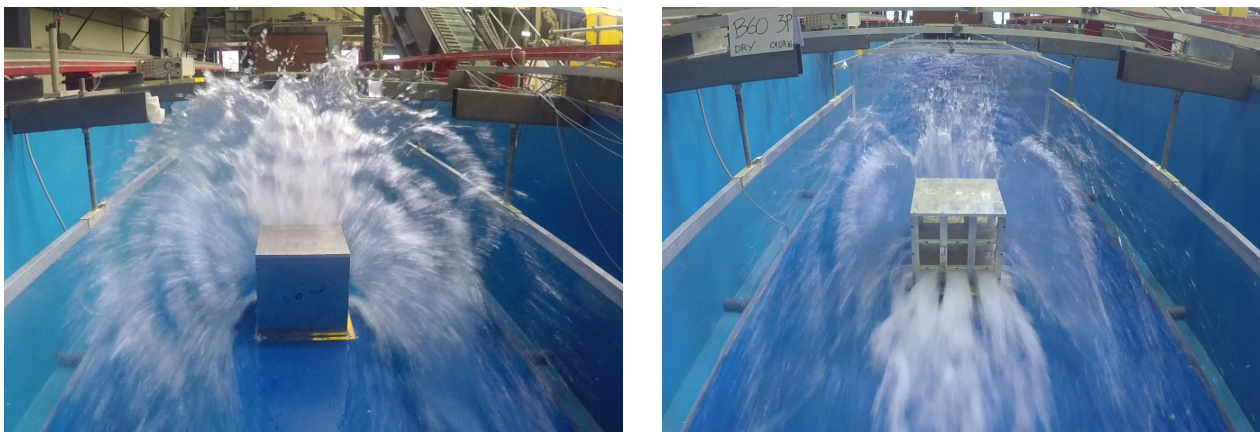


Figure 3. Wave impact against: (left) impervious ($P = 0\%$) and (right) porous ($P = 60\%$) structure for a dry bed surge with equivalent impoundment depth $d_0 = 0.63$ m and front celerity $U = 3.08$ m/s.

Measurements carried out with US probes allowed to measure the run-up heights during the impact; these are presented in Figure 4. One can notice similar run-up heights during the impact (H_{max} , Table 1) for all tests, nevertheless on the upstream side, lower water levels were recorded for larger porosity values. For all

scenarios a fluctuating behaviour was observed, attributed to the presence of a recirculating roller on the upstream side of the building. The intensity of the roller was more important for the impervious structures. Some similar results in terms of visual observations of experimental tests and comparison with numerical simulations were carried out by Hartana and Murakami (2015) for structures with openings and internal slabs.

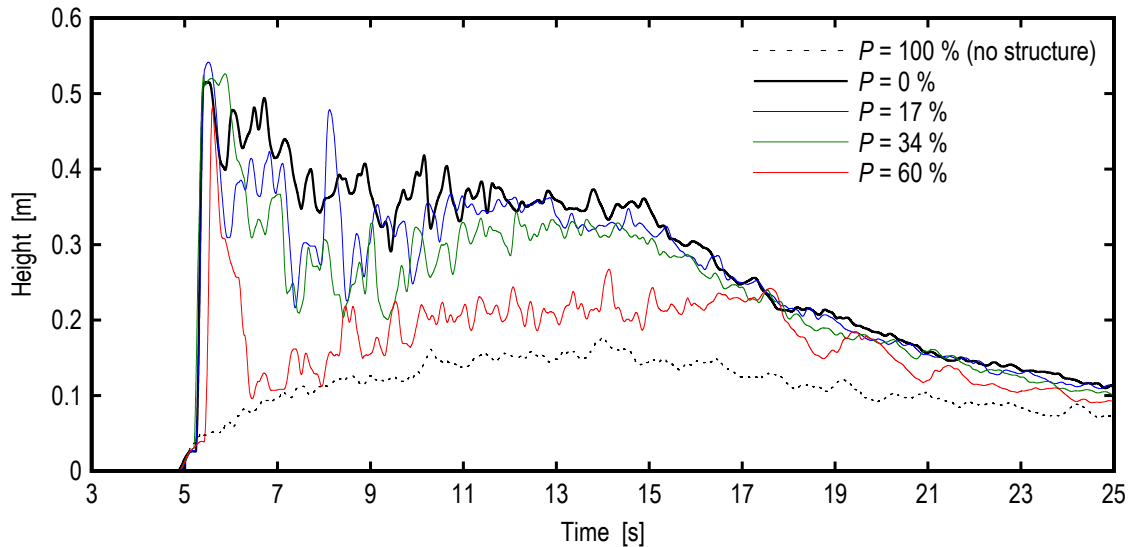


Figure 4. Ultrasonic distance sensors (US) measurements of run-up heights H for various porosity values.

5 LOAD ANALYSIS

The research focused on the effect of building openings on the hydrodynamic loading. The estimation of forces is important to design structure that will withstand the impact of the incoming tsunami. The data obtained for the structures with openings was compared with the reference impervious structure ($P = 0\%$). Both horizontal forces and vertical forces were considered in the present study.

5.1 Horizontal forces on impervious structures ($P = 0\%$)

During a wave impact, horizontal forces F_x are predominant and their estimation is essential to guarantee the survival of the structure. This is important because buildings are rarely dimensioned to resist horizontal forces, unless they are located in seismic areas. The estimation of the horizontal force produced by a flow against a structure can be predicted using Morison's Equation, taking into account a hydrodynamic (or drag) component and an inertia component. For tsunamis, due to their long periods, the inertia component becomes important only at the leading edge, when the wave impacts the structure: this is often called *surge force*. The hydrodynamic component in the x direction $F_{x,D}$ can be computed using the expression presented in Eq. [2]:

$$F_{x,D} = \frac{1}{2} \rho C_D B h v^2 \quad [2]$$

where ρ is the water density, B the structure width, h the flow height and v the flow velocity. A drag coefficient C_D is commonly used, whose value depends on the geometry and on the flow conditions.

In the present study, the total horizontal force F_x produced by a dry bed surge impacting against an impervious structure was measured by means of a dynamometric force plate with a frequency of 1 kHz. The diagram obtained is presented in Figure 5, where one can notice a constant increase of the load until a force oscillating around a constant value was reached. Such behavior was consistent with previous studies, including, among others, Cross (1967), Ramsden (1996), Arnason et al. (2009), Lukkunaprasit et al. (2009b) and Nouri et al. (2010). In the present case, no force overshoot due to surge component was observed during the impact, as previously discussed by Ramsden (1996) and Yeh (2007). This is probably due to the mild slope of the incoming surge. It is therefore reasonable to conclude that for a dry bed surge the inertia component (surge force) can be neglected.

In agreement with what was visually observed, after the impingement, the flow became quasi-steady due to the surge's long period and the estimation of the force could be obtained through the classical hydrodynamic equation presented in Eq. [2]. It is important to point out that the maximum hydrodynamic force $F_{x,D,max}$ does not occur when both h and v are maximal, but when the momentum flux per unit width ($M = hv^2$) is maximum, i.e. $M_{max} = (hv^2)_{max} \neq h_{max}v_{max}^2$ (Yeh et al., 1996; Yeh, 2007). It was shown by Wüthrich et al. (2017) that the depth-averaged profile velocity behind the wave front (V_m) decreased with time with nonlinear behavior. The product of a decreasing V_m with an increasing h lead to a maximum momentum flux occurring around 2/3 of h_{max} .

The behavior of the measured force is plotted in Figure 5 and compared with some formulae commonly found in literature. This study confirms what was previously observed by Ramsden (1996), that the actual measured force F_x was less than the force computed using the run-up height H assuming hydrostatic conditions ($F_x < F_{x,H}$). The measured force was also higher than the force computed with the wave height h without the structure ($F_x > F_{x,h}$). For the present study, the best approximation was found with the hydrodynamic force computed using the depth-averaged profile velocity V_m behind the front, as presented in Eq. [3]:

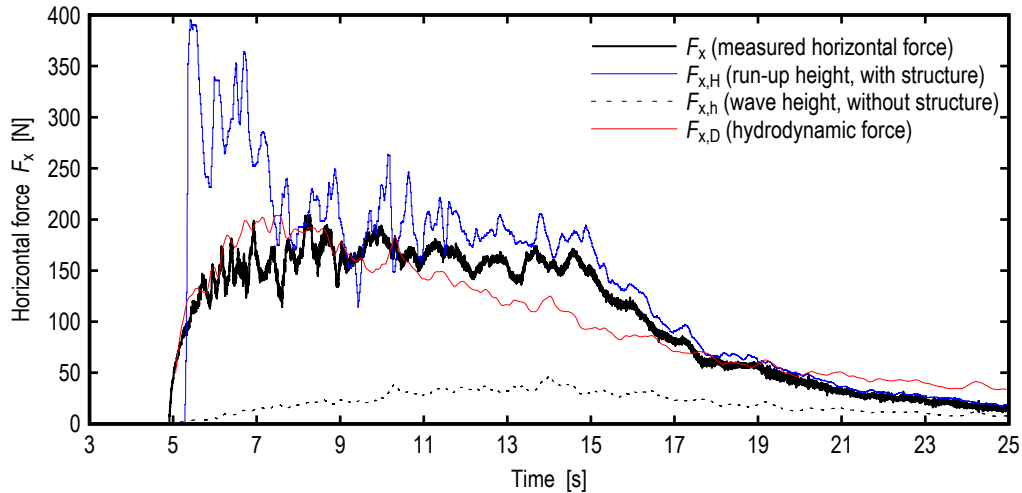


Figure 5. Comparison of force diagram, F_x , for the reference impervious structure ($P = 0\%$) with existing formulae in literature.

$$F_{x,D} = \frac{1}{2} \rho C_R B M = \frac{1}{2} \rho C_R B h V_m^2 \quad [3]$$

where h is the wave height measured without the structure, B the structure width and V_m the depth-averaged wave profile velocity, calculated using the expression presented in Wüthrich et al. (2017). Similarly to Arnason et al. (2009), herein a resistance coefficient $C_R = 2$ was used. The advantage of using a resistance coefficient C_R instead of a drag coefficient C_D was to take into account the hydrostatic pressure difference between the back and the front of the structure, which may contribute to a portion of the measured impact force. The good agreement observed in Figure 5 proved that the force was therefore proportional to the Momentum flux $M = hV_m^2$. One can also notice an underestimation of the force in the post-peak region ($t > 11$ s); this is because all parameters in Eq. [3] refer to the wave without the structure, whose phenomenon is associated with a shorter duration.

5.2 Horizontal Forces on Porous Structures

Once the force produced against the impervious structure was characterized, the following step was to investigate the loads produced on the porous structures. Coastal structures are seldom impervious cubes and most often are characterized by openings such as windows and doors. In the present study four configurations were chosen with total values of $P = 0, 17, 34$ and 60% . The first porosity value (17%) was chosen to represent small windows, the second (34%) large windows and the last (60%) only the load-bearing structure. Surface porosity was uniformly distributed and equally applied on all four vertical surfaces of the structure, simulating an isolated building. Horizontal plates were inserted to simulate the slabs between the floors and the roof (Figure 2). Sketches of the geometries tested are presented in Figure 6.

The time-histories of the four horizontal forces F_x measured for a wave with the same initial release conditions are plotted in Figure 7. One can notice that the overall behaviour was similar for all scenarios: after an initial increase of the force, the load stabilized around a constant value before decreasing once the wave had passed. As previously discussed, for dry bed surges no initial overshoot was observed for any configuration. Major differences could be observed in terms of the vertical stretch of the curve, with large porosities having lower values. This was attributed to the presence of openings on the structure, reducing the inundation depth in front of the building, as previously observed by Hartana and Murakami (2015). Moreover, porous structures had a less steep force increase resulting into a slower and milder loading condition.

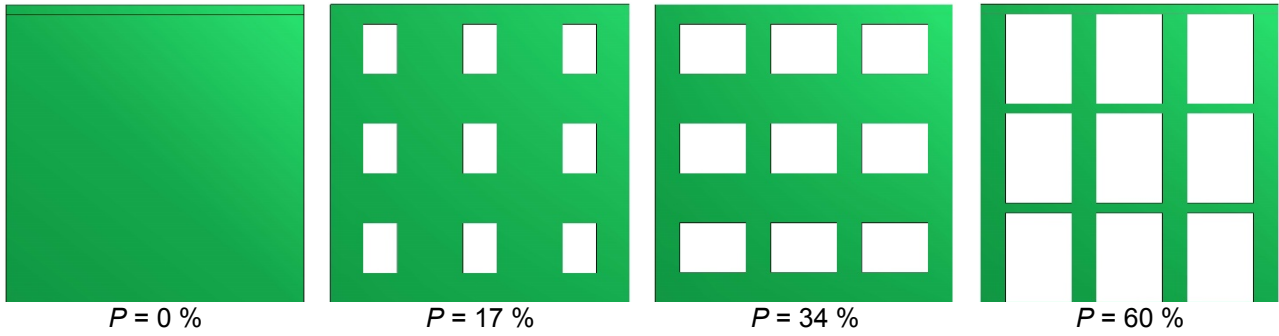


Figure 6. Buildings configurations tested in the present study, with identical geometry on all four sides.

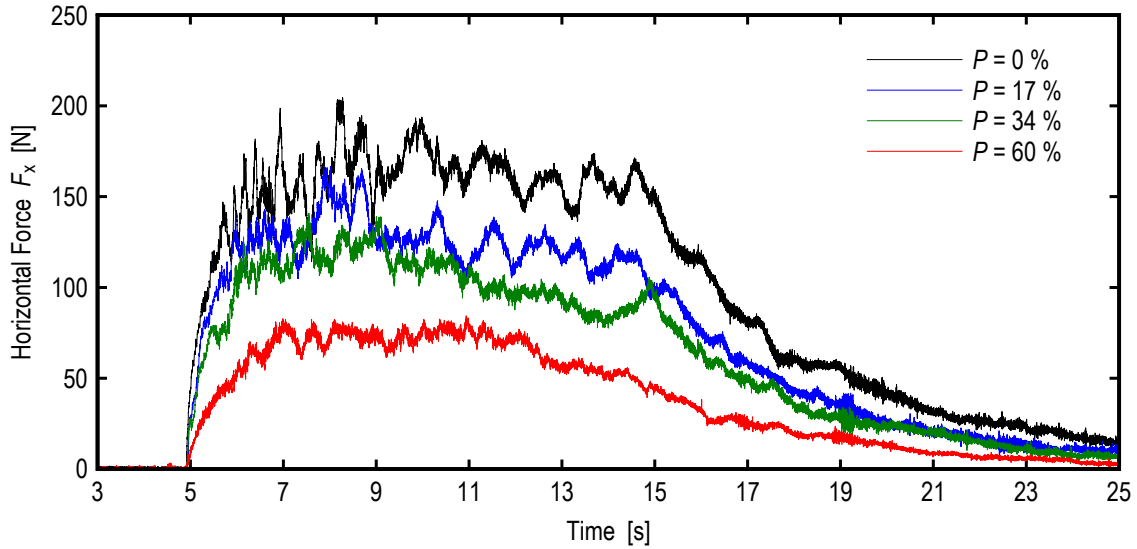


Figure 7. Horizontal force F_x diagrams obtained for a dry bed surge for the same initial release conditions.

For all tested scenarios shown in Figure 7, the absolute maximum $F_{x,max}$ was plotted as a function of the surface porosity P and normalized using the maximum horizontal force measured for the reference impervious structure $(F_{x,max})_{P=0}$. Results are presented in Figure 8, where a linear behavior can be identified. It is hypothesized that the horizontal force F_x is zero in the absence of the structure ($P = 100\%$), allowing to obtain a more precise regression. These preliminary findings suggest that the reduction of the horizontal load is proportional to the surface that is exposed to the incoming wave, as shown in Eq [4]:

$$F_{x,max} \cong (F_{x,max})_{P=0} \cdot (1 - P) \quad [4]$$

where $F_{x,max}$ is the maximum horizontal force, $(F_{x,max})_{P=0}$ is the maximum horizontal force measured for the impervious configuration ($P = 0$) and P the surface porosity of the structure. These findings validated the preliminary conclusions drawn by Lukunaprasit et al. (2009a), who suggested using a linear approximation in lack of experimental tests.

Once the magnitude of the force was defined, designers must know at which height of the structure this force should be applied. Through the moment around the y -axis M_y and the horizontal force F_x it was possible to compute the lever arm L_z , i.e. the application point of the force from the channel bottom, through Eq. [5]:

$$L_z = \frac{M_y}{F_x} \quad [5]$$

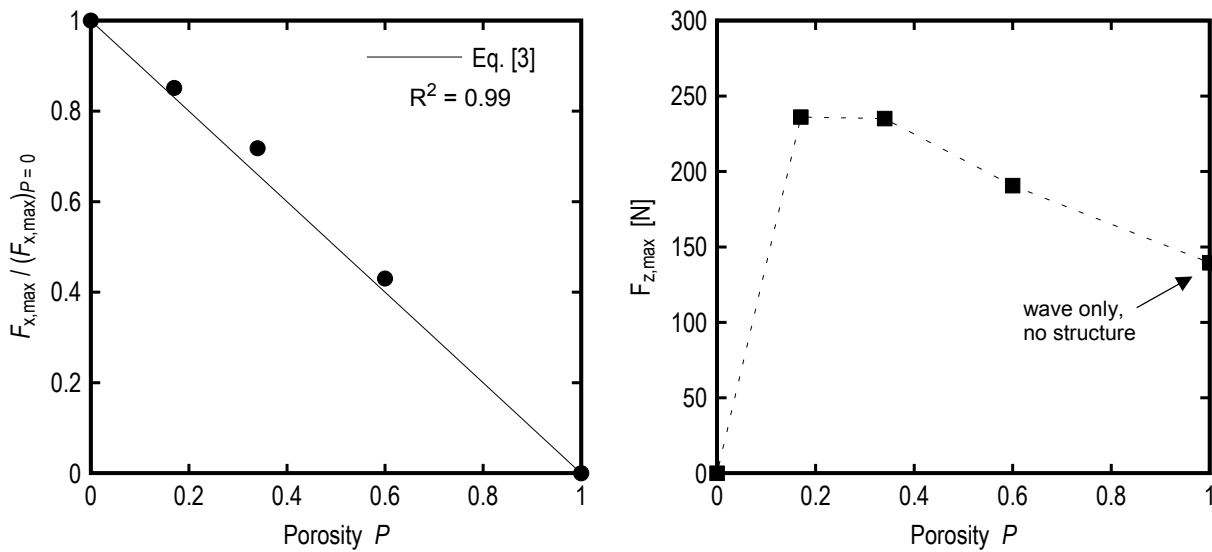


Figure 8. Maximum horizontal force F_x and vertical force F_z as a function of surface porosity P .

The results are plotted for all configurations in Figure 9, normalized using the maximum wave height h_{max} measured without the structure. At impingement, a different behavior can be observed for the tests with larger porosity values, where a minor overshoot can be identified. During the hydrodynamic process following the impact, the lever arm L_z was similar for all scenarios and it corresponded to distances between 75 to 100% of the maximum wave height h_{max} measured without the structure. It is important to point out that the actual water level on the upstream side of the building is highly influenced by the presence of the structure, leading to run-up heights of H greater than h_{max} , as previously shown in Figure 4. These findings pointed out that the surface porosity of the structure does not significantly influence the application point of the force F_x , which can be assumed constant for all configurations (Figure 9).

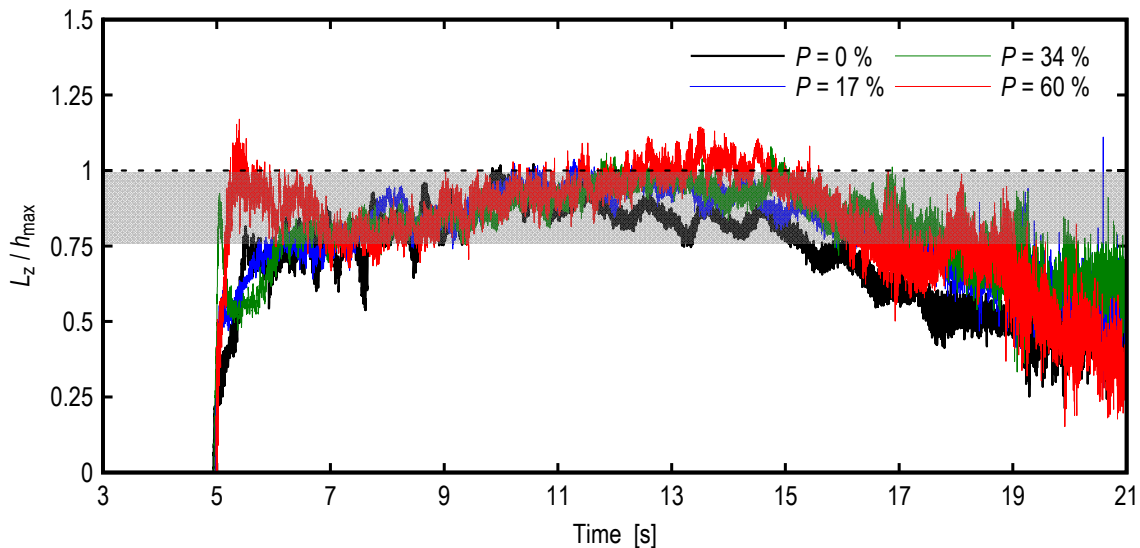


Figure 9. Lever arm, L_z computed as the ratio M_y/F_x for various porosity values.

5.3 Vertical Forces

Along with horizontal forces, **vertical forces** F_z played an important role in guaranteeing the survival of the structure. Two main components can be recognized: buoyancy, $F_{z,B}$ and the gravitational weight of water $F_{z,g}$. In the chosen reference system, the $F_{z,B}$ had to be considered negative, and $F_{z,g}$ positive. Being their signs opposites, the total force at the foundation is the algebraic sum of both components, as shown in Eq. [6]:

$$F_z = F_{z,B} + F_{z,g} \quad [6]$$

As the process was highly unsteady and the upstream water level continuously varied, the isolation of each component is hard to compute. The total force measured by the instrument is presented in Figure 10 for structures with various openings, along with the weight of water without the structure ($P = 100\%$),

corresponding to the weight of the propagating surge. The maximum values of F_z are presented in Figure 8 as a function of P .

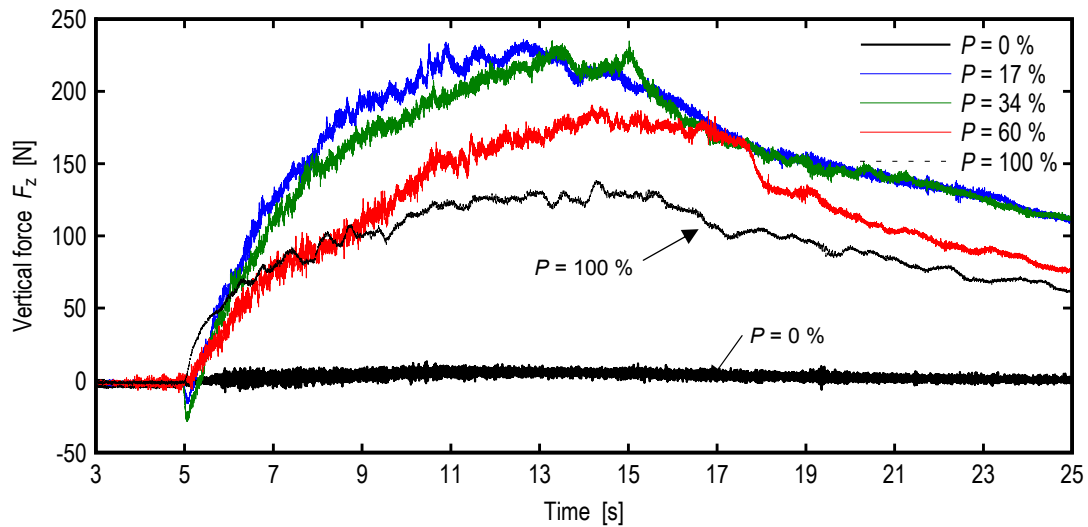


Figure 10. Time history of the total vertical forces, F_z measured for various porosity configurations.

For the impervious scenario, the absence of overflow above the structure resulted in vertical forces F_z close to zero, whereas for porous configurations the weight of the water flowing through the structure was obtained. One can notice that for porosities between 17 and 34 %, similar behaviours were observed, whereas for larger porosity values, smaller vertical forces were recorded. This was probably attributed to the “*accumulation*” of water upstream and inside the structure: in fact larger openings can facilitate the flow through the building and reduce the vertical load. The upper limit was represented by the scenario without structure ($P = 100 %$) showing lesser values if compared to the scenarios with the obstruction.

An initial uplift of the structure was observed for $P = 17$ and $34 %$, attributed to the initial step encountered by the incoming wave, forcing the flow to deviate in the vertical direction and pushing the structure upward (Figure 6). The uplift did not occur for $P = 60 %$ since the structure bottom was located at the same level as the channel. Similar results were previously discussed by Hartana and Murakami (2015).

6 CONCLUSIONS

Tsunamis, impulse waves and the sudden collapse of a dam are rare but catastrophic events, characterized by high reconstruction costs and important human losses. Some events that took place in the last decade showed that measures could be taken to limit devastation and reduce reconstruction costs. Furthermore post-event field trips showed that some structures behaved better than others and that openings seemed to reduce the forces applied to the structures.

The purpose of this experimental study is to reproduce the impact of a dry bed surge against a residential house commonly found in coastal areas. The wave was produced through a vertical release technique and the surge propagated on a smooth horizontal channel with a length of 15.5 m and a width of 1.4 m. The structure was simulated with a 0.3 m aluminum cube with two internal slabs representing the floors. The cubes were designed to be completely rigid, ensuring that the structure’s response could be neglected. Wave height and velocity are measured through 7 Ultrasonic distance Sensors located along the channel.

All tested scenarios visually produced high splashes and similar run-up heights up to twice the building heights. For the configurations with openings, the incoming surge is able to flow through the structure resulting into lower upstream water depths.

The structure was assembled over a Dynamometric Force Plate allowing to measure total forces and momentum with an acquisition frequency of 1 kHz. Porosity values of 0 % (impervious), 17 %, 34 % and 60 % were systematically tested for one wave with identical release conditions. For the impervious structure, the **horizontal forces** in the flow direction showed no initial overshoot and the process was considered quasi-steady due to the long period of the incoming surge. Findings showed a good agreement with the classical drag equation computed with the momentum flux hV_m^2 (Eq. [3]) using the wave height without the structure and the depth-averaged profile velocity behind the wave front. For the structures with openings a reduction of the horizontal force was systematically measured. Furthermore, a less steep increase in the force was noted for the porous configurations, resulting into a lower impulse transferred to the structure. The reduction in horizontal force was shown to be linearly proportional to the porosity values. The application point of the horizontal force was between 75 and 100 % of the wave height measured without the structure, independently of the geometry. Vertical forces represented the sum of both buoyancy and the gravitational weight of water.

An initial uplift was recorded only for the geometries with a vertical step deviating the incoming surge upward. The highest load in the vertical direction were recorded for porosities between 17 and 34 %.

These preliminary tests clearly showed the efficiency of building porosity in the reduction of the hydrodynamic load, pointing out the importance of its estimation for a safer design of coastal structures subjected to tsunami and impulse wave hazards.

ACKNOWLEDGEMENTS

The research reported herein is funded by the Swiss National Science Foundation SNSF (grants 200021_149112/1 and 200021_149112/2). The contribution and support of Prof. Anton Schleiss and Dr. Michael Pfister (Laboratory of Hydraulic Constructions (LCH), Ecole Polytechnique Fédérale de Lausanne (EPFL), Switzerland) are also acknowledged.

NOTATIONS

A_o	opened surface of the structure [m ²]	h_{max}	maximum wave height without the structure [m]
B	building width and height [m]	H	run-up height with the structure [m]
C_D	drag coefficient [-]	H_{max}	maximum run-up height with the structure [m]
C_R	resistance coefficient [-]	k	building stiffness [N/m]
d_0	equivalent impoundment depth [m]	L_z	lever arm [m]
f	Darcy-Weissbach friction factor	M	momentum flux per unit width $M = hv^2$ [m ³ /s ²]
F_x	total Horizontal Force [N]	M_y	moment around the y axis [Nm]
$F_{x,D}$	hydrodynamic force computed using V_m [N]	P	building surface porosity [%]
$F_{x,max}$	maximum horizontal force [N]	t	time [s]
$F_{x,h}$	hydrostatic force computed with wave height (h) [N]	U	wave front celerity [m/s]
$F_{x,H}$	hydrostatic force computed with run-up height (H) [N]	v	flow velocity [m/s]
F_z	total Vertical Force [N]	V_m	depth-averaged wave profile velocity [m/s]
$F_{z,B}$	buoyancy [N]	x	streamwise coordinate [m]
$F_{z,g}$	gravitational weight of water [N]	y	transversal coordinate [m]
$F_{z,max}$	maximum total vertical force [N]	z	vertical coordinate [m]
g	gravity constant [m/s ²]	β	blockage ration defined as $\beta = W/B$ [-]
h	wave height without the structure [m]	ρ	water density [kg/m ³]

REFERENCES

- Arnason, H., Petroff, C. & Yeh, H. (2009). Tsunami Bore Impingement onto a Vertical Column. *Journal of Disaster Research*, 4(6), 391-403.
- CCH (2000). City and County of Honolulu Building Code (CCH). *Department of Planning and Permitting of Honolulu Hawaii*, Chapter 16, Article 11.
- Chanson, H. (2006). Tsunami Surges on Dry Coastal Plains: Application of Dam Break Wave Equations. *Coastal Engineering Journal*, 48(4), 355-370.
- Chanson, H., Aoki, S. & Maruyama, M. (2002). Unsteady Air Bubble Entrainment and Detrainment at a Plunging Breaker: Dominant Time Scales and Similarity of Water Level Variations. *Coastal Engineering*, 46(2), 139-157.
- Chinnarasri, C., Thanasisathit, N., Ruangrassamee, A., Weesakul, S. & Lukkunaprasit, P. (2013). The Impact of Tsunami-Induced Bores on Buildings, *Proceedings of the ICE-Maritime Engineering*, 166(1), 14-24.
- Chock, G., Robertson, I., Kriebel, D., Francis, M. & Nistor, I. (2012). Tohoku Japan tsunami of March 11, 2011 – Performance of structures. *American Society of Civil Engineers (ASCE)*.
- Cross, R. (1967). Tsunami Surge Forces, *Journal of the Waterways and Harbors Division*, 93(4), 201-231.
- FEMA 55 (2000). Coastal Construction Manual. *Federal Emergency Management Agency*, Washington DC, USA.
- Hartana, & Murakami, K. (2015). Numerical and Experimental Simulation of Two-Phase Tsunami Flow Through Buildings with Openings, *Journal of Earthquake and Tsunami*, 9(3) (2015), 1550007, 15 pages.
- Lukkunaprasit, P., Ruangrassamee, A. & Thanasisathit, N. (2009a). Tsunami loading on buildings with openings, *Science of Tsunami Hazards*, 28(5), 303.
- Lukkunaprasit, P., Thanasisathit, N. & Yeh, H. (2009b). Experimental Verification of FEMA P646 Tsunami Loading, *Journal of Disaster Research*, 4(6), 410-418.
- Madsen, P., Fuhrman, D. & Schäffer, H. (2008). On the Solitary Wave Paradigm for Tsunamis. *Journal of Geophysical Research: Oceans*, 113(C12) 1978-2012.
- Meile, T., Boillat, J.L. & Schleiss, A.J. (2013). Propagation of Surge Waves in Channels with Large-Scale Bank Roughness. *Journal of Hydraulic Research*, 51(2), 195-202.
- Nistor, I., Palermo, D., Nouri, Y., Murty, T. & Saatcioglu, M. (2009). Tsunami-Induced Forces on Structures. *Handbook of Coastal and Ocean Engineering*. Singapore, World Scientific, 261-286.
- Nouri, Y., Nistor, I., Palermo, D. & Cornett, A. (2010). Experimental Investigation of The Tsunami Impact on Free-Standing Structures, *Coastal Engineering Journal*, JSCE, World Scientific, 52(1), 43-70.

- Ramsden, J.D. (1996). Forces on a Vertical Wall due to Long Waves, Bores, and Dry-Bed Surges. *Journal of waterway, port, coastal, and ocean engineering*, 122(3), 134-141.
- Thusyanthan, N. & Madabhushi, S. (2008). Tsunami Wave Loading on Coastal Houses: A Model Approach, *Proceedings of the ICE-Civil Engineering*, 161(2), 77-86.
- Van de Lindt, J., Gupta, R., Garcia, R. & Wilson, J. (2009). Tsunami Bore Forces on a Compliant Residential Building Model, *Engineering Structures*, 31(11), 2534-2539.
- Wüthrich, D., Pfister, M., Nistor, I. & Schleiss, A.J. (2017). Experimental Study of Tsunami-like Waves on Dry and Wet Bed Generated with A Vertical Release Technique. *Journal of Waterway, Port, Coastal, and Ocean Engineering*. (under review)
- Wüthrich, D., Pfister, M. & Schleiss, A.J. (2016). Example of Wave Impact on a Residential House. *Proceedings of the 4th IAHR Europe Congress*, Liege, Belgium, 27-29 July 2016.
- Yeh, H. (2007). Design Tsunami Forces for Onshore structures. *Journal of Disaster Research*, 2(6), 531-536.
- Yeh, H., Liu, P. & Synolakis, C. (1996). Long-Wave Run-Up Models, *World Scientific Publishing Co.*, Singapore, 403.

AN ASSESSMENT OF OPTIMIZATION ON LAND RECLAMATION DESIGN BASED ON HYDRAULIC ASPECTS

LIP SAN LEONG⁽¹⁾, JUAN CARLOS SAVIOLI⁽²⁾, JACOB HJELMAGER JENSEN⁽³⁾, KATHISTASAPATHY SHANMUGAPATHY⁽⁴⁾ & KOK SIN WOON⁽⁵⁾

^(1,2,3) DHI Water & Environment (M) Sdn. Bhd., Selangor, Malaysia,
lls@dhi.com.my; jcs@dhi.com.my; jhj@dhi.com.my

^(4,5) Country Garden Pacificview Sdn Bhd, Johor Bahru, Malaysia,
shan@countrygarden.com.my; vincentwoon_fl@countrygarden.com.my

ABSTRACT

Land reclamation refers to the land filling at the coastal area or any form of water body for development purposes. It is one of the popular methods to acquire more land for development purposes. However, undesirable land reclamation designs has raised concerns by various groups such as environmentalists, politicians and other related parties as it potentially can cause major impacts particularly on the marine environment. Subsequently, this leads to various mitigation measures to be undertaken to mitigate the side effects from reclamation. The present paper discuss the optimization process applied for a reclamation site located close to Malaysia-Singapore international border. Key elements in the layout optimization procedure includes understanding of existing guidelines, natural conditions and application of numerical modelling tools (Mike 21 FM HD). Natural conditions such as bathymetry contour is utilized in the optimization process to identify the potential area to be reclaimed and inspired the establishment of the preliminary shape of the land reclamation. MIKE 21 FM HD tool is applied to describe the hydrodynamic characteristics such as ocean, lakes, estuaries, bay and coastal regions with response to various hydraulic forcing. Subsequently, the hydraulic flow condition in the study area can be derived and layout optimization proceeds with streamlined based on the hydrodynamic flows. The result of the study shows the potential impact on the hydraulic environment from optimized layout particularly along the international border is reduced with the increase in land reclamation area size. Thus, benefit of an optimized layout is not limited to reduction in the potential hydraulic impacts but also reduce the need to implement additional mitigation measures which thus assist in cost and time saving.

Keywords: Layout optimization; international border; MIKE 21 FM HD; land reclamation.

1 INTRODUCTION

Land reclamation is defined as a process where new land is artificially created in the sea for various development purposes. Reclamation activities has become a trend in the world to acquire more land for development purposes (Hu and Jiao, 2010). In recent years, it can be observed that land reclamation activities are blossoming in Asia particularly in Malaysia as land reclamation is believed to be the most cost-effective way to pursue economic growth by developing advanced infrastructure and industry on the reclaimed land, however it can cause the degradation of the ecosystem (Chung et al., 2015). Furthermore, the impacts from the reclamation that altered the ecosystem condition can affect the livelihood of human-beings in the coastal area (Nadzir et al., 2014).

Rapid development particularly land reclamation is necessary in Malaysia to provide a sustainable economy. However, few case studies of land reclamation around the world show improper land design has caused severe side effects in the hydraulic environment such as erosion, siltation, flushing issues and others. This has caught the attention of various groups such as decision maker, politician and authorities when making decision that it should not only benefit to the economy but also need to be sustainable with minimal adverse impact on the environment.

However, there is always a conflict of interest between the economic benefit and environmental issues, as many decision-makers tend to ignore the side effects of the environment which resulted in excessive degradation of ecosystem functions and the reduction in provision of ecosystem services (Polasky., 2012). Nevertheless, implementing and strengthening the ecosystem services in this industry is important as it plays an important role in the decision-making process of land reclamation where it provides a system to integrate the impact on the environment as well as the socioeconomic factor. In fact, there is a policy which has been commonly practiced in Malaysia whenever reclamation project is more than 50 ha (Department of Environment Malaysia. Environment Requirements: A Guide for Investor. Eleventh Edition, 2010) will required an environment impact assessment to be carried out which analyze the benefit of the project and the impacts on the environment.

When land reclamation is necessary to be developed under the pressure of economic factor, an undesirable or improper shape of land reclamation are often being encountered or introduced which has exaggerated the negative impacts on the environment. Layout optimization can assist to establish an optimized shape of land reclamation by weighing the balance between the needs of development and environment. Optimizing the layout is considered an advanced mitigation measure for land reclamation to prevent or reduce implementation of unnecessary mitigation work in later stage to mitigate the potential side effects, for example, foul-smelling due to flushing issues, navigation risk due to eddy generation, sedimentation and other hydraulic environment issues. Given some of the issues are permanent or long-term such as sedimentation issues in a drainage and navigation channel, maintenance dredging have to be carried out frequently to maintain the function of the channel. Eventually, a huge cost and time has to be utilised to mitigate this effect.

This paper presents the optimization of land reclamation site located close to Malaysia – Singapore international border. As land reclamation take place at sensitive area which is adjacent to the international border, thus any potential cross border impact can potentially results a politic conflict between Malaysia and Singapore. Evidence that a land reclamation case issue between Singapore and Malaysia has been brought to the International Tribunal for the Law of the Sea (ITLOS) (Request for Provisional Measures Submitted by Malaysia, 2013) where the reclamation work is near to Malaysia and Singapore border.

In this study, optimization is carried out based on an initial design of land reclamation layout. Besides that, there is a recommendation on the international border (DHI, Detail study on Tuas View Extension and Pulau Tekong Land Reclamation. Final Report, Volume VIII Water Quality Impact Assessment, 2004). where the maximum current speed changes should not be more than 10% which act as the main criteria in the present study. Therefore, layout optimization process was carried out on the initial layout to help to provide the best fit design of land reclamation layout to achieve the objective of minimizing the potential hydraulic impact particularly on the sensitive transboundary impact and complied with various guidelines and requirements. The layout optimization process was carried out to correspond to the natural conditions such as bathymetry around the proposed development.

Scientific assessment tools such as spatial modelling, tradeoff analysis, economic valuation and environment policy implantation are utilized in the ecosystem services (Chung et al., 2015). In this case, numerical tool MIKE 21 FM HD was utilized and plays an important role in the optimization process, as it assist to quantify the potential hydraulic impact. MIKE 21 FM HD is a numerical tool developed by DHI which is widely applied in hydraulic phenomena to simulate water level and flow variations in response to a variety of forcing function in oceans, lakes, estuaries, bay and coastal regions. This powerful MIKE 21 FM HD modelling tool able to describe the flow conditions in 2D map. In conjunction, development layout was optimized based on the flow conditions.

Challenges encountered in the development layout optimization consisted of fulfilling the guidelines and regulations which constraints the flexibility of land reclamation layout design. However, conflict often occurs between interest in conversation or development when enacting reclamation policies (Chung et al., 2015).

2 STUDY AREA

A large number of land reclamation work has been carried out in the Johor Straits such as Tanjung Piai, Forest City, Danga Bay and Puteri Cove. Our study area focused on the optimization of land reclamation at the coastal zone of western Johor Straits, Malaysia in which Forest City development is opted as our case study area. Forest City is a massive land reclamation with four islands which consists of a total area of 1,386 ha which is smaller than the originally proposed reclamation by the developer of 1,600 ha (Controversial Johor Strait land reclamation project Forest City gets the go-ahead, *New Straits Time*, 14th January 2015). The development is bounded between Malaysia and Singapore with a complex ecosystem and shallower areas. Land reclamation is located at the coastal zone between PTP and Malaysia-Singapore 2nd Link as shown in Figure 1. Along the Johor coastline, an extensive shallow mudflat covers from PTP to 2nd Link was observed where mangrove is resides in the intertidal of this area. In addition to that, seagrass was observed in the shallow area as well. At the west of the reclamation area exists a navigation channel to access PTP port area. A defined anchorage area can be found at the southwest of study area for vessels to anchor. A small island Pulau Merambong is located between Malaysia and Singapore where corals can be found surrounding it.

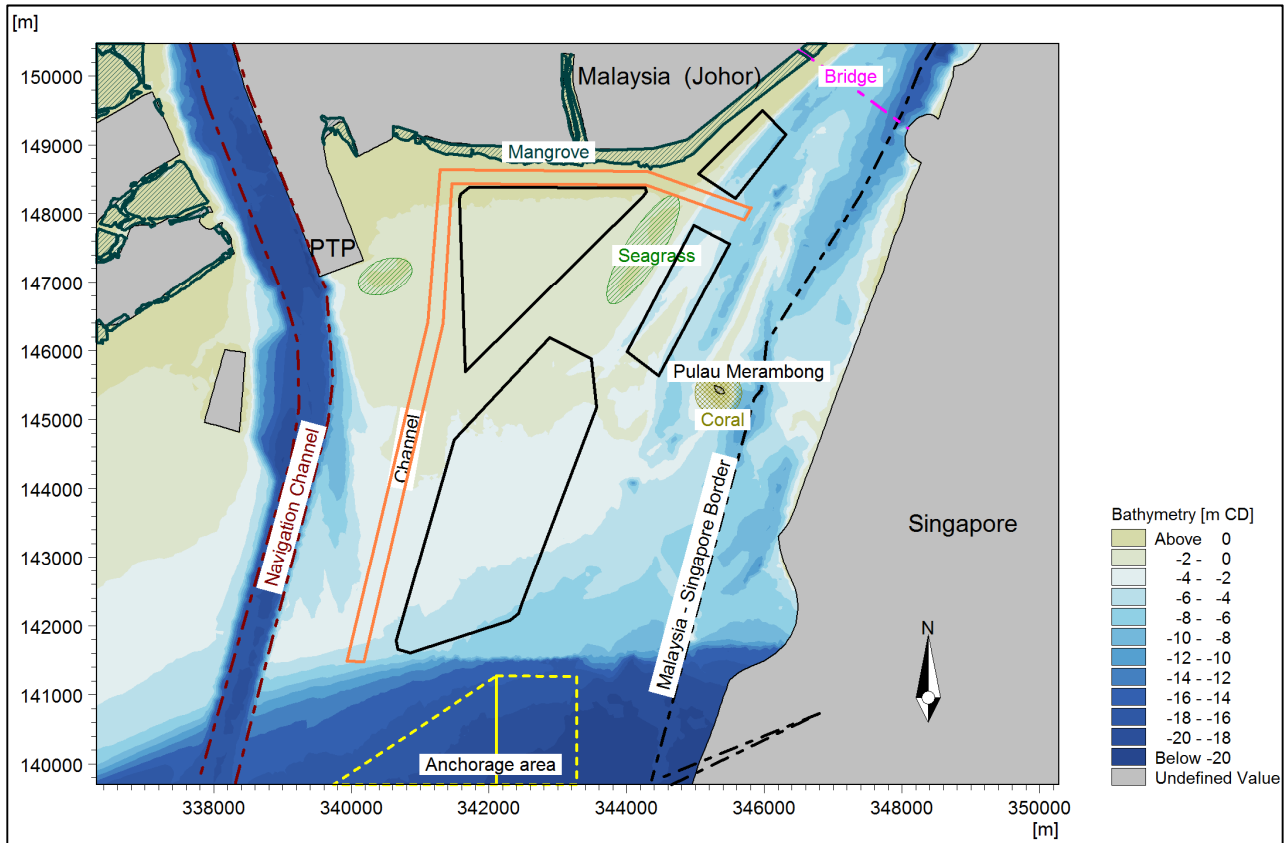


Figure 1. Overview of study area.

3 APPROACH AND METHOD

An artificial initial land reclamation layout was designed based on the Forest City case study. Optimization process was carried out on the initial reclamation layout to establish a new design layout based on hydraulic perspective. In order to carry out the layout optimization, the following components are utilized:

- Understanding existing guidelines, limitations and requirements;
- Understanding geographical conditions in the area of interest; and
- Application of numerical modelling tools

3.1 Understanding existing guidelines, limitations and requirements

This is an important element in the layout optimization process, as by understanding the existing guidelines, limitations and requirements, it assist in defining the restrictions and objectives required to be achieved in the layout optimization. In the present study, there are a number of existing guidelines and requirements required to be applied as outlined in the following:

- Less than 10% changes of maximum current speed on International border;
- No overlapping land title boundary of other owners;
- 100 m buffer zone for seagrass area;
- Preserved mangrove area;
- Away from anchorage area;
- Away from Port area;
- Malaysia state authorities land boundary – within 3 nautical miles boundary;
- Away from the sensitive coral area;
- 500 m buffer zone for bridge;

Seagrass and corals can be found within the study area and they are important species within the ecosystem which required to be preserved for our next generation. As such, a buffer zone (100 m) should be considered in the vicinity of seagrass and coral area as to minimize the potential hydraulic impacts. It is important that the layout design should not encroach near or into navigation channel and anchorage area as it can pose safety risk issues particularly on ships or vessels when navigating through the navigation channel.

3.2 Understanding geographical conditions in the area of interest

Bathymetry is an important element in the layout optimization procedure. A shallow area with extensive mudflat area is observed within the western side of PTP scoured by river flow of Sungai Pulai and tidal flows. The natural channel of Sungai Pulai is artificially deepened to serve as the access channel to PTP port. The east side of PTP which is the present study area, the coastline is characterized by mangroves and shallow mudflat areas. This stipulates the ideal location to be reclaimed as deep water is technically difficult, (Choong, 2006). Introducing existing guidelines and requirement has limited and reduced the potential coverage area to be reclaimed as shown in Figure 2. The established potential area indicates the optimized layout should be within this area.

The shape of the optimized layout is inspired by the triangular shape of natural formation of delta morphology that reflects how the nature in response to achieve a steady state. As the reclamation area is geographically located at the location where the Johor Straits is starting to diverge which has similar structure of the natural formation delta morphology. Therefore the initial islands layout was optimized by imitating the triangle shape of the delta morphology pattern which is shown in Figure 3 and presented as Layout 01 in Figure 4.

Layout 01 was furthered optimized to preserve the seagrass area which are located within reclamation area and presented as Layout 02. Subsequently, the layout was furthered reshaped and streamlined with the bathymetry contour to avoid encroaching to the deeper area and anchorage area and presented as Layout 03. Consideration of the water exchange for the seagrass and mangrove and flushing issues, dredged channel between islands was introduced in the optimized layout which is shown in Figure 4. This implementation allowed more flow go through the channel and subsequently improve flushing between the islands.

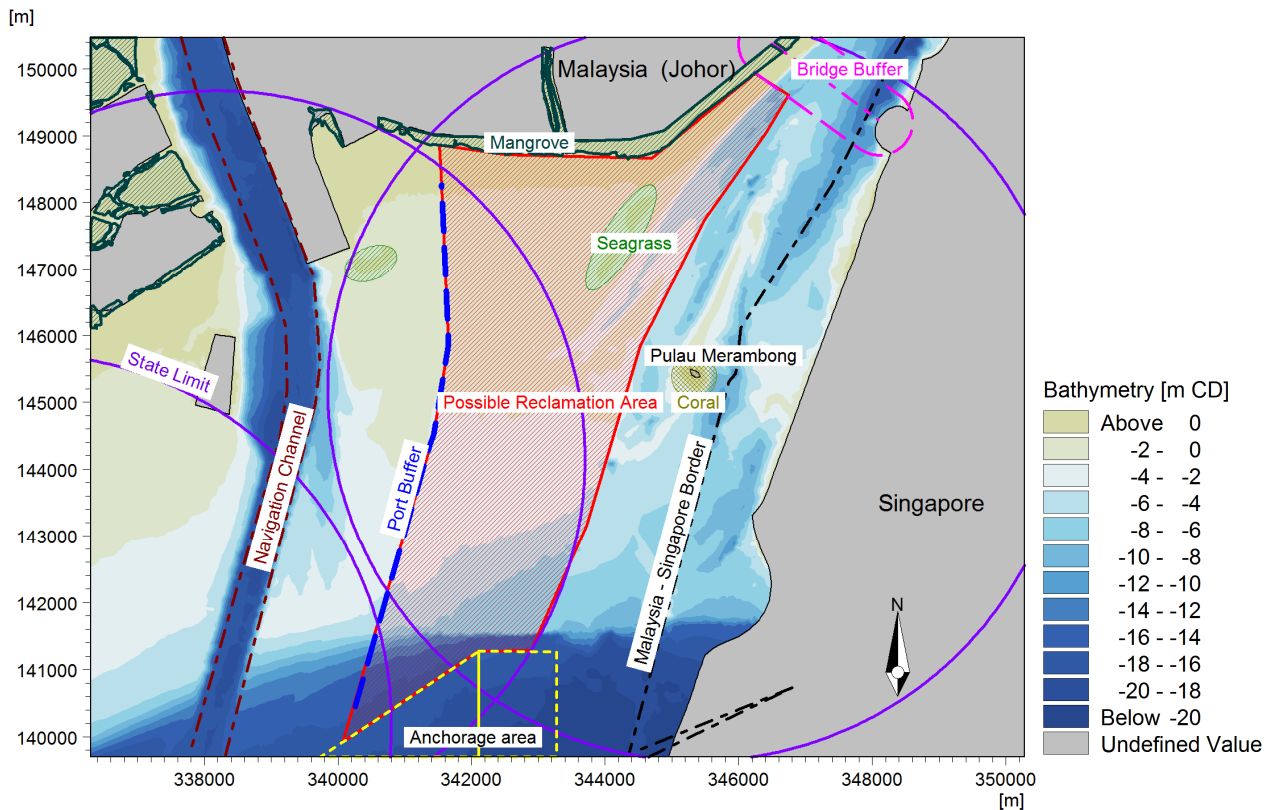


Figure 2. Bathymetry around area of interest.



Figure 3. Example of natural formation of delta morphology. (Blue circle indicates the triangle shape of delta morphology).

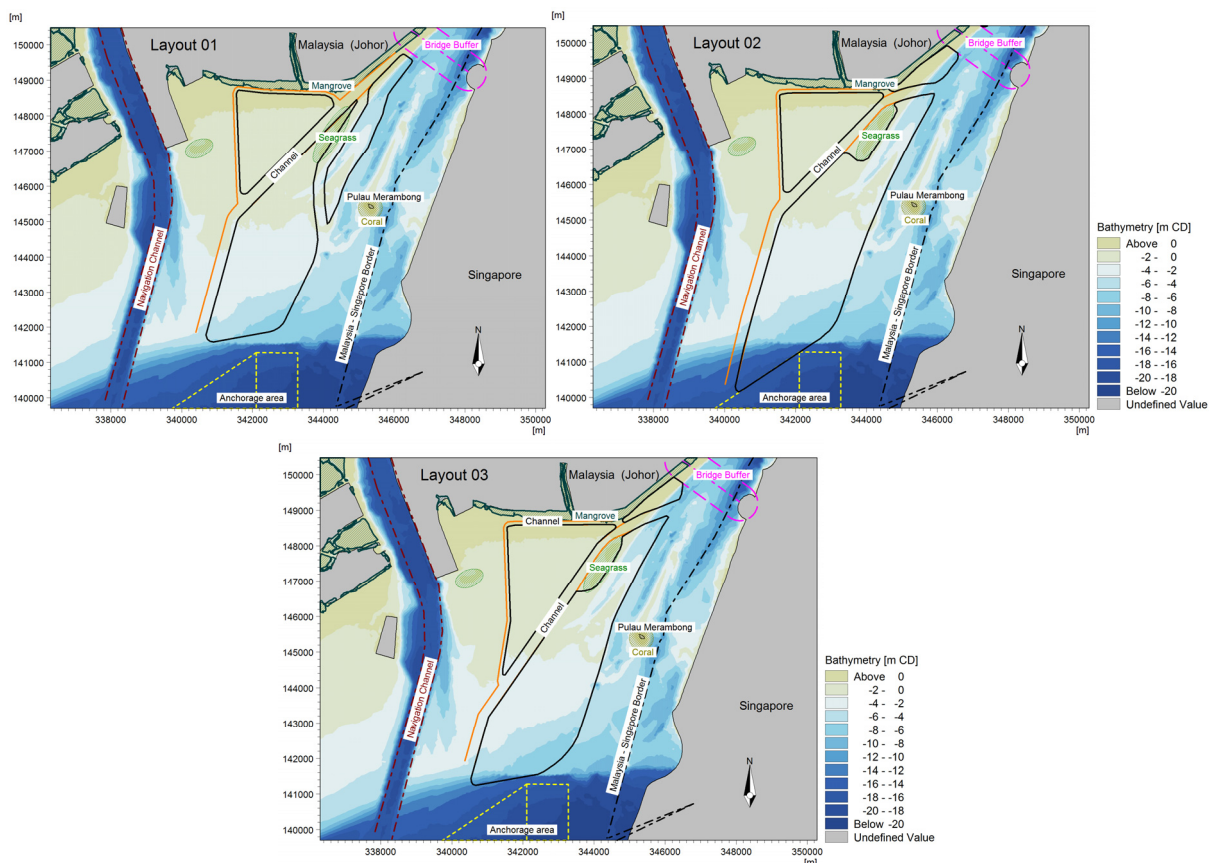


Figure 4. Example of the optimized layout adopting features such as delta morphology, introducing dredged channel and bathymetry contour in Layout 03.

3.3 Application of numerical modelling tools

The usage of numerical modelling tools is inevitable in the modern day. Numerical model MIKE 21 FM HD is a powerful tool in hydrodynamic engineering which has widely applied in describing the hydraulic and environmental phenomena with corresponding to various forcing effects such as bottom shear stress, wind shear stress, barometric pressure gradients, Coriolis force, momentum dispersion, sources and sinks, evaporation, flooding and drying, wave radiation stresses, salinity and temperature.

Mike 21 FM HD tools are utilized to describe the hydrodynamic conditions for pre- and post-development and computed the changes occurred from the development. Existing hydrodynamic conditions derived from the modelling tool provide a useful information in the optimization process. Figure 5 shows the hydrodynamic conditions during ebb and flood tides without any establishment of reclamation. As such, the predicted high

currents flow area, for example location around the navigation channel and along the international border are not an ideal location to undertake reclamation works.

Optimization process was further carried out with refined shape of the islands that designed not to encroach into the high velocity areas, streamlined with parallel to current flow. Besides that, the channel between the islands was optimized by deepening the sea bed to allow some flows to flow through the island to improve the flushing condition. In addition, the dredged channel was optimized by deepening or widening until it achieves the main objective where the maximum flow speed changes is less than 10% at the international border.

Layout was optimized by reshaping the islands to avoid any irregular shape that is perpendicular to the high flows to achieve minimum or no eddy generation particularly at the navigation channel and anchorage area as presented in Figure 6. As generation of eddy can imposed safety risk to ship/vessel navigating through the navigation channel or anchor at the anchorage area. The island's shape was modified to covers area where the current flows are slow thus reducing the potential sedimentation issues within this area.

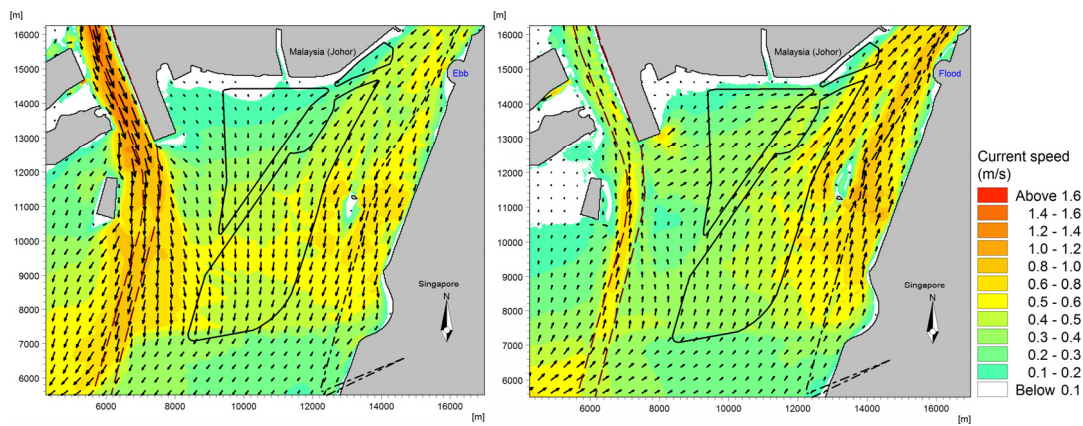


Figure 5. Flows condition during ebb (left) and flood (right) tides.

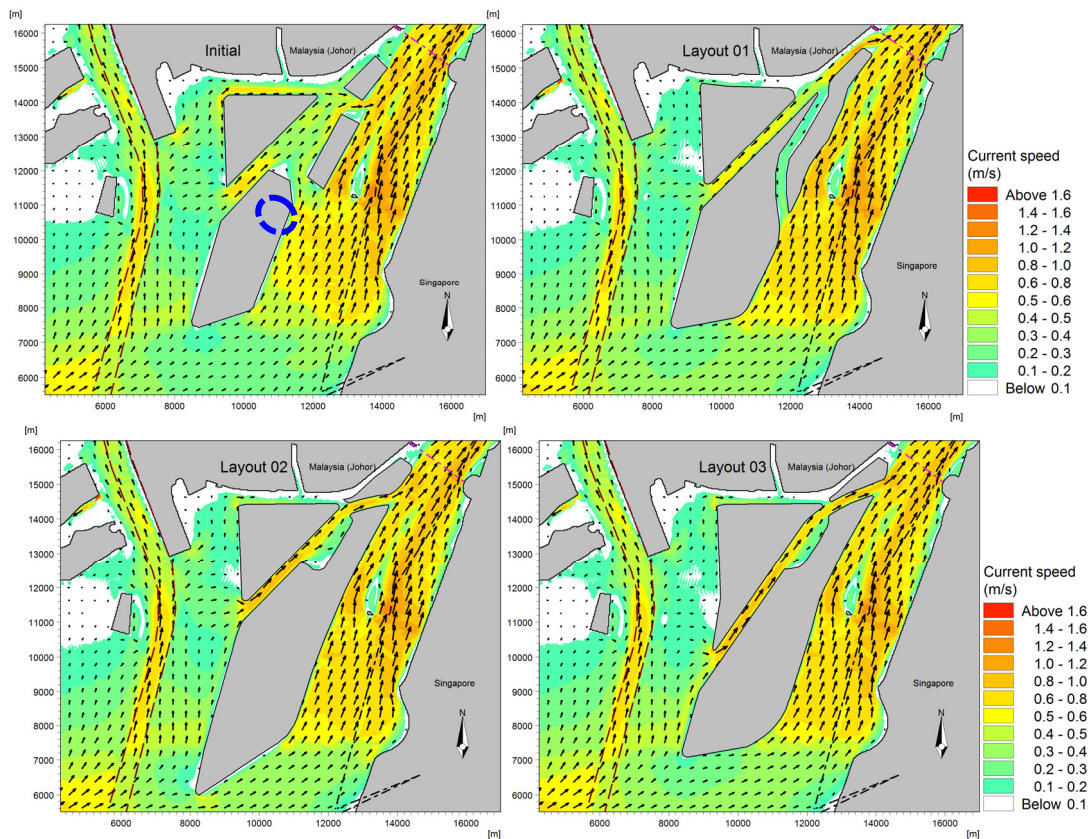


Figure 6. Flow conditions for Initial (top left), Layout 01 (top right), Layout 02 (bottom left) and Layout 03 (bottom right) during flood tides. (Blue circle indicates potential area where eddy is generated at top left plot – Initial layout)

4 RESULTS

Percentage changes of maximum current speed was computed based on the baseline maximum current speed shown in Figure 7. The optimized design layout has produced a significant positive result where the hydraulic impact has been noted to reduce significantly in the Singapore side where percentage maximum current speed changes is less than 10% at majority of the Singapore side compared to the initial layout, as presented in Figure 8. An increase of current speed in the channel between the islands and mainland indicated the flushing condition has improved and more water exchanges occurred. Besides that it is noted the currents changes within the mangrove area is small indicated the impacts on mangrove will be small. At the navigation channel, increased of maximum current speed was observed but no eddies with high velocity was generated which can potentially putting risk to ships navigating through the channel as shown in Figure 6 for all the layout. However result from the initial layout shown a small area where eddies are generated at the tip north of the south artificial island (blue circle dotted line in Figure 6). Layout 02 shows there is an increase of current speed on anchorage area, which poses safety threat to the vessels that anchoring within that area.

Reduction in the current flows can potentially lead to sedimentation issues and can turn the area into muddy area, as finer silt particles tend to deposit with the reduction in current speed and coarser materials tend to settle down in high current speed area (Opreanu et al., 2007). In Layout 02, a reduction of current speed is observed in the channel between the islands indicated sedimentation issues where maintenance is needed to be undertaken frequently to maintain the function of the channel.

After the optimization process, the Layout 03 managed to increase approximately 40% of the land size and has the least potential hydraulic impacts compared to all other layouts. The comparison results are tabulated in Table 1.

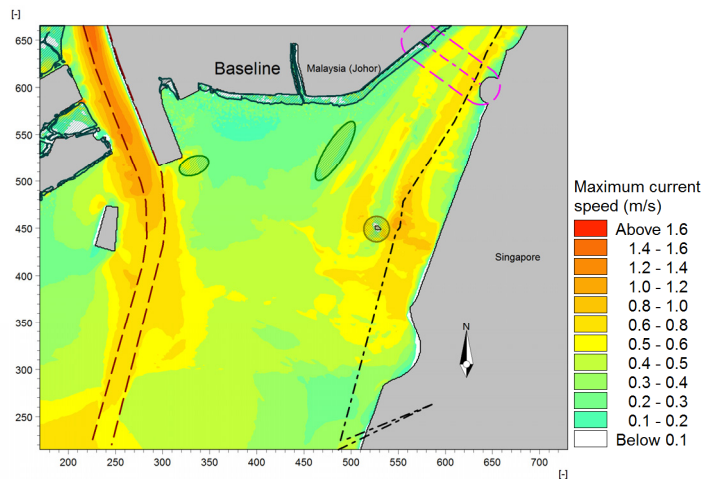


Figure 7. Maximum current speed for baseline (pre-reclaimed) condition.

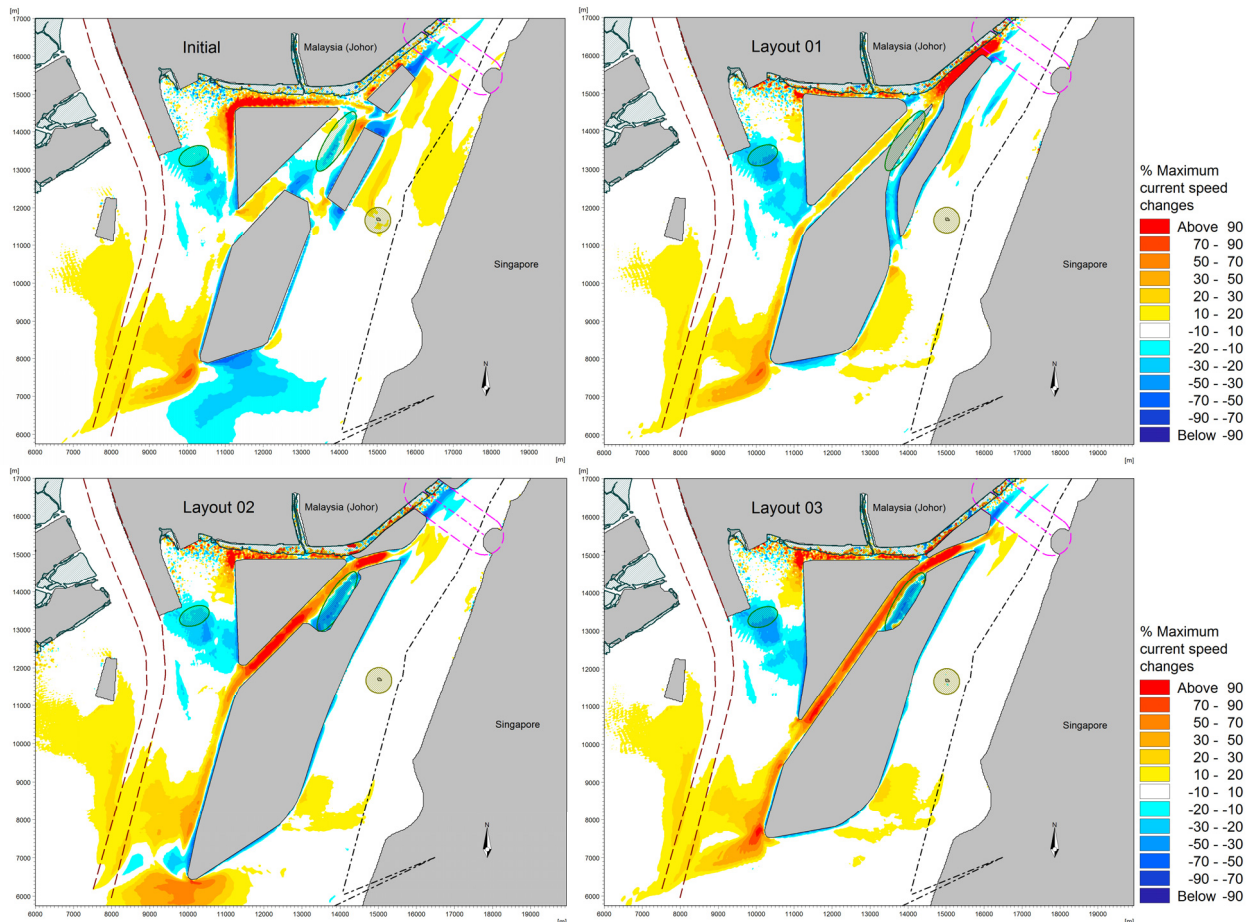


Figure 8. Percentage changes of maximum current speed of compared to baseline condition for Initial (top left), Layout 01 (top right), Layout 02 (bottom left) and Layout 03 (bottom right).

Table 1. Comparison results.

Layout Options	Land Size (%)	Maximum current speed changes <10% trans boundary	Eddies Generated	Flushing between Islands	Changes current Speed on anchorage area
Initial	-	Large area	Yes	Medium	Reduction
Layout 01	+25%	Small area	No	Medium	-
Layout 02	+50%	Small area	No	Good	Increase
Layout 03	+40%	Small area	No	Good	-

5 CONCLUSIONS

Based on the study results, layout optimization managed to minimize the potential hydraulic impact with less than 10% of maximum current magnitude changes at the international border with an increase of land size around 40%. No eddy was generated as compared to initial layout and improvement in flushing capacity between islands. These indicates that with layout optimization process, the beneficial gain are not limited to impact reduction on hydraulic environment aspects but also allowed a larger reclamation land area to be placed at the project development itself. It is noted, although optimization can reduce the impacts but there always will be changes to the environment once reclamation is in place. Nevertheless, layout optimization process should always be encouraged and practiced before commencing any land reclamation activities particularly when decision-makers have decided to proceed with massive land reclamation. This is important as once the land reclamation is established, the impacts on the environment which are in most cases are permanent, and any future modification in the later stages will be difficult and can potentially cause additional degradation of its services. Extra mitigation measures can be avoided and consequently saving of cost and time can occur. Generally, the optimization process is known as work with nature by implementing the land reclamation with the least impact on hydraulic environment.

ACKNOWLEDGEMENTS

First of all, I would like to thank DHI Water and Environment (M) Sdn Bhd which provides me with the opportunity to undertake the optimization layout study. Secondly, I would like to express my gratitude to my fellow team members who has provided guidance and support in the present study. Last but not least, thank you for the support and information provided by Country Garden Pacificview Sdn Bhd for the present study.

REFERENCES

- Choong, K.Y. (2006). No.101 Environment Management and Conflict in Southeast Asia – Land Reclamation and its Political Impact. *Institute of Defence and Strategic Studies Singapore*, 101(6), 1-30.
- Chung, M.G., Kang, H. & Choi, S.U (2015). Assessment of Coastal Ecosystem Services for Conservation Strategies in South Korea. *PLoS ONE*, 10(7), 1-23.
- Hu, L. & Jiao, J.J. (2010). Modelling the Influences of Land Reclamation on Groundwater Systems: A Case Study in Shekou peninsula, Shenzhen, China. *Engineering Geology*, 114(2010), 144-153.
- Nadzir, N.M., Ibrahim, M. & Mansor, M. (2014). The Impact of Coastal Reclamation to the Quality of Life of Tanjung Tokong Community, Penang. *AicQol 2014 Kota Kinabalu AMER International Conference on Quality of Life*, 160-168.
- Opreanu, G., Oaie, G. & Paun, F. (2007). The Dynamic Significance of the Grain Size of Sediments Transported and Deposited by the Danube. *Geo-Eco-Marina Coastal Zone Processes and Management. Environmental Legislation*, 13, 111-119.
- Polasky, S. (2012). *Valuing Nature: Economics, Ecosystem Services and Decision-Making. Measuring Nature's Balance Sheet of 2011 Ecosystem Services Seminar Series*, Ed. Coastal Quest and Gordon Betty Moore Foundation, 71-83.

WAVE SCATTERING FROM SUBMERGED T-TYPE BREAKWATER

GUOYU WANG⁽¹⁾, XIN GUO⁽²⁾ & BING REN⁽³⁾

^(1,2,3) State Key Laboratory of Coastal and Offshore Engineering, Dalian University of Technology, Dalian, P.R. China,
wanggyu@dlut.edu.cn; 1810340513@qq.com; bren@dlut.edu.cn

ABSTRACT

Based on the linear potential wave theory, the scattering of waves normally incident on the submerged T-type breakwater in a channel of finite water depth is investigated. The method of eigenfunction expansions is applied to obtain the unknown constant coefficients determined from the matching conditions. The present mathematical solution is compared with the existing theoretical and experimental results and demonstrates good agreements. The parameters such as the submerged depth of the horizontal plate, the height and the thickness of the vertical plate, those identified with the wave scattering performance of the breakwater are investigated and discussed. The variations of reflection and transmission coefficients along with the above mentioned parameters are also presented.

Keywords: Wave; reflection coefficient; transmission coefficient; T-type breakwater.

1 INTRODUCTION

Breakwaters are applied for the purpose of structure protection, harbor activities and temporary construction in coastal engineering. Compared with the traditional bottom detect breakwaters, some open type breakwaters have generated a great deal of interest in coastal and ocean engineering industry in recent years, with the advantages of material saving, cost reducing and free water exchanging. The open type breakwaters are essentially structures located near the free water surface where the wave energy flux is dominant. They are usually designed to distort orbital motion of the water particles near sea surface, where the amplitudes and velocities of the particle are maximal, thus most of the incident wave energy can be reflected and dissipated. Among the existing open type breakwaters, the research activities for the hydrodynamics performance of the plate-type breakwater, which consists of a single or a combination of multiple plates with different alignments located at various immersion depths in water domain, are in progress for the prevailing of economic and environmental conditions. The typical plate-type breakwaters include a single horizontal plate, twin horizontal plates, inclined plate and T-type barrier, etc.

The theoretical studies have been carried out to analyze the wave propagation over a plate structure. It may be found as the earliest work that Stoker (1957) presented a simple set of analytical solutions to determine the reflection and transmission coefficients of long waves propagating over a plate. Ijima et al. (1970) extended Stoker's analysis to cover the whole spectrum of the incident wave length. For a plate with arbitrary submergence depth, analytical expression of reflection and transmission coefficients for long incident waves were obtained by Siew and Hurley (1977). Using Siew and Hurley's solution, Patarapanich (1984) analyzed the variation of the reflection coefficient versus the plate length and derived the conditions of maximum and zero reflection. Liu and Iskandarani (1991) applied the method of eigenfunction expansions to derive a semi-analytical solution for short-wave groups over a submerged plate with finite thickness. By the same method, Wang and Shen (1999) studied the hydrodynamic performance of multiple plates as a breakwater with numerical method, and found that the factors influencing the wave reflection and transmission are the plate length, submerged depth of the top plate and the gap between plates. The similar study about wave motion over a twin-plate breakwater was carried out by Usha and Gayathri (2005). Cho and Kim (2008) studied the interaction of waves with inclined dual porous plates in the context of two-dimensional linear potential theory and Darcy's law, and the developed theory is verified by both small-scale and full-scale experiments. Evans and Peter (2011) have employed the Wiener–Hopf method and the residue calculus technique to compute the reflection coefficient for semi-infinite and finite submerged horizontal porous plates respectively. Cho and Kim (2013) investigated the transmission of oblique waves by a submerged horizontal porous plate by eigenfunction expansion method. Gayen and Mondal (2016) investigated wave interaction with two symmetric inclined porous plates. The physical quantities were computed using the solutions of two second kind hyper singular integral equations. The numerical estimates for the reflection and the transmission coefficients, amplitudes of the hydrodynamic forces and moments and the wave dissipation coefficient are computed.

Numerical analysis such as the boundary integral method was introduced to solve the submerged plate problem by Liu and Abbaspour (1982) and also Liu and Iskandarani (1991). The finite element method have also been applied to investigate wave propagation past a submerged plate by Patarapanich and Cheong

(1989). Yu and Chwang (1994) applied the boundary-element method to study the performance of a submerged porous plate as a breakwater. Wu et al. (2014) simulated the interaction between surface waves and horizontal plates at water surface by FLUENT CFD software using k- ω turbulence model.

The measurements about the reflection and transmission coefficients of waves from a submerged plate were carried out by Patarapanich and Cheong (1989) for validation of their numerical solutions. Neelamani and Rajendran (2002a; 2002b) experimentally investigated the T-type and \perp -type breakwaters at varying submergence under regular and irregular waves. The experimental studies on the performance of twin-plate and multiple plate breakwater were conducted by Neelamani and Gayathri (2006) and the work for the multiple-plate breakwater are carried out by Wang et al. (2006) respectively. Rao et al. (2009) experimentally explored the wave transmission of a plate at varying inclinations and submergence in regular waves. Other significant experimental results regarding water wave interaction with inclined thin permeable plates are reported in Acanal et al. (2013), Yagci et al. (2014) and Shih et al. (2015).

The research works about the hydrodynamics performance of plate-type breakwaters have been in progress for a long time. Among them, many analytical studies focus on problem of wave interaction with some horizontal, inclined or some vertical plates. In this article, it is derived for the mathematical solution of wave scattering from a submerged T-type structure combined by a horizontal plate and a vertical plate. Especially, in the mathematical model, it is considered the thicknesses not only the horizontal plate but also the vertical plate. By the assumptions of a perfect fluid, and considering the two dimensional motion in xz-direction, the velocity potential in the fluid domain can be expressed appropriately, which means that it is automatically satisfied with both of the free water surface and the structural body surface conditions. Thus, the method of eigenfunction expansions can be applied to obtain the unknown constant coefficients determined from the matching conditions. It is the purpose of this article to determine the reflection coefficient and the transmission coefficient for a prevailing wave climate. The present mathematical solution is compared with the relative theoretical results with good agreements. Additionally, a simple model test is conducted to illustrate that the present model is valid. The hydrodynamic effects of the submergence of the horizontal plate, the height and the thickness of the vertical plate on the wave scattering performance of the structure are investigated and discussed.

2 GENERAL FORMULATION

The submerged T-type breakwater system consisting of an upper horizontal plate and a lower vertical plate is considered in this study. As shown in Figure 1, the incident wave is assumed to be a right-going, small amplitude wave with wave height $H=2A$, frequency ω and wave length L . Cartesian coordinates are employed to define this two-dimensional boundary-value problem. The z axis is directed vertically upwards from an origin on the undisturbed free surface in water of uniform finite depth h . The width of the horizontal plate is denoted by $W_1=2B_1$, and the submerged depth is denoted by h_1 , and the thickness of the horizontal plate is denoted by d_1 . The width of the vertical plate is denoted by $W_2=2B_2$, and the submerged depth is denoted by h_2 , and the thickness of the vertical plate is denoted by d_2 .

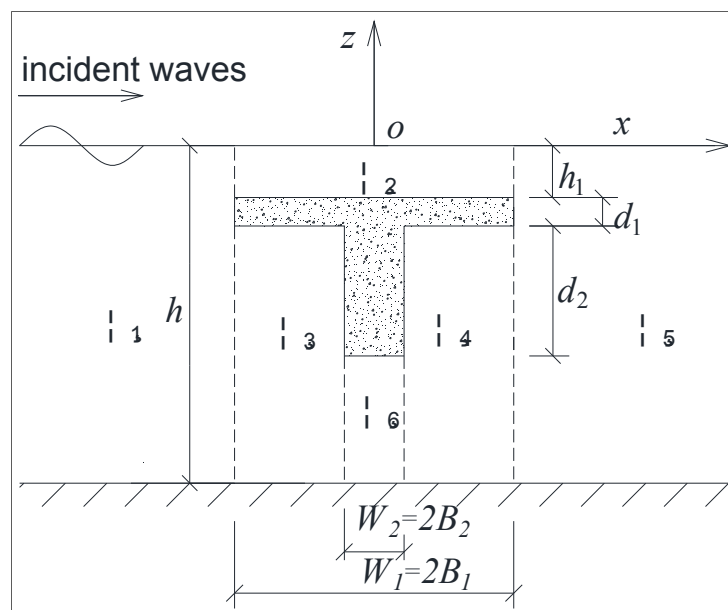


Figure 1. Definition of wave scattering from submerged T-type breakwater.

As shown in figure 1, the fluid domain is divided to the following six sub-domains:

- (1) Ω_1 , where $x < -B_1$ and $-h < z < 0$;
- (2) Ω_2 , where $-B_1 < x < B_1$ and $-h_1 < z < 0$;
- (3) Ω_3 , where $-B_1 < x < -B_2$ and $-h < z < -(h_1 + d_1)$;
- (4) Ω_4 , where $B_2 < x < B_1$ and $-h < z < -(h_1 + d_1)$;
- (5) Ω_5 , where $x > B_1$ and $-h < z < 0$;
- (6) Ω_6 , where $-B_2 < x < B_2$ and $-h < z < -(h_1 + d_1 + d_2)$.

With the usual assumptions of a perfect fluid (the fluid is assumed to be inviscid and incompressible, and the motion is irrotational), the velocity potential:

$$\Phi(x, z, t) = \phi(x, z)e^{i\omega t} \quad [1]$$

satisfies the governing equation:

$$\nabla^2 \phi = 0 \quad [2]$$

and the following conditions:

- (1) The free surface boundary condition:

$$\phi_z(x, z) = \frac{\omega^2}{g} \phi(x, z) \quad \text{at } z = 0 \quad [3]$$

where g is the gravitational acceleration.

- (2) The bottom boundary condition:

$$\phi_z(x, z) = 0 \quad \text{at } z = -h \quad [4]$$

- (3) The plates surface conditions:

$$\frac{\partial \phi}{\partial \mathbf{n}} = 0 \quad \text{at the T plate surface} \quad [5]$$

where \mathbf{n} is the normal direction of the T plate.

- (4) The radiation conditions:

$$\begin{aligned} \frac{\partial \phi_r}{\partial x} &= -ik\phi_r & x &= -\infty \\ \frac{\partial \phi_l}{\partial x} &= ik\phi_l & x &= +\infty \end{aligned} \quad [6]$$

where k is the incident wave number.

- (5) The matching conditions, which require that the potentials and velocities are continuous at the interface of $x = \pm B_1$ and $x = \pm B_2$.

Usually, the above problem can be solved by the matching conditions mentioned above, and it will be explored in detail in the following section.

3 THEORETICAL SOLUTION

As shown in figure 1, the potential velocity in domain Ω_1 can be expressed as:

$$\phi_1(x, z) = -\frac{igA}{\omega} \left[\left(e^{ik_{10}(x+B_1)} + A_{10} e^{-ik_{10}(x+B_1)} \right) Z_{10}(z) + \sum_{n_1=1}^{\infty} A_{1n_1} e^{k_{1n_1}(x+B_1)} Z_{1n_1}(z) \right] \quad [7]$$

where $k_{10}=k$ is the incident wave number, and it is the root of dispersion Eq. [8].

$$\omega^2 = gk \tanh kh \quad [8]$$

and k_{1n_1} ($n_1=1,2,3,\dots$) is the real roots of Eq. [9].

$$\omega^2 = -gk \tan kh \quad [9]$$

and the depth-dependent functions $Z_{1n_1}(z)$ ($n_1=0,1,2,\dots$) are given by:

$$\begin{aligned} Z_{10}(z) &= \frac{\cosh k_{10}(z+h)}{\cosh k_{10}h} \\ Z_{1n_1}(z) &= \frac{\cos k_{1n_1}(z+h)}{\cos k_{1n_1}h} \end{aligned} \quad [10]$$

The above functions satisfy the orthogonal relationship between $[-h, 0]$.

The potential velocity in domain Ω_2 can be expressed as:

$$\phi_2(x, z) = -\frac{igA}{\omega} [A_{20}Z_{20}(z) + \sum_{n_2=1}^{\infty} A_{2n_2}Z_{2n_2}(z) \cosh k_{2n_2}x + B_{20}Z_{20}(z)x + \sum_{n_2=1}^{\infty} B_{2n_2}Z_{2n_2}(z) \sinh k_{2n_2}x] \quad [11]$$

where k_{2n_2} ($n_2=1,2,3,\dots$) is the real roots of Eq. [9].

$$\omega^2 = -gk \tan kh_1 \quad [12]$$

and the depth-dependent functions $Z_{2n_2}(z)$ ($n_2=0,1,2,\dots$) are given by:

$$\begin{aligned} Z_{20}(z) &= \frac{\cosh k_{20}(z+h_1)}{\cosh k_{20}h_1} \\ Z_{2n_2}(z) &= \frac{\cos k_{2n_2}(z+h_1)}{\cos k_{2n_2}h_1} \end{aligned} \quad [13]$$

where k_{20} it is the root of dispersion Eq. [14].

$$\omega^2 = gk \tanh kh_1 \quad [14]$$

and the above functions satisfy the orthogonal relationship between $[-h_1, 0]$.

The potential velocity in domain Ω_3 can be expressed as:

$$\phi_3(x, z) = -\frac{igA}{\omega} [A_{30}Z_{30}(z) + \sum_{n_3=1}^{\infty} A_{3n_3}Z_{3n_3}(z) \cosh k_{3n_3}x + B_{30}Z_{30}(z)x + \sum_{n_3=1}^{\infty} B_{3n_3}Z_{3n_3}(z) \sinh k_{3n_3}x] \quad [15]$$

where k_{3n_3} ($n_3=1,2,3,\dots$) is:

$$k_{3n_3} = \frac{n_3\pi}{h-h_1-d_1} \quad [16]$$

and the depth-dependent functions $Z_{3n_3}(z)$ ($n_3=0,1,2,\dots$) are given by:

$$\begin{aligned} Z_{30}(z) &= \frac{\sqrt{2}}{2} \\ Z_{3n_3}(z) &= \cos k_{3n_3}(z+h) \end{aligned} \quad [17]$$

The above functions satisfy the orthogonal relationship between $[-h, -(h_1+d_1)]$.

In the fluid domain Ω_4 , the potential velocity is same with that in the domain Ω_3 , and it can be expressed as:

$$\phi_4(x, z) = -\frac{igA}{\omega} \left[A_{40} Z_{40}(z) + \sum_{n_4=1}^{\infty} A_{4n_4} Z_{4n_4}(z) \cosh k_{4n_4} x + B_{40} Z_{40}(z) x + \sum_{n_4=1}^{\infty} B_{4n_4} Z_{4n_4}(z) \sinh k_{4n_4} x \right] \quad [18]$$

where k_{4n_4} ($n_4=1,2,3,\dots$) and the depth-dependent functions are same with those in the domain Ω_3 .

In the fluid domain Ω_5 , the potential velocity can be expressed as:

$$\phi_5(x, z) = -\frac{igA}{\omega} \left[A_{50} e^{ik_{50}(x-B_1)} Z_{50}(z) + \sum_{n_5=1}^{\infty} A_{5n_5} e^{-k_{5n_5}(x-B_1)} Z_{5n_5}(z) \right] \quad [19]$$

where k_{5n_5} ($n_5=0,1,2,\dots$) and the depth-dependent functions $Z_{5n_5}(z)$ ($n_5=0,1,2,\dots$) are same with those of k_{1n_1} ($n_1=1,2,3,\dots$) and $Z_{1n_1}(z)$ ($n_1=0,1,2,\dots$) in fluid domain Ω_1 .

And in the fluid domain Ω_6 , the potential velocity is also same with that in the domain Ω_3 , and it can be expressed as: and the depth-dependent functions are same with those in the domain Ω_3 , except that k_{6n_6} ($n_6=1,2,3,\dots$) is:

$$\phi_6(x, z) = -\frac{igA}{\omega} \left[A_{60} Z_{60}(z) + \sum_{n_6=1}^{\infty} A_{6n_6} Z_{6n_6}(z) \cosh k_{6n_6} x + B_{60} Z_{60}(z) x + \sum_{n_6=1}^{\infty} B_{6n_6} Z_{6n_6}(z) \sinh k_{6n_6} x \right] \quad [20]$$

where k_{6n_6} ($n_6=1,2,3,\dots$) is:

$$k_{6n_6} = \frac{n_6 \pi}{h - h_1 - d_1 - d_2} \quad [21]$$

and the depth-dependent functions $Z_{6n_6}(z)$ ($n_6=0,1,2,\dots$) are given by:

$$Z_{60}(z) = \frac{\sqrt{2}}{2} \quad [22]$$

$$Z_{6n_6}(k_{6n_6} z) = \cos k_{6n_6} (z + h)$$

The above functions satisfy the orthogonal relationship between $[-h, -(h_1+d_1+d_2)]$.

In the above Eq. [7], [11], [15], [18], [19] and [20], all of A_{ini} ($i=1,2,\dots,6$), B_{inj} ($j=2,3,4,6$) are unknown coefficients, and they can be obtained by applying the matching conditions that the potentials and velocities are continuous at the interface of $x = \pm B_1$ and $x = \pm B_2$.

4 EXPERIMENTAL SET-UP AND MEASUREMENTS

Experiments for the wave interactions with the submerged T-type breakwater were conducted in the hydraulics laboratory wave flume of the State Key Laboratory of Coastal and Offshore Engineering, Dalian University of Technology, P.R.China. The wave flume dimensions were 22.0 m in length, 0.5 m in width and 0.8 m in depth, as shown in Figure 2. A motor type wave generator was installed at one end of the flume with a computer to generate regular waves of different heights and frequencies, and a wave energy dissipator in the form of porous beach was installed at the other end of the flume to dissipate wave energy.

The proposed submerged T-type breakwater models were constructed of a horizontal plate with width of 0.5 m, and thickness of 0.06 m, and a vertical plate with height of 0.12 m and thickness of 0.06 m. The submergence of the breakwater was 0.1 m. The plates were made of organic glasses. The T-type breakwater model is shown in figure 3(a), and the wave motion over the model is shown in figure 3(b).

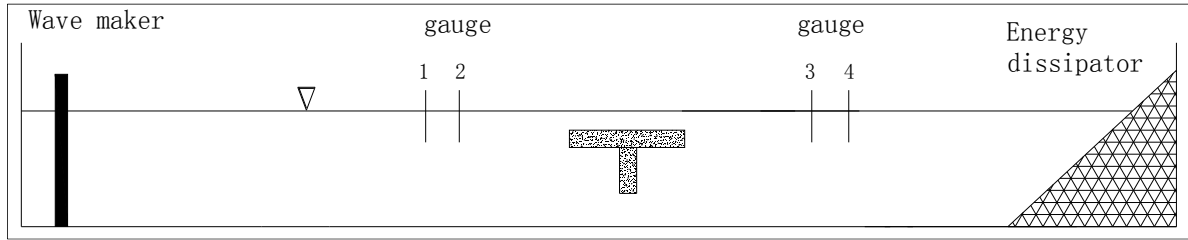


Figure 2. Schematic diagram of experimental set up.



(a) model photo

(b) wave motion over the model

Figure 3. T-type breakwater model in experiments.

The model was located in the middle of the flume, and the water surfaces were measure by four wave gauges, as shown in figure 2. Two gauges were located in the sea side of the model so as to calculate the reflection coefficient by Goda's two points method (Goda and Suzuki, 1976). The transmission waves were measured by the other two wave gauge located in the lee side of the model. The maximum reflection coefficient of the energy dissipator is about 5%, so the reflected waves from the dissipator is negligible.

The experiments were carried out with a constant water depth (h) of 0.40m, and the wave conditions were listed in Table 1.

Table 1. Wave conditions in the experiments.

Water depth	Wave height	Wave period
h (m)	H (m)	T (s)
0.40	0.04	0.80, 0.90, 1.00, 1.15, 1.30, 1.50

5 RESULTS AND DISCUSSIONS

The results of wave scattering from a submerged plate (the thickness is negligible), a submerged plate with certain thickness and experimental data of T-type structure are compared in subsection 5.1. The discussions are presented in subsection 5.2, which are laid on the hydrodynamic effects of the submergence of the horizontal plate, the height and thickness of the vertical plate on reflection and transmission coefficients.

5.1 Results comparison

The proposed mathematical model for T-type submerged breakwater was validated by comparing the results for one limiting case with the results of Wang and Shen (1999). Figure 4 shows the transmission coefficient for a single submerged horizontal thin plate as a function of kB_1 . The plate thickness is 0.0005 m, and it is too small to be taken into account. When d_2 is zero, the vertical plate of the T-type breakwater vanish. Then the T-type breakwater becomes to a single submerged horizontal plate, as presented in Figure 4 by Wang and Shen (1999). It can be seen from the figure that the present theoretical results for a submerged horizontal plate agree well with Wang and Shen's solution.

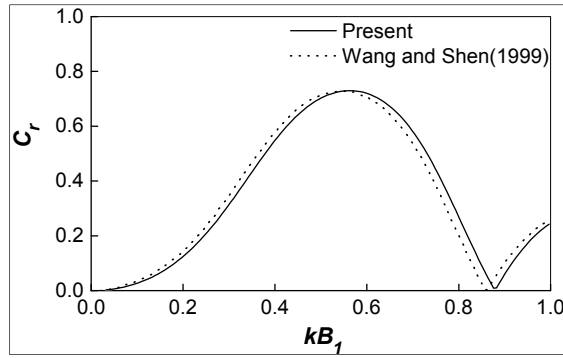


Figure 4. Comparison of present theoretical results (C_r) with Wang and Shen (1999) solution for a submerged horizontal plate.

Furthermore, the present model was also validated by comparing the results for another limiting case with the results of Philip. Liu and Iskandarani (1991). Figure 5 gives the transmission coefficient and reflection coefficient for a submerged horizontal plate with a given thickness. In this figure, the C_r and C_t are plotted as a function of kB_1 . As shown in Figure 5, the results obtained by the present model agree very well with the results of Liu and Iskandarani (1991).

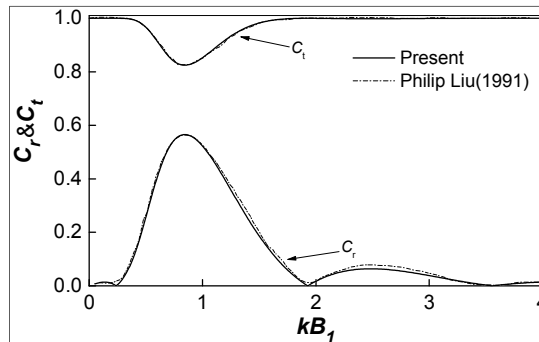


Figure 5. Comparison of present theoretical results (C_r , C_t) with Liu and Iskandarani (1991) solution for a submerged horizontal plate.

The proposed mathematical model was validated also by comparing its results with the experimental data at $H=0.04$ m, which conducted in Section 4. Figure 6 (a) and (b) shows the reflection coefficient and the transmission coefficient for the submerged T-type breakwater as a function of kB_1 , respectively. It can be seen from the comparison that the mathematical results have the same tendency with the experimental data. Yet it should be noticed that the present model results overestimate the magnitudes of the reflection coefficient and the transmission coefficient, comparing with the experimental data. In fact, many wave energy are dissipated because of the turbulence induced shoaling in the model test conducted in Section 4. But it is not taken into account the wave energy dissipation in the present mathematical model. In the model tests, when the incident waves propagate to the submerged T-type structure, with the sudden change of water depth, the horizontal plate of the T-type structure tends to steepen the waves over the plate due to the shoaling and some wave energy are dissipated by turbulence, friction on the plate, and even wave breaking.

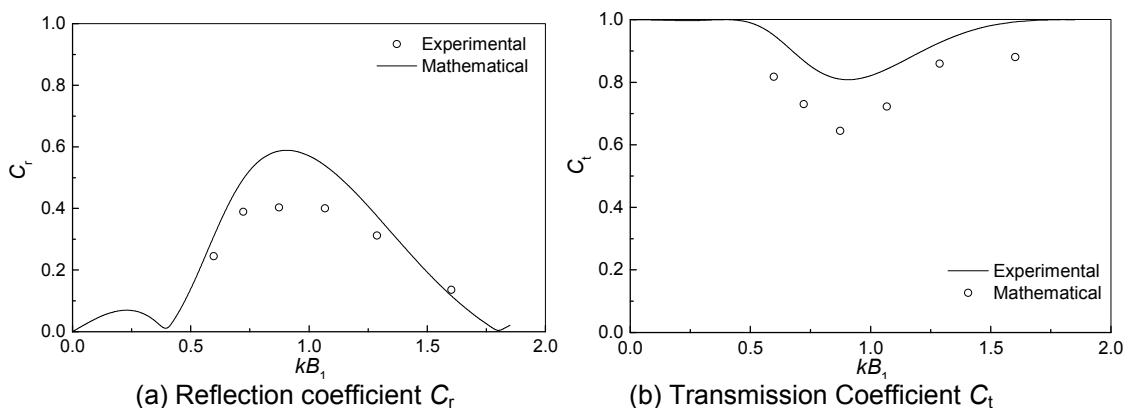


Figure 6. Comparison of present mathematical results (C_r , C_t) with experimental data ($H=0.04$ m, $h=0.4$ m, $B_1=0.25$ m, $d_1=0.06$ m, $B_2=0.03$ m, $d_2=0.12$ m)

5.2 Discussion for wave scattering from submerged T-type breakwater

Based on the mathematical solutions, the effects of the submerged depth, the vertical plate height and the vertical plate thickness on the hydrodynamic properties of the submerge T-type breakwater are examined and discussed in this subsection.

5.2.1 The effect of the submerged depth

Figure 7 shows the effects of the submerged depth of horizontal plate on the wave scattering performance of the breakwater. The relative submersions h_1/h are 0.15, 0.25, 0.35 and 0.45 respectively, the variations of reflection coefficient C_r and transmission coefficient C_t as a function of kB_1 are presented in Figure 7. It is a common phenomenon that the reflection coefficient and the transmission coefficient will vary periodically for a submerged obstacle (Newman, 1965; Mei and Black, 1969; Yu and Chwang, 1994), and the same tendencies appear in figure 7. Moreover, the maximum reflection coefficient is reduced with the increasing of the relative submergence h_1/h , and it is opposite for the maximum transmission coefficient. It can be seen the wave-damping performance of the T-type breakwater is much better when the breakwater gets closer to the free surface of water.

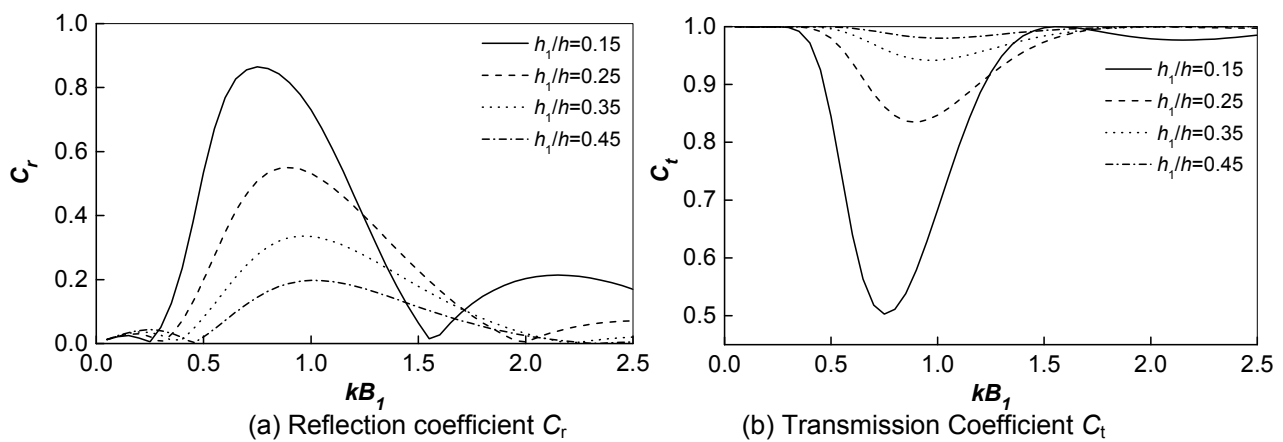


Figure 7. Effects of the relative submersions h_1/h on the reflection coefficient C_r and the transmission coefficient C_t ($h/B_1=2$, $B_1/B_2=5$, $d_1/d_2=0.2$).

5.2.2 The effect of the vertical plate height

Figure 8 shows the effects of the vertical plate height on the wave scattering performance of the breakwater. Similarly, the reflection coefficient and the transmission coefficient vary periodically as a function of kB_1 . But it is an interesting phenomenon that the maximum reflection coefficient C_r increases with the decreasing of the relative vertical plate height d_2/h , and the transmission coefficient C_t is opposite. Obviously, this is not of benefit to a breakwater, as in fact has been implied by Zheng et al. (2000) and Liu et al. (2009) for a submerged rectangular structure. Thus as far as the strength requirement of the plate is satisfied, a thinner plate is more effective in practice, which is also more economical.

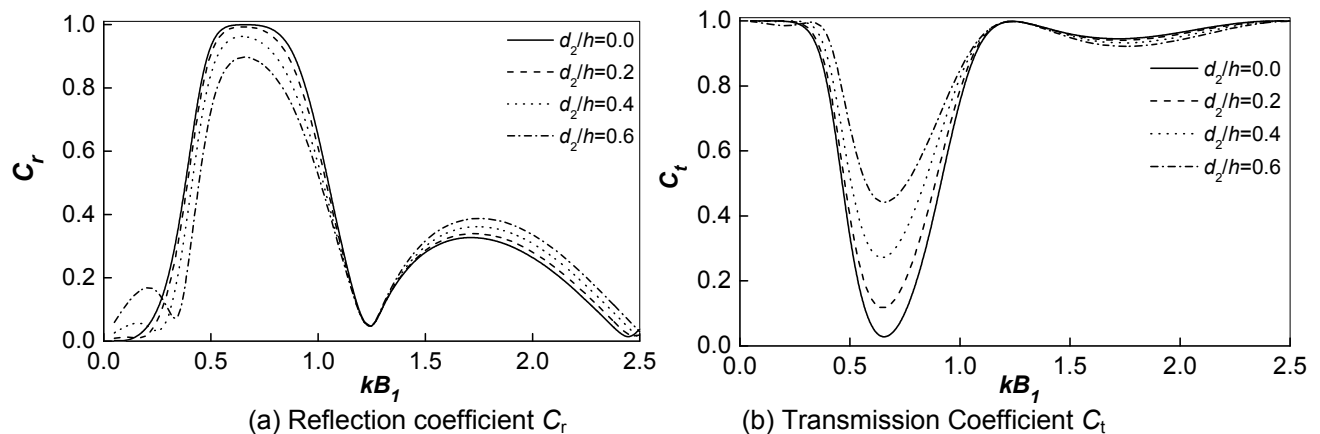


Figure 8. Effects of the relative vertical plate height d_2/h on the reflection coefficient C_r and the transmission coefficient C_t ($B_1/B_2=5$, $B_1/h=0.5$, $h_1/h=0.1$, $h_1/d_1=2$).

5.2.3 The effect of the vertical plate thickness

Figure 9 shows the effects of the vertical plate width on the wave scattering performance of the breakwater. The reflection coefficient C_r and the transmission coefficient C_t are plotted as a function of kB_1 . It can be seen that the maximum reflection coefficient increases with the decreasing of the relative vertical plate thickness, and the minimum transmission coefficient seems to be opposite. When the thickness of the vertical plate increases equal to the width of the horizontal plate, the T-type breakwater becomes to be a submerged plate, which thickness is equal to the sum of d_1 and d_2 . It can be seen that the T-type breakwater has better wave damping performance than the submerged plate with the same total thickness.

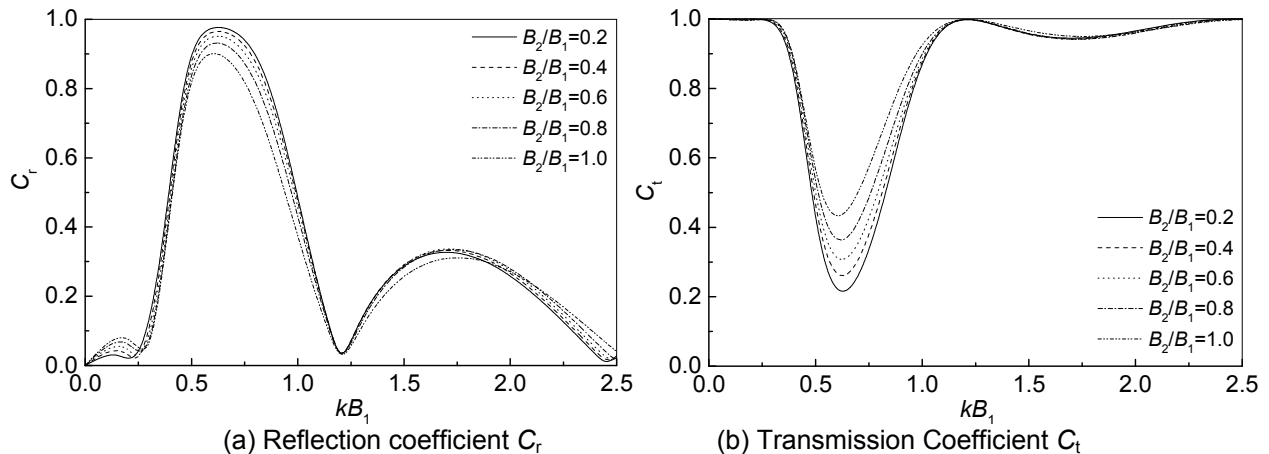


Figure 9. Effects of the relative vertical plate width B_2/h on the reflection coefficient C_r and the transmission coefficient C_t ($B_1/h=0.5$, $h_1/h=0.1$, $d_1/h=0.1$, $d_1/d_2=0.4$).

6 CONCLUSIONS

The wave scattering problem arising from the interaction of linear water waves with a submerged T-type breakwater is mathematically derived in this article. The fluid domain is divided into six parts along the boundary of the breakwater, and the velocity potential is expressed appropriately in each domain. The eigenfunction expansion matching method is applied to obtain the unknown constant coefficients. The analytical expressions for the reflection and transmission coefficients are given and verified. The effects of the submergence of the horizontal plate, the height and the thickness of the vertical plate on the reflection and transmission coefficients are examined, which may provide some important information for engineering designers.

ACKNOWLEDGEMENTS

The research reported herein is funded by National Natural Science Foundation of China under Grant No. 50809015.

REFERENCES

- Acanal, L., Loukogeorgaki, E., Yagci, O., Kirca, V.O. & Akgül, A. (2013). Performance of an Inclined Thin Plate in Wave Attenuation. *Journal of Coastal Research*, 65(sp 1), 141–146.
- Cho, I.H. & Kim, M.H. (2008). Wave Absorbing System using Inclined Perforated Plates. *Journal of Fluid Mechanics*, 608, 1–20.
- Cho, I.H. & Kim, M.H. (2013). Transmission of Oblique Incident Waves by a Submerged Horizontal Porous Plate. *Ocean Engineering*, 61, 56–65.
- Evans, D.V. & Peter, M.A. (2011). Asymptotic Reflection of Linear Water Waves by Submerged Horizontal Porous Plates. *Journal of Engineering Mathematics*, 69(2), 135–154.
- Goda, Y. & Suzuki, Y. (1976). Estimation of Incident and Reflected Waves in Random Wave Experiments. In: *Proceedings of the 10th Coastal Engineering Conference*, ASCE, New York, USA, 828–845.
- Gayen, R. & Mondal, A. (2016). Water Wave Interaction with Two Symmetric Inclined Permeable Plates. *Ocean Engineering*, 124(15), 180–191.
- Ijima, T., Ozaki, S., Eguchi, Y. & Kobayashi, A. (1970). Breakwater and Quay Well by Horizontal Plates. In *Proceedings of the 12th Coastal Engineering Conference* on ASCE, New York, USA, 1537–1556.
- Liu, P.L. & Abbaspour, M. (1982). Wave Scattering by a Rigid Thin Barrier. *Journal of the Waterway, Port, Coastal and Ocean Division*, 108(4), 479–491.
- Liu, P.L. & Iskandarani, M. (1991). Scattering of Short-Wave Groups by Submerged Horizontal Plate. *Journal of the Waterway, Port, Coastal and Ocean Engineering*, 117(3), 235–246.
- Liu, Y., Li, Y.C. & Teng, B. (2009). Wave Motion over Two Submerged Layers of Horizontal Thick Plates. *Journal of Hydrodynamics, Ser.B*, 21(4), 453–462.

- Mei, C.C. & Black, J.L. (1969). Scattering of Surface Waves by Rectangular Obstacles in Waves of Finite Depth. *Journal of Fluid Mechanics*, 38(03), 499-511.
- Neelamani, S. & Gayathri, T. (2006). Wave Interaction with Twin Plate Wave Barrier. *Ocean Engineering*, 33(3), 495-516.
- Neelamani, S. & Rajendran, R. (2002a). Wave Interaction with \perp -Type Breakwaters. *Ocean Engineering*, 29(5), 561-589.
- Neelamani, S. & Rajendran, R. (2002b). Wave Interaction with T-Type Breakwaters. *Ocean Engineering*, 29(2), 151-175.
- Newman, J.N. (1965). Propagation of Water Waves Past Two-Dimensional Obstacle. *Journal of Fluid Mechanics*, 23(1), 23-29.
- Patarapanich, M. (1984). Maximum and Zero Reflection from Submerged Plate. *Journal of the Waterway, Port, Coastal and Ocean Engineering*, 110(2), 171-181.
- Patarapanich, M. & Cheong, H.F. (1989). Reflection and Transmission Characteristics of Regular and Random Waves from a Submerged Horizontal Plate. *Coastal Engineering*, 13(2), 161-182.
- Rao, S., Shirlal, K.G., Varghese, R.V. & Govindaraja, K.R. (2009). Physical Model Studies on Wave Transmission of a Submerged Inclined Plate Breakwater. *Ocean Engineering*, 36(15), 1199-1207.
- Shih, R.S., Weng, W.K. & Chou, C.R. (2015). The Performance Characteristics of Inclined Highly Pervious Pipe Breakwaters. *Ocean Engineering*, 100, 54-66.
- Siew, P. & Hurley, D. (1977). Long Surface Waves Incident on a Submerged Horizontal Plate. *Journal of Fluid Mechanics*, 83(01), 141-151.
- Stoker, J. (1957). *Water Waves: The Mathematical Theory with Applications*. Interscience Publishers, Inc., New York, 60-62.
- Usha, R. & Gayathri, T. (2005). Wave Motion over a Twin-Plate Breakwater. *Ocean Engineering*, 32(8), 1054-1072.
- Wang, K.H. & Shen, Q. (1999). Wave Motion over a Group of Submerged Horizontal Plates. *International journal of engineering science*, 37(6), 703-715.
- Wang, Y.X., Wang, G.Y. & Li, G.W. (2006). Experimental Study on the Performance of the Multiple-Layer Breakwater. *Ocean Engineering*, 33(13), 1829-1839.
- Wu, J.P., Xu, L., Mei, T.L., Yi, S. & Wang, L.Q. (2014). Numerical Simulation of the Interaction between Surface Waves and Horizontal Plates at Free Surface. In *Applied Mechanics and Materials*, 441, 456-460.
- Yagci, O., Kirca, V.O. & Acanal, L. (2014). Wave Attenuation and Flow Kinematics of an Inclined Thin Plate Acting as an Alternative Coastal Protection Structure. *Applied Ocean Research*, 48, 214-226.
- Yu, X.P. & Chwang, A.T. (1994). Water Waves above Submerged Porous Plate. *Journal of Engineering Mechanics*, 120(6), 1270-1282.
- Zheng, Y.H., Liu, P.H. & Shen, Y.M. (2000). On the Radiation and Diffraction of Linear Water Waves by an Infinitely Long Rectangular Structure Submerged in Oblique Seas. *Ocean Engineering*, 34(3-4), 436-450.

NUMERICAL MODELING OF BRAGG REFLECTION OVER SEMI-CIRCULAR SUBMERGED BREAKWATERS

MOHAMMAD KAZEM SHARIFIAN⁽¹⁾ & YOUSEF HASSANZADEH⁽²⁾

^(1,2) School of Civil Engineering, University of Tabriz, Tabriz, Iran,
m.sharifian@tabrizu.ac.ir; yhassanzadeh@tabrizu.ac.ir

ABSTRACT

Breakwaters submerged in the sea have the merits of not affecting coastal environment and allowing water circulation and fish passage. Thus, the submerged breakwaters are often used for providing partial sheltering to coastlines and coastal structures. Semi-circular breakwaters have major merits from the hydrodynamic viewpoint. Nevertheless, there has been little research about these kinds of breakwaters and their engineering performance in wave energy reflection. In this study, characteristics of the Bragg reflection due to multiple semi-circular submerged breakwaters are investigated by 2DV numerical modeling based on Reynolds Averaged Navier-Stokes (RANS) equations. The results show that, high Bragg reflections can be achieved by increasing the number of the breakwaters. The investigation of velocity and turbulent kinetic energy contours show that velocities become larger at the upper side of submerged bars and decrease at the back side which is due to the fact that significant amounts of the incident wave energy is reflected by the Bragg reflection effects. Also, the study of flow physics shows that the amounts of vorticity and vortex generation are very low in case of semi-circular submerged breakwaters.

Keywords: Bragg reflection; submerged breakwaters; reflection coefficient; transmission coefficient; coastline protection.

1 INTRODUCTION

During the past few decades, a considerable amount of research has been conducted on the hydrodynamics of breakwaters due to their importance in coastal engineering, environmental protection, recreation and military operations. Breakwaters play an imperative role in protection beaches from erosion and also in protection of offshore facilities such as floating docks, oil drilling rigs, floating wind turbines and aquaculture facilities near the coastal region. Conventional emerged breakwaters are becoming increasingly unpopular, mainly because of their adverse impact on beach amenity and aesthetic considerations (Ranasinghe and Turner, 2006). In contrast, submerged breakwaters have become ever more popular because, besides reflecting a significant amount of the incident wave energy, they retain the landward flow of water, preserve the ecosystem and maintain attractive esthetics, which is critical to the tourism industry in most coastal areas. As a result, there is a growing tendency in coastal management authorities and government agencies to consider submerged structures for beach protection.

In order to improve the sheltering capability, multiple parallel breakwaters could be built. In this case, when the wave number of the incident wave and the breakwater spacing, D , satisfy the relation of $kD=n\pi$ ($n=1,2,\dots$), the wave reflection will become much more significant (Mei, 1985). This phenomenon is called Bragg resonant reflection and accordingly, the multiple submerged breakwaters are referred to as Bragg reflection breakwaters.

Based on the Bragg resonant reflection mechanism of natural sand bars and sand ripples, Mei et al. (1988) proposed the concept of submerged artificial bars to protect drilling platforms from wave damage in the oil fields of Ekofisk, in the North Sea. Belzons et al. (1988) presented the experimental evidence of the localization of linear waves on a rough bottom in a one-dimensional channel. Conducting experiments on a series of equally spaced submerged breakwaters of rectangular section, Mattioli (1990) investigated the role of the evanescent modes and found that the resonant reflection does not occur only in correspondence with the waves of length twice the wavelength of the Fourier components of the bottom behaviour, but also in correspondence with waves of the same length as the distance between the breakwaters. Bailard et al. (1992) numerically examined the feasibility of using Bragg reflection to protect a beach against storm wave attack. The results show that a Bragg reflection bar field must reflect about one quarter of the incident wave energy to provide a significant measure of storm erosion protection. They found that bar fields with uniform spacing are capable of producing the required magnitude of wave reflection, but lack sufficient bandwidth. They mentioned that bandwidth can be increased by staggering the spacing between the bars; however, this produces a concurrent decrease in wave reflection magnitude. Using numerical modeling, Hsu et al. (2003) indicated that the performance of the Bragg resonance for multiply composite artificial bars can be greatly improved by increasing both the relative bar height and the number of bars with different intervals. The resulting higher-

order harmonic components of the Bragg resonance are shown to be significant and increase the bandwidth of high performance. Cho et al. (2004) conducted a series of laboratory experiments to investigate the strong reflection of regular water waves over a train of rectangular and trapezoidal shaped submerged breakwaters. They found that reflection coefficients of permeable submerged breakwaters are less than those of impermeable breakwaters and recommended the trapezoidal shape for a submerged breakwater in terms of reflecting capability and practical application. Based on the linear wave theory and the improved Biot's theory of poro-elastic media with suitable matching conditions, Lan et al. (2011) obtained an analytical solution for the Bragg scattering of water waves propagating over a series of rectangular poro-elastic submerged breakwaters, as a function of elasticity, permeability and geometry. Zhang et al. (2012) used numerical modeling based on the Volume-Averaged Reynolds-Averaged Navier-Stokes (VARANS) equations and Biot's theory to investigate the wave motion and seabed response around multiple permeable submerged breakwaters, which were subjected to different levels of Bragg reflection. Their results show that the reflection coefficient is highly dependent on the wave period and the configuration/number of arrayed breakwaters. Also, the Wave motion and its induced seabed response around breakwaters can be largely changed due to Bragg reflection and energy dissipation of permeable structures. Karmakar and Guedes Soares (2014) used the least square approximation method to analyze the interaction of the waves with multiple vertically moored bottom-standing flexible porous breakwaters. Liu et al. (2014) proposed analytical solutions for linear long-wave reflection for bars with triangular, rectified cosinoidal and idealized trapezoidal shapes. The results showed that the magnitude of the peak Bragg resonant reflection still depends on the bar number, the dimensionless bar height, and the dimensionless bar width. They also presented three sets of optimal curves to determine the optimal collocation of the three types of artificial bars. Deploying boundary discretization technique, Ouyang et al. (2016) numerically investigated the wave characteristics of Bragg reflections for a train of surface water waves from a series of submerged bottom breakwaters. Their results showed that, high Bragg reflections could be achieved by increasing the number of breakwaters in the train and the height of the breakwaters.

Despite several studies on breakwaters with different shapes, the Bragg reflection of multiple semi-circular breakwaters has not been considered until recently. The submerged semicircular breakwaters were first developed in Japan in the early 90's and are composed of a precast reinforced concrete structure built with a semicircular vault and a bottom slab which is placed on a prepared rubble mound foundation (Yuan and Tao, 2003). The submerged semicircular breakwater has the following major advantages: (1) In contrast to the construction of conventional breakwaters, there is no need for rock filling inside the semicircular structure, which reduces the material cost; (2) There is no in-situ concrete casting work and it is easy to re-lift the erected structure in case of necessity. Also, As long as the prefabricated structure is placed on the rubble foundation, it can bear the attack of waves immediately after installation, making it specifically suitable to rough sea areas; (3) The wave pressure on the semicircular surface passes through the center of the circle, hence no overturning moment is induced by the wave pressure, which is favorable to the soft soil foundations; and (4) The lateral wave force acting on a semicircular breakwater is smaller than that on a vertical breakwater with the same height, which increases the stability against sliding.

Liu et al. (2016) used analytical and experimental methods to examine the Bragg reflection of water waves by multiple submerged semi-circular breakwaters, and gave some significant results for engineering applications. They used analytical solutions based on the wide-spacing approximations to examine the effects of the bar number and radius, and the arrangement of bar spacing. However, their theoretical predictions neglected the role of the viscosity and were based on only considering the reflection coefficients. In the present study, the flow physics, viscous effects of fluid on vortex evolution and turbulent intensity in the vicinity of submerged semi-circular breakwaters under Bragg resonance of water waves are investigated numerically using a model based on RANS equations. The computational results were validated by comparing with analytical and experimental results and the processes of vortex generation and dissipation in the Bragg resonance process are discussed in detail.

2 NUMERICAL MODEL

olaFOAM (Higuera, 2015), the model used in this work, is a newly developed 3D numerical two-phase flow solver specially designed to simulate coastal, offshore and hydraulic engineering processes. Inheriting its basic structure from OpenFOAM, the model solves the three-dimensional Reynolds Averaged Navier-Stokes (RANS) equations for two incompressible phases using a finite volume discretization and the volume of fluid (VOF) method. Turbulence modeling can be included by means of different approaches (RANS, LES and DNS) and a number of models available. The most remarkable features that olaFOAM offers are physically correcting two-phase flow through porous media, wave generation and active wave absorption handled at the boundaries of the domain (no increase in computational cost) and moving-boundary wave generation and absorption to mimic laboratory wave makers of all kinds. Also, the code features other OpenFOAM advanced capabilities, such as dynamic mesh refinement and mesh motion for floating body simulation.

olaFOAM solves the RANS equations for two incompressible phases, and tracks the free surface movement using the VOF technique. They include conservation of mass (Eq. [1]), conservation of momentum (Eq. [2]) and the VOF function advection equation (Eq. [3]) (Higuera et al., 2014):

$$\nabla \cdot \mathbf{U} = 0 \quad [1]$$

$$\frac{\partial \rho \mathbf{U}}{\partial t} + \nabla \cdot (\rho \mathbf{U} \mathbf{U}) - \nabla \cdot (\mu_{\text{eff}} \nabla \mathbf{U}) = -\nabla p^* - \mathbf{g} \cdot \mathbf{X} \nabla \rho + \nabla \mathbf{U} \cdot \nabla \mu_{\text{eff}} \quad [2]$$

$$\frac{\partial \alpha}{\partial t} + \nabla \cdot \mathbf{U} \alpha + \nabla \cdot \mathbf{U}_c \alpha (1 - \alpha) = 0 \quad [3]$$

Where:

- \mathbf{U} is the velocity vector,
- ρ is the density, p^* is the pseudo-dynamic pressure,
- \mathbf{g} is the acceleration of gravity,
- \mathbf{X} is the position vector and,
- $\mu_{\text{eff}} = \mu + \rho \nu_{\text{turb}}$ is the efficient dynamic viscosity,

which takes into account the molecular dynamic viscosity plus the turbulent effects. The solver assumes water and air as incompressible, which is considered a valid assumption in the case study because air behaves as an incompressible fluid on the small-scale.

Eq. [3] describes the movement of the phases (air and water). The solver considers only one single phase function (α), which is defined as the quantity of water per unit of volume at each cell. This statement means that if $\alpha = 1$, the cell is full of water, and, if $\alpha = 0$, the cell is full of air; in any other case, it belongs to the interface. In Eq. [3] \mathbf{U}_c is an artificial compression term used to preserve a sharp interface between air and water.

The pressure-velocity equations are solved by a two-step method called PIMPLE, derived from PISO (Pressure Implicit with Splitting of Operators) and SIMPLE (Semi-Implicit Method for Pressure-Linked Equations). PIMPLE's main structure is inherited from the original PISO, but it allows equation under-relaxation, as in SIMPLE, to ensure the convergence of all the equations at each time step.

The wave generation and active absorption (Higuera, 2015) increase the model range of applications in order to study both coastal and offshore problems. The active absorption implemented is to overcome the limitations of other existing approaches based on the use of artificial damping or relaxation zones to dissipate outgoing waves, increasing the numerical domain and consequently the computational cost. The use of active wave absorption just at the boundaries allows simulation of realistic wave conditions and speeds-up simulations by reducing the computational domains. Moreover, the combined use of wave generation and absorption is necessary to correctly represent the wave transformation in the vicinity of structures, where re-reflected waves are relevant.

3 SIMULATION SETUP AND MODEL VALIDATION

To validate the numerical model, wave data from the physical experiments of Liu et al. (2016) were utilized. The wave tank was 60m long and 3m wide with a wave generator used for wave generation at one end of it. Single and two submerged semi-circular bars were located in the flume as shown in Figure 1. The water surface elevations around the bars were measured by four capacitive-type wave probes.

In order to reduce the computational cost, three different grid resolutions in x-direction were used. In the two ends of the numerical flume, the horizontal grid size was equal to 0.04m, and in the middle section, in the vicinity of the structures, the grid size of 0.01m was chosen. In the vertical direction, the uniform size of 0.01m was adapted. The k- ϵ turbulence model was employed to describe turbulence dynamics and active absorption system was used at the end of the flume. The simulations time was 120s with time step of 0.01s. All the experimental cases and conditions are listed in Table 1. In the experiments, the positions of bar 1 and No. 2 probe were fixed, and the spacing between them was 2.5m.

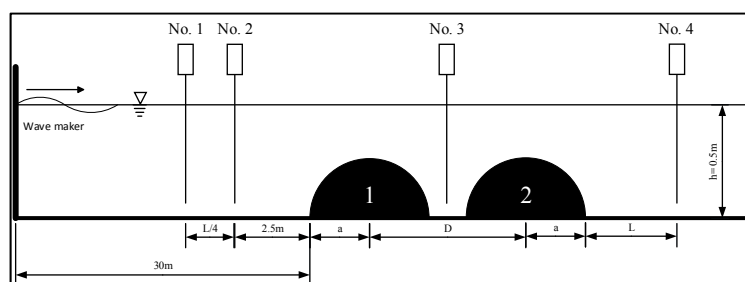


Figure 1. Schematic plot of semi-circular submerged breakwaters.

Table 1. Experimental conditions for model validation.

Cases	Bar numbers	h (m)	a (m)	H (m)	L (m)	T (s)	D (m)
1	One	0.5	0.3	0.0151	1.51	1.0	-
		0.5	0.3	0.0205	2.05	1.2	-
		0.5	0.3	0.0257	2.57	1.4	-
		0.5	0.3	0.0309	3.09	1.6	-
		0.5	0.3	0.0357	3.57	1.8	-
		0.5	0.3	0.0406	4.06	2.0	-
		0.5	0.3	0.0453	4.53	2.2	-
		2	Two	0.5	0.3	0.0151	1.51
0.5	0.3			0.0205	2.05	1.2	0.83
0.5	0.3			0.0257	2.57	1.4	0.83
0.5	0.3			0.0309	3.09	1.6	0.83
0.5	0.3			0.0357	3.57	1.8	0.83
0.5	0.3			0.0406	4.06	2.0	0.83
0.5	0.3			0.0453	4.53	2.2	0.83
0.5	0.3			0.0151	1.51	1.0	1.37
0.5	0.3			0.0205	2.05	1.2	1.37
0.5	0.3			0.0257	2.57	1.4	1.37
0.5	0.3			0.0309	3.09	1.6	1.37
3	Two			0.5	0.3	0.0151	1.51
		0.5	0.3	0.0205	2.05	1.2	1.75
		0.5	0.3	0.0257	2.57	1.4	1.75
		0.5	0.3	0.0309	3.09	1.6	1.75
		0.5	0.3	0.0357	3.57	1.8	1.75
		0.5	0.3	0.0406	4.06	2.0	1.75
		0.5	0.3	0.0453	4.53	2.2	1.75
		0.5	0.3	0.0406	4.06	2.0	0.7~3.2

Figure 2 shows the surface elevation comparison between the measured data (Nos. 1 and 2 probes) and simulated results for case 2 at $T=1.6$ s and $D=1.37$ m. As shown in this figure, the numerical results agree well with the experimental measurements, indicating that the model can accurately simulate wave propagation over submerged breakwaters.

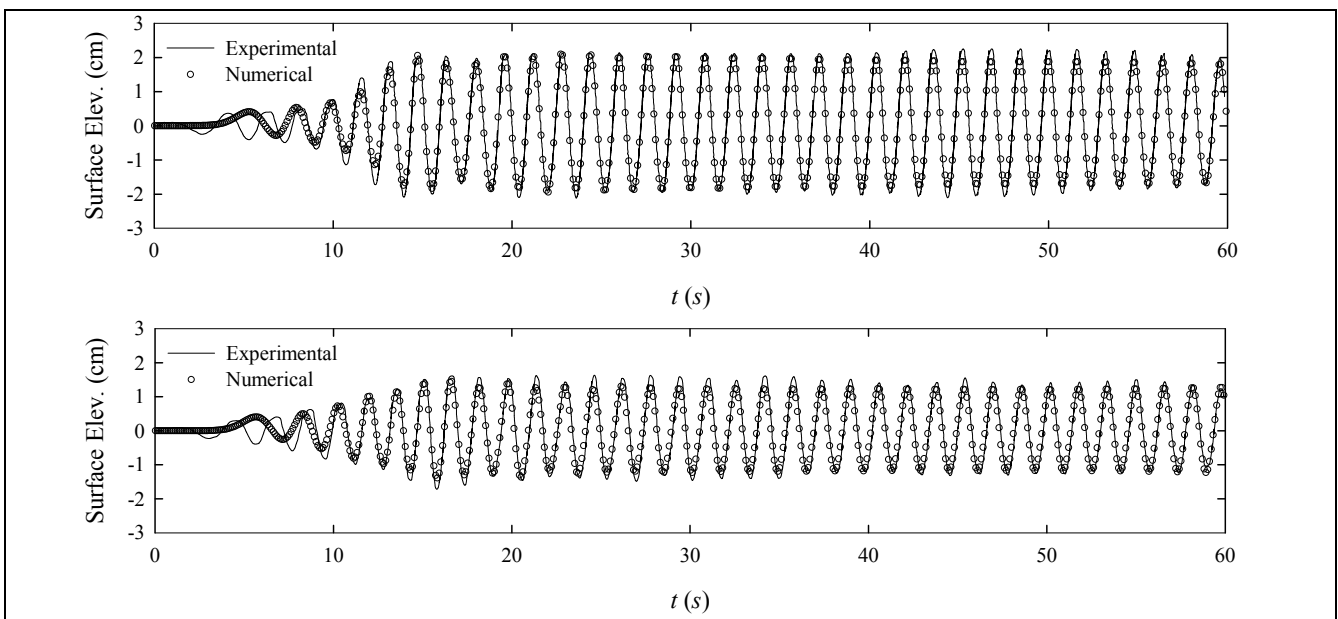


Figure 2. Comparison of water surface elevation between experimental and numerical results for case 2 with $T=1.6$ s and $D=1.37$ m, for probe No. 1 (top) and No. 2 (bottom).

4 RESULTS AND DISCUSSION

4.1 Reflection and transmission coefficients

The wave reflection and transmission coefficients were calculated using a MATLAB code based on the method of Goda and Suzuki (1976). Figures 3-7 show the comparison of the reflection and transmission coefficients for different cases calculated by the present numerical model and analytical and experimental results of Liu et al. (2016).

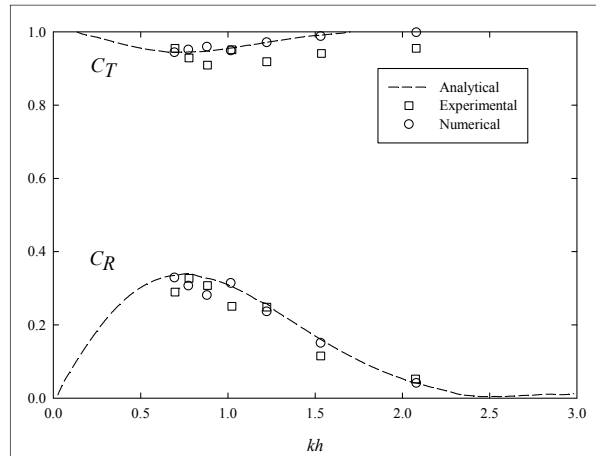


Figure 3. Comparison of reflection (C_R) and transmission (C_T) coefficients resulted from present numerical model with analytical and experimental data of Liu et al. (2016) for case 1.

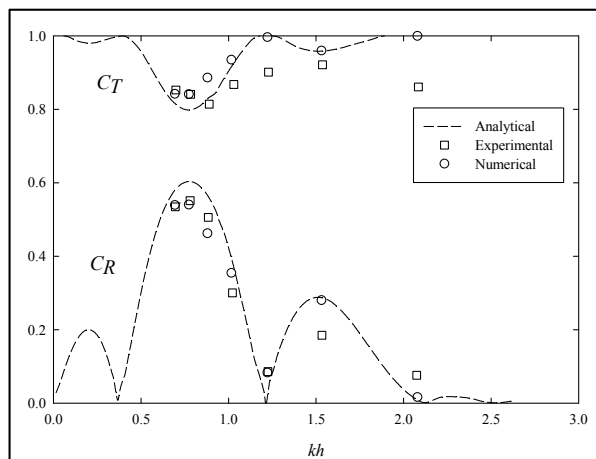


Figure 4. Comparison of reflection (C_R) and transmission (C_T) coefficients resulted from present numerical model with analytical and experimental data of Liu et al. (2016) for case 2 ($D=1.75\text{m}$).

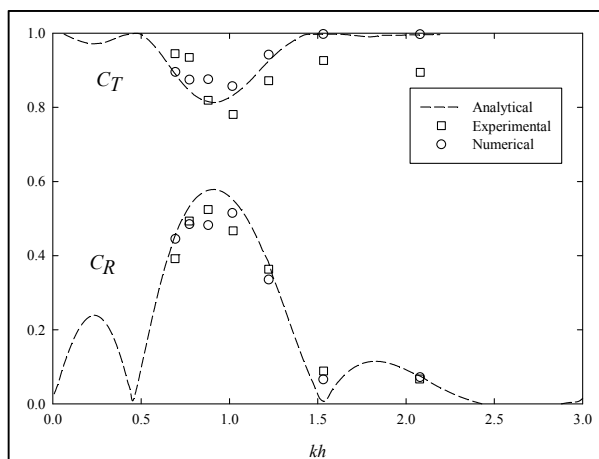


Figure 5. Comparison of reflection (C_R) and transmission (C_T) coefficients resulted from present numerical model with analytical and experimental data of Liu et al. (2016) for case 2 ($D=1.37\text{m}$).

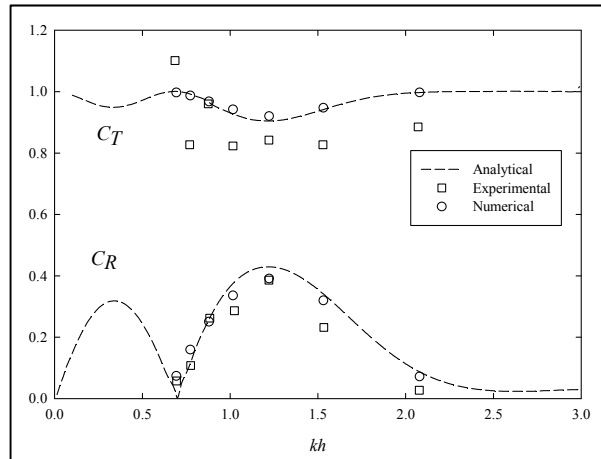


Figure 6. Comparison of reflection (C_R) and transmission (C_T) coefficients resulted from present numerical model with analytical and experimental data of Liu et al. (2016) for case 2 ($D=0.83\text{m}$).

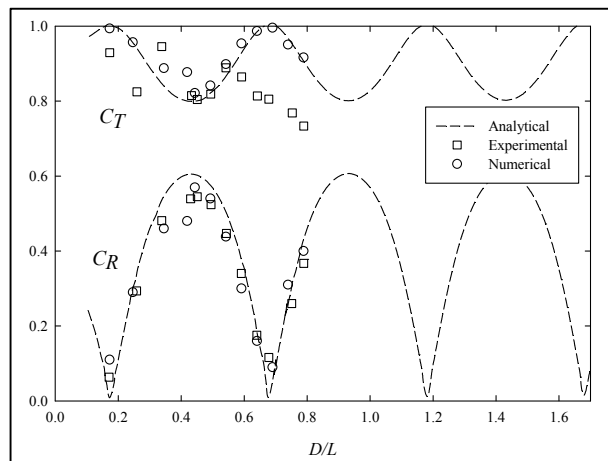


Figure 7. Comparison of reflection (C_R) and transmission (C_T) coefficients resulted from present numerical model with analytical and experimental data of Liu et al. (2016) for case 3 ($T=2.0\text{s}$).

As can be seen in the figures above, the numerical results are in good agreement with the analytical and experimental data. However, the analytical results are slightly larger than the experimental and numerical data because, in contrast to numerical model, the viscous effects of real fluids cannot be modeled by the analytical solution. Figures 4-7 show that the occurrence of resonant reflection by two semi-circular submerged breakwaters is obvious. In Figure 7, the maximum values of the reflection coefficient has a periodic pattern as expected. Also, the amount of the wave reflection in case of two semicircular breakwaters is more than a single breakwater.

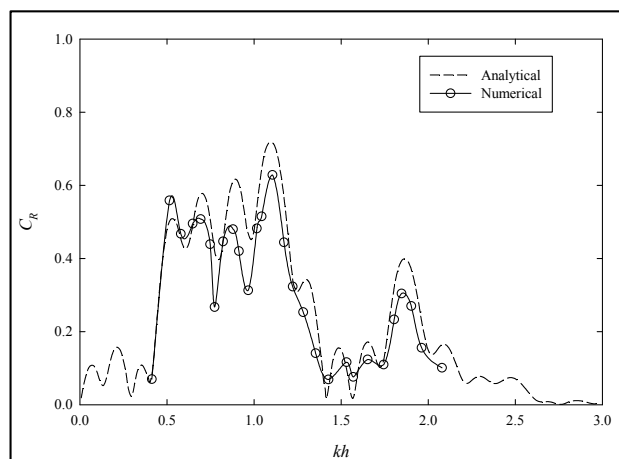


Figure 8. Comparison of reflection (C_R) and transmission (C_T) coefficients resulted from present numerical model with analytical data of Liu et al. (2016) for five bars with different spacing, $D_1=D_2=5h$ and $D_3=D_4=3h$.

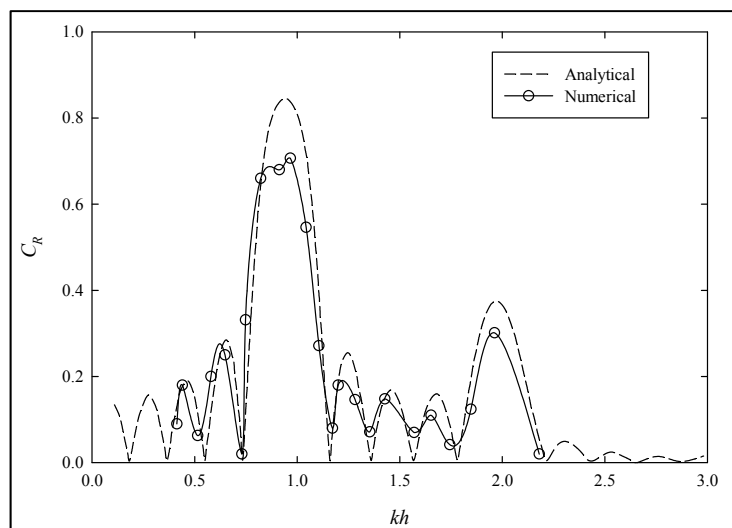


Figure 9. Comparison of reflection (C_R) and transmission (C_T) coefficients resulted from present numerical model with analytical data of Liu et al. (2016) for five bars with identical spacing, $D_1=D_2=D_3=D_4=3h$.

Liu et al. (2016) considered the effect of number of bars, relative bar radius and relative bar spacing using wide-spacing approximations and suggested that considering multiple bars will guarantee better reflections. In order to verify those findings, two configurations with $D_1=D_2=5h$ and $D_3=D_4=3h$ and $D_1=D_2=D_3=D_4=3h$ are simulated using the present model. Figure 8 and 9 show the comparison of the reflection coefficients for two cases with multiple semi-circular bars, calculated by the present numerical model and analytical results of Liu et al. (2016). Similar to conclusion of Liu et al. (2016), our numerical results show that the reflection coefficient of the case with $D_1=D_2=5h$ and $D_3=D_4=3h$ is not less than 0.4 in a very wide range of frequencies ($kh=0.5-1.2$), which is very favorable in practical design of breakwaters, where the coverage of more wave frequencies is important.

4.2 Flow physics

As reported in the literature, wave propagation over submerged obstacle cause the development of a boundary layer over the obstacle surface and could induce formation and shedding of vortices (Hsu et al., 2004). When compared with the surrounding flow fields, a vortex flows faster and imposed greater scouring impact on structures which usually causes damage to the surface of the submerged breakwater or washout to the structure toe. Regarding this problem, the simulation of waves over semi-circular submerged breakwater and the velocity pattern and vortex generation are studied next. The simulations are performed in the case of five bars with different spacing, $D_1=D_2=5h$ and $D_3=D_4=3h$, as the most favorable practical design, based on our previous analysis. The wave period, height and length are equal to $T=1.5s$, $H=0.0284m$ and $L=2.84m$, respectively, corresponding to the case with the highest reflection coefficient of $C_R=0.63$ (See Figure 8).

In order to investigate the flow physics, the wave profile was divided into eight phases, as shown in Figure 10, and the results are studied in these phases.

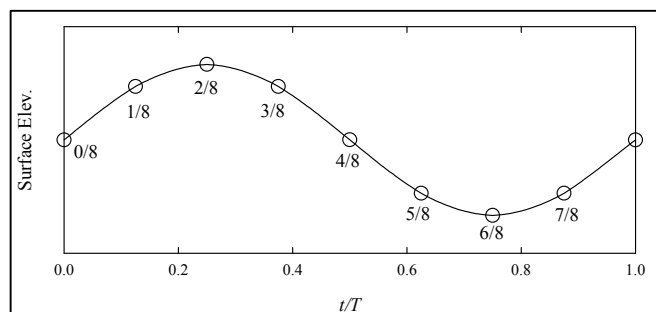


Figure 10. Schematic plot of wave phases.

The numerical results for free-surface elevations along the wave flume at different phases are shown in Figure 11, which obviously shows the wave damping while passing over the submerged bars. Also, Figure 12 shows the velocity contours around the whole five bars. The amount of the velocities decreases considerably after the bars, which is a display of the sheltering performance of the system due to Bragg reflection.

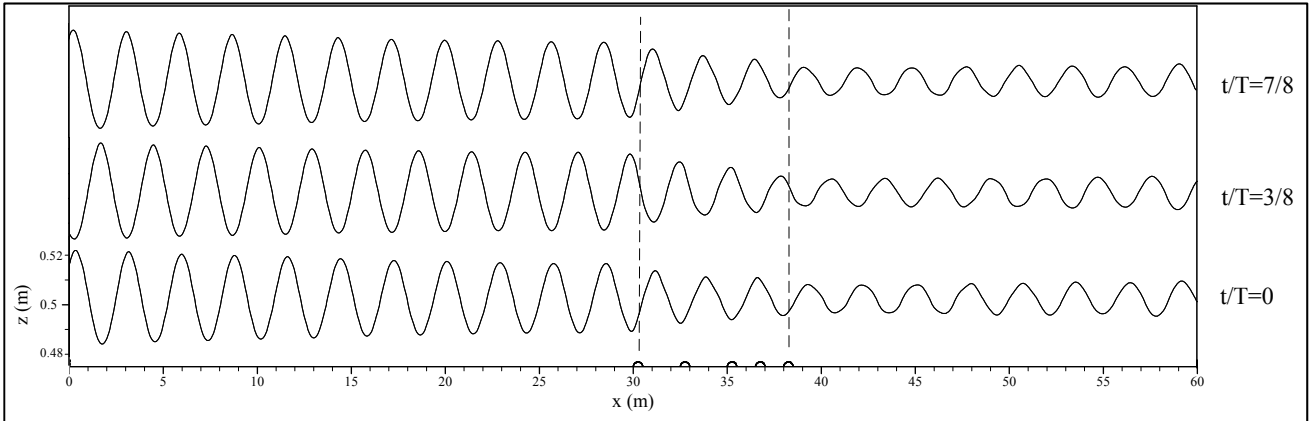


Figure 11. Water surface elevations at different phases.

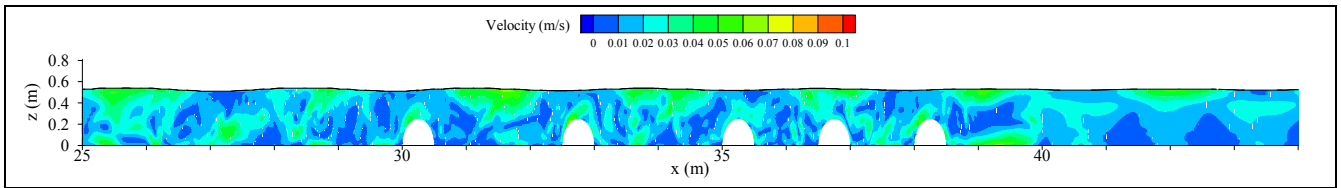


Figure 12. Snapshot of velocity contours at $t/T=7/8$.

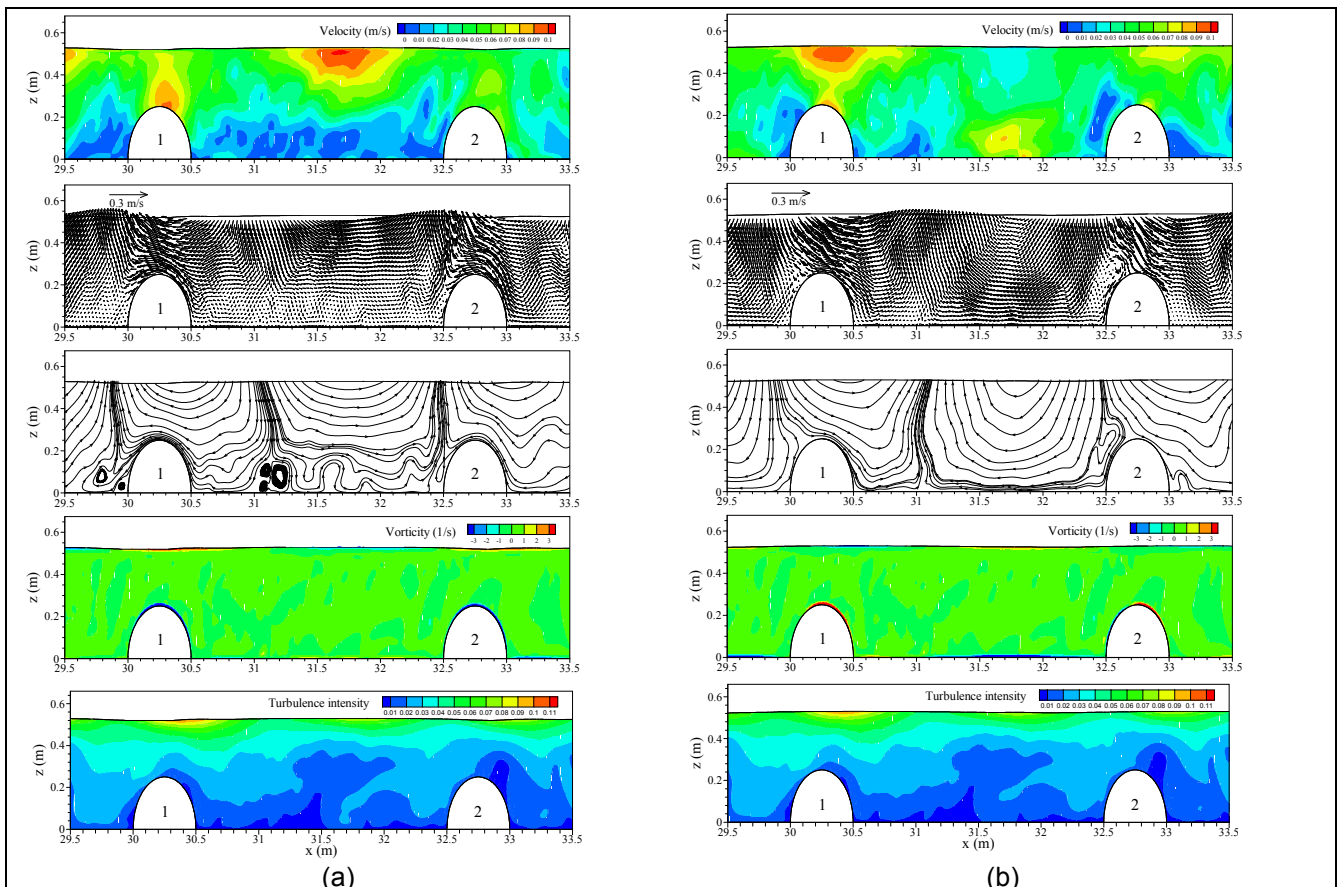


Figure 13. Snapshots of numerical results at (a) $t/T=1/8$ and (b) $t/T=5/8$. From top to bottom: velocity contours, velocity vectors, streamlines, vorticity contours and turbulence intensity contours.

Figure 13 demonstrates the velocity field, streamlines, vorticity contours and turbulence intensity contours obtained from the present numerical model in the vicinity of bars No.1 and No.2 at $t/T=1/8$ (accelerating phase) and $t/T=5/8$ (decelerating phase) phases.

- The vorticity field Ω is calculated based on the formula $\Omega = \partial w / \partial x - \partial u / \partial z$
- Turbulence intensity is defined as $q = (2k)^{1/2}$ where k is the turbulent kinetic energy.

The velocity contours show that the magnitude of velocity increases at the upper side of the first bar and decreases at the back side of the structure. This is caused by the fact that the energy of incident waves is considerably reflected by Bragg reflection effects. The investigation of velocity vectors shows that no major eddies form in vicinity of the semi-circular bars and streamlines are parallel to the surface, conforming the circular shape of the structures. This also confirms the vorticity contours, which shows that amount of vorticity is very low in vicinity of the bars. This is unlike the case of rectangular submerged breakwaters, which have been reported to cause much higher amounts of vorticity on the surface of the submerged structures (e.g. Hsu et al., 2003; 2004). The turbulence intensity contours are also much lower in vicinity of the structures, compared to the surface, which shows the sheltering and reflection effects of the bars.

5 CONCLUSIONS

In the present work, a numerical model based on RANS equations is used to study the hydrodynamic behavior of the Bragg reflection semi-circular submerged breakwaters. The numerical model uses VOF method to track free fluid surfaces and applies a $k-\epsilon$ turbulence closure. First, the numerical results are compared with recent experimental and analytical results. The comparison shows that the numerical model accurately predicts the occurrence of Bragg reflection phenomena when the waves propagate over a series of submerged semi-circular breakwaters. Second, the model is used to simulate and study the Bragg reflection breakwaters from a hydrodynamic point of view. The results show the impacts of Bragg reflection on the velocity and vorticity fields. It is concluded that vorticity and vortex generation are very low in the case of semi-circular submerged breakwaters, which along with other constructional merits, make them an efficient choice to be used as coastal protection structures.

REFERENCES

- Bailard, J.A., DeVries, J.W. & Kirby, J.T. (1992). Considerations in using Bragg Reflection for Storm Erosion Protection. *Journal of Waterway, Port, Coastal, and Ocean Engineering*, 118(1), 62-74.
- Belzons, M., Guazzelli, E. & Parodi, O. (1988). Gravity Waves on a Rough Bottom: Experimental Evidence of One-Dimensional Localization. *Journal of Fluid Mechanics*, 186, 539-558.
- Cho, Y.S., Lee, J.I. & Kim, Y.T. (2004). Experimental Study of Strong Reflection of Regular Water Waves Over Submerged Breakwaters in Tandem. *Ocean Engineering*, 31(10), 1325-1335.
- Goda, Y. & Suzuki, Y. (1977). Estimation of Incident and Reflected Waves in Random Wave Experiments. In *Coastal Engineering 1976*, (828-845).
- Higuera, P. (2015). Application of Computational Fluid Dynamics to Wave Action on Structures, *Ph.D. Thesis*. University of Cantabria.
- Higuera, P., Lara, J.L. & Losada, I.J. (2014). Three-Dimensional Interaction of Waves and Porous Coastal Structures using OpenFOAM®. Part I: Formulation and Validation. *Coastal Engineering*, 83, 243-258.
- Hsu, T.W., Tsai, L.H. & Huang, Y.T. (2003). Bragg Scattering of Water Waves by Multiply Composite Artificial Bars. *Coastal Engineering Journal*, 45(02), 235-253.
- Hsu, T.W., Hsieh, C.M. & Hwang, R.R. (2004). Using RANS to Simulate Vortex Generation and Dissipation Around Impermeable Submerged Double Breakwaters. *Coastal Engineering*, 51(7), 557-579.
- Hsu, T.W., Lin, J.F., Hsiao, S.C., Ou, S.H., Babanin, A.V. & Wu, Y.T. (2014). Wave Reflection and Vortex Evolution in Bragg Scattering in Real Fluids. *Ocean Engineering*, 88, 508-519.
- Karmakar, D. & Soares, C.G. (2014). Wave Transformation Due to Multiple Bottom-Standing Porous Barriers. *Ocean Engineering*, 80, 50-63.
- Lan, Y.J., Hsu, T.W., Lai, J.W., Chang, C.C. & Ting, C.H. (2011). Bragg Scattering of Waves Propagating Over a Series of Poro-Elastic Submerged Breakwaters. *Wave Motion*, 48(1), 1-12.
- Liu, Y., Li, H.J. & Zhu, L. (2016). Bragg Reflection of Water Waves by Multiple Submerged Semi-Circular Breakwaters. *Ocean Research*, 56, 67-78.
- Liu, H.W., Luo, H. & Zeng, H.D. (2014). Optimal Collocation of Three Kinds of Bragg Breakwaters for Bragg Resonant Reflection by Long Waves. *Journal of Waterway, Port, Coastal, and Ocean Engineering*, 141(3), 1-17.
- Mattioli, F. (1990). Resonant Reflection of a Series of Submerged Breakwaters. *Il Nuovo Cimento C*, 13(5), 823-833.
- Mei, C.C. (1985). Resonant Reflection of Surface Water Waves by Periodic Sandbars. *Journal of Fluid Mechanics*, 152, 315-335.
- Ouyang, H.T., Chen, K.H. & Tsai, C.M. (2016). Wave Characteristics of Bragg Reflections from a Train of Submerged Bottom Breakwaters. *Journal of Hydro-environment Research*, 11, 91-100.
- Ranasinghe, R. & Turner, I.L. (2006). Shoreline Response to Submerged Structures: A Review. *Coastal Engineering*, 53(1), 65-79.
- Yuan, D. & Tao, J. (2003). Wave Forces on Submerged, Alternately Submerged, and Emerged Semicircular Breakwaters. *Coastal Engineering*, 48(2), 75-93.
- Zhang, J.S., Jeng, D.S., Liu, P.F., Zhang, C. & Zhang, Y. (2012). Response of A Porous Seabed to Water Waves over Permeable Submerged Breakwaters with Bragg Reflection. *Ocean Engineering*, 43, 1-12.

DYNAMIC RESPONSE OF A VESSEL IN FIXED PIER AND FLOATING PIER

SITHALAKSHMI.S⁽¹⁾, RAHUL DEV.R⁽²⁾, R.PANNEER SELVAM⁽³⁾ & R.SUNDARAVADIVELU⁽⁴⁾

^(1,2,3,4) Ocean engineering Department, IIT Madras, Chennai-600036
sitz1993@gmail.com; rahuldevriitmadras@gmail.com; pselvam@iitm.ac.in; rsun@iitm.ac.in

ABSTRACT

In the recent past, there have been several accidents owing to the failure of mooring lines and excessive movement of the vessel at berth. Proper analysis of the adequacy of vessel's mooring gear, pier's mooring points and the vessel's mooring arrangement is required. In this paper, mooring analysis is conducted on a large LNG vessel named Qmax Mozah. The dynamic responses from the vessel when moored in a conventional fixed pier are compared to that of the responses when the vessel is moored to a floating pier. Planning and simulation tool namely, OPTIMOOR is used to plan mooring arrangements in advance and manage the mooring lines when subjected to a variety of environmental conditions. The forces acting on vessel, forces on QRHs (Quick Release Hooks), fender loads, mooring line loads and the vessel motions for vessel, berth and environmental conditions are found. The analysis is done for the environmental conditions specified by OCIMF (Oil Companies International Marine Forum) guidelines. Based on the analysis, the forces acting on the vessel, forces on QRHs, fender loads, mooring line loads and vessel motions are compared for fixed and floating pier, as well as the optimum conditions for the vessel to operate are recommended.

Keywords: Mooring; wave; tide; fixed pier; floating pier; vessel response.

1 INTRODUCTION

The demand for energy has been increasing in the past decade. Natural gas is an excellent alternative to petroleum. Natural gas is found beneath the seabed and the gas is extracted, liquefied and transported to the required areas. LNG is of significance because it occupies less space when converted to liquid state which makes it easier for storage and transport. LNG is safe and if there is a leakage on the water it is quickly evaporated and causes no harm to the aquatic life forms. Proposal to bring gas from Gulf countries to India through pipelines have been floated and have been sheltered.

The extracted natural gas is transported through the LNG carriers. The safe operation and mooring of vessel in the terminal is essential. Recently many accidents have been reported due to the failure of the mooring lines.

An efficient mooring system is essential for the safety of the ship, the terminal and the environment. Safe mooring requires close cooperation between ship and shore operators and between terminal designers (Schellin et al., 1995). The mooring arrangements for a very large oil tanker comprise of six groups of mooring lines which are head line, fore-breast line, fore-spring line, aft-spring line, aft-breast line and stern line. The mooring lines are distributed and aligned as symmetrical as possible to the centre of gravity of the vessel. Six mooring lines are only used to avoid the congestion in the mooring lines. The spring lines are to be placed as parallel as possible to prevent the vessel from surge motion. The breast lines are placed as perpendicular as possible to the vessel's longitudinal axis to prevent the sway motions. Head and stern lines are used to reduce ship motions overall but its contribution is less (Das et al., 2015). The orientation of berth depends on the environmental conditions and the effects of environmental conditions on the ship. The orientation of berth should be in such a way that the resultant force from wind, waves and currents is minimal on the ship. The dolphin and island type terminals are suitable for the large oil tankers (Apurva et al., 2016).

Floating pier systems are widely used around the world and include elements such as pontoons and mooring piles. The size of container ships is rapidly increasing and capacity of container ships is found to increase and hence an efficient cargo handling system is important. Floating pier is considered as an efficient way to easily modify and upgrade existing ports and harbours to have a dual port cargo handling function. Unloading system is considered as an efficient way to easily modify and upgrade port and harbours if required (Hong et al (2006)). Modular hybrid floating pier (MHP) has higher structural efficiency and durability, lower environmental impact, and better sustainable functionality than a fixed pier. Buildable off site, the MHP is re-locatable, reconfigurable floating structure that adapts to a sea level rise, has higher quality with better material utilization, and provides better operational functionality (Zueck and Wernli, 2010). The mooring line tensions were observed to be lower for floating pier, and it is valuable information for tsunami disaster prevention plans in harbour management for floating bodies, including ships. New measures can be adopted for moored vessels to break free from vessels as well as to mitigate tsunami (Masuda et al., 2013).

2 MOORING ANALYSIS

The prediction of the behaviour of a moored vessel on a timely basis is required which is done by the use of the software namely OPTIMOOR (2012). It enables the operator to make better decisions, resulting in improved performance of the vessel. When the vessel data, berth data are inputted, it finds the forces produced by prevailing environmental conditions. The mooring analysis is done by OPTIMOOR following the OCIMF and PIANC (1995) (Permanent International Association of Navigation Congresses) guidelines which enlists a number of principles based on which the mooring arrangement is arrived. Using this software the behaviour of the vessel in various conditions can be predicted beforehand. OPTIMOOR checks the static or dynamic response of any type of inshore or offshore mooring to wind, current and waves, tide and draft changes, producing clear results very quickly even for the most complex arrangements. The input required includes the vessel data including mooring line properties, fairlead positions and vessel size, as well as the berth data including fender properties. The input data also includes QRH data as well as environment data including wind, wave, current and tide details.

3 ENVIRONMENTAL CONDITIONS

The OCIMF (2008) Mooring Equipment Guidelines (3rd Edition 2012) give a set of environmental conditions for the selection of fenders, QRHs and mooring lines. The environmental conditions specified by OCIMF conditions are:

60 knots wind from any direction simultaneously with

1. 3 knots current at 0° or 180°.
2. 2 knots current at 10° or 170°.
3. 0.75 knots current from the direction of maximum current loading.

The analysis is carried out using the above three conditions specified by OCIMF guidelines incorporating the wave data available at the berth location. The significant wave height of 1.5 m and wave period of 8 s is used along with wind and current. The conditions used for mooring analysis are enlisted as case one to four in Table 1. In case four, wind is considered acting in the transverse direction from land to the vessel and berth. The analysis is carried out for loaded and ballast condition of the vessel in fixed pier and floating pier for High Astronomical Tide (HAT) and Low Astronomical Tide (LAT). The environmental conditions adopted are enlisted below.

Table 1. Environmental conditions.

Case	Wind speed (knots)	Wind direction (°)	Current speed (knots)	Current direction (°)
1	60	0	3	0
2	60	170	2	170
3	60	90	0.75	90
4	60	-90	0.75	90

Wave height = 1.5 m, Wave direction = 14°, Wave period = 8 s

4 DETAILS OF VESSEL, BERTH, FENDER AND MOORING LINES

4.1 Vessel data

Mooring analysis is carried out for the vessel named Qmax Mozah. All the vessel particulars are listed in Table 2. Qmax is the largest LNG carrier in the world. It is a membrane type tank having a carrying capacity of 2, 66,000 m³.

Table 2. Particulars of the vessel.

TYPE	LNG CARRIER
Length Overall	345 m
Length Between Perpendiculars	332 m
Breadth	53.8 m
Depth	27 m
Loaded Draught	12 m
Ballast Draught	9.6 m
Deadweight	1,78,564 t

4.2 Berth data

The berth has four berthing dolphins with double QRHs and six mooring dolphins with triple QRHs. Quick Release Hooks (QRHs) are used instead of bollards. The permissible vessel motions are given by PIANC guidelines. The permissible surge excursion is ± 2 m, permissible sway excursion is +2 m, permissible roll, pitch and yaw is $\pm 2^\circ$, Pier height above datum is 7.5 m for fixed pier and 5 m for floating pier. The heave limit

considered is ± 1 m. Each arm of QRH has an allowable capacity of 150 tonnes. Thus, allowable capacity for double QRHs is 300 tonnes and allowable capacity for triple QRHs is 450 tonnes. 'D' and 'G' are double quick release hooks whereas 'A', 'B', 'I' and 'J' are triple quick release hooks.

4.3 Fender details

The fenders are designed as per IS 4651 part-III (1974). Four SCK 2250 cell fenders, one each at the berthing dolphins of the berth are used here. The maximum reaction force for each fender is 269 t, the maximum allowable deformation is 1.18 m and the rated energy absorption for the fender is 266 tm. The fender panel used here can take pressure upto 20 t/m^2 .

4.4 Mooring line properties

The material of the mooring line is Ultra High Molecular Weight polyethylene (UHMWPE) of diameter 44 mm. The Minimum Breaking Load (MBL) of the wire is 137 t. The tail diameter is 100 mm and the MBL of the tail is 187 t. A factor of safety of two is used for mooring line loads. So the allowable limit for the mooring line loads is up to 50% of its MBL.

5 MOORING ARRANGEMENT

The mooring arrangement is arrived by following the mooring equipment guidelines specified by OCIMF. The mooring arrangement obtained from OPTIMOOR for fixed and floating pier is shown in the Figure 1.

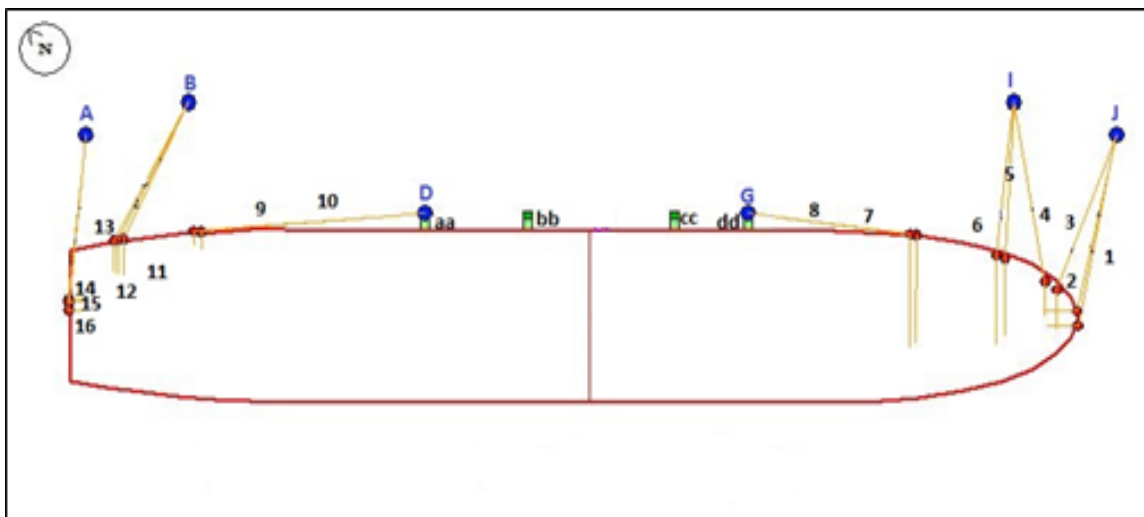


Figure 1. General mooring arrangement plan of Qmax-Mozah for fixed and floating pier.

16 mooring lines are used and they are numbered from 1 to 16. The QRHs are named alphabetically from A-J. The lines 7 and 8 are forward spring lines moored to QRH 'G' located on berthing dolphin and 9 and 10 are aft spring lines moored to QRH 'D' located on berthing dolphin. The lines 4, 5, 6 are forward breast lines moored to QRH 'I' located on mooring dolphin and 11, 12, 13 are aft breast lines moored to QRH 'B' located on mooring dolphin. 14, 15, 16 are aft breast lines moored to QRH 'A' and 1, 2, 3 are forward breast lines moored to QRH 'J'. The fenders on each of the berthing dolphins are named as aa, bb, cc and dd.

6 RESULTS AND DISCUSSIONS

The mooring analysis is carried out for the environmental conditions specified by OCIMF guidelines incorporating the wave data at the site for the loaded and ballast conditions of the vessel in the fixed and floating pier for HAT and LAT condition.

6.1 Mooring line loads and forces on QRH

The mooring line loads and the forces acting on the QRHs when vessel is moored to the fixed pier and floating pier are obtained for the given mooring arrangement for ballast and loaded condition. Mooring line load includes line tension and percentage strength for mooring lines.

The Table 3 provides the mooring line forces and the forces in QRHs for the vessel considering the tidal variations for the two loading conditions and for the two piers. For case one, the tension and the percentage strength of mooring lines is maximum for the line 2 and 3 for ballast and loaded condition respectively. For case two, the tension and the percentage strength of mooring lines is maximum for the lines 4 and 2 for ballast and loaded condition respectively. For case three, the tension and the percentage strength of mooring lines is maximum for lines 1 and 2 for ballast condition and mooring line 2 for loaded condition. For case four,

the tension and the percentage strength of mooring lines is maximum for the aft breast line 14 for both ballast and loaded condition. The mooring line loads are not exceeding the allowable limit and are within the MBL for case one to three. For case four, when the wind is from the beam sea direction, the strength of the mooring lines are exceeding 50% limit. Thus these mooring lines are failing for both the loaded and ballast condition. Line tension in floating pier is significantly higher than that in fixed pier by 1%-14%.

The forces acting on QRHs are within their allowable capacity for all the cases considered here. The forces acting on the QRH when moored to floating pier is higher than that when the vessel is moored to fixed pier in the range of 1%-5%. In case four, the forces acting on the QRH are high since the mooring lines are loaded maximum. Since the mooring lines makes larger vertical angle for floating pier compared to fixed pier, the mooring forces will be higher for floating pier. So the mooring line exerts higher pull on the QRHs when moored to floating pier compared to that of fixed pier.

Table 3. Mooring Line Loads and Forces on QRH.

			Max QRH force		Max Mooring line load			
					Fixed		Floating	
			Fixed	Floating	T(t)	S (%)	T(t)	S (%)
Case 1	B	HT	84.9	85.1	42.9	31	43.1	31
		LT	84.6	85.4	42.7	32	43.4	32
	L	HT	90.5	92.1	43.3	32	43.6	32
		LT	87.6	92.8	43	31	44	32
Case 2	B	HT	111.9	112.1	57	42	57.3	42
		LT	111.3	112.7	56.3	41	57.6	42
	L	HT	107.2	107.7	54.3	40	54.7	40
		LT	106.7	107.6	53.8	39	54.8	40
Case 3	B	HT	43.5	43.6	15.2	11	15.3	11
		LT	42.4	43.4	14.7	11	15.3	11
	L	HT	50.9	51.1	16.9	12	16.9	12
		LT	45.9	51.8	15.7	11	18	13
Case 4	B	HT	233.9	234.2	80.1	58	80.5	59
		LT	232.7	234.2	79.3	58	80.9	59
	L	HT	229.8	232	78.3	57	79.3	58
		LT	224.2	231.7	76	56	79.6	58

B- Ballast condition, L-Loaded condition, HT-High Tide, LT-Low Tide, H-Total horizontal force, T-Tension, S-Strength

6.2 Fender forces and forces on the vessel

The fender forces, fender compression, wave force and wind force in the longitudinal and transverse direction for the various vessel loading conditions and tidal conditions are in Table 4. For the case one to case three, the vessel is in contact with the fender panel, so the vessel exerts forces on the fender and fender panel.

For case four, since wind is acting from land to sea, there won't be any contact between the vessel and fender. The maximum compression of fender obtained is 0.39 m when the wind is acting normal to the vessel, which is below the permissible limit of 1.18 m.

The pressure on the fender panel is exceeding the allowable limit i.e. 20 t/m² for case three and case four. The vessel should be moved out of the berth for higher wind speed for case three and four, since the wind is acting normal to vessel and the total force acting on the vessel is the maximum.

The forces exerted by the wave, wind and current on the vessel remains same for both the type of piers. It can be seen that the force acting in the transverse direction of the vessel is more than that in the longitudinal direction. The forces on the vessel remain the same for both the type of piers. The positive sign denotes that the movement of current or wave or wind is towards the berth and the negative sign denotes that movement is away from the berth. The wind forces on the vessel in ballast condition are more than that when the vessel is in loaded condition because the exposed windage area of the vessel is more. In case four, the current forces are higher in case of loaded condition due to less underwater clearance of the vessel. The total force acting on the vessel is more for the ballast condition than the loaded condition for all the cases.

Table 4. Comparison of forces on fenders and Forces on the vessel.

			Max. Fender Force			Wave force		Wind force		Current force				
			Fixed pier		Floating pier	Fixed and floating pier								
			F (t)	P (t)	C (m)	F(t)	P(t)	C(m)	LD(t)	TD(t)	LD(t)	TD(t)	LD(t)	TD(t)
Case 1	B	HT	86	8.2	0.11	90	8.5	0.12	3.6	7.8	110.5	-0.2	14.9	-0.3
		LT	84	8	0.11	89	8.5	0.12	3.6	8.1	110.5	-0.2	14.9	-0.3
	L	HT	89	8.4	0.11	88	8.4	0.11	4.7	8.7	102.3	-0.2	18.2	-0.5
		LT	91	8.7	0.12	90	8.6	0.12	4.6	9.2	102.3	-0.2	17.9	-0.6
Case 2	B	HT	91	8.7	0.12	95	9.1	0.12	3.6	7.8	-98.5	101.4	-9.5	16.3
		LT	89	8.5	0.12	95	9.1	0.12	33.6	8.1	-98.5	101.4	-9.5	16.9
	L	HT	101	9.6	0.13	101	9.6	0.13	4.7	8.7	-91.2	93	-10.5	32.5
		LT	105	10	0.14	105	10	0.14	4.6	9.2	-91.2	93	-10.1	34.9
Case 3	B	HT	226	21.7	0.38	227	21.5	0.39	3.6	7.8	-2.1	629.8	-0.2	21.4
		LT	225	21.7	0.38	227	21.4	0.39	3.6	8.1	-2.1	629.8	-0.2	21.7
	L	HT	219	20.8	0.36	219	20.8	0.35	4.7	8.7	-1.9	577.3	-0.2	35.9
		LT	220	21	0.36	220	21	0.36	4.6	9.2	-1.9	577.3	-0.1	40.2
Case 4	B	HT	Free	Free	Free	Free	Free	Free	3.6	7.8	-2.1	-629.8	-0.2	21.4
		LT	Free	Free	Free	Free	Free	Free	3.6	8.1	-2.1	-629.8	-0.2	21.7
	L	HT	Free	Free	Free	Free	Free	Free	4.7	8.7	-2	-577.3	-0.2	35.9
		LT	Free	Free	Free	Free	Free	Free	4.6	9.2	-2	-577.3	-0.1	40.2

F-Fender Force, P-Pressure, C-Compression, LD-Longitudinal Direction, TD-Transverse Direction

6.3 Vessel response

Table 5 enlists the vessel motion in all six degrees of freedom is recorded for both the fixed and the floating pier considering the high tide and low tide. The vessel motions are within permissible surge of ± 2 m and permissible sway limit of +2.0 m, permissible roll, permissible pitch and permissible yaw of $\pm 2^\circ$ as specified by PIANC. The angular motions (Roll, pitch and yaw) and heave remains same for all the cases irrespective of the vessel and site condition. For case four, when the wind is acting from the land to vessel, the sway motion is negative and is the maximum.

Table 5. Comparison of vessel motion.

			Vessel motions (m)				Vessel motions ($^\circ$)			
			Surge Fixed	Surge Float	Sway Fixed	Sway Float	Heave Both	Roll Both	Pitch Both	Yaw Both
Case 1	B	HT	-0.67	-0.68	0.11	0.11	0.1	0.2	0.1	0
		LT	-0.66	-0.69	0.11	0.10	0.1	0.2	0	0
	L	HT	-0.62	-0.62	0.08	0.08	0.1	0.1	0.2	0
		LT	-0.60	-0.62	0.08	0.08	0.1	0.1	0.1	0
Case 2	B	HT	1.41	1.42	0.11	0.11	0.1	0.2	0.1	0
		LT	1.39	1.43	0.10	0.10	0.1	0.2	0.0	0
	L	HT	1.31	1.32	0.09	0.09	0.1	0.1	0.2	0
		LT	1.30	1.33	0.09	0.09	0.1	0.1	0.1	0
Case 3	B	HT	0.21	0.21	0.32	0.32	0.1	0.2	0.1	0
		LT	0.21	0.21	0.31	0.31	0.1	0.2	0.0	0
	L	HT	0.21	0.21	0.27	0.27	0.1	0.1	0.2	0
		LT	0.21	0.21	0.28	0.27	0.1	0.1	0.1	0
Case 4	B	HT	1.2	1.21	-1.18	-1.2	0.1	0.2	0.1	0
		LT	1.19	1.22	-1.18	-1.22	0.1	0.2	0	0
	L	HT	1.08	1.09	-1.04	-1.05	0.1	0.1	0.2	0
		LT	1.07	1.09	-1.02	-1.05	0.1	0.1	0.1	0

7 CONCLUSIONS

On comparing the dynamic response of a vessel when moored to a fixed pier to that when it is moored to floating pier for an LNG vessel, the following conclusions can be made.

- The line tension in floating pier is significantly higher than that in fixed pier by up to 1%-14%, since the mooring line makes large vertical angles for floating pier.
- Forces on QRHs in floating pier are 1% to 5% higher than that of fixed type, since the mooring lines are loaded maximum in floating pier.

- In both loaded and ballast condition, forces acting on vessel and fender compression remains almost same when the vessel is moored to fixed pier and floating pier. This is due to the fact that the effective contact area with the fender panel remains same for both fixed and floating pier.
- The maximum obtained fender compression is 0.39 m, which is within the permissible compression of 1.18 m and is obtained when the wind is acting from the sea to vessel (90°).
- The fender forces are obtained for the first three cases only. For the fourth case, i.e. where wind is acting from land to vessel, the fender forces becomes zero since there is no contact of the fender with the berth.
- The pressure on the fender panel is exceeding the allowable limit i.e. 20 t/m² for case three and case four. The vessel should be moved out of the berth for higher wind speed for case three and four, since the wind is acting normal to vessel and the total force acting on the vessel is the maximum.
- The forces acting on the vessel when moored to fixed pier and floating pier remains the same since the windage area under water clearance and under water area remains the same.
- The forces acting in the transverse direction of the vessel is more than that in the longitudinal direction for cases three and four.
- Wind force in the ballast condition is more than that in the loaded condition since the exposed area of the vessel in case of ballast condition is more.
The current force is higher in case of loaded condition due to less underwater clearance of the vessel.
- The total force acting on the vessel is more for the ballast condition than the loaded condition for all the cases, since the wind forces contributes higher to the total force acting on the vessel than the wave and current forces.
- The surge response for floating pier is higher than the fixed pier, the sway response for floating pier is marginally higher than the fixed pier in certain cases. The angular motion and heave response is same for both fixed and floating pier.

The proposed mooring arrangement is found to be suitable for both the type of pier for all the first three OCIMF cases, but for the fourth case, where wind is acting in the beam sea direction from land to sea, the mooring lines are experiencing maximum loads. The critical cases are hence analysed and found. The vessel responses, fender forces, mooring line tensions and the QRH forces obtained are not same when the vessel is moored to fixed pier and floating pier. The responses of both the type of piers in several loading conditions and tidal conditions are also compared. The pattern of response of both the type of piers is studied. Floating pier is experiencing higher QRH force, fender forces and mooring line loads than the fixed pier. It is observed that the vessel motions namely surge and sway response is higher for floating pier.

The mooring forces and the vessel motions are within permissible limit as prescribed by PIANC guidelines, thus the proposed arrangement is found to be suitable for the vessel. In this paper, the dynamic response of the vessel is computed in terms of vessel motions, mooring line loads, QRH forces and pressure on fender. The mooring line loads and QRHs forces are higher for floating pier compared to fixed pier for the given site conditions analysed here for the given site conditions analysed here. For the berth location conditions analysed here, fixed pier is found to be advantageous compared to floating pier. In general, these days floating pier are used. Since the floating pier has found to be advantageous over the fixed pier in several aspects and also lately, floating pier is often used, here in this paper the dynamic responses of the vessel when moored to the fixed pier are compared to that of the responses from the vessel when it is moored to floating pier.

REFERENCES

- Apurva, K., Vidula, S. & Sadhana, K. (2015). Mooring System for Very Large Ships at Berth. *International Journal of Current Engineering and Technology*, 6(4), India.
- Das, S.N., Kulkarni, S. & Kudale, M.D. (2015). Design of Safe Mooring Arrangement for Large Oil Tankers. *8th International Conference on Asian and Pacific Coasts (APAC 2015)*, 528 – 534.
- Hong, E.T. & Chen, H.C. (2006). A Feasibility Analysis of a Floating Pier. *Proceedings of the Sixteenth International Offshore and Polar Engineering Conference*. San Francisco, California, USA, 1-7.
- Masuda, K., Ikoma, T., Masuda, S. & Kazuki, M. (2013). Fundamental Research on the Behaviour of Floating Vessels Moored to Floating Piers in Tsunami. *Proceedings of the ASME 32nd International Conference on Ocean, Offshore and Arctic Engineering*. Nantes, France, 1-6.
- OCIMF. (2008). *Mooring Equipment Guidelines (MEG3), 3rd Edition*, Witherby Seamanship International, UK, 292.
- OPTIMOOR. (2012). *Mooring Analysis Computer Program Users Guide*, Tension Technology International, Morristown, NJ, 130.

- PIANC. (1995). *Criteria for Movements of Moored Ships in Harbours: A Practical Guide*, Report of Working Group No.24, Permanent Technical Committee II, Brussels.
- Schelfn, T.E., & Østergaard, C. (1995). The Vessel in Port: Mooring Problems. *Marine structures*, 8(5), 451-479.
- Indian Standard, IS. (1974). *IS 4651 Part 3: Code of practice for planning and design of port and harbours*, India.
- Zueck, R.F. & Wernli, M. (2010). Development and Qualification of a Floating Pier for the US Navy Fleet. In *Ports 2010: Building on the Past, Respecting the Future*, 1344-1353.

TECHNOLOGY OF ICE PIER CONSTRUCTION: STATE-OF-THE-ART AND FUTURE

HERY RUSTANTO⁽¹⁾

⁽¹⁾ Master of Offshore and Coastal Engineering, Far Eastern Federal University (FEFU), Vladivostok, Russia
h.rustanto@gmail.com

ABSTRACT

In the Arctic and Antarctic area, there are some places inhabited either as research areas (station centers) or small towns. The areas are covered with ice almost all year around, those places need means of transportation to ensure population access for their needs. Since road transportations in some places are impossible to be developed due to lack of supporting facilities and high construction cost, port will be an alternative measure. To date, there is McMurdo station—the first (and the only) man made ice pier to assist ship unloading in Antarctic. This study analyzes an improved method on the utilization of ice as material for pier, especially in polar region. The construction method of McMurdo station will be used as a basis of analysis in this study. Then, by adopting the method utilize in ice bridges and ice building, this study suggests an improvement on the strength of ice as a material for a pier. The purpose of this improvement method is to have a reliable, safe, inexpensive, and easy construction process. This study finds that reinforcing ice with pykrete and geogrid, adopting sandwich type of ice composites (multi layers) during constructing process, and the utilization of columnar grain ice, pressurized pipe and dynamic absorber will create stronger structure of ice pier than the one in McMurdo ice pier station. Furthermore, this study suggested steps in the construction of ice pier with improved method.

Keywords: Arctic; Antarctic; construction; ice pier; McMurdo Station.

1 INTRODUCTION

Even though the Arctic and Antarctic areas are covered with ice almost all year round, there are some places inhabited either as research areas (station centers) or small towns around the Arctic Circle in Northern coast of Canada, Alaska, Russia and Scandinavian countries. Those places need means of transportation to ensure population access to their needs. Since road transportations in some places are impossible to be developed—due to lack of supporting facilities and high cost of construction, a port will be an alternative mode of transportation with more reliable and low construction cost.

There are some advantages of using ice as material in pier construction. The availability of abundance of materials makes the construction of ice pier economical and easy. However, its weaknesses are limited load that can be borne, high dependency on temperature (the lower the temperature, the stronger the ice), and has probability of damage because of wave or storm. Therefore, further experiments are needed to define ice strength to avoid ice pier damage. To date, there are still limited researches on this area.

The purpose of this study is to analyze and suggest an improved method towards the utilization of ice as material in pier, especially in polar region. The construction method of McMurdo station—which uses less reinforcement—will be used as basis of analysis in this study. McMurdo station Ice pier was strong but it is only for limited load carriage. By adopting the concept of Ice Bridge and Ice Building in various studies, this study gives improved method to increase the strength of Ice as material for a pier. The study is organized as follows. The next session explains literature review on sea ice properties, ice strength, and various structural applications which use ice as material. Research methodology is explained in Section three, while Section four discusses method to improve ice strength through reinforcement on ice based weaknesses of McMurdo Ice pier. Finally, section five is conclusion.

2 LITERATURE REVIEWS

2.1 Sea Ice Properties

The atomic structure of ice crystal comprised of repeating tetrahedral coordination of oxygen atoms, in which each oxygen atom is connected by hydrogen bonds to four others oxygen atoms. Figure 1 shows the arrangement of atoms in ice, both through c-axis perspective (Figure 1a) and basal-plane layers (Figure 1b).

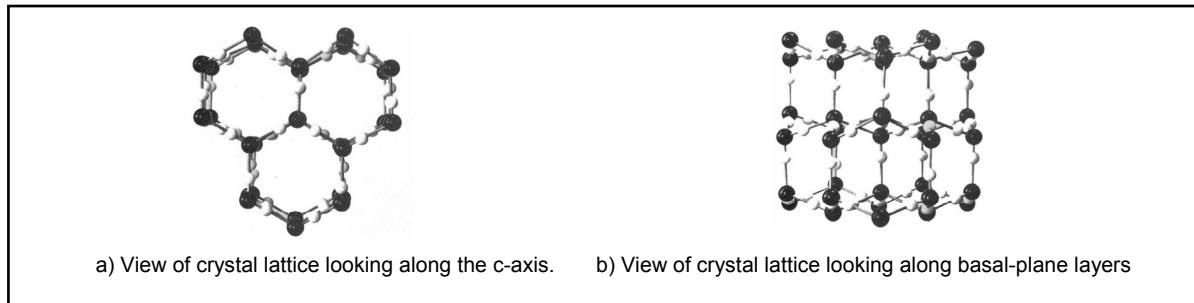


Figure 1. Idealization of atoms arrangement on ice structures, Oxygen atoms are shown in black and hydrogen atoms as white (Sanderson, 1988).

The texture of ice consisted of granular and columnar. Crystals that are elongated in irregular direction (randomly oriented crystals) is called granular shaped crystals. Meanwhile, those which are elongated in the vertical direction are known as columnar shaped crystals (Petrich and Eicken, 2017). Even though the crystal direction of columnar ice is vertically elongated, it has substructure consisting of platelets with horizontal c-axes. In most cases, the c-axes are randomly oriented in the horizontal plane of the ice sheet and have specific c-axis in vertical direction. Then the material can be said to be anisotropic. If there is no preferred orientation of the c-axes in the horizontal plane and vertical, then the ice is in isotropy property (Sand, 2008).

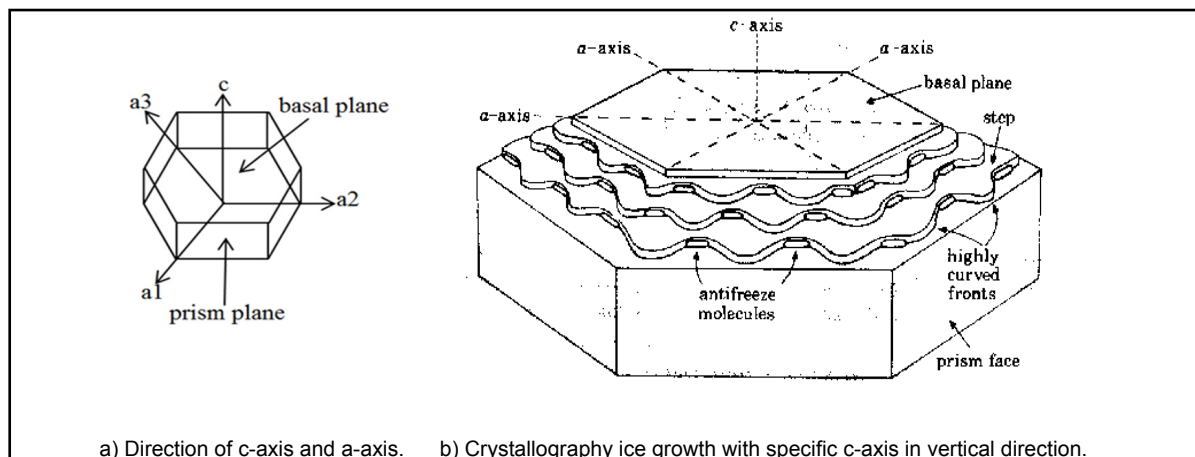


Figure 2. Ice growing direction: c-axis and a-axis direction (Capicciotti *et al.*, 2013).

The formation of granular and columnar crystals depends on freezing nature of water (Gow and Tucker, 1991). Figure 3 depicts ice growth over time and the formation of both granular and columnar crystals during the growth process of ice. In principal, the formation of ice cover depends on temperature, salinity, and the presence of wave and current. It starts from the development of granular crystal (at the sea surface), followed by the development of a mixed of granular and columnar crystal, before it becomes a fully columnar crystal. The development of aligned columnar ice requires 6-7 days (Stander and Michel, 1989).

The process is as follow: Ice cover growth occurs initially at sea surface—which could occur, among others, due to snow cover at the surface and mixing of water from turbulent wave. Then, the ice sheet flooded with water—which might occur due to the presence of currents (both stable and rough currents), infiltration of sea water, and/or due to melted snow on the ice sheet due temperature change. The stable current will make the ice sheet formation easy and make the crystal grow towards preferred orientation or columnar manner. Otherwise rough current will make granular orientation or it will ultimately prevent the ice sheet formation. An example of failed ice sheet formations due to rough current occurs in Norwegian Sea. Although Norwegian Sea has high altitude, the sea ice does not form due to rough current and Gulf Stream. On the other hand, in Gulf of Bothnia and Gulf of Finland in Baltic Sea, the forming of sea ice has always been in winter season even though its latitude is lower than Norwegian Sea.

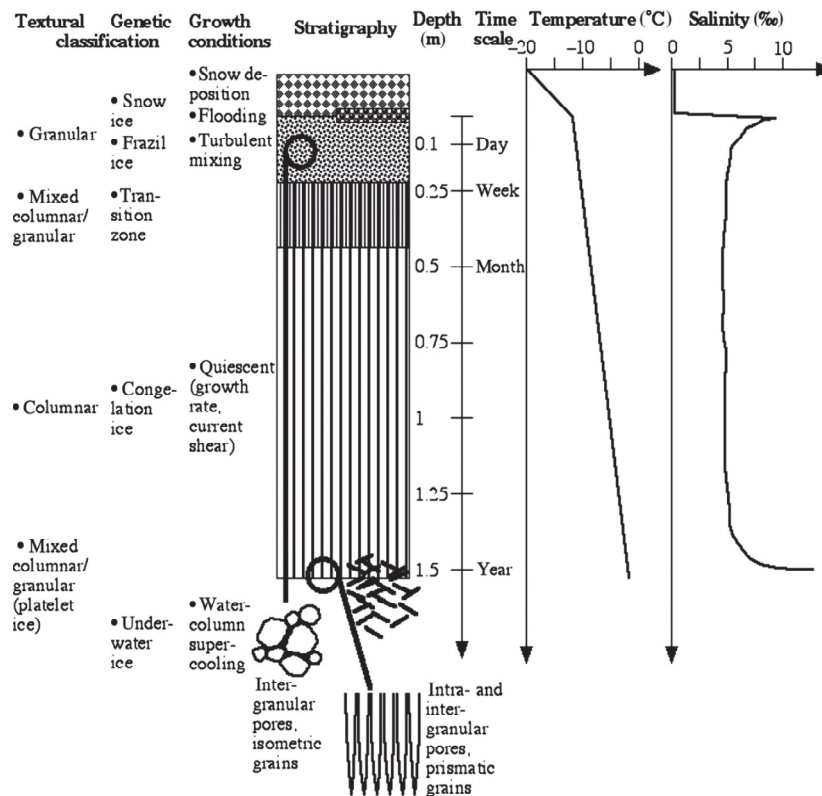


Figure 3. Schematic of ice textures, growth conditions, timescales and typical winter temperature and salinity profiles (Petrich and Eicken, 2010).

2.2 Sea Ice Strength

Ice is usually used as a load to define load obstructed to the structure, such as to the structure of offshore platform and in designing ship hull in arctic and subarctic region. The concept of using ice as a material was rarely used rather than the utilization of ice as a load. Since the construction of ice pier analysis in this study utilize ice as material, the knowledge of ice material is essential to gain an understanding about ice strength, which then enables us to use ice as a construction material.

The most common test on ice is uniaxial unconfined compressive strength test since it is easily performed on cylindrical and prismatic specimens. However, the result of this test does not represent the actual condition on the field, since ice cover will have pressure in each direction of principal stress and shear stress parallel to the surface. With this manner, the real stress on ice cover will have lesser strength than the uniaxial strength test during it is failure.

Compressive strength has a linear correlation to temperature, salinity, grain type (columnar and granular), loading direction and strain rate (Sand, 2008). Ice strength is temperature-dependent, in low temperature it will be more brittle while in high temperature will behave as ductile manner. Regarding the salinity, the higher the salinity rate, the lower the compressive strength of ice. Under the same strain rate, the value of compressive strength that parallel to the crystalline growth of columnar ice will be around four times higher than the compressive strength that is in perpendicular direction. Meanwhile, when the value of the compressive strength is in perpendicular direction, granular ice strength will be about a quarter higher than the columnar ice strength (Timco and Frederking, 1986; 1990). Values of uniaxial compressive strength can be 0.5 MPa at low strain rate and high temperature, and around 12 MPa at high strain rate and low temperature.

2.3 Ice as Material in Structural Application

The strength of ice as a material is relatively lower than that of the conventional building materials such as concrete and steel. In addition, its tendency to creep and fracture is higher than the other solid materials. However, there are some structures that have used ice as a material. One of the most common and famous ice structures is Igloo house of Inuit peoples, who lives stretch along the eastern part of Russia cross to Alaska, Northern Canada, and Greenland. The other structures are ice platform in Canadian Arctic, pykrete dome in Finland, Ice Dam (Ice retaining wall) in Siberia Russia, and Ice road in Canada. A more detail explanation of the utilization of ice as materials in the above structures will be provided in the following sub section.

2.3.1 Ice Platform

Ice platform in Canadian Arctic Island was developed in 1970's since there is a great potential of hydrocarbon resource in the area of latitude above 75° N and there was an expansion of efforts to find oil and gas reserve in northern Canada. During that time, there were 22 ice platforms that have been built in Canadian Arctic Region. However, the development was stopped due to expensive exploration cost. The ice platform is using ice sheet as platform for drilling rig. It was not possible to bring in offshore platform rig or even drilling ship to the area because the area was covered by ice all year round, even in summer season. The ice sheet thickness was from 2 to 5.3 meters. However, the thickness of each area was not the same on natural condition.

Ice thickness was used to sustain load of ice platform drilling rig. One of the drilling well was Hecla-52, where it has 450 tons drilling rig and the ice thickness is 5.3 meters—consisting of 2.3 meters natural sea ice and 3 meters built-up ice through a mechanism of flooding and freezing water on the surface of ice (Ekelund and Masterson, 1980). The weather condition in the region—very low temperature and calm waves—support the method of construction, contributing to the stability of ice platform. The ice platform structure was strong enough to sustain the drilling rig during the operation.



Figure 4. Rig 1 Drake F-76 in the Canadian Arctic Island (Ekelund and Masterson, 1980).

2.3.2 Pykrete Dome

Pykrete is a frozen composite material comprised of approximately 14% sawdust and 86% ice (Vasiliev and Pronk, 2015). To date only few structures have been made with pykrete materials, pykrete dome have been built in Juuka, Finland in 2015. The concept of pykrete as a material, have been developed since 1943 by G. Pyke during World War II to build ice ships.

Pykrete has unique properties, notably a relatively slow melting rate (due to low thermal conductivity), and its ability to greatly improve the strength and toughness ice—nearly closer to concrete strength. Below is comparison of strength between regular ice and pykrete composites with 10% sawdust (Vasiliev and Pronk, 2015).

Table 1. Strength Comparison of Regular Ice and Pykrete Composites (Vasiliev and Pronk, 2015).

	Compressive Strength (MPa)	Flexural Strength (MPa)
Regular Ice	3	1.2
Pykrete Composites	12	3.7

The future of pykrete as a material construction is prospective, since it can improve the strength of ice more than 3 times.



Figure 5. Pykrete Dome in Juuka, Finland, built with inflatable mould (Vasiliev and Pronk, 2015).

2.3.3 Ice Dam

The utilization of ice for Dam construction was developed in Irelyakh hydro-system Dam in Siberia, Russia. About 51 tons of aqueous solutions of polyvinyl alcohol with additives were pumped into five holes made in cold base ground Dam and act as retaining wall (Vasiliev and Pronk, 2015). Unfortunately, the concept only works in the area which has constantly low temperature over the year, like the one in Siberia, Russia. The Dam was in the area of permafrost soil. The temperature is very crucial for keeping the aqueous solution in freezing condition during life time; any melting and high temperature will be dangerous for the structure stability. Figure 6 illustrates the concept of water retaining wall and heat isolating construction.

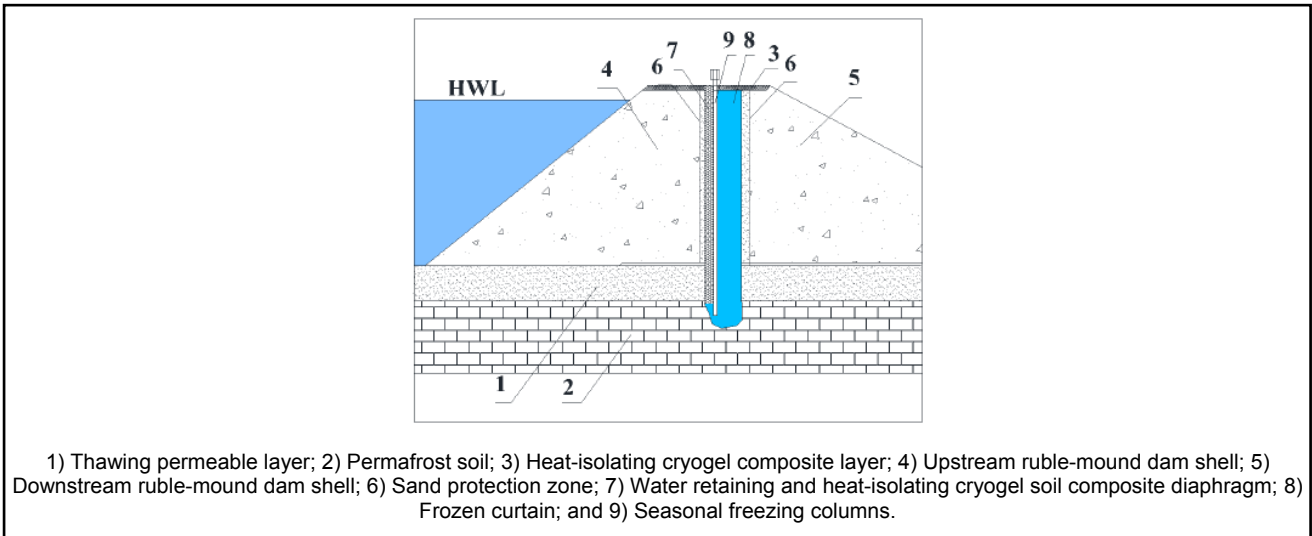


Figure 6. Cross Section of Dam Retaining Wall with aqueous solutions (Vasiliev and Pronk, 2015).

2.3.4 Ice Road

There are many places in the northern hemisphere that utilize frozen ice as a road—the most common ones are in Northwest territory of Canada, Scandinavian countries, Alaska, and Northern part of Russia. This ice road is commonly built on lakes, rivers or swamp—indicating that the ice is from fresh water. Sea water ice has lower strength than fresh water strength since sea ice has higher properties in salinity and porosity which reduce its strength.

The utilization of frozen ice mostly depends on the bearing capacity and the thickness of ice itself. Some countries have some brief report and regulation to protect the safety for road users. Bearing capacity is a key to declare that an ice road is safe to be used. The following is a simple formula to calculate bearing capacity (Gold's formula). Base on below formula the flexural strength of the ice sheet was decisive to bearing capacity:

$$P = C * F * h^2 \quad [1]$$

where **P** is the loads; **h** is the thickness of the ice sheet; **C** is a proportionality constant between flexural strength and bearing strength; **F** is the flexural strength as measured in simple beam tests with the top in tension

Note: the value of **C * F** is 1 based on a recommendation from A.J. Gow, H.T Ueda and J.A.Ricard (Bob, 2016)

The flexural have direct influence on bearing capacity. There is a method to improve bearing capacity of ice road. i.e. through the utilization of geo-materials/geogrid as reinforcement. The reinforcement concept is similar to the common geogrid used for soil improvement. Vasiliev and Pronk (2015) find that Geogrid reinforcement increased the maximum load-carrying capability up to 300% depending on the thickness of the ice road. Another research indicates that increasing bearing capacity with geogrid is effective in thin layers (up to 50 cm) and the thickness of the frozen layer should not exceed 30% of the natural thickness of ice (MIAK, 2013). However, all of the above improved bearing capacity is only for fresh water. None of the researches have analyzed the application of improved bearing capacity on sea ice, particularly with geogrid method.

2.3.5 Ice Pier

Ice Pier is a man-made structure which used ice as a main material to build pier in cold region. The Ice Pier has sophisticated structure but offers low cost and simple ways of construction—by using material with abundance availability in the nature. The most recent Ice Pier is in McMurdo station center in Antarctic which

the size is 100 meters long, 45 meters wide and around 7 meters thickness. The McMurdo Station ice pier that was made in 1999 could survive for 10 years due to, among others, temperature factor—average temperature in 2000 was -16.6°C .

The ice pier is needed since ships need moored place to unload their cargo. This structure was designed to assist unloading ships in Antarctica, particularly in McMurdo Station. In the early of 1960's, the unloading process usually uses small ship to transfer cargo to the land. Since the method is not efficient, the engineer in McMurdo station developed ice pier by using sea ice as material. It is inexpensive and easy to be constructed.

This Ice pier has been used since 1973, it is located at Winter Quarters Bay ($77^{\circ}50\text{ S}$, $166^{\circ}40\text{ E}$)—the southernmost port in the Earth. In year round, ships which are docking in this Station rely on icebreaker since the area is freezing even in the summer season, because of ice Pack covering around Winter Quarters Bay in southern of Ross Island, Antarctica.



Figure 7. USCGC Polar moored at McMurdo Ice Pier (Donenfeld, 2015).

3 RESEARCH METHODOLOGY

This study is an exploratory study based on desk research. To analyze an improved method towards the utilization of ice as material for a pier in polar region, the construction of ice pier in McMurdo station will be used as the referral analysis. Firstly, a brief explanation of McMurdo station will be provided, as well as its weakness in term of its strength (capacity of load carriage). Improved methods to increase the strength of future ice piers will be explored by analyzing methods that have been theoretically proven to increase structural strength on various structures which use ice as materials, with some caution.

4 ANALYSIS: IMPROVED METHOD OF ICE PIER

This section will provide an analysis of improvement methods for future construction of stronger ice pier. The construction method of McMurdo ice pier station will be explained first, altogether with identification of its weaknesses. Then, an analysis will be provided to improve ice pier construction in the future.

4.1 Construction Method of McMurdo Ice Pier Station

Method to construct McMurdo Ice Pier Station was simple—by flooding and freezing sea water above ice sheet which thickness is half a meter. Prior to it, snow dike was constructed around the pier with up to 2.7 meters thick. Steel cable was added during construction. However, this cable was not for structural reinforcement. Instead, it is for stringing the ice pier together when cracking occurred (Wagner et al., 2013). About 2.5 mm diameter of steel cables were installed in a crisscrossed way at the pier (see Figure 8). As a result, only limited load can be sustained by this structure. Moreover, due to the limited load capacity, the mooring rope has to be anchored directly to the mainland and unloading cargo will be directly stored to the mainland by container trucks after unloading process from the ships.



Figure 8. Steel cable was being installed in McMurdo Ice Pier construction (Wagner et al., 2013).

The ice pier is extended more than seven meters below the water line (Stone, 2006). The stability of floating ice pier depends on the five bollards installed on the ice pier and shore side, connected by wire (Barthelemy, 1975). For creating non-slip surface, the pier is then covered with gravel. Its normal lifespan is between 3 to 7 years. The ice pier which was made in 1999 was able to last over a decade (Wagner et al., 2013).

4.2 Analyzing the method to improve ice pier strength

As indicated above, McMurdo Ice Pier had limited load that can be borne. Therefore, improvement on ice pier construction will not only be crucial for increasing its strength, but also improve the economic value of the pier. Ability to improve ice pier strength will increase the life span of the ice pier, which then lower the re-construction cost of the ice pier. To date, McMurdo ice pier lifespan was only between 3 to 7 years, if no major disaster occurred.

Various properties of ice can be used to improve ice pier construction. Since ice have higher strength in c-axis direction of crystallography, the columnar grain which was loaded along with crystallography growth will be stronger than Granular grain. The compressive strength of columnar ice with loading direction parallel to the crystal growth will be around four times than perpendicular direction (Timco and Frederking, 1986; 1990).

Salinity also became major aspect to determine the ice strength. However, since it is not possible to separate salinity solution on nature, a method of spraying water into the air can make brine to be rejected during freezing process (Wagner et al., 2013).

Furthermore, properties of ice and sea ice can also be improved through reinforcement method (by creating ice composites) (Vasiliev and Pronk, 2015). There are 2 kinds of methods to improve ice strength with reinforcement composites. First is microscopic reinforcement where mixing ice with a substance to make homogeneous mixtures (this method will reduce creep and increase strength). The second one is macroscopic reinforcement by utilizing continuous materials such as steel, wire mesh and geogrid. Reinforcement or composites materials will enable higher load to be borne and reduce deflection and creep which is potential for initiating ice fracture. Reinforcement also provided protection from crack and reduced deflection up to 40 percent (Haynes et al., 1992).

A common method of reinforcement is by employing Geogrid or steel wire/nets to improve bearing capacity of ice. Another reinforcement method is the utilization of pykrete composites. Both methods were able to produce ice sheet with high value in compression and flexural strength. Thermosyphons also were proposed to increase ice strength by keeping the freezing temperature (Wagner et al., 2013). Thermosyphons was pressurized sealed pipes that are installed with one end buried and the other end exposed.

To conclude, this study suggests using various properties of ice so that it can be used to improve strength of ice pier construction. Among the suggested methods is the utilization of columnar ice, controlling sea ice salinity, and employing reinforcement method.

4.3 Suggested Sequence of Ice Pier Construction with Improved Method

This section offers construction sequence of ice pier with improved method to achieve more flexural strength than in McMurdo ice pier. It was proposed in this study to use the concept of sandwich multilayer between sea water, pykrete and reinforcement.

The ice pier construction should begin in the early of winter seasons, which make preparation procedure, area and materials of construction easy to be transported. The minimum ice thickness should be at least one meter for safety operation (Wagner et al., 2013). Then, dike should be made around the ice pier position. Along the dike, peg of steel column is used as anchor system to withstand the ice pier in position and placed monitoring gauge to measure deflection and horizontal movement of the ice sheet as wind and current impact. Another advance monitoring system is with satellite positioning system which will make measurement more accurate.

The next step is flooding the dike with seawater and allowing it to freeze. This procedure should be done quickly in the middle of winter season because the temperature is at the lowest at that time. There are two options of ice texture that can be used in the flooding and freezing stage: formed columnar ice and the granular one. The utilization of columnar ice will increase flexural strength. However, it takes time to form columnar ice; according to Stander and Michel (1989) and Petrich and Eicken (2010), it will be formed after 1-2 weeks. A time saving solution in creating columnar ice is by using Aluminum plexiglass freezing plate to stimulate the ice crystal growth in an unidirectional way (Kuehn et al., 1990). Actually, this method is developed to form columnar ice in the laboratory, but to stimulate faster process in the nature, it could be possible.

After the flooding and freezing process and the ice thickness reaches 1.5 meters, the next step is spraying pykrete (sawdust and water) or additive along the surface of the ice layer. Then, reinforce the ice by installing steel or geogrid to the layer and tie it to the column/anchor. Repeat the flooding seawater process to form columnar ice again. The sequences of spraying pykrete/additive, reinforcing the ice, and seawater flooding will be repeated until the thickness of 6 meters is achieved. It will consist of 4 layers in total.

This study suggested that the thickness of 6 meters to be obtained for the ice pier. This thickness is lower than the one in the McMurdo ice pier which has average ice depth of about 7 meters, but higher than ice platforms in Canada Arctic. An ice platform in the Canada that has natural ice thickness of 2 meters can hold drilling rig up to 140 ton, while the other platform which has 5.3 meters thickness of sea ice and built up ice have compressive strength between 14 to 34 MPa for natural sea ice and 6 MPa for flooding/built up ice (Ekelund and Masterson, 1980). The 5.3 meters Canadian arctic ice platform was built without any reinforcement but can stand load up to 450-ton drilling rig, which means equal to more than ten times of the heaviest ocean container at 45 feet high cube load (TSi Logistics, undated).



Figure 9. Offloading cargo from the ships at McMurdo Ice Pier, Antarctic (SeaWaveMagazine, 2016).

The ice pier with improved method, even though its thickness is less than the one in McMurdo Station, apparently will have ability to withstand more loads since it uses reinforcement. The reinforcement has ability to transfer shear stress from the ice sheet to the reinforcement (Wagner et al., 2013). The reinforcement also reduces deflection up to 40% and prevent initial crack (Haynes et al., 1992). Further reinforcement by adding pykrete will give it strength at least 3 times higher than normal ice (Vasiliev and Pronk, 2015). However, for the application of sea ice as a material, further research is needed towards the application of pykrete and steel reinforcement/geogrid. Compressive test should be conducted to obtain real value of compressive and flexural strength. By estimating the maximum strength of ice, it can propose maximum load that can withstand by ice pier. Simple bearing calculation in equation 1 can be applied to estimate the maximum load. However, it should firstly define the flexural strength value by testing the material. Calibration with the Scale Model or Finite Element Analysis should be conducted to confirm the feasibility in real application.

Structure stability is a major issue during construction and lifetime. During the construction process, the stability of ice pier should be maintained since some parts of the pier will be loaded with some equipment and will be covered by snow cover during snow storm, which will create unequal ice depth. This condition could be dangerous for the pier stability. Furthermore, it needs regular checks of ice pier bottom to avoid collision with seabed. There should be clear space between bottom of pier and seabed to avoid abrasion and scouring that will impact structure stability and can initiate creep and fracture. During summer season, ice sheet around the pier break away; it would be critical condition to the ice pier structure due to wave impact. Flexural failure under long wave is responsible to the break up the McMurdo ice pier in 1991 and possibility resonance response of the ice pier when the wave length approximately equal to pier length. Dynamic absorber would be suitable equipment to control the resonance between ice pier and wave amplitude (Wagner et al., 2013).

The design purpose of ice pier is mainly to cover compressive and flexural load from containers, trucks and equipment. Therefore, mooring and stability of the ship should depend on the ships anchor and anchor rope that directly tied to the mainland. The ice pier structure is not designed to receive mooring impact from ship. Therefore, any horizontal load should be minimized. The concept of using aqueous solution (Ice Dam) to make ice pile could be done in ice pier structure because ice pier is a floating structure with minimum steel anchor reinforcement. The pile is very important part on the general model of pier construction, to withstand horizontal load from mooring impact. However, application in ice pier would be challenging since ice pile is only suitable for permafrost region structure, where substructure condition is frozen all the time to maintain ice pile strength.

Safety is the main issue of any structure. This applies also to the structure, which uses ice as a material. In addition, besides strength as parameter of the structure reliability, there is another parameter that should be considered. That is deflection, where also play important role for ascertaining the safety of the structure. The creep or deflection on ice structure is usually the limiting factor of the design rather than the ice strength (Ekelund and Masterson, 1980).

The following tables shows the comparison data from Minnesota DNR for ice sheet from fresh water, without any reinforcement and bearing capacity from ice sheet with geogrid reinforcement from CRREL. Comparison from the table 2 and 3 shows that for 10 cm ice thickness maximum load with geogrid

reinforcement was more than 4 times higher than without reinforcement. However, application of any reinforcement in sea ice still need further verification, with compressive, flexural and deflection test.

Table 2. Estimated load base on ice thickness (Bob, 2016).

Minimum Thickness (cm)	Estimated Load (kg)	Load Condition
5 or less	-	STAY OFF
10	356	4 Skaters or 3 Fisherman
12.5	534	Snowmobile
20	1423	Car
22.5	1780	Car
25	2220	Small Pickup
30	3110	Medium Truck
40	4890	Medium Truck

Table 3. Bearing load with geogrid reinforcement (Haynes *et al.*, 1992).

Ice Thickness (cm)	Forced Load, Crack Formed (kg)	Maximum Load (kg)
3	39	161
4.9	113	398
6.5	182	705
9.6	335	1524
10.8	350	1563
13.5	-	1656

The final construction step is spreading gravel or cast asphalt layer to cover ice from melting on summer season and as anti-slip layer. The purpose of the cover layer is also for reducing the effect of heat in the summer season—temperature is among a major issue to maintain ice pier from melting.

5 CONCLUSIONS

The development ice as a material construction is not commonly used because its strength depends on some parameter which is, in some case, unable to be controlled (temperature, salinity and crystallography). However, some structure has been made by using sea ice as a material, one of them is ice pier. Application of sea ice in ice pier construction have some advantage, from easy to construct, abundant material and inexpensive in construction. Since, ice have less strength than other materials, it is necessary to make improvement method to make sure ice becomes a quality material. In the field of ice pier construction, there are some methods that can be used to increase ice strength. Reinforcement with wire mess or geogrid, pykrete composite, the utilization of crystallography direction was some ways to increase the strength.

Some researchers have made empirical evidence by observation and experimentation in ice strength improvement method. By combining reinforcement method, pykrete and utilization of columnar grain, the strength of ice can be improved. Use of ice as a material in ice pier construction, means there would be increase in load capacity. As the strength increased, the capability to overcome deflection also increased. The advantage of using reinforcement in ice materials is its ability to localize the failure. Without reinforcement, the failure will occur over a large area because initiated crack or deflection will propagate to the whole ice sheet. Unfortunately, the currently available researches on reinforcement and pykrete are for fresh water. Their applications on sea ice still need empirical research. Since sea ice strength is salinity dependant.

The main issue of ice pier is its lifetime during service period. It is highly dependent to the regional temperature and wave action during summer season. The wave amplitude can make resonance to the ice pier. Pressurized pipe and dynamic absorber can be used to handle the problem (Wagner *et al.*, 2013).

With all of the above result, the ice pier improvement method will give more strength than McMurdo ice pier model. The calibration of the value of increased strength should be conducted to give solid evidence from the analysis method. In the future with this base of concept, it is expected that development of ice pier could be significantly improved.

ACKNOWLEDGEMENTS

Authors would like to acknowledge Associate Professor Olga A. Sabodash, PhD as lecture at Offshore and Port Equipment subject at Offshore and Coastal Engineering Department and Mr. Egor E. Pomnikov, PhD as Head of Ice Laboratory at Far Eastern Federal University (FEFU, Vladivostok, Russia).

REFERENCES

- Barthelemy, J.L (1975). *The Man-Made McMurdo Ice Wharf-History, Construction and Performance*. Civil Engineering Laboratory Naval Construction Battalion Center Port Huaneme, CA, USA.
- Bob. (2016). The Bearing Strength of Ice for Recreational Activities. [Retrieved 30/09, 2016, from <http://lakeice.squarespace.com/bearing-strength/>].
- Capicciotti, M. J., Doshi, M., & Ben, R. N. (2013). Ice Recrystallization Inhibitors: From Biological Antifreezes to Small Molecules.[Retrieved 30/09, 2016, from <http://www.intechopen.com/books/recent-developments-in-the-study-of-recrystallization/ice-recrystallization-inhibitors-from-biological-antifreezes-to-small-molecules>].
- Donenfeld, J. (2015). Ship Operations at the World's Southernmost Seaport. [Retrieved 30/09, 2016, from <https://www.jeffreydonenfeld.com/blog/2015/01/ship-operations-at-the-worlds-southernmost-seaport/>].
- Ekelund, M.J. & Masterson, D.M. (1980). *Floating Ice Platform for Oil Exploration in the Arctic Islands*. Calgary: Arctic Institute of North America's.
- Engineering, MIAK. (2013). Recommendations for The Use of the Materials Geositeticheskikh Gc "MIAK" for The Reinforcement of the Ice Crossings. [Retrieved 30/09, 2016, from http://miakoming.ru/InfoTech/Ledovie_perepravvy/].
- TSi Logistics. (undated). *Ocean Container Specifications*. [Retrieved 09/01, 2017, from http://www.tsilogistics.com/pdf/ocean_container.pdf]
- Gow, A. J. & Tucker, W. B. (1991). Physical and Dynamic Properties of Sea Ice in the Polar Oceans. US. [Retrieved 30/4,2017, from http://acwc.sdp.sirsi.net/client/en_US/default/index.assetbox.assetactionicon.view/1011783?rm=MONOGRAPHS0%7C%7C%7C1%7C%7C%7C0%7C%7C%7Ctrue&Im=WES].
- Haynes, F.D., Collins, C.M. & Olson, W.W. (1992). Bearing Capacity Test on Ice Reinforced with Geogrid. *Special Report, 92-28*, US Army Corps of Engineers.
- Kuehn, G.A., Lee, R.W., Nixon, W.A. & Schulson, E.M. (1988). The Structure and Tensile Behavior of First Year Sea Ice and Laboratory-Grown Saline Ice. *International Conference on Offshore Mechanics and Arctic Engineering (OMAE)*, Houston, USA.
- Petrich, C. & Eicken, H. (2010). Growth, Structure and Properties of Sea Ice. *Blackwell Publishing Ltd*.
- Petrich, C. & Eicken, H. (2017). Overview of Sea Ice Growth and Properties. In D. N. Thomas (Ed.), *Sea Ice: Third Edition*. New Jersey: Wiley Blackwell.
- Sand, B. (2008). Nonlinear Finite Element Simulations of Ice Forces on Offshore Structure, *Doctoral Thesis*. Lulea University of Technology, Sweden.
- Sanderson, T. J. (1988). *Ice mechanics - Risks to offshore Structures*. Graham & Trotman, London.
- Schwarz, J. & Weeks, W. F. (1977). Engineering Properties of Ice. *Journal of Glaciology*, 19(81), 49-530.
- SeaWavesMagazine. (2016). MSC Chartered MV Ocean Giant Continues Conducts Cargo Ops in Support of 2016 Operation Deep Freeze. [Retrieved 10/02, 2017, from <http://seawavesmagazine.blogspot.ru/2016/02/msc-chartered-mv-ocean-giant-continues.html>].
- Stander, E. & Michel, B. (1989). The Development of Aligned Columnar Sea Ice: A Field Investigation. *Journal of Glaciology*, 35 (120), 217-223.
- Stone, E. (2006). *Antarctic Sun*. Published during the austral summer at McMurdo station, Antarctica.
- Timco, G. W. & Frederking, R. M. W. (1986). Confined Compression Tests: Outlining the Failure Envelope of Granular/Discontinuous Columnar Sea Ice. *Cold Region Science and Technology*, 12, 13-28.
- Timco, G. W. & Frederking, R. M. W. (1990). Compressive Strength of Sea Ice Sheets. *Cold Region Science and Technology*, 17, 227-240.
- Vasiliev, N.K., Pronk, A.D.C. (2015). Ice Composites as Construction Materials in Project of Ice Structures. *Port and Ocean Engineering under Arctic Condition (POAC)*, Trondheim, Norway.
- Wagner, A.M., Knuth, M.A., Sodhi, D.S., Blaisdell, G. & Shelton, C., (2013). Ship Offload Infrastructure in McMurdo Station, Antarctica. *ISCORD 2013: Planning for Sustainable Cold Regions*.

HYDRO-ENVIRONMENTAL MODELLING OF A SEVERN BARRAGE WITH VERY LOW HEAD TURBINES

REZA AHMADIAN⁽¹⁾, ROGER A FALCONER⁽²⁾ & BETTINA BOCKELMANN-EVANS⁽³⁾

^(1,2,3)Hydro-environmental Research Centre, School of Engineering, Cardiff University, Cardiff, United Kingdom
AhmadianR@cardiff.ac.uk; FalconerRA@cardiff.ac.uk; Bockelmann-Evans@cardiff.ac.uk

ABSTRACT

There is a desire to increase utilisation of renewable energy across the globe considering the impacts associated with fossil fuels and growing demand for electricity due to need to changes in technology and growing global population. Amongst various type of renewable energy, marine renewable energy and particularly tidal range has the advantage of being predictable. This predictability would be of great interest considering the less predictable nature of other sources of renewable energy, such as wind and solar, and increasing utilisation of less flexible schemes, such as nuclear power stations. Severn Estuary and Bristol Channel located in the South-West of Britain, with the second tidal range in the world, have excellent potential for marine renewable energy and therefore have attracted a wide range of proposals to build marine renewable energy schemes (Kadiri et al., 2012). A barrage across the estuary to impound the water at high or low water and then generate electricity by realising the impounded water through the turbines has been the oldest option and have the potential to generate up to 5% of UK electricity demand. However, there are several ecological and environmental concerns with such a scheme. Recent studies have shown that implementation of a two-way generation scheme would cause less changes to the existing condition and therefore could reduce the impacts of such a scheme (Ahmadian et al., 2014a). This study investigates the hydro-environmental impact of a Severn Barrage using Very Low Head (VLH) turbines (DECC, 2010a). The study implement hydro-environmental models set up for the Severn Estuary and Bristol Channel and the potential impacts of the scheme will be investigated by comparing the pre- and post-barrage. The model predictions show less significant changes in the currents to the existing condition while the barrage could be implemented as a flood alleviation structure.

Keywords: Marine renewable energy; very low head turbine modeling; severn barrage; tidal lagoons; coastal flooding.

1 INTRODUCTION

Greenhouse gasses emission is identified as one of the main contributors to climate change and subsequently there has been significant efforts globally targeted towards reduction of greenhouse gases. These efforts include both international agreements such as The Paris Agreement (Accord de Paris) and national mandates such as the UK Climate Change Act which requires greenhouse gas emissions to be cut by 80 percent by 2050 compared to 1990 levels. Amongst different approaches, “decarbonisation” of the electricity sector through utilization of renewable and “cleaner” sources to generate electricity is considered as one of the main pathways to reduction of CO₂ emissions. Amid different renewable energy sources, tidal energy has the advantage of being predictable. Tidal renewable energy resources and particularly tidal range schemes could be a significant part of the electricity generation mix in some countries. For instance, in the UK, the Severn and Mersey Barrages can potentially generate more than 18 TWh/year (Sustainable Development Commission, 2007). Whilst Tidal range schemes could provide a large scale predictable renewable energy, the hydro-environmental and ecological impacts of such schemes are not fully understood. There have been several studies on the hydro-environmental and ecological impacts of the barrages and more recently lagoons. Falconer et al. (2009a), Xia et al. (2010b) and Ahmadian et al. (2014a) showed that the barrage using reduces the currents, both upstream and downstream, and the flood risk upstream. Zhou et al. (2014) and Bray et al. (2016) demonstrated the significance of domain extension and accurate implementation of hydraulic structures in modelling tidal range schemes. Aggidis and Benzon (2013) investigated operational optimization of a barrage using a 0-D model. Ahmadian et al. (2010) and Kadiri et al. (2012) showed that barrages operating under different generation schemes reduces the suspended sediment and faecal bacteria concentrations, both upstream and downstream, of the barrage while the extent of reduction depends on the operation scheme. Kirby and Retière (2009) compared the environmental impacts of The Rance and Severn Barrages and highlighted their similarities and differences. Fairley et al. (2014) studied the impact of the barrage with ebb-only operation on the wave conditions and found that the barrage would have little impact on the wave conditions downstream.

Most these studies are based on utilizing a bulb turbine in the structure and there has been little research on implementing different type of turbines, this study investigate hydro-environmental impact of a Severn Barrage implementing Very Low Head (VLH) turbines (DECC, 2010a).

2 Very Low Head (VLH) Severn Barrage

One of the main sites considered for tidal renewable energy, and particularly tidal range structures in the UK, is the Severn Estuary and Bristol Channel, in the South West of the UK. The tidal range in Severn Estuary is in excess of 14 m and the shape of the estuary provides the potential of a large basin for barrages. Feasibility of a number of barrages proposed to be built in Severn Estuary and Bristol Channel were considered in Department of Energy and Climate Change (DECC, 2010b). DECC short-listed schemes, including a Severn Barrage (option B3), are illustrated in Figure 1. There are also a number of lagoons proposed to be built in the Severn Estuary and Bristol Channel and the independent Hendry Review commissioned by the UK government recommended construction of the world's first tidal lagoon in Swansea Bay, in January 2017.

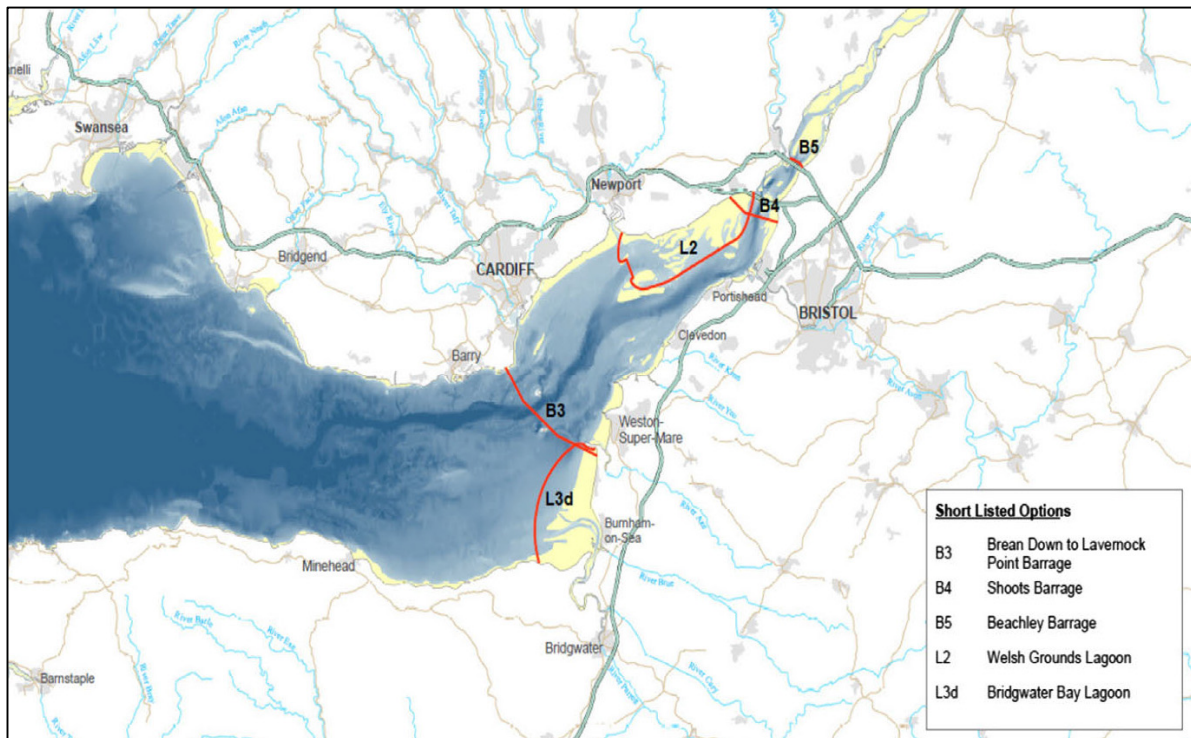


Figure 1. Department of energy and climate change short-listed schemes, including the seven barrage(B3) (DECC, 2010b).

The Severn Barrage studied in the DECC study (DECC, 2010b) was based on Severn Tidal power Group (STPG) proposal which includes 216×9 m diameter turbines each producing a peak output of 40MW. Various aspects of this scheme have been investigated by different researchers as highlighted in Introduction section. This scheme, similarly to many other schemes, only consider bulb turbines. The current study consider a similar Severn Barrage with 1016 ×9 m diameter VLH turbines (DECC, 2010a). Unlike the STPG scheme, this VLH scheme is based on a 2-way generation. Although, both STPG and VLH schemes connect to land at similar locations, they are using different lines as shown in Figure 1 and 3.

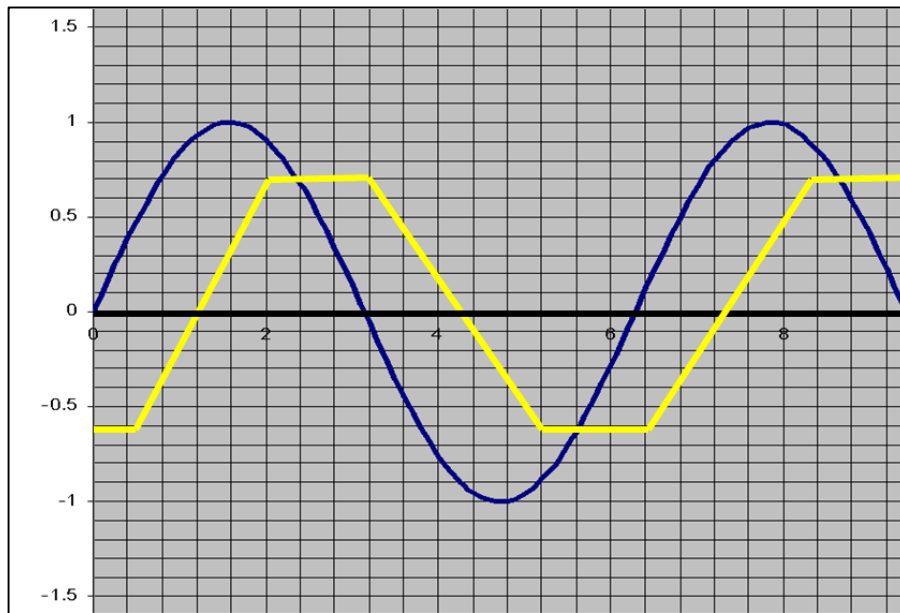


Figure 2. Schematic water levels inside (Yellow Line) and outside (Navy Line) the barrage basin using ebb-flood generation.

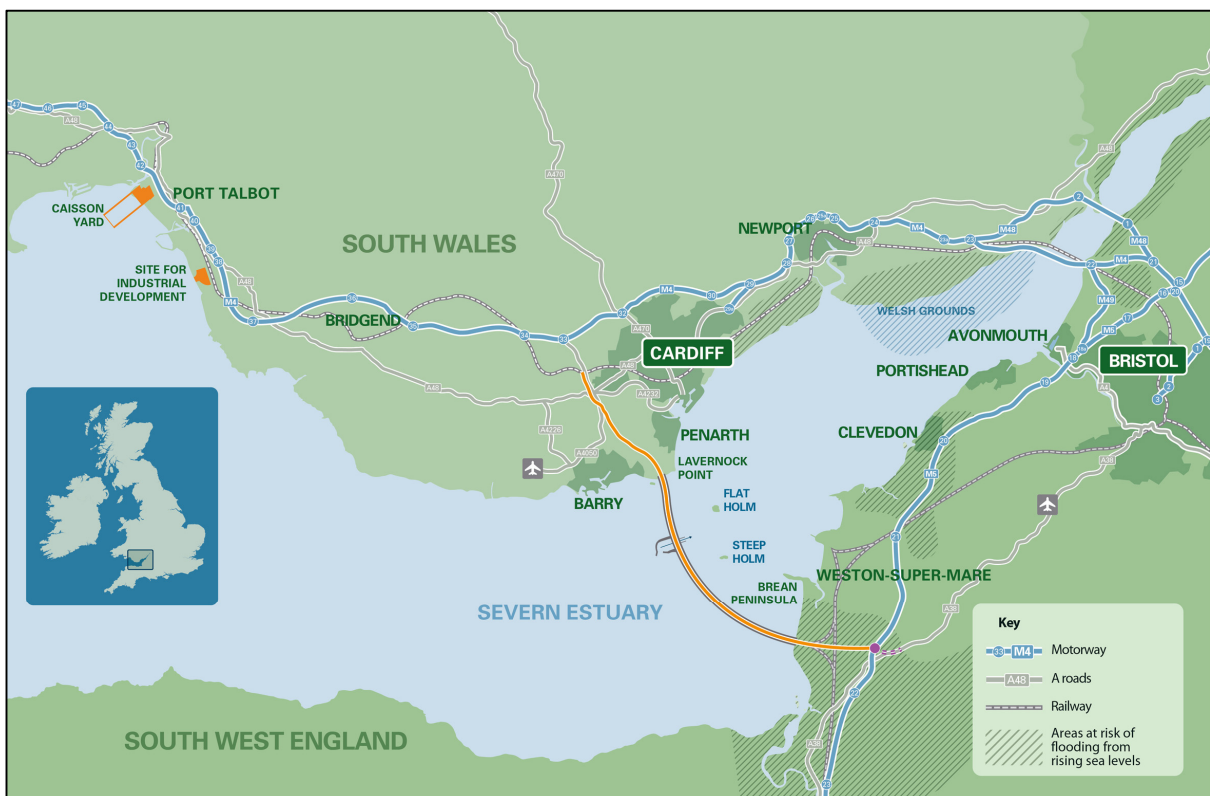


Figure 3. The very low head (VLH) barrage layout shown in orange (Courtesy of Hafren Power Ltd.).

3 HYDRO-ENVIRONMENTAL MODELLING

3.1 Model Details

The 2D governing equations used in the model are briefly given in this section, with more details of the 1D and 2D models being given in Falconer (Falconer and Li, 1992) and Kashefipour (Kashefipour et al., 2000). The 2-D depth-integrated governing equations were derived by integrating the governing 3-D equations over the depth to give for the x-direction (Falconer, 1993):

$$\frac{\partial \xi}{\partial t} + \frac{\partial q_x}{\partial x} + \frac{\partial q_y}{\partial x} = 0 \quad [1]$$

$$\frac{\partial q_x}{\partial t} + \beta \left[\frac{\partial u q_x}{\partial x} + \frac{\partial v q_x}{\partial y} \right] = f q_y - g H \frac{\partial \xi}{\partial x} + \frac{\tau_{xw}}{\rho} - \frac{\tau_{xb}}{\rho} + \varepsilon \left[2 \frac{\partial^2 q_x}{\partial x^2} + \frac{\partial^2 q_x}{\partial y^2} + \frac{\partial^2 q_y}{\partial x \partial y} \right] \quad [2]$$

$$\begin{aligned} \frac{\partial \phi H}{\partial t} + \frac{\partial \phi q_x}{\partial x} + \frac{\partial \phi q_y}{\partial y} - \frac{\partial}{\partial x} \left[H D_{xx} \frac{\partial \phi}{\partial x} + H D_{xy} \frac{\partial \phi}{\partial y} \right] \\ - \frac{\partial}{\partial y} \left[H D_{yx} \frac{\partial \phi}{\partial x} + H D_{yy} \frac{\partial \phi}{\partial y} \right] = H \sum \Phi \end{aligned} \quad [3]$$

where q_x, q_y = discharges per unit width in the x, y directions ($m^2 s^{-1}$), ξ = water surface elevation above datum (m), H = total water depth (m), β = momentum correction factor for non-uniform vertical velocity profile (dimensionless), f = Coriolis parameter ($rad s^{-1}$), g = gravitational acceleration ($m s^{-2}$), τ_{xw}, τ_{xb} = surface and bed shear stress components respectively in the x -direction ($N m^{-2}$), ε = depth averaged eddy viscosity ($m^2 s^{-1}$), ϕ = depth averaged concentration (unit/volume) or temperature ($^{\circ}C$), $D_{xx}, D_{xy}, D_{yx}, D_{yy}$ = depth averaged dispersion-diffusion coefficients in the x, y directions respectively ($m^2 s^{-1}$) and Φ = total depth average concentration of the source or sink solute. The momentum equation (equation 2) was derived by assuming the no-slip bed boundary condition and including the other external forces such as: wind shear, bottom friction, and the earth's rotation.

3.2 Model setup

2-D hydro-environmental model, namely the DIVAST (Depth Averaged Velocity And Solute Transport) model, which is widely used to model marine renewable energy Schemes (Ahmadian et al., 2012; 2014b; Angeloudis et al., 2016; Falconer et al., 2009b), has been used for this study. The model domain extended from the River Severn tidal limit, located close to Gloucester, to the outer Bristol Channel, where the Channel joins with Irish Sea. The upstream boundary condition was set at a flow rate varying between 60 and 106 m^3/s (i.e. the normal River Severn condition for the simulation period). The downstream water level boundary condition for the existing condition was obtained from the Proudman Oceanographic Laboratory (POL) (Heaps and Jones, 1981) Irish Sea model as implemented by Ahmadian et al. (2010). A 100 m grid size and SeaZone digital bathymetry (SeaZone, 2013) were used in this study, while a grid dependency analysis showed no significant grid dependency (Ahmadian et al., 2010). The model was calibrated using values obtained from the Admiralty Charts, while model calibration was undertaken using the four data sets acquired and published by Stapleton et al. (Stapleton et al., 2007a; 2007b) at two sites along the estuary. Typical calibration and validation graphs are shown in Figure 4.

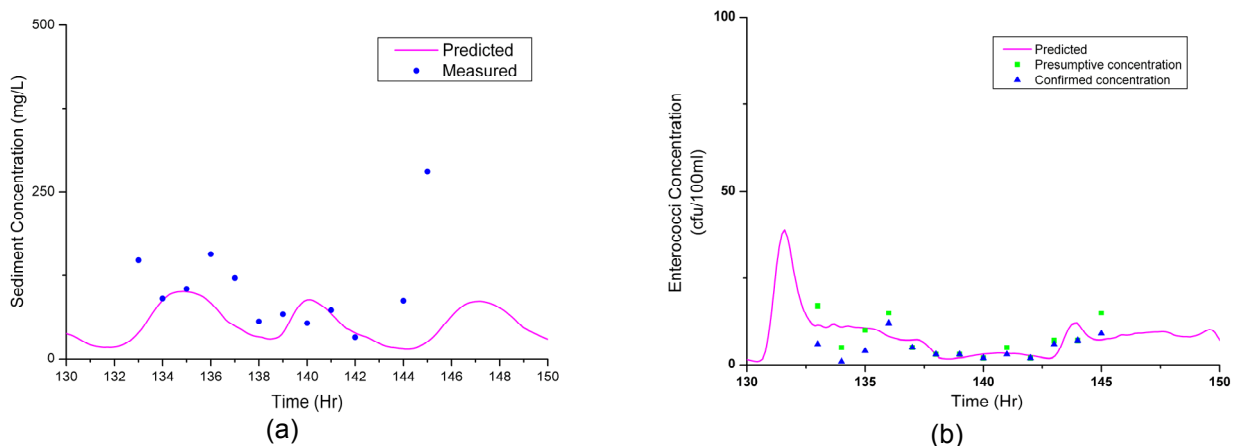


Figure 4. Comparison of predicted and measured: (a) suspended sediments, and (b) enterococci concentrations at Southerndown (Ahmadian et al., 2010).

4 Results

Pre- and post- barrage conditions by running the model for each condition. The impact of the operation of the barrage on the boundary condition was implemented using a continental shelf model including the scheme

(Bray et al., 2016; Zhou et al., 2014). The turbines and sluice gates are modeled as (Ahmadian et al., 2010; Baker, 1991; Xia et al., 2010a). Figure 5 demonstrate the operation of the barrage by illustrating water levels upstream and downstream of the barrage.

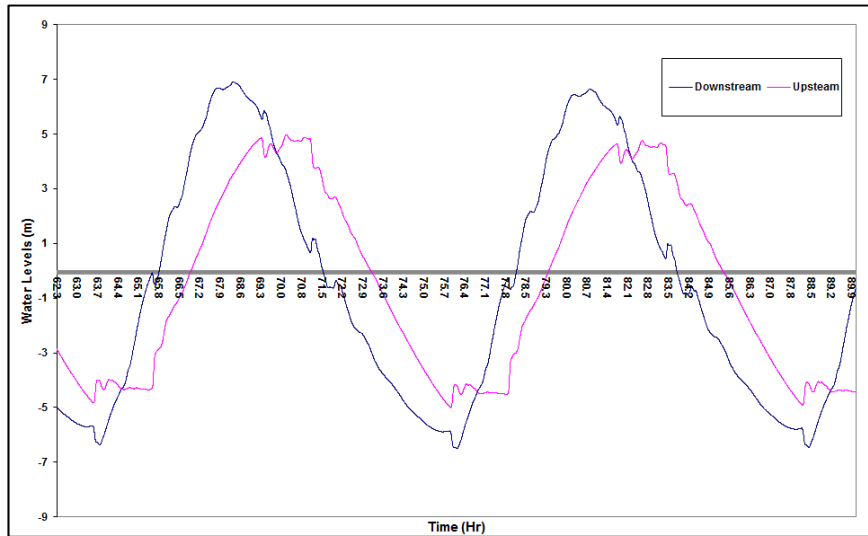


Figure 5. Water Levels across the barrage. blue: downstream. magenta: upstream.

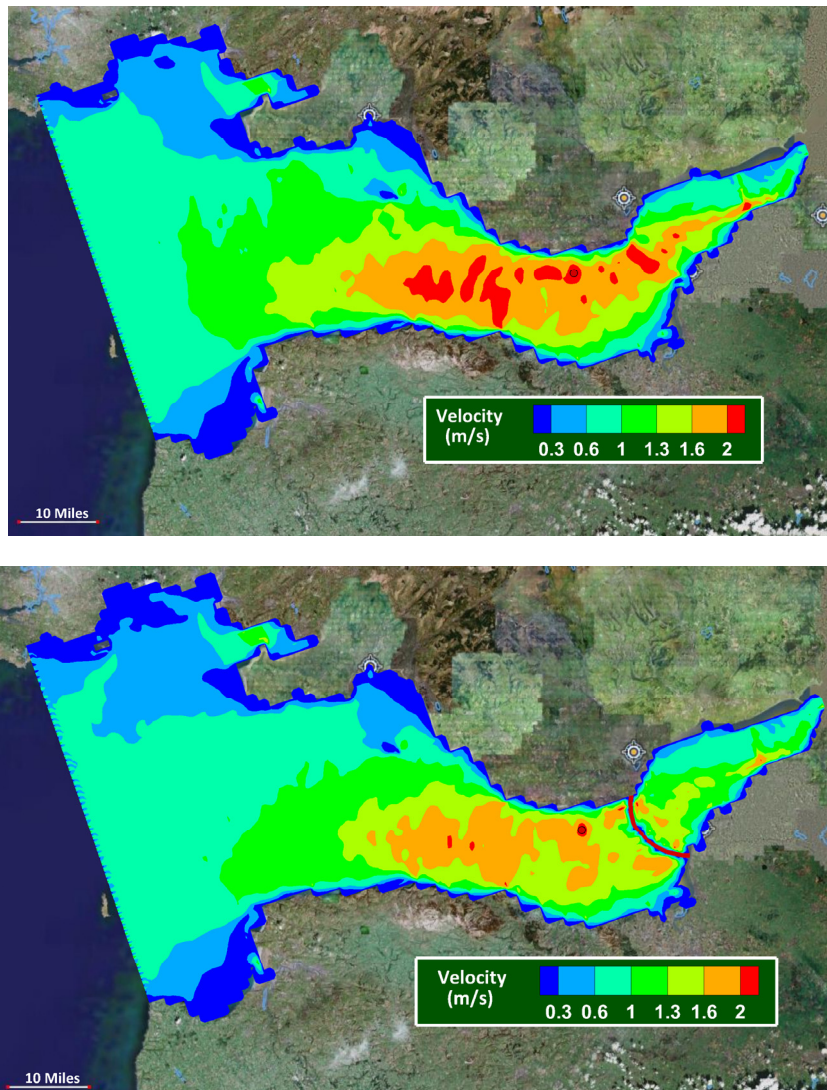
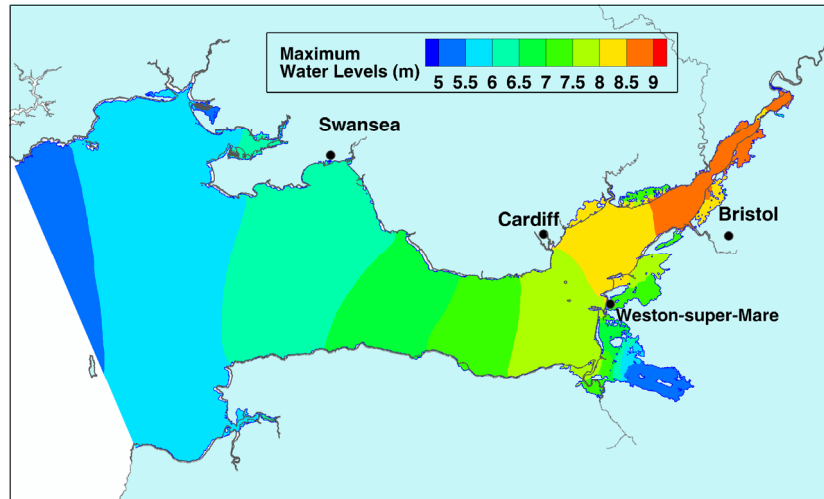
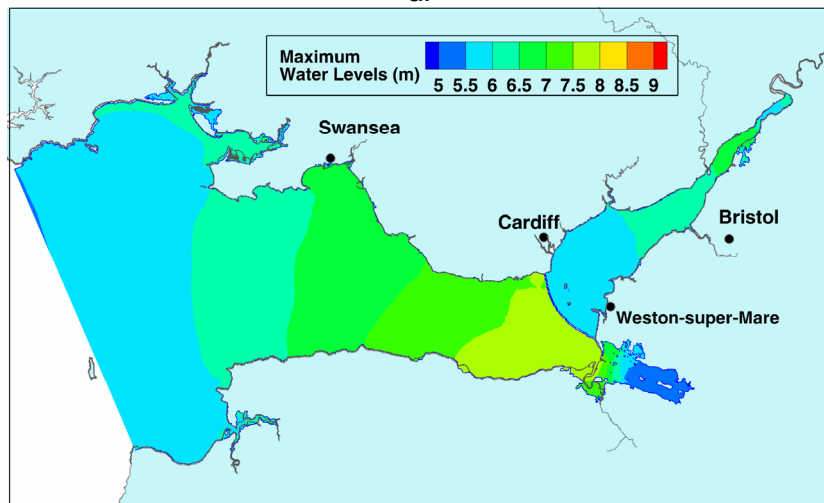


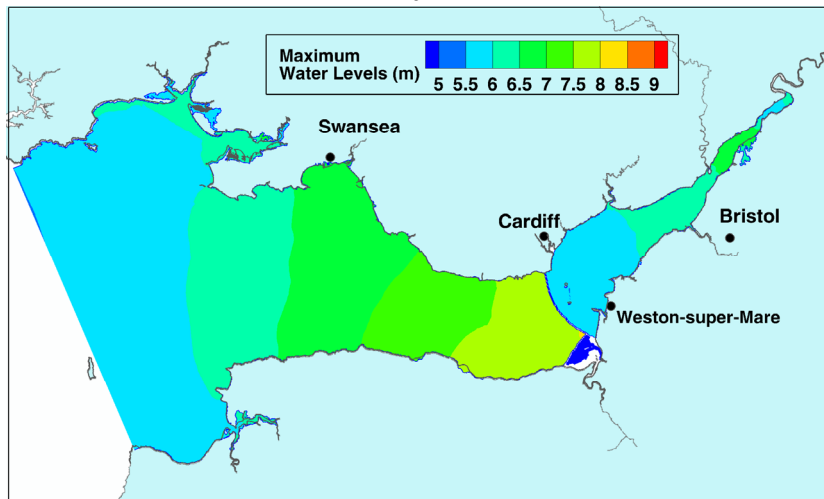
Figure 6. Velocity magnitudes across the domain at mean ebb at Barry Site (shown with a Red dot). up: pre-barrage. down: post-barrage.



a:



b:



c:

Figure 7. 2100 water levels relative to Ordnance Datum - a: No Barrage b: Barrage c: Barrage with the Bond.

Comparison of velocities pre- and post-barrage, shows a reduction of about 0.3 m/s in velocities for post-barrage scenario. This reduction is visible up to about 30 km upstream and 50 km downstream of the barrage. Observation of reduction in velocity is consistent with STPG barrage results (Ahmadian et al., 2014a; Ahmadian et al., 2010), however, less reduction in magnitude of velocities observed for VLH barrage comparing to the STPG barrage. Figure 6 shows typical velocities across the estuary pre- and post-barrage construction for an ebb tide at the model reference point which is shown with a red dot in that figure. Impact of the barrage on flooding for present time and future scenarios were investigated. The values for sea level rise were extracted from DECC (2010b). Predicted magnitude of sea level rise for 2100 is about 90 cm and the

impacts of the barrage on flood risk as a result of sea level rise relative to Ordnance Datum is shown in Figure 7. This includes the impact of building a bond to protect Somerset levels. Moreover, accumulated impact of the sea level rise and a storm surge was investigated. Impact of the barrage on flood mitigation as a result of the sea level rise and highest storm surge relative to Ordnance Datum is shown in Figure 8. It can be seen that the barrage will reduce the impact of Sea Level Rise on the areas located upstream the barrage under normal operation. This reduction is less than the reduction reported by SPTG scheme (Ahmadian et al., 2014b).

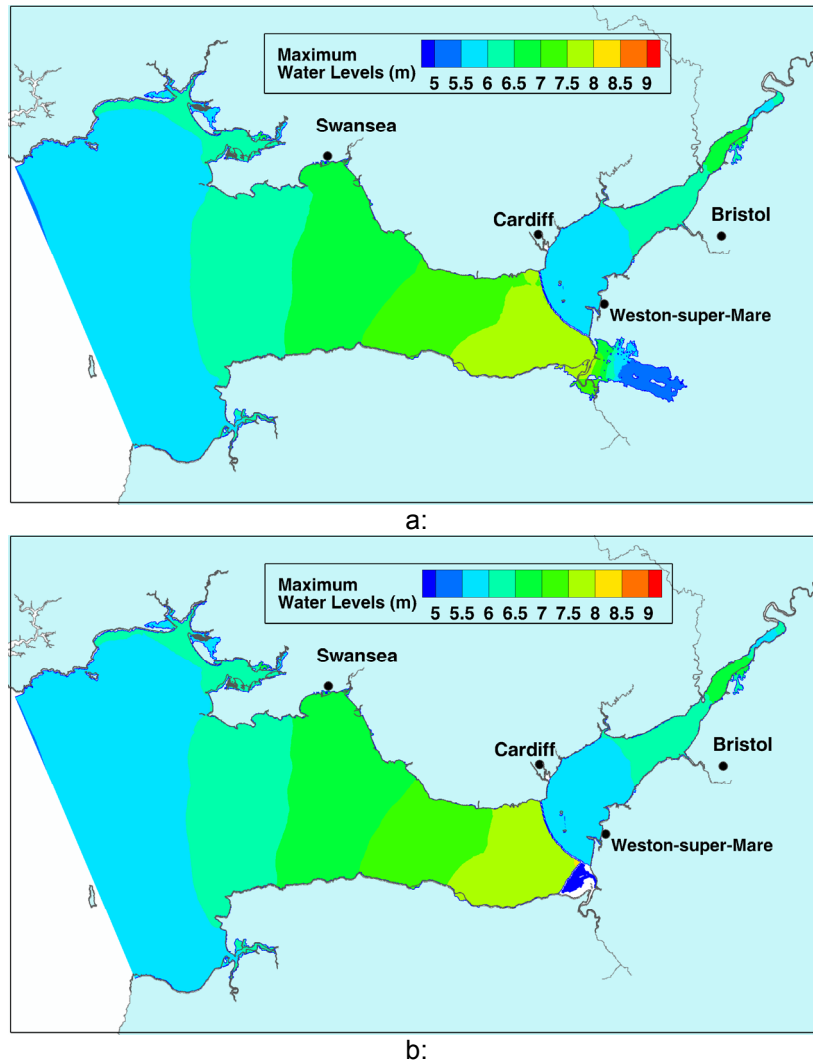


Figure 8. 2100 water levels and a historical storm surge relative to Ordnance Datum- a: Barrage b: Barrage with the Bond.

5 CONCLUSIONS

This study investigates and compares the hydro-environmental impacts of a Severn Barrage using very low head turbines and two-way generation scheme. DIVAST model is adopted to model the tidal range structures and implemented for this study. The model was validated for the existing conditions. This study has shown that implementing a two-way generation scheme for a barrage with Very Low Head (VLH) turbines will reduce currents both upstream and downstream of the barrage and therefore alter the transport processes. However, the changes to the estuary hydrodynamics which, in turn, would lead to less environmental impacts are significantly less in comparison with the STPG barrage under ebb-only generation. The barrage could also play a significant role in reducing the flood risk in existing condition and further flood risk induced by climate change.

ACKNOWLEDGEMENTS

The study has been carried out as part of the MAREN and MAREN2 projects, which is part funded by the European Regional Development Fund (ERDF) through the Atlantic Area Transnational Programme (INTERREG IV).

REFERENCES

- Aggidis, G. & Benzon, D. (2013). Operational Optimisation of a Tidal Barrage across the Mersey Estuary using 0-D Modelling. *Ocean Engineering*, 66, 69-81.
- Ahmadian, R., Falconer, R.A. & Bockelmann-Evans, B. (2012). Far-field Modelling of the Hydro-environmental Impact of Tidal Stream Turbines. *Renewable Energy*, 38, 107-116.
- Ahmadian, R., Falconer, R.A. & Bockelmann-Evans, B. (2014a). Comparison of Hydro-Environmental Impacts for Ebb-Only and Two-Way Generation for a Severn Barrage. *Computers & Geosciences*, 71, 11-19.
- Ahmadian, R., Falconer, R.A. & Lin, B. (2010). Hydro-Environmental Modelling of Proposed Severn barrage, UK. *Proceedings of the Institution of Civil Engineers-Energy*, 163(3), 107-117.
- Ahmadian, R., Olbert, A.I., Hartnett, M. & Falconer, R.A. (2014b). Sea level rise in the Severn Estuary and Bristol Channel and impacts of a Severn Barrage. *Computers and Geosciences*, 66, 94-105.
- Angeloudis, A., Ahmadian, R., Falconer, R.A. & Bockelmann-Evans, B. (2016). Numerical Model Simulations for Optimisation of Tidal Lagoon Schemes. *Applied Energy*, 165, 522-536.
- Baker, A.C. (1991). *Tidal Power*. Peter Perengrinus Ltd, London, 250.
- Bray, S., Ahmadian, R. & Falconer, R.A. (2016). Impact of Representation of Hydraulic Structures in Modelling a Severn barrage. *Computers and Geosciences*, 89, 96-106.
- DECC. (2010a). *Independent Report: Severn Embryonic Technologies Scheme- Final Report and Development Route Map (Rolls Royce)*, London.
- DECC. (2010b). *Severn Tidal Power Feasibility Study: Conclusions and Summary Report*.
- Fairley, I., Ahmadian, R., Falconer, R.A., Willis, M.R. & Masters, I. (2014). The Effects of a Severn Barrage on Wave Conditions in the Bristol Channel. *Renewable Energy*, 68, 428-442.
- Falconer, R.A. (1993). An Introduction to Nearly Horizontal Flows. In *Coastal, Estuarial and Harbour Engineers' Reference Book*, 27-36.
- Falconer, R.A. & Li, G.Y. (1992). Modeling Tidal Flows in an Islands Wake Using a 2-Equation Turbulence Model. *Proceedings of the Institution of Civil Engineers-Water Maritime and Energy*, 96, 43-53.
- Falconer, R.A., Xia, J.Q., Lin, B.L. & Ahmadian, R. (2009a). The Severn Barrage and Other Tidal Energy Options: Hydrodynamic and Power Output Modelling. *Science in China Series E-Technological Sciences*, 52, 3413-3424.
- Falconer, R.A., Xia, J.Q., Lin, B.L. & Ahmadian, R. (2009b). The Severn Barrage and Other Tidal Energy Options: Hydrodynamic and Power Output Modelling. *Science in China Series E-Technological Sciences*, 52, 3413-3424.
- Heaps, N.S. & Jones, J.E. (1981). Three-Dimensional Model for Tides and Surges with Vertical Eddy Viscosity Prescribed in Two Layers—II. Irish Sea with Bed Friction Layer. *Geophysical Journal of the Royal Astronomical Society*, 64, 303-320.
- Kadiri, M., Ahmadian, R., Bockelmann-Evans, B., Rauen, W. & Falconer, R. (2012). A Review of the Potential Water Quality Impacts of Tidal Renewable Energy Systems. *Renewable and Sustainable Energy Reviews*, 16, 329-341.
- Kashefipour, S.M., Falconer, R.A., Lin, B. & Harris, E.L. (2000). *FASTER Model Reference Manual*, Hydro-environmental Research Centre Report, Cardiff University.
- Kirby, R. & Retière, C. (2009). Comparing Environmental Effects of Rance and Severn barrages. *Proceedings of the Institution of Civil Engineers - Maritime Engineering*, 162, 11-26.
- SeaZone. (2013). Available: <http://www.seazone.com/HydroSpatialOne.php> [Accessed: 2013/04/24].
- Stapleton, C.M., Wyer, M.D., Kay, D., Bradford, M., Humphrey, N., Wilkinson, J., Lin, B., Yang, L., Falconer, R.A., Watkins, J., Francis, C.A., Crowther, J., Paul, N.D., Jones, K. & McDonald, A.T. (2007a). *Fate and Transport of Particles in Estuaries, Volume II: Estimation of Enterococci Inputs to the Severn Estuary from Point and Diffuse Sources*, Environment Agency Science Report, Bristol.
- Stapleton, C.M., Wyer, M.D., Kay, D., Bradford, M., Humphrey, N., Wilkinson, J., Lin, B., Yang, L., Falconer, R.A., Watkins, J., Francis, C.A., Crowther, J., Paul, N.D., Jones, K. & McDonald, A.T. (2007b). *Fate and Transport of Particles in Estuaries, Volume IV: Numerical Modelling for Bathing Water Enterococci Estimation in the Severn Estuary*, Environment Agency Science Report, 139.
- Sustainable Development Commission. (2007). *Turning the Tide: Tidal Power in the UK*, Sustainable Development Commission London.
- Xia, J.Q., Falconer, R.A. & Lin, B.L. (2010a). Hydrodynamic Impact of a Tidal Barrage in the Severn Estuary, UK. *Renewable Energy*, 35, 1455-1468.
- Xia, J.Q., Falconer, R.A. & Lin, B.L. (2010b). Impact of Different Operating Modes for a Severn Barrage on the Tidal Power and Flood Inundation in the Severn Estuary, UK. *Applied Energy*, 87, 2374-2391.
- Zhou, J., Pan, S. & Falconer, R.A. (2014). Effects of Open Boundary Location on the Far-Field Hydrodynamics of a Severn Barrage. *Ocean Modelling*, 73, 19-29.

GEOMETRY AND ALIGNMENT OPTIMIZATION OF BREAKWATERS USING A GENETIC ALGORITHM

MAHSA JAHANGARD⁽¹⁾ & KOUROSH HEJAZI⁽²⁾

^(1,2) Civil Engineering Department, K. N. Toosi University of Technology, Tehran, Iran,
m.jahangard@email.kntu.ac.ir; hejazik@kntu.ac.ir

ABSTRACT

In this study, a genetic algorithm is developed which incorporates a hydrodynamic numerical model to achieve an efficient design strategy for the planform of breakwaters in order to optimize the breakwater geometry by minimizing wave heights entering the harbor. The optimization approach of the genetic algorithm finds the best possible solution among different geometries for the breakwater by minimizing the wave height in the harbor, while applying the economic considerations through the constraints of the length of the breakwater. An optimized geometry is reached by optimizing the length and angles of a broken line for the breakwater alignment. The simple crossover (single-point) method is compared to the convex crossover method, which allows definition of convex search zones. By changing the range of variables of the problem, different breakwater shapes resulted from the optimization operations and their effects on the results are studied.

Keywords: Optimization; genetic algorithm; breakwaters; wave attenuation; REF/DIF numerical model.

1 INTRODUCTION

The layout of breakwaters, and their shape and location are usually designed under some hydrodynamic assumptions, with the aid of the structural analysis, and based on the experience of the designer (Isebe et al., 2008b). The design, however, may not include the optimal economic and hydrodynamic considerations. A shape optimization procedure may include an iterative process in which the optimal design meets the criteria and the constraints. On the other hand, optimization algorithms have been widely used in solving engineering problems. For the optimization of the shape of coastal structures, also numerous studies have been recently carried out (Isebe et al., 2008b; Elchahal et al., 2013; Diab et al., 2014).

Ryu et al. (2005) made an optimization approach for design of a composite breakwater by a recently developed metropolis genetic algorithm (MGA). Clauss and Birk (1996) focused on hydrodynamic shape optimization for large offshore structures (oil platforms) based on nonlinear programming algorithms. Kagemoto (1992) worked on the position of floating bodies to minimize the forces acting on them. Isebe et al. (2008a) utilized a shape optimization approach to tackle beach erosion problems. They addressed the shape optimization of geotextile tubes placed on the seabed in order to change the sea bottom shape and subsequently reduce beach erosion effects.

Elchahal et al. (2013) optimized design of detached breakwaters in Port of Beirut in Lebanon using a genetic algorithm and obtained the optimum layout of the detached breakwater considering wave disturbance inside the port and navigational constraints. Diab et al. (2014) addressed an optimization problem of the design of detached breakwaters at offshore terminals. A genetic algorithm was used to solve the problem and the hydrodynamic model was based on mild-slop equations. Michailides and Angelides (2015) developed a multi objective optimization process of a flexible floating structure subjected to regular and irregular incident waves.

Isebe et al. (2008b) worked on the optimal shape design of defense structures for minimizing the short-wave impact for a fixed bathymetry in coastal areas. They solved a specific simplified boundary value problem describing the short-wave propagation toward a vertical sea cliff or vertical wall and modified the shape of the defense structures in order to minimize a pre-defined cost function, and taking into account the strength (energy) of the water waves.

The main objective of this paper is to develop an optimization approach for the breakwater geometry using a genetic algorithm. The algorithm finds the optimum shape for a breakwater by minimizing the wave height inside the harbor and considering a length constraint, described in Section 2. In Section 3, the genetic algorithm approach is defined, where the random generation method is explained, and the selection, mutation and crossover processes are elaborated. The cost function is also described in this section, which is defined by the minimum wave height and a constraint function. The hydrodynamic model REF/DIF (Kirby and Dalrymple, 1994), which simulates wave propagation inside the domain, and was used to calculate the fitness of each individual, is presented in Section 4. Optimization-numerical modeling procedure is described in Section 5. Section 6 includes the optimization results, and various modes of problem solving are investigated. A conclusion is provided in Section 7.

2 OPTIMIZATION PROBLEM

The optimization problem is assumed to be a finite dimensional constrained minimization problem, which symbolically may be considered to find a design variable vector $x \in R^n$; to minimize the cost function $f(x)$ and subject to the m constraints $g_i(x) \leq 0$.

In this study, a genetic algorithm (GA) is developed which incorporates the REF/DIF numerical model to optimize the geometry and location of breakwaters while the wave height is minimized. A series of x parameters form a new construction, and the height of waves is estimated in the harbor according to the planform geometry of the breakwater using the wave hydrodynamic model. The wave height is then minimized, by collaboration between the GA and the REF/DEF numerical model, which is the objective function value with the observation of the economic constraints.

2.1 Parameterization of the structure

The choice of control parameters is very important for the quality of the optimization. A suitable space control set-up should be defined and the constraints need to be correctly accounted to reach a realistic optimal structure (Elchahal et al., 2013). Figure 1 shows an initial shape for a breakwater with an angle of 45° with the x -axis, which has been utilized for the present study. It is assumed that no definite shape is preferred. The structure is parameterized by several points. Each point could move within a certain area (Figure 2), and therefore, form different shapes for the breakwater. The coordinates of these points determine genetic algorithm variables.

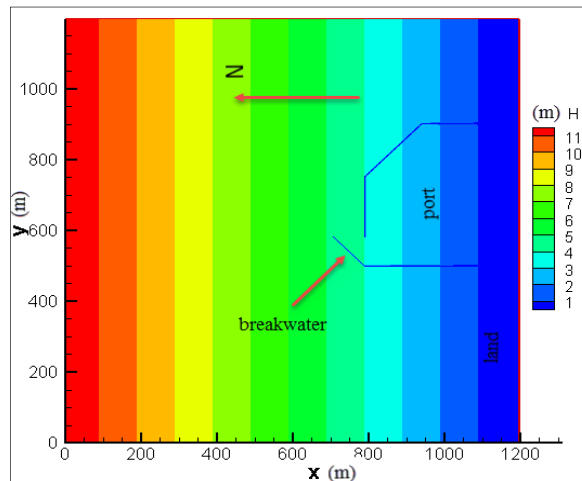


Figure 1. Bathymetry and initial shape of the harbor.

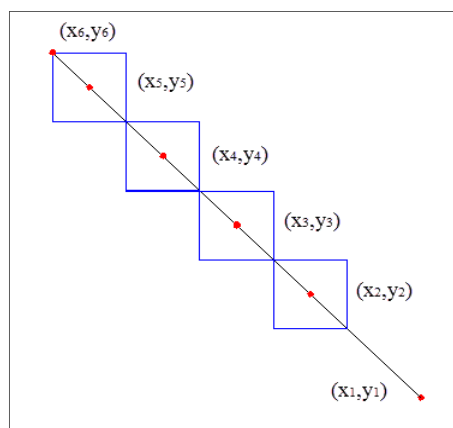


Figure 2. Parameterization of the structure.

2.2 Bathymetry definition

The bathymetry of the harbor used in the present study is illustrated in Figure 1, which exhibits a constant mild slope where the water depth varies from twelve meters in sea line, to zero in the coast.

3 GENETIC ALGORITHM

Genetic algorithm is a stochastic global search method based on the principles of natural selection and survival of the fittest elements that operates on a population of the potential solutions to produce better approximations to an optimal solution (Elchahal et al., 2013). It is structured as demonstrated in the flow chart

shown in Figure 3 for the present study. The primary population is generated randomly and the hydrodynamic model is used to calculate the fitness of each individual. For the production of a new generation three main operations are needed; selection, crossover, and mutation. In this study, the best individuals are selected via the tournament method according to their level of fitness in the problem. Each pair of the selected parents is combined via convex crossover. The mutation allows random access to different parts of the search zone by changing a number of variables, and thus produces individuals with new properties in the generation. The operation is repeated to achieve an optimum solution, unless the stopping criteria stop the routine.

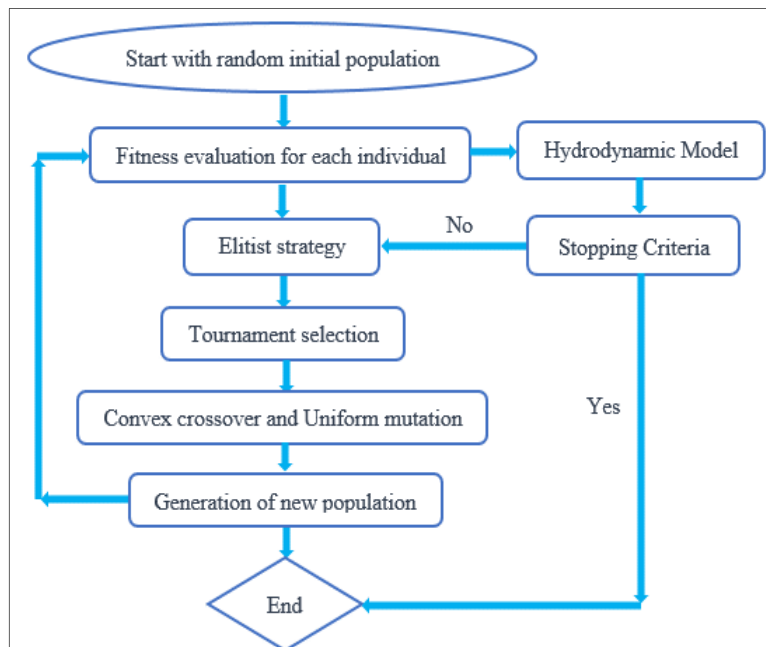


Figure 3. Flow chart of the GA for optimization of shape of a breakwater.

This process leads to the evolution of populations of individuals that are better suited to their environment than the individuals that they were created from (Elchahal et al., 2013). The genetic algorithm operation may be validated by using benchmark functions which are used to assess the optimization algorithm such as Ackley's function and Levi function N.13.

3.1 Fitness function

The genetic algorithm is used to solve the problem where the fitness function consists of the objective function penalized by the constraint function. The objective is to determine an optimal layout of the breakwater which minimizes the wave height in the harbor. The hydrodynamic model computes the height of the wave in the harbor corresponding to the planform geometry of the breakwater. The objective function is defined as follows:

$$f(x_i) = H_{avg} \quad [1]$$

where H_{avg} is the average of the wave heights in the harbor or access channel. A fifteen-percent limit for the length increase of the original breakwater is imposed to observe the economic considerations. Most structural optimization problems are the constrained minimization problems and they need to be transformed into unconstrained minimization problems. For this purpose, SUMT-exterior penalty function method may be effectively used (Ryu et al. 2005). The fitness function is formulated from the objective function and the breakwater length constraint as follows:

$$h(x_i) = f(x_i) + q \left[\left(\frac{l_i}{l_{tot}} - 1.15 \right) + \left| \frac{l_i}{l_{tot}} - 1.15 \right| \right]^2 \quad [2]$$

Here, $h(x_i)$ is a transformed objective function to be minimized, $f(x_i)$ is the objective function, q is a penalty parameter, which is set to $q = 10^5$ in this study, l_i is the length of each new shape of the breakwater and l_{tot} is the total (initial) length of breakwater. Since GA is a maximization algorithm, the minimization problem must be converted to the maximization form. To convert the GA from minimization to maximization, the fitness function is defined as follows:

$$F(x_i) = \frac{1}{h(x_i)} \quad [3]$$

Here, $F(x_i)$ is the fitness function to be maximized.

3.2 Search zone

To conduct a search the algorithm uses a crossover operator. The combination of parents results from the convex crossover method, in which a convex search zone is created to allow the offspring to be in the allowable spatial zone and inherit properties of their parents through application of a random variable. The offspring which results from this combination is defined by Eq. [4] as follows:

$$x'_1 = \lambda_1 x_1 + \lambda_2 x_2, x'_2 = \lambda_1 x_2 + \lambda_2 x_1 \quad [4]$$

where x_1 and x_2 are the first and second parents, x'_1 and x'_2 are the first and second offsprings and λ is a random number smaller than 1 and is defined according to the Eq. [5] as follows:

$$\lambda_1 + \lambda_2 = 0, \lambda_1 > 0, \lambda_2 > 0 \quad [5]$$

4 HYDRODYNAMIC MODELING

The REF/DIF numerical model has been utilized to study the propagation of waves from deep water toward the area of interest. REF/DIF describes the propagation of water waves over a weakly irregular sea bottom for which shoaling, refraction, diffraction, and energy dissipation are taken into account (Kirby and Dalrymple, 1994). In general, the diffraction process is of primary importance at the tips of breakwaters or the harbor entrance. The refraction plays a secondary role at areas with a relatively flat bottom, but is very relevant when passing over dredged navigation channels (Elchahal et al., 2013). REF/DIF is a nonlinear combined refraction and diffraction code for the incident wave based on a Stokes expansion of the water wave problem. Combined refraction/diffraction models include both effects explicitly, thus permitting modeling of waves in regions where the bathymetry is irregular and where diffraction is important (Kirby and Dalrymple, 1994). The parabolic model used in REF/DIF combines the essential features of the two wave models which are described in the following sections.

4.1 Linear mode of wave propagation based on mild slope equation

Berkhoff's equation (1973), known as the mild slope equation, is in terms of the surface displacement, $\eta(x, y)$. The equation, in terms of horizontal gradient operator, reads as follows:

$$\nabla_h \cdot (CC_g \nabla_h \eta) + \sigma^2 \frac{C_g}{C} \eta = 0 \quad [6]$$

Here, $C = \sqrt{\left(\frac{g}{k}\right) \tanh kh}$ is the wave celerity and $C_g = C\{1 + 2kh/\sinh 2kh\}/2$ is the group velocity, where the local water depth is $h(x, y)$ and g is the acceleration of gravity. For the linear mild slope equation, Radder (1979) developed a parabolic model and Booij (1981) developed a splitting of the elliptic equation (Kirby and Dalrymple, 1994).

4.2 Diffraction models

Mei and Tuck (1980) developed a simple parabolic equation for wave diffraction as follows:

$$\frac{\partial A}{\partial x} = \frac{i}{2k} \frac{\partial^2 A}{\partial y^2} \quad [7]$$

where A is a complex amplitude related to the water surface displacement by Eq. [8] as follows:

$$\eta = Ae^{i(kx - \sigma t)} \quad [8]$$

Yue and Mei (1980), by using multiple scales approach, developed a nonlinear form of this equation, which accurately predicts the propagation of a third order Stokes wave. Kirby (1983) by using a Lagrangian approach, and Kirby and Dalrymple (1983a) with a multiple-scales technique, developed the predecessor to the REF/DIF1 model, which bridged the gap between the nonlinear diffraction models and the linear mild slope equation.

This method has a distinct disadvantage in that it becomes invalid in the limit of shallow water. Hedges (1976) has proposed simple modifications to the linear dispersion relation, which models amplitude dispersion in shallow water and becomes asymptotic to the linear wave dispersion relation in deep water, given by Eq. [9] as follows (Kirby and Dalrymple, 1986b):

$$\omega^2 = gk \tanh(k[h + |A|]) \quad [9]$$

Kirby and Dalrymple (1986b) proposed a simple, empirical extension to the last two methods which has the effect of smoothly connecting the analytic results for Stokes wave (intermediate and deep water) and an empirical relation due to Hedges (1976) for shallow water which has been used in REF/DIF1 model described by Dalrymple and Kirby (1985) and has been used in this study. This method has been validated by Kirby and Dalrymple (1986b), whereby the results of composite dispersion relation have been compared with the data taken from the experiments described by Berkhoff et al. (1982).

5 OPTIMIZATION-NUMERICAL MODELING PROCEDURE

The hydrodynamic model is coupled with the genetic algorithm to compute the wave heights corresponding to different scenarios designed for the optimization procedure. The initial population for the genetic algorithm (GA), which consists of different breakwater geometries, is generated based on the nodes defined along the breakwater length and random displacement of these nodes in a range of spatial allowances. The initial population size is assumed to vary between 35 and 55 in proportion to the size of search zone. Therefore, with an increase in the range of variables, the initial population size escalates to enable the algorithm to search the solution zone appropriately so that the absolute optimum solution is achieved. Fitness of each solution is evaluated by using the computed wave heights by the hydrodynamic model, bounded by a length increase constraint, which has been taken to be equal to fifteen percent of the original length of the breakwater in this study.

The member with the highest level of fitness is selected as the elite member. To save the best member of each generation, it is transferred to the next generation without any change. After placing the elite member in the new generation, the tournament method is used to combine and generate the remaining offspring. To this end, three members are randomly selected from the existing population to compete with each other based on fitness. The two members with higher fitness are selected as parents. Since each parent pair generates an offspring pair, selection is repeated for half the number of parents required for reproduction. The crossover rate is set to 0.9. Therefore, 0.9 new members are generated through crossover and the rest of the population is obtained by transferring the previous generation parents to the next generation without making any change. After generating the new generation, some of the variables are selected randomly to mutate from some members, but the number of these variables depends on the mutation rate, which is determined to vary between 0.07 and 0.1 in proportion to the number of design variables to avoid variation of all members and preserve the population diversity.

The genetic algorithm, by searching among the initial solutions, anticipates new formations for the breakwater. The superior solutions remain in the next generations and finally the algorithm is converged toward the optimized solution and the optimum shape is achieved.

6 RESULTS

In this paper, to show the positive effect of the convex combination method on searching the solution space, the results of this method are compared to the results of the simple single-point combination method, which generates the offsprings by connecting the parents at the cut-off point and moving their attributes on both sides of this point.

Figure 4 shows that when the parent composition is based on the creation of a convex search zone, the convergence to the optimal solution takes place rapidly without generation of local optima, and within 12 generations. However, in the simple crossover, convergence is reached over a relatively long period of time and several local optima at the 68th generation. Hence, the convex crossover method yields the absolute optimum solution in a shorter period of time and sometimes with higher precision due to the search of the solution space extensively and creating a wider range of solutions in the early generations.

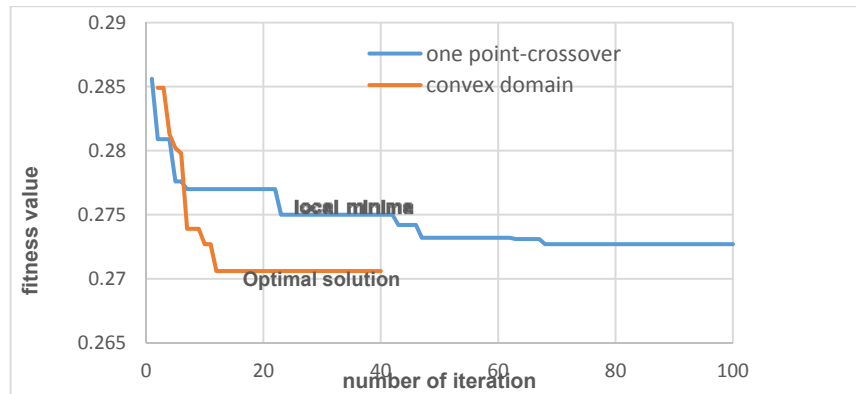


Figure 4. Fitness value for the best generation in each population using GA with one-point-crossover and convex domain.

The integration of the wave numerical model and genetic algorithm was utilized to optimize the shape of the breakwater. Figure 5 shows the change of water elevation (wave crest/trough) around the breakwater in harbor before and after the application of the optimization algorithm and figure 6 depicts the range of allowance for displacement of points around the breakwater, and the resultant optimal alignment of the breakwater.

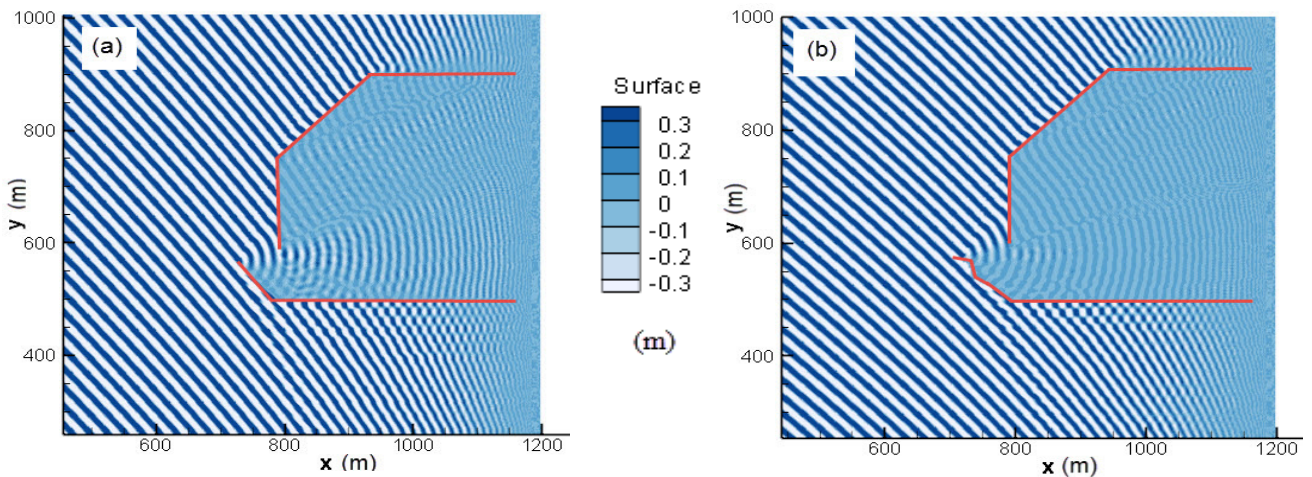


Figure 5. (a) Change of water elevation around initial structure. (b) Change of water elevation around optimized structure. (NW incoming waves with $T = 2s$ and $a = 0.5m$).

Figure 6 shows several fractures created in the optimal shape of breakwater, which increase the attenuation of wave energy, and therefore the water surface turbulence subsides behind the optimal breakwater (Figure 5-b). In the present example, the average wave height in the access channel decreases from 0.454 to 0.278 m which shows a reduction of 38%. Water elevation in intended space changes from -0.6 to 0.6 m, however, for a higher resolution of the wave height reduction in figure 5, it is graphed from -0.3 to 0.3 m).

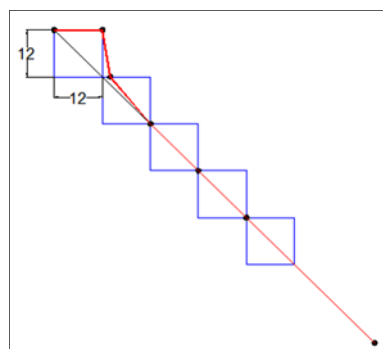


Figure 6. Defined range for the movement of points along the breakwater for optimized shape in first case (Dimensions are meters).

Considering the optimum breakwater shape and fractures along its length, it is concluded that effective fractures occurred in the vicinity of the harbor entrance and the lower parts of the breakwater remain unchanged. Hence, as the ranges for the movement of points move toward the entrance, the effect of fracture on the decrease in wave height is expected to increase. In the next example the ranges for the movement of points are increased in size and are arranged by assuming a 6-m overlap toward the entrance.

Figure 7 shows the water elevation around the breakwater before and after the application of the optimization algorithm. Here after the optimization, the average height of waves in the access channel decreases from 0.454 to 0.261 m, which shows a 43% decrease, with the same presentation as Figure 5.

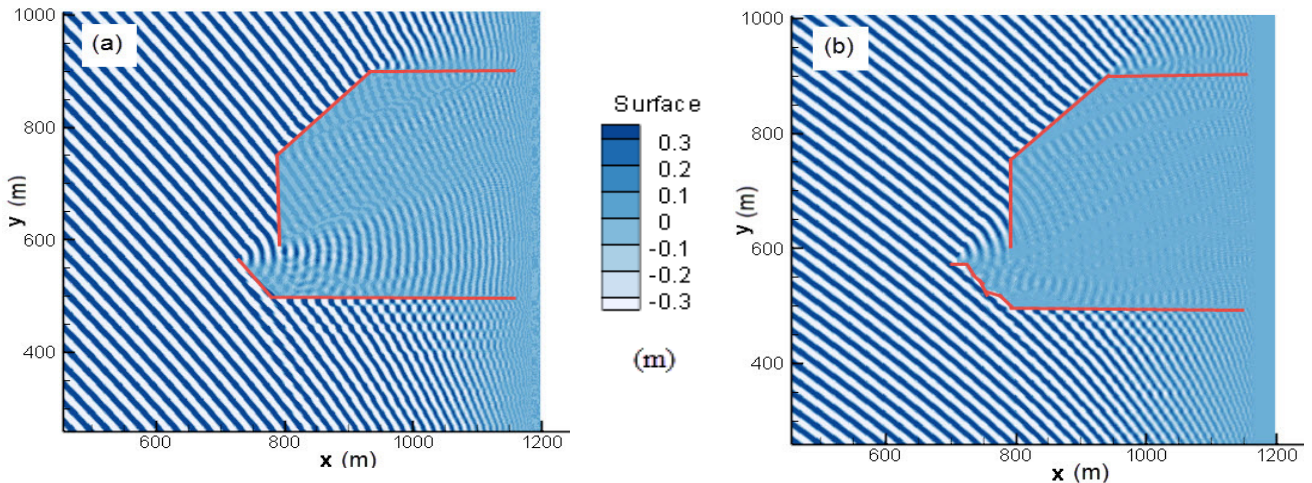


Figure 7. (a) Change of water elevation around initial structure. (b) Change of water elevation around optimized structure. (NW incoming waves with $T = 2s$ and $a = 0.5m$)

The optimum breakwater shape (Shown in figure 8) provides a high percentage of wave height reduction behind the breakwater. However, the number of fractures along the breakwater and their angles can result in difficulties of breakwater construction. To overcome this, fewer points were defined along the breakwater length and their displacement range was determined such that fractures occur at mild angles.

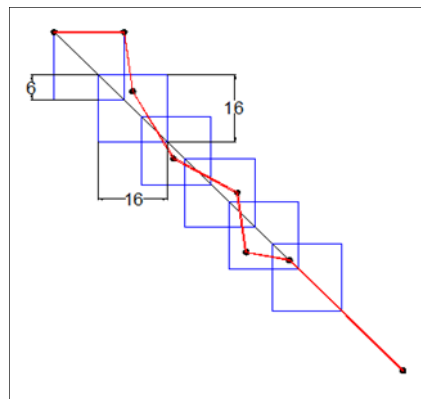


Figure 8. Defined range for the movement of points along the breakwater for optimized shape in second case (Dimensions are meters).

In next example, Figure 9, the initial average of wave height is equal to 0.454 m in the access channel, which is reduced to 0.33 m after the application of the optimization algorithm. This means a decrease of wave height equal to 27.3% compared to the initial structure in the access channel. Figure 10 depicts the range of the allowance for the displacement of the points along the breakwater, and the resultant optimal shape of the breakwater.

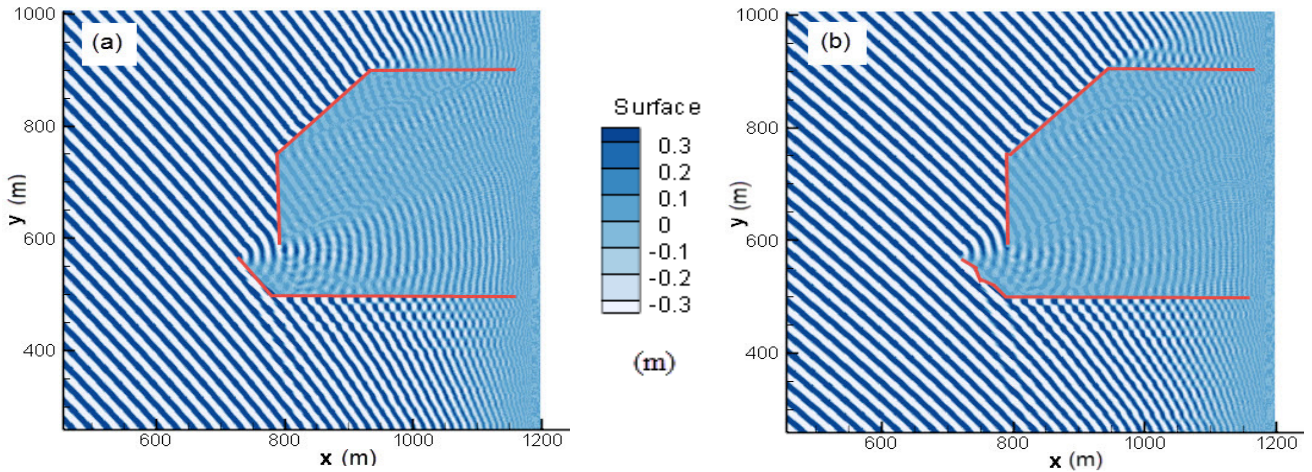


Figure 9. (a) Change of water elevation around initial structure. (b) Change of water elevation around optimized structure. (NW incoming waves with $T = 2$ s and $a = 0.5$ m).

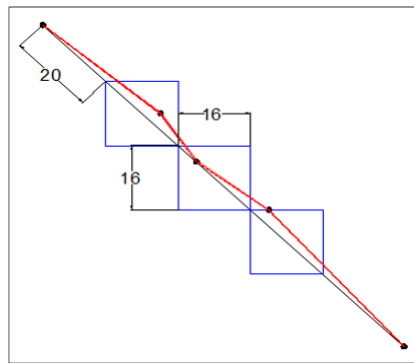


Figure 10. Defined range for the movement of points along the breakwater for optimized shape in third case (Dimensions are meters).

Hence, with a decrease in the number and angle of bends, although the resulting optimum breakwater geometry will be more suitable from the operational point of view, the wave height reduction decreases behind the breakwater.

By changing the defined ranges for the movement of point, and their placement along the breakwater, the search space magnitude, number of variables, size population and optimum shape are obtained and the resulting optimality changes. Table 1 presents the results for different scenarios. Figure 11 shows the geometrical properties of parameters including: the allowance for zoning variation (a); the overlapping length for zones (b) and the distance from the tip of the breakwater (c).

Table 1. Optimality percentage for different zones of variables.

scenarios	a(m)	b(m)	c(m)	Optimum percentage of wave attenuation in access channel (%)
1	16	6	0	41.5 - 43
2	16	0	0	38.32 - 40.3
3	12	0	0	35.24 - 38.54
4	8	0	0	33.92 - 34.58
5	16	0	6	27.75 - 30.39
6	16	0	20	26.87 - 27.31

Due to the random performance of the genetic algorithm the program was conducted 10 times for each scenario and a range was determined depending on the optimality percentage. In view of the results, the user will be able to select the related range of design variables depending on desired optimality.

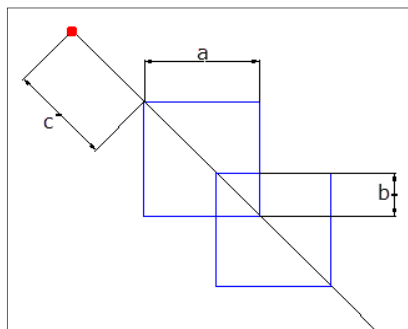


Figure 11. Definition of variables for the allowance of the geometry change.

7 CONCLUSIONS

An integrated wave modeling-genetic algorithm procedure has been deployed to minimize the wave height in harbors and access channels, and to achieve an optimized shape for breakwaters. The strategy may be deployed for designing breakwaters to accommodate sheltered zones in harbors.

According to the above discussion, with optimized shape of breakwater using genetic algorithm, reduction of waves height increased to a value of 43%. By defining different ranges around the breakwater for movement of points, different optimum shape for breakwaters and different levels of wave height reduction will be achieved which can be used according to need. Shapes with angle smooth fracture are more suitable in terms of performance and this is while with fractures smoothly impact of breakwater is reduce for reduction of wave energy.

REFERENCES

- Berkhoff, J.C.W. (1973). Computation of Combined Refraction—Diffraction. In *Coastal Engineering 1972*, 471-490.
- Berkhoff, J.C.W., Booy, N. & Radder, A.C. (1982). Verification of Numerical Wave Propagation Models for Simple Harmonic Linear Water Waves. *Coastal Engineering*, 6(3), 255-279.
- Booij, N. (1981). Gravity Waves on Water with Non-Uniform Depth and Current, *Doctoral dissertation*. Delft University of Technology.
- Clauss, G. F. & Birk, L. (1996). Hydrodynamic Shape Optimization of Large Offshore Structures. *Applied Ocean Research*, 18(4), 157-171.
- Dalrymple, R.A. & Kirby, J.T. (1985). *Combined Refraction/Diffraction Model REF/DIF 1, User's Manual*", Coastal and Offshore Engineering and Research. Inc., Newark, DE.
- Diab, H., Lafon, P. & Younes, R. (2014). Optimisation of Breakwaters Design to Protect Offshore Terminal Area. In *Proceedings of the IASTED International Conference on Modelling, Simulation and Identification, MSI*, Acta Press, 70-75.
- Elchahal, G., Younes, R. & Lafon, P. (2013). Optimization of Coastal Structures: Application on Detached Breakwaters in Ports. *Ocean Engineering*, 63, 35-43.
- Kagemoto, H. (1992). Minimization of Wave Forces on an Array of Floating Bodies—The Inverse Hydrodynamic Interaction Theory. *Applied ocean research*, 14(2), 83-92.
- Isebe, D., Azerad, P., Mohammadi, B. & Bouchette, F. (2008). Optimal Shape Design of Defense Structures for Minimizing Short Wave Impact. *Coastal Engineering*, 55(1), 35-46.
- Isebe, D., Azerad, P., Bouchette, F., Ivorra, B. & Mohammadi, B. (2008). Shape Optimization of Geotextile Tubes for Sandy Beach Protection. *International journal for numerical methods in engineering*, 74(8), 1262-1277.
- Kirby Jr, J.T. (1983). *Propagation of Weakly Nonlinear Surface Water Waves in Regions with Varying Depth and Current* (No. CE-83-37), DELAWARE UNIV NEWARK DEPT OF CIVIL ENGINEERING.
- Kirby, J.T. & Dalrymple, R.A. (1983). A Parabolic Equation for the Combined Refraction—Diffraction of Stokes Waves by Mildly Varying Topography. *Journal of Fluid Mechanics*, 136, 453-466.
- Kirby, J.T. & Dalrymple, R.A. (1986). An Approximate Model for Nonlinear Dispersion in Monochromatic Wave Propagation Models. *Coastal Engineering*, 9(6), 545-561.
- Kirby, J.T. & Dalrymple, R.A. (1994). *Combined Refraction/Diffraction Model REF/DIF 1, Version 2.5: Documentation and User's Manual*, Center for Applied Coastal Research, Department of Civil Engineering, University of Delaware.
- Mei, C.C. & Tuck, E.O. (1980). Forward Scattering by Long Thin Bodies. *SIAM Journal on Applied Mathematics*, 39(1), 178-191.
- Michailides, C. & Angelides, D.C. (2015). Optimization of a Flexible Floating Structure for Wave Energy Production and Protection Effectiveness. *Engineering Structures*, 85, 249-263.
- Radder, A.C. (1979). On the Parabolic Equation Method for Water-Wave Propagation. *Journal of fluid mechanics*, 95(01), 159-176.

- Ryu, Y.S., Park, K.B., Kim, T.B., Na, W.B. & Younes, R. (2005). Optimum Design of Composite Breakwater with Metropolis GA. *Proceedings of 6th World Congresses of Structural and Multidisciplinary Optimization, Rio de Janeiro, Brazil*, 30.
- Yue, D.K. & Mei, C.C. (1980). Forward Diffraction on Stokes Waves by a Thin Wedge. *Journal of Fluid Mechanics*, 99(1), 33-52.

PULL OUT CAPACITY OF SUBMERGED GABIONS

SRINEASH VIJAYA KUMAR⁽¹⁾ & MURALI KANTHARAJ⁽²⁾

^(1,2) Department of Ocean Engineering, Indian Institute of Technology Madras, Chennai, India,
srineash@gmail.com; murali@iitm.ac.in

ABSTRACT

Gabions are being used in wave environment to prevent coastal erosion. Gabion being porous in nature helps in energy dissipation. It is essential to know the engineering properties of gabions for its real-time application and design. The gabions may be used as an artificial reef, groynes, or a breakwater; the idea of forces required to displace the gabions is essential to study the stability characteristics. The ease of construction and shorter span of installation makes gabion apt for wave dominated coastal environment. Further it has been reported in literatures that gabions promote marine life in its vicinity, hence use of gabions may be considered as environmentally friendly engineering approach. The present study involves determination of minimum force required to displace an individual gabion arranged as a coastal structure. The pull-out tests are carried out at the Wave Flume facilities in the Department of Ocean Engineering, IIT Madras. Further, the pull out tests helps to determine the friction properties and the influence of stacking method on gabions. For the experimental study, scaled gabion models are used with a scale ratio of 1: 20. The optimum stacking arrangement based on the friction coefficient will be brought out in the study.

Keywords: Gabions; porosity; stability; friction coefficient; pull-out.

1 INTRODUCTION

Gabions are becoming increasingly popular in coastal engineering owing to its several advantages. The porous nature of gabions helps in wave attenuation. Using gabion boxes as coastal structures such as breakwaters, groynes, training walls the construction time can be minimized as it involves placing of pre-filled gabion boxes. Gabions may also be used as artificial reefs which will help in offshore wave dissipation (Srineash and Murali, 2015). The advantages of low-crested structures as offshore breakwaters are discussed in detail by Pilarczyk (2003). The ease of construction and porous nature may suite the gabion for a wave environment. Further, it has been reported in literature that gabions promote marine life. Hence, gabions may also promote marine life in its vicinity (Firth et al., 2014). Further, there is a need for ecofriendly, economical and sustainable solutions to mitigate coastal disasters. Pre-filled gabions may also be suited for remote locations where the availability of concrete may be scarce. In order to use gabions for coastal protection, design guidance for gabions is essential. Since the literature relevant to gabions are available scanty, the present study aims at bringing out the force required to deform the gabions, this is done using pull out tests. This is brought out in terms of frictional coefficient (μ). In the study, the slope of the structure is varied; in other words, the method of stacking of gabions is varied and the resulting change in the frictional coefficient is examined Pilarczyk (2003).

2 EXPERIMENTAL SET UP

The physical model study was performed in the glass flume which is 20 m long, 0.6 m wide and 0.8 m deep. A schematic sketch showing the experimental setup is shown in Figure 1. Gabion boxes are fabricated from a mesh of PVC coated galvanized iron with 0.9 mm diameter having an embedded GI wire of 0.45 mm. The mesh has a center to center spacing of 6 mm. The gabion boxes are filled with gravels of size ranging between 7.5 mm to 12.5 mm. Each gabion was weighed to a mass of 0.624 kg in order to maintain a porosity of 37%. A scale ratio of 1:20 is adopted in the study. The method of stacking of gabions were varied which in turn varies the slope of the structure and the contact area between the adjacent gabions. The slope of the typical configuration shown in the Figure 1 is 1 Vertical: 2 Horizontal in seaward direction (i.e., face of the structure where the load is applied) and 1 Vertical: 1 Horizontal: in leeward direction. The gabions are arranged such that the longer side of the gabion is parallel to the direction in which the load is applied. The water level maintained at the test section is 0.25 m throughout the study, (the water level was maintained till the top of the structure). In real time application as a coastal structure, in order to maintain tranquility conditions, most often the structure would be surface piercing. The surface piercing structure which has a free board above the water level will be subjected to wave action. Once the water level increases at the free board due to the effect of waves, there will be buoyancy effect which may lead to failure due to reduction of mass. And thus, in the present case, the buoyancy effects are accounted throughout the vertical direction. In other words, the gabion structures are considered to be submerged considering the critical condition for failure.

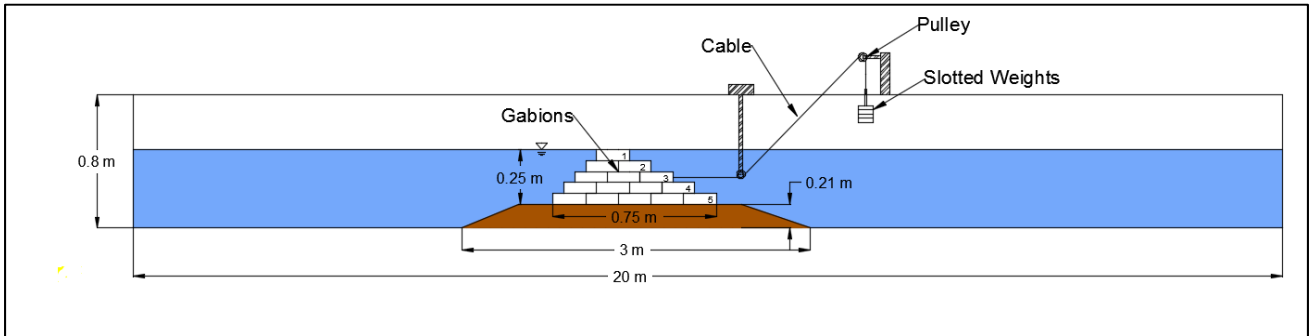


Figure 1. Schematic sketch of experimental setup.

The size of each gabion model measure 0.15 X 0.05 X 0.05 m. The pull-out test is conducted by loading each gabion individually at different layers. Similar examination has been studied by Dassanayake et al. (2011), Dassanayake and Oumeraci (2012) and Recio (2007) for Geotextile containers. Five layers of gabions were used for each configuration. Five different configurations were studied in this manuscript. Pulleys are used to transfer the load horizontally to the gabions. The height of the pulley near the face of the gabions is adjusted in accordance with the gabion layer in order to make sure that the gabion is pulled out horizontally. Further the gabions were fitted with rings in front as shown in Figure 2. This provision helps to anchor the cable on to the gabions. Slotted weights with successive increments are used to pull the individual gabions out. For each layer, the minimum weight to deform a single gabion out of the structure was noted. These values will be used to obtain the friction coefficient in the following sections.

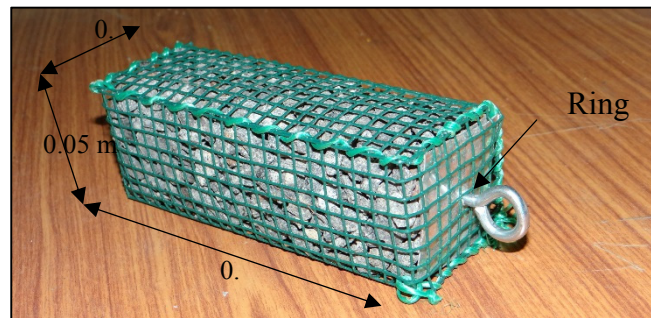


Figure 2. Gabion fitted with ring.

Table 1 shown below describes the parameters considered in the study and the corresponding prototype values. It has to be noted that the porosity was maintained same between the model and the prototype. The gabion size is fixed in the study as 3 m X 1 m X 1 m in prototype scale this is based on literature (Chinnarasri et al., 2008).

Table 1. Comparison of dimensional parameters between models and prototype

Parameter	Units	Typical Prototype	Laboratory model
Mass	kg	4992	0.624
Gabion Dimension	m	3 X 1 X 1	0.15 X 0.05 X 0.05
Stone Size	m	0.15 – 0.25	0.0075 – 0.0125
Porosity	-	37 %	37 %

3 METHODOLOGY

The gabions are stacked in different configurations in order to attain the most optimum stacking arrangement. The face slope was varied for each configuration. Five different configurations are chosen for the study they are listed below:

- (i) Face slope of 1 Vertical : 3.0 Horizontal
- (ii) Face slope of 1 Vertical : 2.0 Horizontal
- (iii) Face slope of 1 Vertical : 1.5 Horizontal
- (iv) Face slope of 1 Vertical : 1.0 Horizontal
- (v) Face slope of 1 Vertical : 0.0 Horizontal

The friction coefficient (μ) is obtained as shown below:

$$\text{The friction coefficient } (\mu) = \frac{\text{Pull out force (N)}}{\text{Weight of the gabion (N)}} \quad [1]$$

In the above equation, the weight of the gabions is corrected for overburden (surcharge loading). The load distribution factor is considered to be 0.5.

$$\text{Corrected Weight at layer } n = W + (W \times F) \times 0.5 (n-1)$$

where,

n is the layer considered

W is the weight of the Gabion

F is the load division factor based on configuration

Area ratio is the ratio of area of the gabion offering resistance to the to the peripheral area of a gabion it is given as,

$$\text{Area Ratio} = \frac{\text{Resistive Area of Gabion}}{\text{Periphral Area of Gabion}} \quad [2]$$

The pull-out force is defined as the minimum force required to deform the gabion at a given layer. This pullout force is experimentally obtained by placing slotted weights which gets transmitted as horizontal load to the gabions through the pulleys. The resistive area is defined as the area of gabion which helps in resisting the applied load by developing friction with the adjacent gabion units. The contact area of gabion with the adjacent unit is different from that of the resistive area. The contact area includes all the area of the gabion which gets in contact with the adjoining gabions whereas resistive area of the gabions corresponds to the area which prevents or resists the gabion movement during the loading (pull-out) with the frictional effect. For a particular layer, the slotted weights are added in successive increments till the gabion gets pulled out from the structure. The minimum mass with which the individual gets pulled out of the unit or structure is observed, this process is done for various levels and configurations. For each of the test case, five trials were conducted for each case and the mean value of 5 trials is adopted for the study. The variability between the test results is about 5%. Overall, a good repeatability between the experiments is observed. However, for practical field implementation, the test results should be used with suitable factor of safety as there may be scale effects due to viscous effects and density of water. These scale effects are inevitable in experiments and this can be overcome by adopting suitable factor of safety during field implementation. This factor may be established by a separate study with different scale ratio.

4 RESULTS AND DISCUSSIONS

The results of the laboratory tests for various configurations will be discussed in the upcoming sections. The results are plotted with friction coefficient as against gabion layers. The experiments are performed for five different configurations the variation of friction coefficient across various layers and the stacking arrangement will be brought out in this section.

4.1 Configuration 1 – 1 Vertical: 3 Horizontal

In Figure 3 the variation friction coefficient (μ) is plotted across the gabion layers. For better understanding, the sketch containing the configuration details is embedded in the plot. In the present plot, the gabions are arranged longitudinally and the slope on the face of the gabion is maintained as 3 horizontal to 1 vertical (i.e., 1 in 3). It has to be noted that in this method of stacking there is no overlap of gabions. Further, the resistive area of this arrangement is found to be 0.643. The resistive area is defined as the area of gabion which helps in resisting the applied load by developing friction with the adjacent units. The water level is maintained till the brim of the structure. From the Figure 3, it may be observed that the minimum friction coefficient (μ) observed is 1.87 and maximum value is found to be 2. Thus, the average friction coefficient was found to be around 1.95. Further in the present configuration, there is no effect of surcharge on the face of the gabion structure. And hence no correction to the weight is required, (i.e.,) Stabilizing force is the weight of the individual gabion.

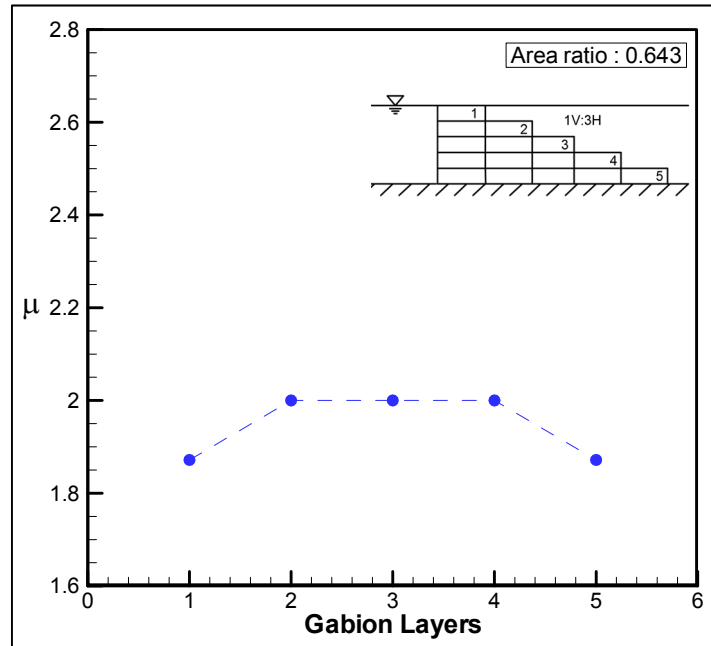


Figure 3. Variation of friction coefficient (μ) with gabion layers for a slope of 1 vertical: 3 horizontal.

Configuration 2 – 1 Vertical: 2 Horizontal

The variation friction coefficient (μ) with gabion layers is plotted in Figure 4. The sketch containing the configuration details is embedded in the plot. In the present plot, the gabions are arranged longitudinally with a slope of 2 horizontal to 1 vertical (i.e., 1 in 2). In this method of stacking there is overlap of gabions as the gabions are staggered with a slope of 1 in 2. The resistive area of this arrangement is found to be 0.714. The water level is maintained till the brim of the structure. From the Figure 4, it may be interpreted that the minimum μ observed is 2.22 and maximum μ is found to be 2.46. The average value of friction coefficient was found to be 2.31. Further, the effect of surcharge is taken into account here and hence the expression for corrected weight has to be used. For this configuration, the value of F will be $1/3$. The value of F is taken as $1/3$ since the one third of weight of the topmost gabion gets transmitted underneath (the staggered arrangement has got one-third overlap with the underlying unit).

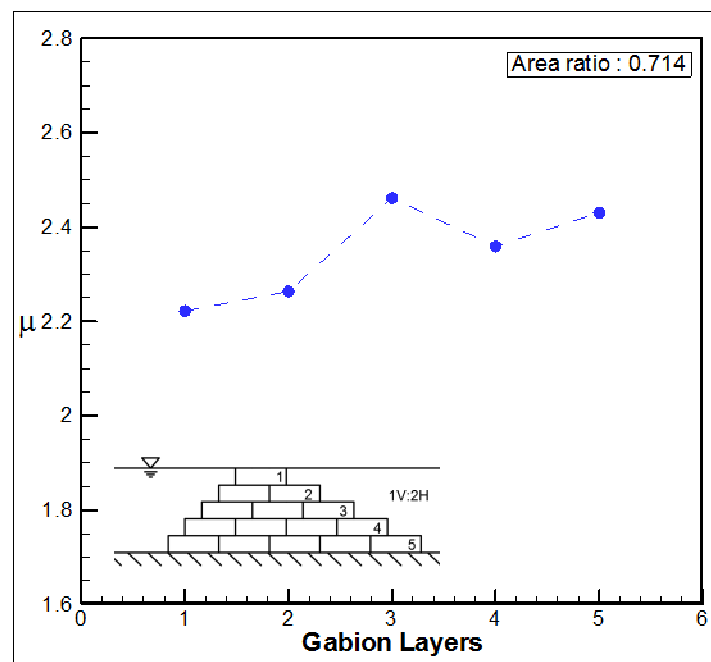


Figure 4. Variation of friction coefficient (μ) with gabion layers for a slope of 1 vertical: 2 horizontal.

Configuration 3 – 1 Vertical: 1.5 Horizontal

Figure 5 corresponds to the configuration 3, where the face slope of gabion is maintained to be 1 vertical to 1.5 Horizontal. The area ratio of this configuration is found to be 0.75. From the Figure 5, it may be inferred

that the minimum (μ) observed is 2.3 and maximum (μ) is found to be 2.52. The average value of friction coefficient is observed as 2.43. Further, the effect of overburden (surcharge) is to be considered and hence the expression for corrected weight has to be used. For this configuration, the value of F will be $\frac{1}{2}$, since half of the gabion rests over the underlying gabion assembly.

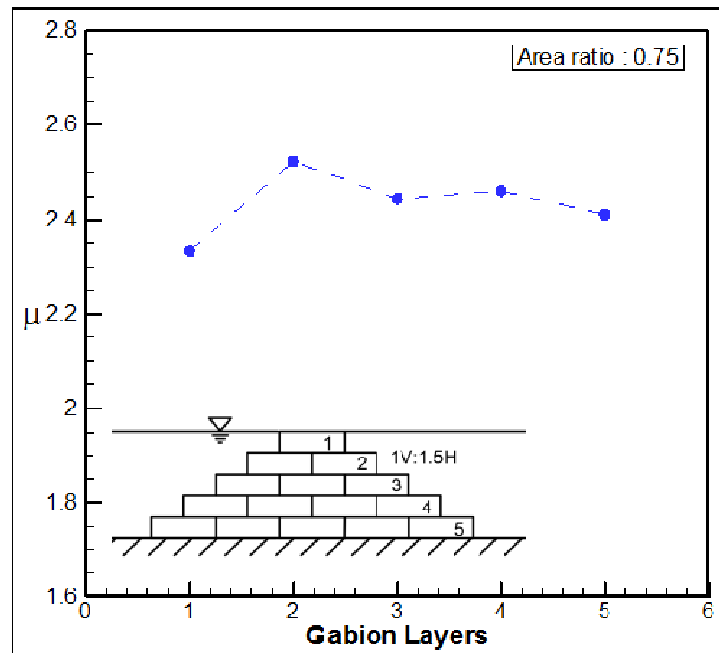


Figure 5. Variation of friction coefficient (μ) with gabion layers for a slope of 1 vertical: 1.5 horizontal.

4.2 Configuration 4 – 1 Vertical: 1 Horizontal

The plot corresponding to the configuration 4 is shown in the Figure 6. The plot depicts the variation of friction coefficient with gabion layers. The friction coefficient varies from a minimum value of 2.34 to a maximum of 2.56. The average value of μ across layers is 2.46. This arrangement has got a slope of 1 in 1 which means that 2/3rd of weight of topmost gabion gets transmitted to the gabion below. This also means that the stacking is such that the 2/3rd of the gabion overlaps over the underlying gabion. The value of F will be 2/3 since the slope maintained here is 1 in 1. The area ratio of this arrangement is seen to be 0.786.

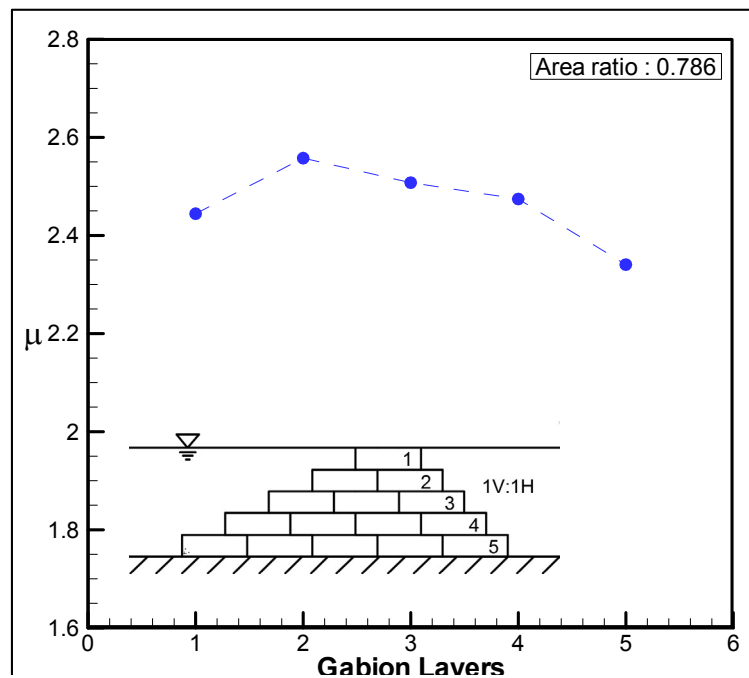


Figure 6. Variation of friction coefficient (μ) with gabion layers for a slope of 1 vertical: 1 horizontal.

4.5 Configuration 5 – 1 Vertical: 0 Horizontal

The Figure 7 shows the variation friction coefficient (μ) against the gabion layers. In the plot, the gabions are stacked longitudinally with a face slope maintained as 1 horizontal to 0 vertical (i.e., 1 in 0). It has to be noted that in this method of stacking there is no overlap of gabions. Further the area ratio of 0.857 is seen for this placement method. From the Figure 7, it may be observed that the minimum friction coefficient (μ) observed is 1.86 and maximum value is found to be 2.1. Further in the present configuration, there is effect of surcharge on the face of the gabion structure. And hence correction to the weight is required. For this configuration, the $F = 1$; where, F is the load division factor. Since the entire load of a gabion is borne by the unit below it, this arrangement has got the maximum Area ratio among the study.

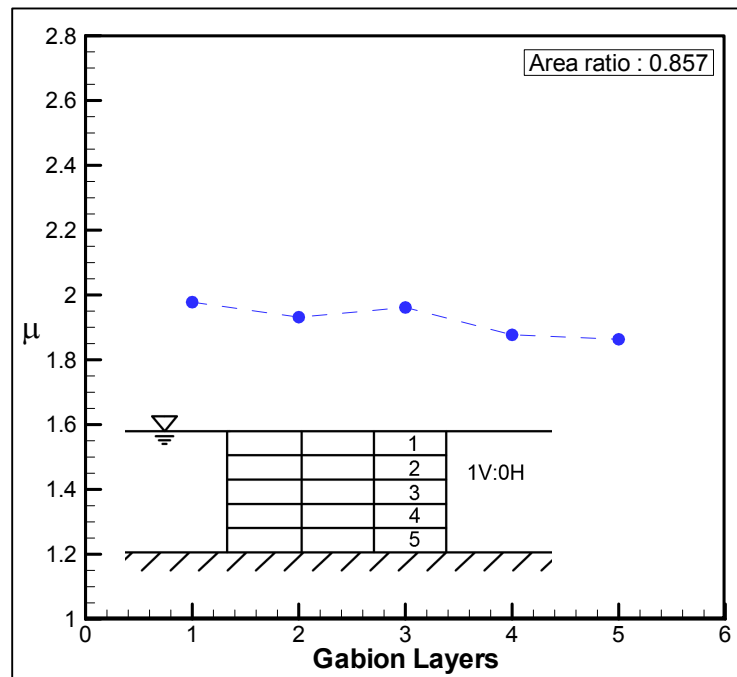


Figure 7. Variation of friction coefficient (μ) with gabion layers for a slope of 1 vertical: 0 horizontal.

Based on the experimental results from various configurations, the friction coefficient is plotted as a function of area ratio in Figure 8.

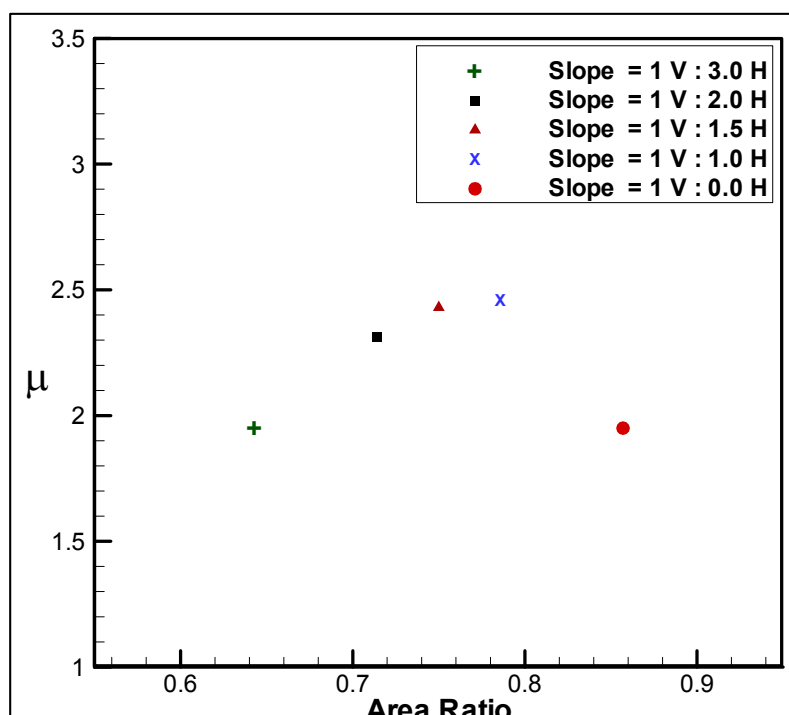


Figure 8. Variation of friction coefficient (μ) with area ratio.

From the figures, it may be inferred that the configuration 1 with a slope of 1 in 3 and configuration 5 with a slope of 1 in 0 has got lesser friction factor. This is due to the fact that the gabions are not stacked overlapping adjacent layers. Though configuration 5 has got the highest area ratio, (which may promote greater resistance) the friction factor is observed to be lower because of the stacking arrangement with no overlap with gabions over the adjacent levels. Configurations 2, 3 and 4 seem to have higher value of friction coefficient. This is due to the reason that the stacking of gabions in these configurations are done such that the gabions gets overlaid over one another. There is an increasing trend seen for these three configurations with increase in area ratio. This indirectly depicts that the increase in resistive area increases the friction coefficient. The maximum value of friction factor is observed to be for slope of 1 in 1. In Figure 8, the friction factor for each configuration is obtained by taking an average across all the layers.

5 CONCLUSIONS

A comprehensive experimental study has been carried out with the variation friction coefficient for various stacking arrangement is brought out. Further, it has been shown that the area ratio has a definite bearing on the friction coefficient. Based on the tests, it is seen that the configurations with the overlap of gabions over the adjoining levels has got maximum friction coefficient, added to this effect, the area ratio also plays an important role. From the study, it is seen that the configuration 4 with the face slope of 1 vertical to 1 horizontal has got the maximum friction coefficient which is about 2.5. Further, in wave environment, the effect of wave on the structure must be also considered. Considering the waves, a mild slope is often preferred and hence the configuration 2 with the face slope of 1 vertical: 2 horizontal may be suitable for wave environment which may help in better wave damping. Furthermore, configuration 2 has got a friction coefficient of 2.3 which is also comparable with configuration 4. The quantification of friction coefficient may be correlated to stability of gabion based structure which is very essential to know the amount of load that the structure may sustain. The present study may be considered as a source of knowledge in designing gabion structure in the wave environment.

ACKNOWLEDGEMENTS

The authors would like to thank the Department of Ocean Engineering, IIT Madras, India for providing the experimental facilities to conduct this study.

REFERENCES

- Chinnarasri, C., Donjadee, S. & Israngkura, U. (2008). Hydraulic Characteristics of Gabion-Stepped Weirs. *Journal of Hydraulic Engineering*, 134(8), 1147-1152.
- Dassanayake, D.T., Soysa, A., Munnith-Hadi, F. & Oumeraci, H. (2011). *Hydraulic Stability of Low-Crested GSC-Structures*. Internal report, Leichtweiß-Institute for Hydraulic Engineering and Water Resources, Braunschweig, Germany.
- Dassanayake, D.T. & Oumeraci, H. (2012). Important Engineering Properties of Geotextile Sand Containers and their Effect on the Hydraulic Stability of GSC-Structures. *Terra et Aqua Journal*, 127, 3-11.
- Firth, L.B., Thompson, R.C., Bohn, K., Abbiati, M., Airolidi, L., Bouma, T.J., Bozzeda, F., Ceccherelli, V.U., Colangelo, M.A., Evans, A., Ferrario, F., Hinz, H., Hoggart, S.P.G., Jackson, J.E., Moore, P., Morgan, E.H., Perkol-Finkel, S., Skov, M.W., Strain, E.M., Van Belzen, J. & Hawkins, S.J., (2014). Between a Rock and a Hard Place: Environmental and Engineering Considerations when Designing Coastal Defence Structures. *Journal of Coastal Engineering*, 87, 122–135.
- Pilarczyk, K.W. (2003). Design of Low-Crested (Submerged) Structures – An Overview. *6th International Conference on Coastal and Port Engineering in Developing Countries*, Colombo, Sri Lanka.
- Recio, J. (2007). Hydraulic Stability of Geotextile Sand Containers for Coastal Structures – Effect of Deformations and Stability Formulae, *PhD Thesis*. Leichtweiss-Institute for Hydraulic Engineering and Water Resources. Braunschweig, Germany.
- Srineash, V.K. & Murali, K. (2015). Hydrodynamic Performance of Gabion Box Artificial Reefs. *Proceedings of the Twenty-fifth International Ocean and Polar Engineering Conference (ISOPE)*, Kona, Big Island, Hawaii, USA, June 21-26, 1438-1442.

THE EFFECT OF SUBMERGED BREAKWATER SHAPE AND SIZE ON WAVE ENERGY DISSIPATION

FATEMEH HAJIVALIE⁽¹⁾

⁽¹⁾ Ocean Engineering and Technology Research Center, Iranian National Institute for Oceanography and Atmospheric Science (INIOAS),
Tehran, Iran,
hajivalie@inio.ac.ir

ABSTRACT

In this paper, the effect of submerged breakwater shape and size has been studied using a two dimensional numerical model based on Navier-Stokes equations. For this purpose, two different shapes of submerged breakwaters have been selected for numerical simulations, rectangular and trapezoidal. For each shape, six different simulations are conducted with six different widths. The results show that increasing the crest width can increase the energy dissipation in rectangular submerge breakwater, however it is ineffective in case of trapezoidal ones. Therefore, in some cases, the trapezoidal submerged breakwaters can unexpectedly dissipate more energy than the rectangular breakwaters. In case of this study with relative submergence depth equal to 0.2, it occurs when the crest width is less than about half of a wave length.

Keywords: Transmission coefficient; trapezoidal breakwater; rectangular submerged breakwater; wave breaking.

1 INTRODUCTION

Submerged breakwaters are commonly used for coastal protection purposes. They dissipate wave energy and reduce coastal erosion. Energy dissipation around submerged breakwaters is due to two main mechanisms: (a) wave breaking over the breakwaters and (b) vortex generation at both sides of the submerged breakwaters.

Because of their importance in coastal protection, many researchers have studied submerged breakwaters, Abdul Khader and Rai (1980) calculated the transmission coefficient, the ratio of transmitted to incident wave height, for different type of submerged breakwaters. They concluded that rectangular breakwater is the most effective one between other types of submerged breakwaters in energy dissipating.

Hsu et al. (2000; 2004), Chang et al. (2001; 2005) studied the velocity field and vortex generation around the submerged breakwaters. Young and Testik (2009; 2011) studied wave reflection from submerged breakwaters. Liao et al. (2013) experimentally studied the wave breaking and energy loss over porous submerged breakwater. Hajivalie and Yeganeh-Bakhtiary (2012) and Hajivalie (2014) studied the scouring around rectangular submerged breakwater.

Hajivalie et al. (2015) used a RANS equations based numerical model in closure with a standard $k-\varepsilon$ model to investigate the effect of vertical breakwater dimension on transmission coefficient and vortex generation around the breakwaters. They concluded that unless the breakwater width is wider than a certain rate which may vary depend on the relative submergence depth, increasing the breakwater width would not noticeably increase wave energy dissipation by the breakwater. They explain that under this specific width, the wave breaking doesn't occur over the submerged vertical breakwater.

Considering this finding, the previous estimations that suggested the vertical breakwater can dissipate more wave energy in comparison with other shape of submerged breakwaters like trapezoidal and semicircular in every circumstance became doubtful.

In this paper, to study this conflict, the same model has been used to study the effect of submerged breakwater shape and size on its wave transmission coefficient. In order to do that, twelve simulations have been conducted on two shapes of submerged breakwater, rectangular and trapezoidal, with different crest widths. Then the transmission coefficient for each case has been calculated from the results and compared.

2 NUMERICAL MODEL

In the numerical model, the RANS equations with a standard $k-\varepsilon$ turbulence closure model were applied to simulate wave hydrodynamics around the submerged breakwaters. The governing equations consist of the continuity, momentum and $k-\varepsilon$ equations in two-dimensional coordinates and are as follows:

$$\frac{\partial U_j}{\partial x_j} = 0 \quad [1]$$

$$\frac{\partial U_j}{\partial t} + U_i \frac{\partial U_j}{\partial x_i} = -\frac{1}{\rho} \frac{\partial P}{\partial x_j} - g_j + \frac{\partial}{\partial x_j} \left(2\Gamma \frac{\partial U_j}{\partial x_j} \right) + \frac{\partial}{\partial x_i} \Gamma \left(\frac{\partial U_j}{\partial x_i} \right) \quad [2]$$

$$\frac{\partial k}{\partial t} + \frac{\partial}{\partial x_j} (kU_j) = \frac{\partial}{\partial x_j} \left[\left(\nu + \frac{\nu_t}{\sigma_k} \right) \frac{\partial k}{\partial x_j} \right] + P_r - \varepsilon \quad [3]$$

$$\frac{\partial \varepsilon}{\partial t} + \frac{\partial}{\partial x_j} (\varepsilon U_j) = \frac{\partial}{\partial x_j} \left[\frac{\nu_t}{\sigma_\varepsilon} \frac{\partial \varepsilon}{\partial x_j} \right] + C_{1\varepsilon} \frac{\varepsilon}{k} P_r - C_{2\varepsilon} \frac{\varepsilon^2}{k} \quad [4]$$

$$P_r = \nu_t \frac{\partial U_i}{\partial x_j} \left[\left(\frac{\partial U_i}{\partial x_j} + \frac{\partial U_j}{\partial x_i} \right) \right] \quad [5]$$

$$\nu_t = C_\mu \frac{k^2}{\varepsilon}, \quad \Gamma = \nu + \nu_t \quad [6]$$

here U_i and U_j are the mean velocity components of flow in the i th and j th directions; P is the mean pressure; g_j is the acceleration of gravity in the j th direction; ρ is the fluid density; ν and ν_t respectively are the kinematic and kinetic eddy viscosity; k is the turbulence kinetic energy; P_r is the production of turbulence kinetic energy; and ε is the turbulence dissipation rate. For more details about the model calculation scheme please refer to Hajivalie and Yeganeh-Bakhtiary (2009) and Yeganeh-Bakhtiary et al. (2010).

The initial condition for velocity and pressure selected to be stationary flow field. In addition, the initial condition for the turbulence field was set according to Lin (1998). In this model we have four boundary conditions, free surface, solid boundaries, the inlet and outlet.

The free surface motion was tracked by the VOF technique proposed by Hirt and Nichols (1981). The conservation of F or the volume fraction of fluid, a variable between 0 and 1, is expressed as follows:

$$\frac{\partial F}{\partial t} + U_i \frac{\partial F}{\partial x_i} = 0 \quad [7]$$

At the inlet boundary, the generating-absorbing boundary condition, introduced by Petit et al. (1994) is implemented to generate waves and absorb the reflected waves from the breakwater at the same time, the outlet is an open boundary. Near solid boundaries including bed and submerged breakwater surfaces, the law of the wall is implemented. The model was validated by Chang et al. (2001) and Ohyama et al. (1995) experimental data (Hajivalie et al., 2015). Figure 1 shows a schematic view of the numerical domain. It is discretized with a 2.5 cm×1.0 cm mesh.

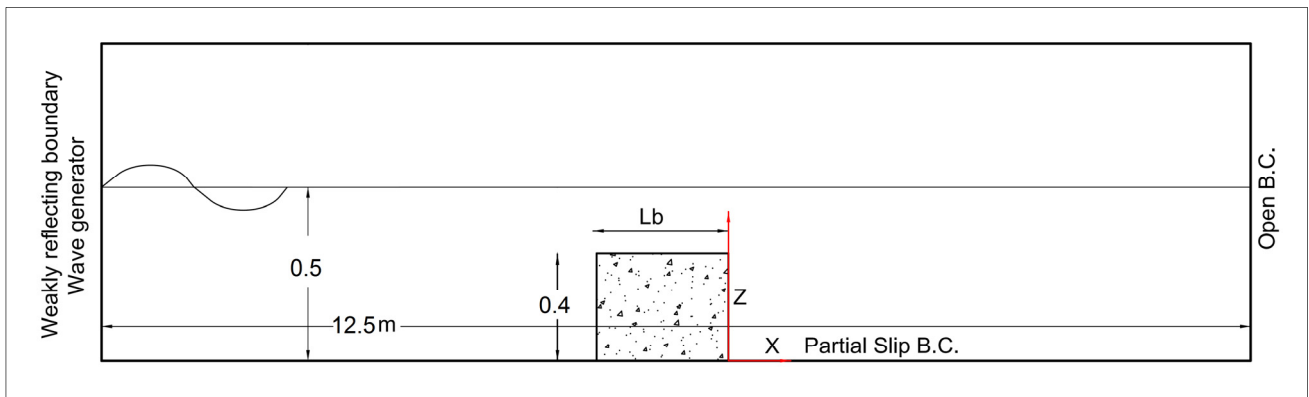


Figure 1. A schematic view of the numerical domain.

3 RESULTS AND DISCUSSION

In this study, two different series of simulation on two shapes of submerged breakwater, rectangular and trapezoidal, with six different crest width were performed. The breakwater crests varied from 0.5 m to 1.3 m with the same height. Second order Stokes waves were generated at the inlet boundary condition and propagate through the numerical domain regularly. Wave height and wave period was set to 5.5 cm and 1.35 s respectively. Table (1) summarized the physical characteristics of these simulations, in this table, h is the water depth, H_r , T and L_o are the regular waves height, period and length respectively and L_b and h_b are the submerged breakwater crest width and height respectively. Figure 2 shows the geometrical arrangements for twelve series of simulations.

Table 1. Physical characteristics of numerical simulations.

No.	h	H _i (cm)	T (s)	L ₀ (m)	L _b (m)	L _b /L ₀	h _b (m)	slope
V1	0.5	5.5	1.34	2.4	1.35	0.56	0.4	∞
V2	0.5	5.5	1.34	2.4	1.20	0.50	0.4	∞
V3	0.5	5.5	1.34	2.4	0.96	0.40	0.4	∞
V4	0.5	5.5	1.34	2.4	0.72	0.30	0.4	∞
V5	0.5	5.5	1.34	2.4	0.60	0.25	0.4	∞
V6	0.5	5.5	1.34	2.4	0.50	0.20	0.4	∞
T1	0.5	5.5	1.34	2.4	1.35	0.56	0.4	1:4
T2	0.5	5.5	1.34	2.4	1.20	0.50	0.4	1:4
T3	0.5	5.5	1.34	2.4	0.96	0.40	0.4	1:4
T4	0.5	5.5	1.34	2.4	0.72	0.30	0.4	1:4
T5	0.5	5.5	1.34	2.4	0.60	0.25	0.4	1:4
T6	0.5	5.5	1.34	2.4	0.50	0.20	0.4	1:4

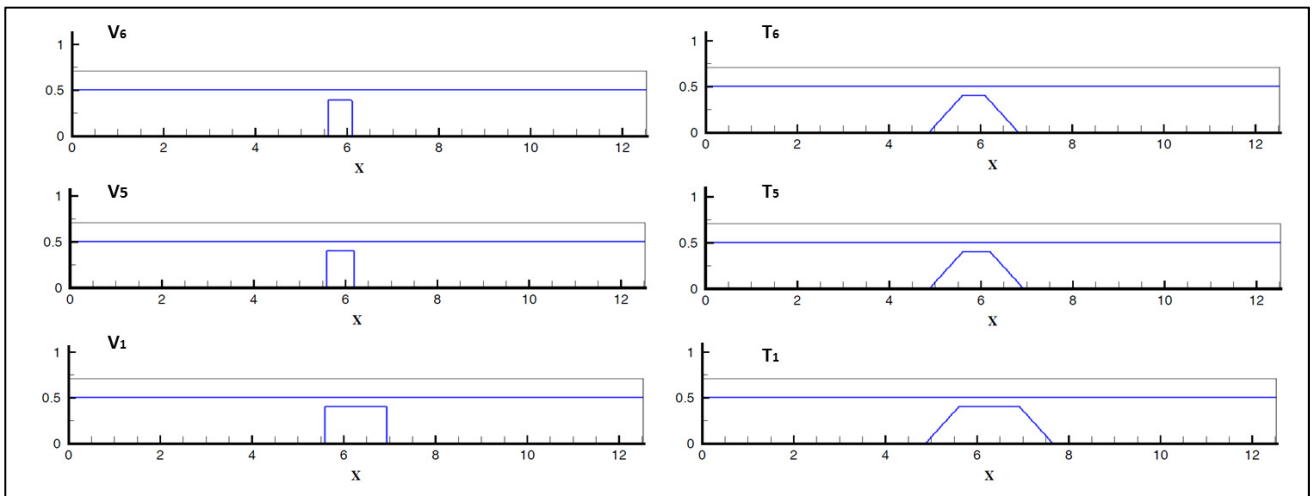


Figure 2. Geometrical arrangements in the numerical simulations.

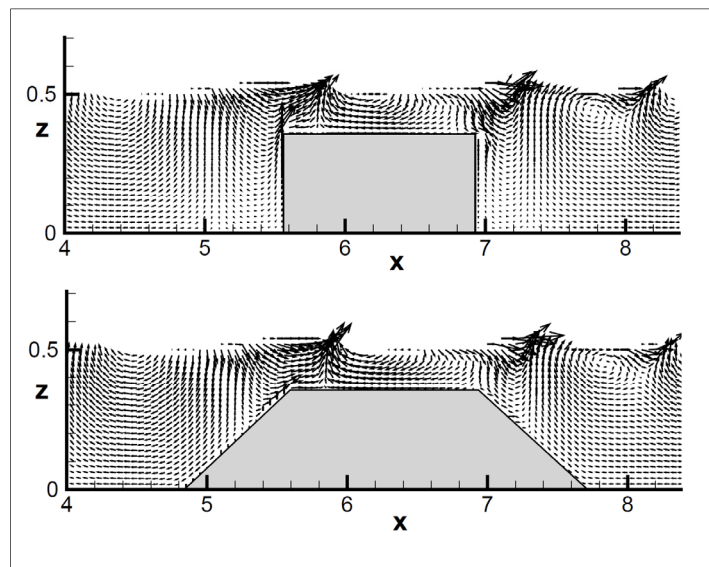


Figure 3. Vortex generation around submerged breakwaters.

The results of these simulations then have been analyzed to indicate the effect of the submerged breakwater shape and crest width. Figure 3 show a comparison between vortex generation around the two breakwater shapes. The generation of leeside vortex is observable in this figure, the vortexes doesn't have noticeable difference between them.

Figure 4 shows the influence of submerged breakwater shape and crest width on the regular waves' height and regularity for three different crest widths. As could be seen in this figure, in case of rectangular submerged breakwater, wider breakwaters affect waves' regularity and height more than the thinner ones; on the other hand, the width of rectangular breakwater crest does not have noticeable effect on the breakwater action.

According to Hajivalie et al. (2015), the width of rectangular breakwater affect the wave breaking over the breakwater, they concluded that breaking does not occur over the submerged breakwater unless the breakwater width is bigger that a certain amount, in other case increasing the breakwater width wouldn't noticeably increase wave energy dissipation. Therefore we can conclude that the breaking take place over the trapezoidal submerged breakwater even the breakwater width is very small. Therefore in case of trapezoidal breakwaters similar wave energy dissipation is observed for breakwaters with different crest width.

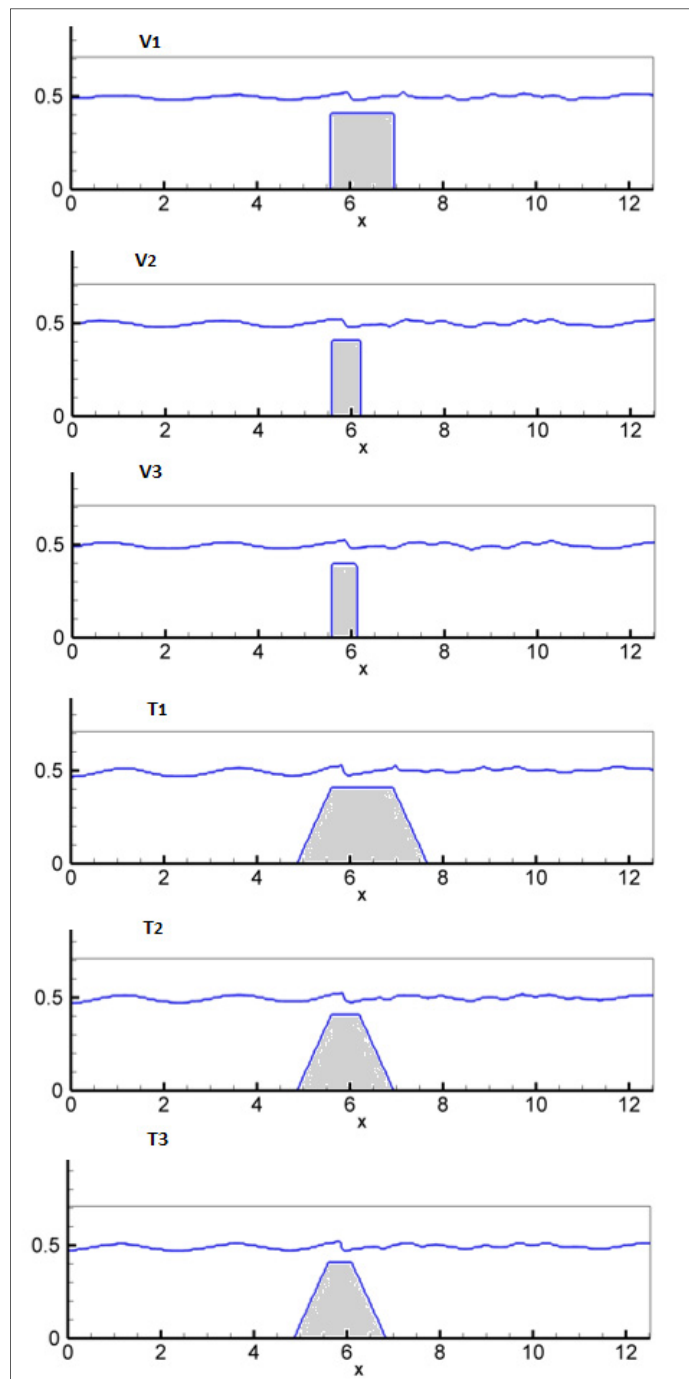


Figure 4. Simulation results for different submerged breakwaters' effect on wave height.

According to their experiments, Abdul Khader and Rai (1980) concluded that increasing of breakwater width enhances energy dissipation. They also concluded that rectangular submerged breakwaters dissipate more energy in comparison with trapezoidal ones.

In each twelve simulation, the transmission coefficient has been calculated by dividing the breakwater downstream wave height at the distance of $2L$ (≈ 4.8 m) from the breakwater leeside edge to the incident wave height. Figure 5 shows the comparison of transmission coefficient for rectangular and trapezoidal submerged breakwaters. As one can see, in agreement with Hajivalie et al. (2015), the transmission coefficient decreases dramatically with increasing the breakwater crest width larger than $0.3L$. On the other hand there is not any

noticeable change in transmission coefficient for trapezoidal submerged breakwater with increasing breakwater crest width.

It could suggest that in some cases, trapezoidal submerged breakwater could dissipate more wave energy in comparison with vertical breakwater which believed to dissipate more wave energy. According to Figure 5, for this case with h_b/h equals to 0.8 and H/h equals to 0.11; the energy dissipation in trapezoidal breakwaters is more that the rectangular ones until L_b/L_0 is less that about 0.5; then the energy dissipation in rectangular submerged breakwaters overtakes the trapezoidal ones.

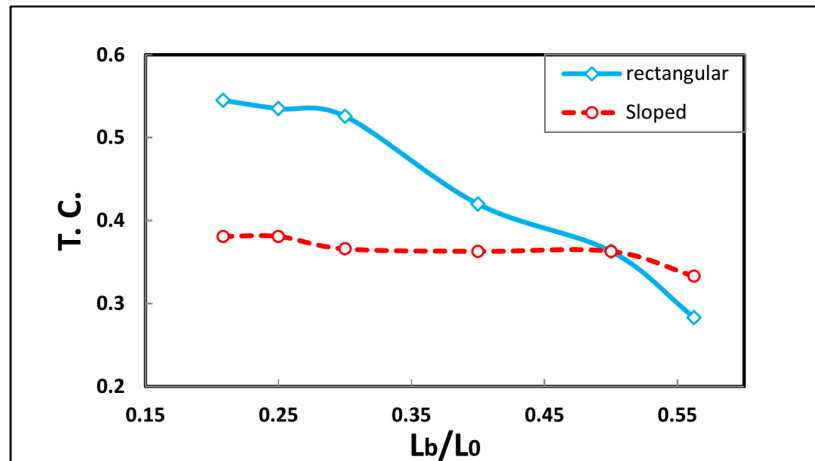


Figure 5. Transmission coefficient versus relative width for rectangular and trapezoidal submerged breakwater.

4 CONCLUSIONS

In this paper, the Hajivalie et al. (2015) two-dimensional numerical model has been used to study the effect of submerged breakwater shape and dimension on wave energy dissipation. The model is based on RANS equation in closure with a standard $k-\epsilon$ turbulence model. The free surface configuration is tracked by so called VOF method proposed by Hirt and Nichols (1981). Twelve different simulations were set for two different shapes submerged breakwater, the rectangular and trapezoidal, with six different crest widths. The results of these simulations concluded that:

- In case of rectangular submerged breakwater, the increasing in breakwater width can decrease the transmission coefficient when the breakwater width is bigger than $0.3L$, however, in case of trapezoidal submerged breakwater, the crest width doesn't have noticeable effect on the transmission coefficient. It can suggest that unlike the rectangular shape, the trapezoidal shape submerged breakwater can cause wave breaking even with small crest width trough shoaling effects.
- Although rectangular submerged breakwaters considered to cause more wave energy dissipation in comparison with the trapezoidal submerged breakwater, the results of this research indicated that in some cases, trapezoidal submerged breakwater can dissipate more wave energy in comparison with the rectangular ones. In the case of this research, it happen when the crest width is less that about $0.5L$.
- More studies, numerical and experimental, on different wave and submerged breakwater characteristics are needed to suggest a general optimum criteria for each type of submerged breakwaters.

REFERENCES

- Abdul Khader, M.I. & Rai, S.P. (1980). A Study of Submerged Breakwaters. *Journal of Hydraulic Research*, 18(2), 113-121.
- Chang, K.N., Hsu, T.J. & Liu, P.L.F. (2001). Vortex Generation and Evolution in Water Waves Propagating over a Submerged Rectangular Obstacle: Part I. Solitary waves. *Coastal Engineering Journal*, 44(1), 13-36.
- Chang, K.N., Hsu, T.J. & Liu, P.L.F. (2005). Vortex Generation and Evolution in Water Waves Propagating over a Submerged Rectangular Obstacle: Part II: Cnoidal waves. *Coastal Engineering Journal*, 52(3), 257-283.
- Hajivalie, F. (2014). Two-Phase Modeling of Wave Induced Scour around the Vertical Submerged Breakwaters. Proceeding of *ICOPMAS*, 533-536.
- Hajivalie, F. & Yeganeh-Bakhtiary, A. (2012). Two-Phase Flow Model for Scouring in Front of a Vertical Impermeable Submerged Breakwater. Book of abstracts, *IAHR-APD Conference*, 148-149.

- Hajivalie, F. & Yeganeh-Bakhtiary, A. (2009). Numerical Study of Breakwater Steepness Effect on the Hydrodynamics of Standing Waves and Steady Streaming. *Journal of Coastal Research*, SI(56), 514-518.
- Hajivalie, F., Yeganeh-Bakhtiary, A. & Bricker, J.D. (2015). Numerical Study of Submerged Vertical Breakwater Dimension Effect on the Wave Hydrodynamics and Vortex Generation. *Coastal Engineering Journal*, 57(03), 1-21.
- Hirt, C.W. & Nichols, B.D. (1981). Volume of Fluid (VOF) Method for the Dynamics of Free Boundaries. *Journal of Computational Physics*, 39(1), 201-225.
- Hsu, T.W., Ou, S.H, Hou, H.S & Shin, C.Y. (2000). Wave-Induced Vortices around a Submerged Breakwater by FLDV and PIV. *Proceedings of the 27th International Conference on Coastal Engineering*, 2278-2291.
- Hsu, T.W., Hsieh, C.M. & Hwang, R.R. (2004). Using RANS to Simulate Vortex Generation and Dissipation around Impermeable Submerged Double Breakwaters. *Coastal Engineering Journal*, 51(7), 557-579.
- Liao, Y.C., Jiang, J.H., Wu, Y.P. & Lee, C.P., (2013). Experimental Study of Wave Breaking Criteria and Energy Loss Caused by a Submerged Porous Breakwater on Horizontal Bottom. *Journal of Marine Science and Technology*, 21(1), 35-41.
- Lin, P. (1998). Numerical Modeling of Breaking Waves, *PhD Thesis*. Cornell University.
- Ohyama, T., Kioka, W. & Tada, A. (1995). Applicability of Numerical Models to Nonlinear Dispersive Waves. *Coastal Engineering Journal*, 24(3), 297-313.
- Petit, H.A.H, van Gent, M.R.A. & van den Boscj, P. (1994). Numerical Simulation and Validation of Plunging Breakers using a 2D Navier-Stokes Model. *Proceedings 24th International Coastal Engineering Conference*, ASCE, Kobe, Japan, 511 –524.
- Yeganeh-Bakhtiary, A., Hajivalie, F. & Hashemi-Javan, A. (2010). Steady Streaming and Flow Turbulence in Front of Vertical Breakwater with Wave Overtopping. *Applied Ocean Research*, 32(1), 91-102.
- Young, D.M. & Testik, F.Y. (2009). Onshore Scour Characteristics around Submerged Vertical and Semicircular Breakwaters. *Coastal Engineering Journal*, 56(8), 868-875.
- Young, D.M. & Testik, F.Y. (2011). Wave Reflection by Submerged Vertical And Semicircular Breakwater. *Ocean Engineering*, 38(10), 1269-1276.

SHORE PROTECTION USING DOUBLE PLATE VERTICAL POROUS BREAKWATER

LAMANTO THOMAS SOMERVELL⁽¹⁾, SANTOSH GOPALAKRISHNAN THAMPI⁽²⁾ & AIKOT PALLIKKARA SHASHIKALA⁽³⁾

⁽¹⁾Research Scholar, Department of Civil Engineering, National Institute of Technology Calicut, Kozhikode, India.
lamanto@gmail.com

^(2,3)Professor, Department of Civil Engineering, National Institute of Technology Calicut, Kozhikode, India.
santoshthampi@yahoo.com; apska@nitc.ac.in

ABSTRACT

Porous breakwaters are becoming popular due to the relatively minor impacts that they cause on the coastal environment and neighbouring beaches when compared to those by conventional breakwaters. In this study, a breakwater consisting of two vertical permeable plates supported by two rows of vertical piles with perforated upper and lower part was proposed. The wave transmission, reflection and energy dissipation characteristics of the breakwater under regular waves for a normal angle of incidence were studied analytically by the eigenfunction expansion method. The analytical results were compared with published results - both experimental and analytical. This demonstrated the capability of the analytical model to reproduce most of the important features of the interaction.

Keywords: Vertical porous breakwater; transmission; reflection; energy dissipation; Eigen function expansion.

1 INTRODUCTION

The construction of a breakwater parallel to an eroding shoreline results in reduction in wave energy reaching the shoreline and thus reduces erosion. Prefabricated vertical porous breakwaters are widely used to protect the shore from wave action because of its simple design and easiness in construction (Koraim 2013). Porous breakwaters help to maintain water quality near the coast by facilitating better circulation of water as well as the passage of fishes and bottom dwelling organisms across the structure (Rageh and Koraim 2010). The main advantages of vertical permeable coastal structures are the saving in construction cost in relatively deep waters and less disturbance to coastal water environments (Huang et al. 2011). These advantages steered many studies on the hydrodynamic characteristics of porous structures, to enable understanding of the performance of the structure (Koraim 2015). Jarlan (1961) first introduced perforated wall caisson breakwaters which consist of a perforated front wall and a solid vertical rear wall. Isaacson et al. (2000) developed a numerical model based on eigenfunction expansion method, to predict the performance of a Jarlan-type breakwater with a rock-filled core. Sahoo et al. (2000) discussed the problem of oblique incident surface waves scattered by a single permeable vertical barrier in finite water depth for different barrier configurations using the eigenfunction expansion method. Laju et al. (2011) analysed wave reflection and transmission by a double barrier breakwater, varying both the depth of submergence of the impermeable barrier and the spacing between the barriers. A numerical model based on the eigenfunction expansion theory was used for effective evaluation of its performance; it was recommended that the double barrier breakwater performs better than a single barrier breakwater. It is clear from the literature that, the analytical approach based on the eigenfunction expansion method can be employed to predict the hydrodynamic characteristics of vertical porous breakwaters. It is also observed that, double walled breakwaters with different upper part and lower part porosities have not been considered so far in the literature.

The breakwater proposed in this study consists of two vertical porous walls supported by piles as shown in Figure 1. The vertical wall consists of a perforated upper part and a lower part with vertical slots. The upper portion of the vertical wall works as a wave energy dissipater. This system is expected to have minimum effect on sediment transport and shoreline morphology. The new system will facilitate excellent water circulation due to its permeable upper part and will minimize obstruction to aquatic life.

2 FORMULATION OF THE ANALYTICAL MODEL

The breakwater considered in this study consists of two vertical permeable walls, separated by some distance. A normally incident regular wave train with wave height H_i and angular wave frequency ω ($\omega = 2\pi/T$, where T is the wave period) propagates in constant water depth h past two permeable walls at a distance $2a$ apart as shown in Figure 1. D_1 and D_2 are the submergence of upper part from the still water level for seaward side and shoreward side wall respectively. A 2-dimensional model of the breakwater (cartesian coordinate system (x,z)) was considered here. The origin of the coordinate system is located mid-way between the vertical walls on the still water level. The horizontal coordinate x is measured positive towards the shore (direction of wave propagation) and the z axis is vertical, measured upwards from the still water level. The

waves are assumed to be regular, of small amplitude and to be normally incident on the breakwater to simplify the problem. The fluid domain is divided into three regions; region 1 - located seaward of the breakwater at $x \leq -a$, region 2 - located between the two walls ($-a \leq x \leq a$), and region 3 - located shoreward of the breakwater at $x \geq a$. The effect of horizontal connections between the vertical walls was neglected. The fluid was assumed incompressible and inviscid and the flow is irrotational. Therefore, fluid motion can be described by the velocity potential $\phi_p(x, z, t)$, which satisfies the Laplace equation. The expression for velocity potential is given by Isaacson et al. (1999) as:

$$\phi_p(x, z, t) = \text{Re} \left[-\frac{igH_i}{2\omega} \frac{1}{\cosh(kh)} \phi_p(x, z) e^{-i\omega t} \right] \quad p = 1, 2, 3 \quad [1]$$

in which Re represents the real part of the complex expression between the $[\]$, $i = \sqrt{-1}$, g is the acceleration due to gravity, k is the wave number ($k=2\pi/L$), L is the wavelength, and $p = 1, 2, 3$ refers to the three wave regions.

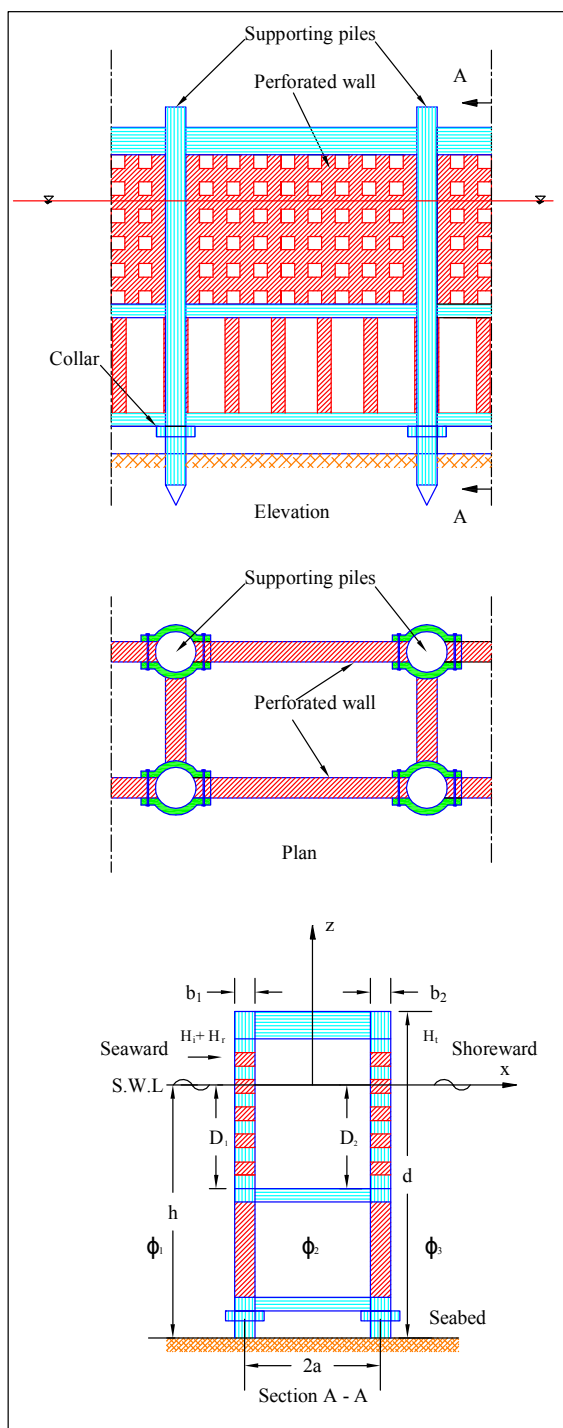


Figure 1. Schematic diagram of a double plate vertical porous breakwater.

2.1 Boundary conditions

The velocity potential satisfies the following boundary conditions at the still water level, seabed and far fields:

$$\frac{\partial \phi_p}{\partial z} = 0 \quad z = -h, \text{ (seabed condition)} \quad p = 1,2,3 \quad [2]$$

$$\frac{\partial \phi_p}{\partial z} - \frac{\omega^2}{g} \phi_p = 0 \quad z = 0, \text{ (free surface condition)} \quad p = 1,2,3 \quad [3]$$

$$\lim_{|x| \rightarrow \infty} \left[\frac{\partial \phi_p}{\partial |x|} - ik \phi_p \right] = 0 \quad \text{(radiation condition)} \quad p = 1,3 \quad [4]$$

The velocity potentials must satisfy the matching boundary conditions at the interfaces. The matching boundary conditions were developed based on the formulation of Sollit and Cross (1972). For the two walls at their upper parts, the matching boundary conditions may be expressed as

$$\frac{\partial \phi_1}{\partial x} = \frac{\partial \phi_2}{\partial x} = -iG_{1U}^{\setminus} (\phi_2 - \phi_1), \quad x = -a, \quad -D_1 < z < 0 \quad [6]$$

$$\frac{\partial \phi_2}{\partial x} = \frac{\partial \phi_3}{\partial x} = -iG_{2U}^{\setminus} (\phi_3 - \phi_2), \quad x = a, \quad -D_2 < z < 0 \quad [7]$$

The matching boundary conditions for the two walls at the lower parts may be expressed as

$$\frac{\partial \phi_1}{\partial x} = \frac{\partial \phi_2}{\partial x} = -iG_{1L}^{\setminus} (\phi_2 - \phi_1), \quad x = -a, \quad -h < z < -D_1 \quad [8]$$

$$\frac{\partial \phi_2}{\partial x} = \frac{\partial \phi_3}{\partial x} = -iG_{2L}^{\setminus} (\phi_3 - \phi_2), \quad x = a, \quad -h < z < -D_2 \quad [9]$$

The conditions above, i.e. eq. (6) to (9) match and describe that the horizontal velocities on the lower and upper parts, on both sides of the each wall are equal. Likewise, the horizontal velocity at the opening is proportional to the variance of velocity potentials, or the pressure difference, across the breakwater. The proportionality constants $G_{1U}^{\setminus} = G_{1U}/b_1$, $G_{2U}^{\setminus} = G_{2U}/b_2$, $G_{1L}^{\setminus} = G_{1L}/b_1$ and $G_{2L}^{\setminus} = G_{2L}/b_2$, G_{1U} , G_{2U} , G_{1L} and G_{2L} are the generally complex permeability parameters. b_1 and b_2 are the thickness of the first and second walls. The real parts G_{1U} , G_{2U} , G_{1L} and G_{2L} correspond to slot resistances and the imaginary parts correspond to the phase differences between velocity and the pressure. In this study, the method proposed by Isaacson et al. (1999) was adopted, G_{1U} , G_{2U} , G_{1L} and G_{2L} are expressed as:

$$G_{iU} = \varepsilon_{iU} / (f_U - i s_{iU}), \quad i = 1,2 \quad [10]$$

$$G_{iL} = \varepsilon_{iL} / (f_L - i s_{iL}), \quad i = 1,2 \quad [11]$$

in which, ε_{iU} and ε_{iL} are the porosities of the upper and lower parts of each wall, f_U and f_L are the friction coefficients obtained by linearization of the velocity squared term associated with the head loss across the permeable part. In the present study, the values of friction coefficients of the upper and lower parts of the vertical walls were assumed to be 3 ($f_U = f_L = 3$) (Koraim et al. 2011). Also s_{iU} and s_{iL} are the inertia coefficients given by

$$s_{iU} = 1 + C_{mU} \left(\frac{1 - \varepsilon_{iU}}{\varepsilon_{iU}} \right) \quad i = 1,2 \quad [12]$$

$$s_{iL} = 1 + C_{mL} \left(\frac{1 - \varepsilon_{iL}}{\varepsilon_{iL}} \right) \quad i = 1,2 \quad [13]$$

in which C_{mU} and C_{mL} are added mass coefficients (treated as constants - C_{mU} and $C_{mL} = 0$ as suggested by Isaacson et al. (1999) and Koraim (2011)).

2.2 Solution of the flow potential

The velocity potentials ϕ_1, ϕ_2 and ϕ_3 that satisfy the conditions of seabed, free surface, radiation, and the conditions at the two walls along $x = \pm a$ were obtained using the eigenfunction expansion method. The expressions for velocity potentials were developed in terms of four sets of coefficients A_{1n}, A_{2n}, A_{3n} and A_{4n} which are initially unknown. The coefficients A_{1n} and A_{2n} account for reflected and transmitted components with respect to the seaward side wall, and the coefficients A_{3n} and A_{4n} account for reflected and transmitted components with respect to the shoreward side wall (Laju et al. 2011). More details about the solution can be found in Isaacson et al. [10] and Koraim et al. [12].

2.3 Reflection, transmission and energy dissipation coefficients

The reflection coefficient K_R is defined as the ratio of the reflected wave height to the incident wave height and the transmission coefficient K_T is defined as the ratio of the transmitted wave height to the incident wave height. These are expressed in terms of A_{1n} and A_{4n} by

$$K_T = |A_{40}| \quad [14]$$

$$K_R = |A_{10}| \quad [15]$$

From considerations of energy conservation, these are related to the energy dissipation coefficient K_D :

$$K_D = \sqrt{1 - K_R^2 - K_T^2} \quad [16]$$

in which, K_D is the part of incident wave energy dissipated by the structure as given by Isaacson et al. (1999), Laju et al. (2011) and Koraim (2011).

3 RESULTS AND DISCUSSIONS

3.1 Verification of Analytical model

The analytical model employed in this study was validated by comparing the results with previous predictions and experiments reported by Laju et al. (2011) and the analytical results of Koraim (2014).

Figure 2 presents a comparison between the results of the analytical model employed in this study and the analytical and experimental results of Laju et al. (2011) and the analytical results of Koraim (2014) as a function of h/L . The case study was a double wall breakwater with impermeable upper part ($\varepsilon_U = 0$) and permeable lower part ($\varepsilon_L = 0.25$), when $D_1/h = D_2/h = 0.35$, $2a/h = 0.5$ and $f = 1.2$, where D_1 and D_2 are the depths of submergence of the impermeable upper part from the still water level of the seaward and shoreward side walls respectively. The transmission coefficient decreased with increasing h/L , while the reflection coefficient exhibited the opposite trend. A very close agreement was obtained with published results (Fig. 2).

In Figure 3, the results of the analytical model employed in this study and the analytical and experimental results of Ji and Suh (2010) and the analytical results of Koraim (2014) as a function of h/L were compared. The case study was a double wall breakwater with impermeable upper part ($\varepsilon_U = 0$) and permeable lower part ($\varepsilon_L = 0.5$), when $D_1/h = D_2/h = 0.5$, $2a/h = 1$ and $f = 2$, where D_1 and D_2 are the depths of submergence of the impermeable upper part from the still water level of the seaward and shoreward side walls respectively. The transmission coefficient decreased with increasing h/L , while the reflection coefficient exhibited the opposite trend. A very close agreement was obtained with published results.

3.2 Analytical results

3.2.1 Effect of relative spacing between the breakwater walls

Figure 4 shows the effect of relative spacing between the breakwater walls ($2a/h$) on K_T , K_R and K_D when $D_1/h = D_2/h = 0.5$, $\varepsilon_{1U} = \varepsilon_{2U} = 0.4$ and $\varepsilon_{1L} = \varepsilon_{2L} = 0.75$. It is observed from Figure 4a that K_T decreased with increasing h/L . The peaks points shifted towards smaller h/L as $2a/h$ increases. These peaks are due to the transmission of re-reflected waves from the shoreward side wall of the breakwater.

It can be observed from Figure 4b that K_R decreased initially with increasing h/L (until approximately $h/L = 0.27$) and thereafter it increased. This can be explained by considering the spacing between the breakwater walls. As this spacing increases, the volume of water in between the walls increases; trapping of waves increases for smaller values of h/L . For higher values of h/L , the particle motion of waves tended towards the still water level and upper part of the shoreward side wall reflected the waves. Thus, the values of K_R increased for $h/L > 0.27$. The peak points, due to multiple reflections, were shifting towards smaller h/L as $2a/h$ increases.

As shown in Figure 4c, the values of K_D increased up to $h/L = 0.35$ and then decreased. This effect is due to the initial decrease in reflection coefficient. After that, the effect of the shoreward side wall of the breakwater dominated and due to this K_D started to decrease. Further, peaks were observed for higher values of h/L , due to the multiple reflections of waves from both the vertical walls of the breakwater.

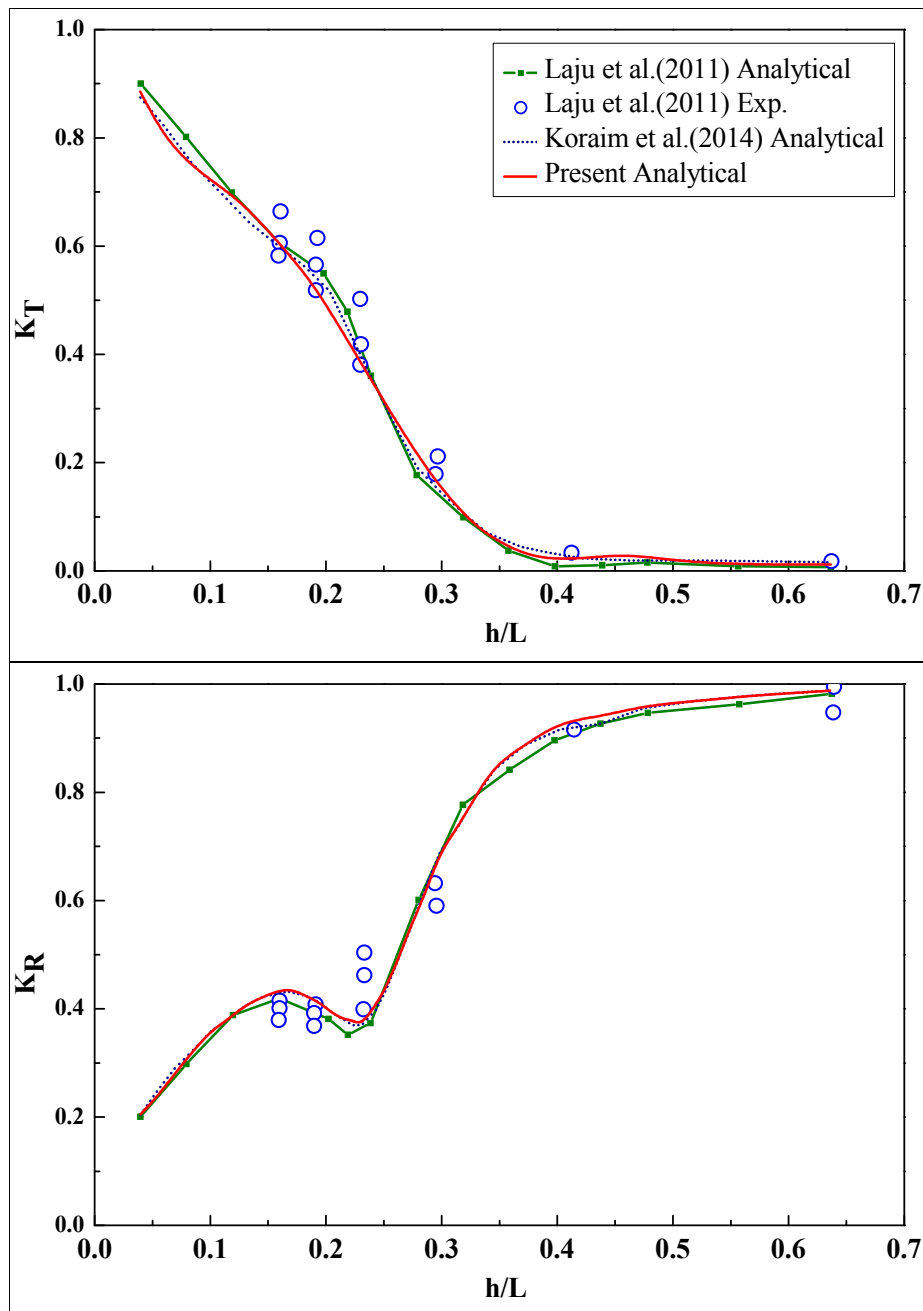


Figure 2. Comparison of predicted hydrodynamic coefficients (K_T and K_R) with results obtained by Laju et al. (2011) and analytical results of Koraim (2014) as a function of h/L , when $D_1/h = D_2/h = 0.35$, $2a/h = 0.5$, $\varepsilon_U = 0$, $\varepsilon_L = 0.35$ and $f = 1.2$

3.2.2 Effect of equal upper part depth

Figure 5 presents a sample of the results (values of different hydrodynamic coefficients) obtained from the analytical model, showing the effect of equal upper part depths from SWL ($D_1/h = D_2/h = D/h$) varying from 0.4 to 0.8 when $\varepsilon_{1U} = \varepsilon_{2U} = 0.3$, $\varepsilon_{1L} = \varepsilon_{2L} = 0.75$ and $2a/h = 0.8$. It is observed from Figure 5a that the transmission coefficient K_T decreased with increasing h/L and D/h . As h/L increases, water particle velocity and acceleration increases; the turbulence created between the breakwater walls reduce the wave height on the shoreward side of breakwater. It is observed from Figure 5a that the upper part submergence had only negligible effect (less than 10%) on wave transmission.

Figure 5b presents the relationship between the analytical values of reflection coefficient (K_R) and h/L for different D/h . It is observed that K_R decreased up to $h/L = 0.25$ and then increased. This is due to the fact

that, for higher values of h/L ($h/L > 0.25$), a large percentage of the wave energy is concentrated towards the SWL (Reddy and Neelamani 1992). Therefore, for higher values of h/L , the effect of upper part porosity dominates and reflection increases. The effect on reflection was not significant for different upper part depths studied.

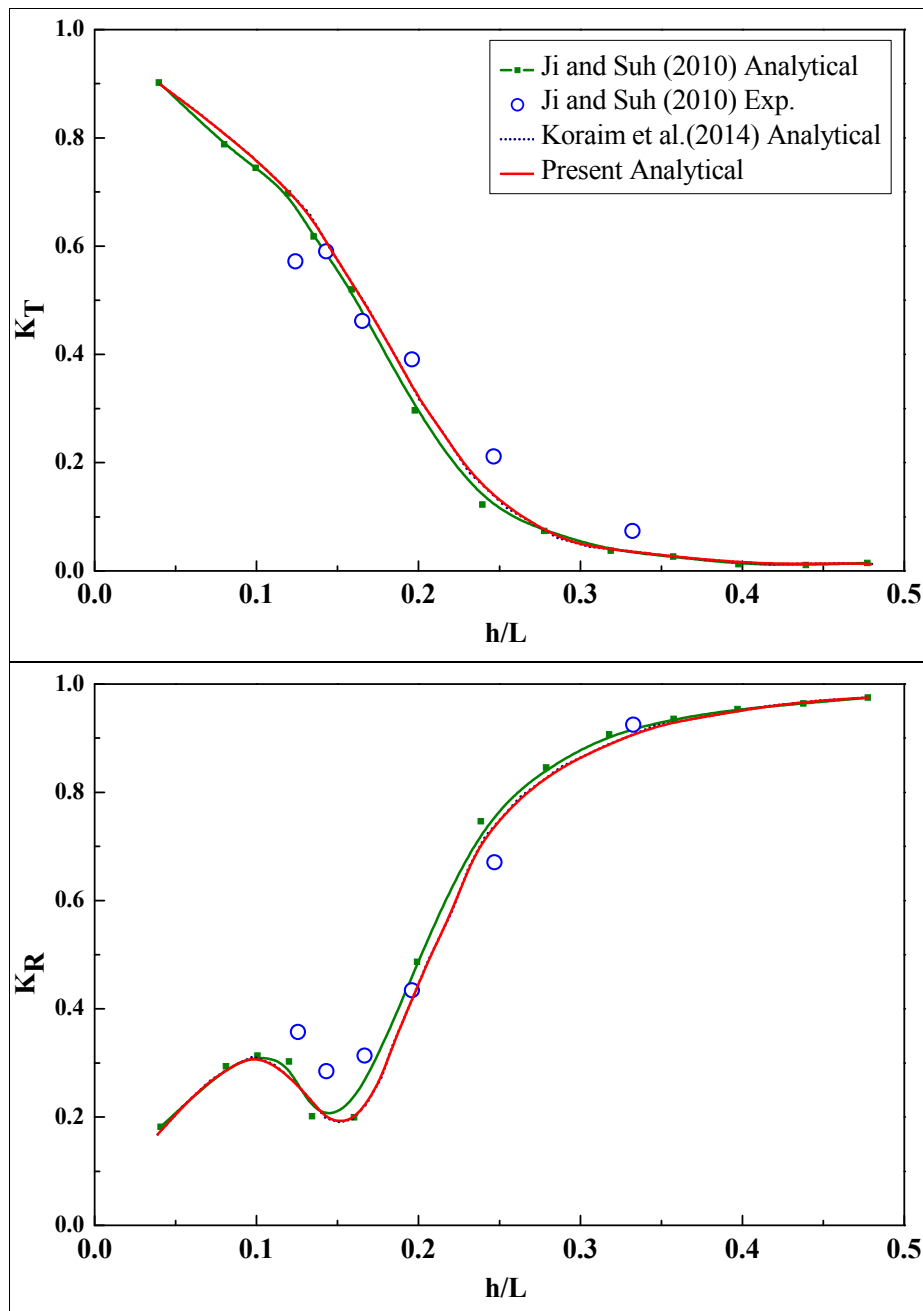


Figure 3. Comparison of predicted hydrodynamic coefficients (K_T and K_R) with results obtained by Ji and Suh (2010) and analytical results of Koraim (2014) as a function of h/L , when $D_1/h = D_2/h = 0.5$, $2a/h = 1$, $\varepsilon_U = 0$, $\varepsilon_L = 0.5$ and $f = 2$

Figure 5c shows the variation of the energy dissipation coefficient (K_D) with respect to h/L for different D/h . K_D increased up to $h/L = 0.3$ and then decreased. The increase in K_D occurred because, when h/L is small, the wave energy distribution from SWL to seabed level is almost of the same order. Hence, the energy available in the lower part of the breakwater is more when compared to that in deep waters. This energy is used for transmission through the lower part of the seaward side wall of the breakwater (porosity, $\varepsilon_{1L} = 0.75$). For higher h/L values (closer to deep water condition), the wave energy is maximum closer to the SWL and reduces significantly towards the seabed. Hence, the total energy available for transmission is less compared to that in the case of lower h/L values (Neelamani and Rajendran 2002a; b). The slight reduction in K_D (for $h/L \geq 0.3$) is due to the increase in reflection of waves from the breakwater. It is also observed that K_D was less affected by variation in D/h .

3.2.3 Effect of equal upper part porosity of the vertical walls

Figure 6 presents the effect of equal upper part porosity of the vertical walls ($\varepsilon_{1U} = \varepsilon_{2U} = \varepsilon_U$) on the hydrodynamic coefficients K_T , K_R and K_D when $D_1/h = D_2/h = 0.5$, $\varepsilon_{2U} = 0.2$, $\varepsilon_{1L} = \varepsilon_{2L} = 0.75$ and $2a/h = 0.75$. It is observed from Figure 6a that the transmission coefficient K_T decreased with increase in h/L . In addition, K_T decreased with decreasing ε_U and the effect of ε_U was pronounced with an increase in h/L .

Figure 6b shows that the values of the reflection coefficient K_R decreased as h/L values increased from 0.1 to 0.3; thereafter, K_R increased as h/L increased. This can be explained by considering the combined effect of turbulence caused water particle velocity and the equal upper part porosity of vertical wall (ε_U). For example, for relatively small values of h/L and $\varepsilon_U = 0.4$, water particle velocities are small and more transmissions occur through the lower part of seaward side wall of the breakwater. These transmissions create turbulence in the water between the two breakwater walls. As h/L increases, the turbulence created increases and reflection decreases. The effect of turbulence dominates up to $h/L = 0.25$ (for $\varepsilon_U = 0.4$) and thereafter the effect of upper part porosity of the vertical walls (ε_U) slowly becomes apparent. For deep waters, the kinetic energy of waves is concentrated towards the still water level and the less porous upper part of the breakwater reflects a major percentage of the waves.

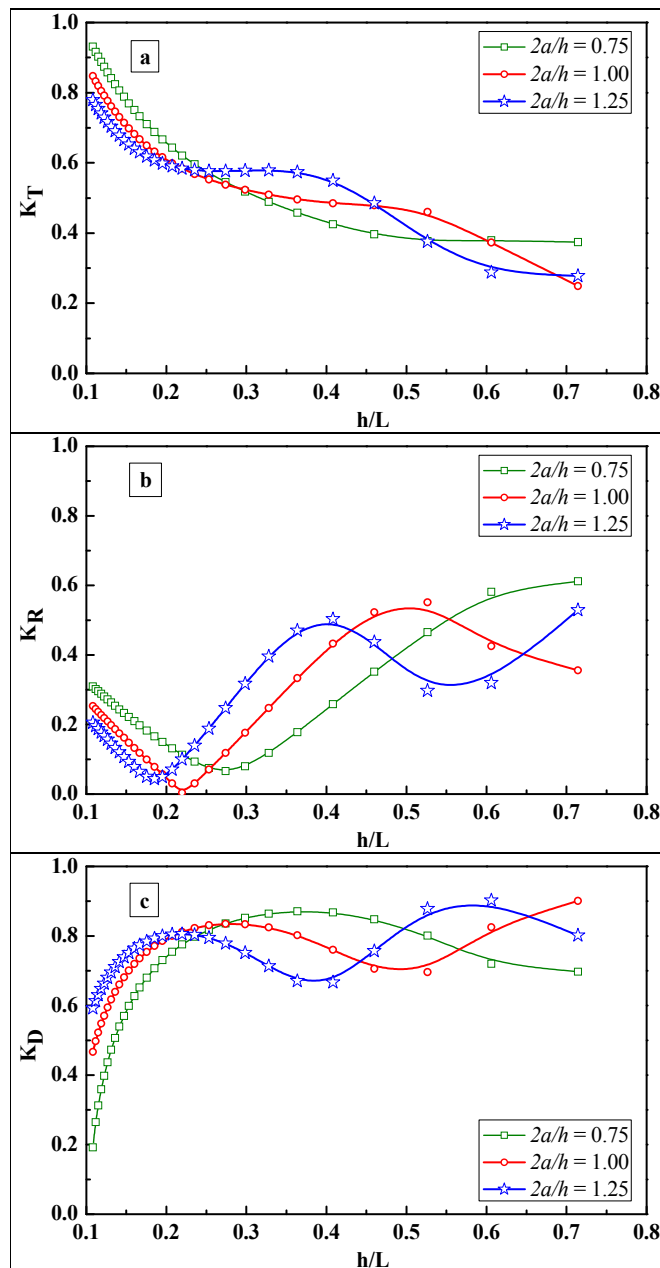


Figure 4. Effect of relative spacing between the breakwater walls ($2a/h$) on K_T , K_R and K_D when $D_1/h = D_2/h = 0.5$, $\varepsilon_{1U} = \varepsilon_{2U} = 0.4$ and $\varepsilon_{1L} = \varepsilon_{2L} = 0.75$

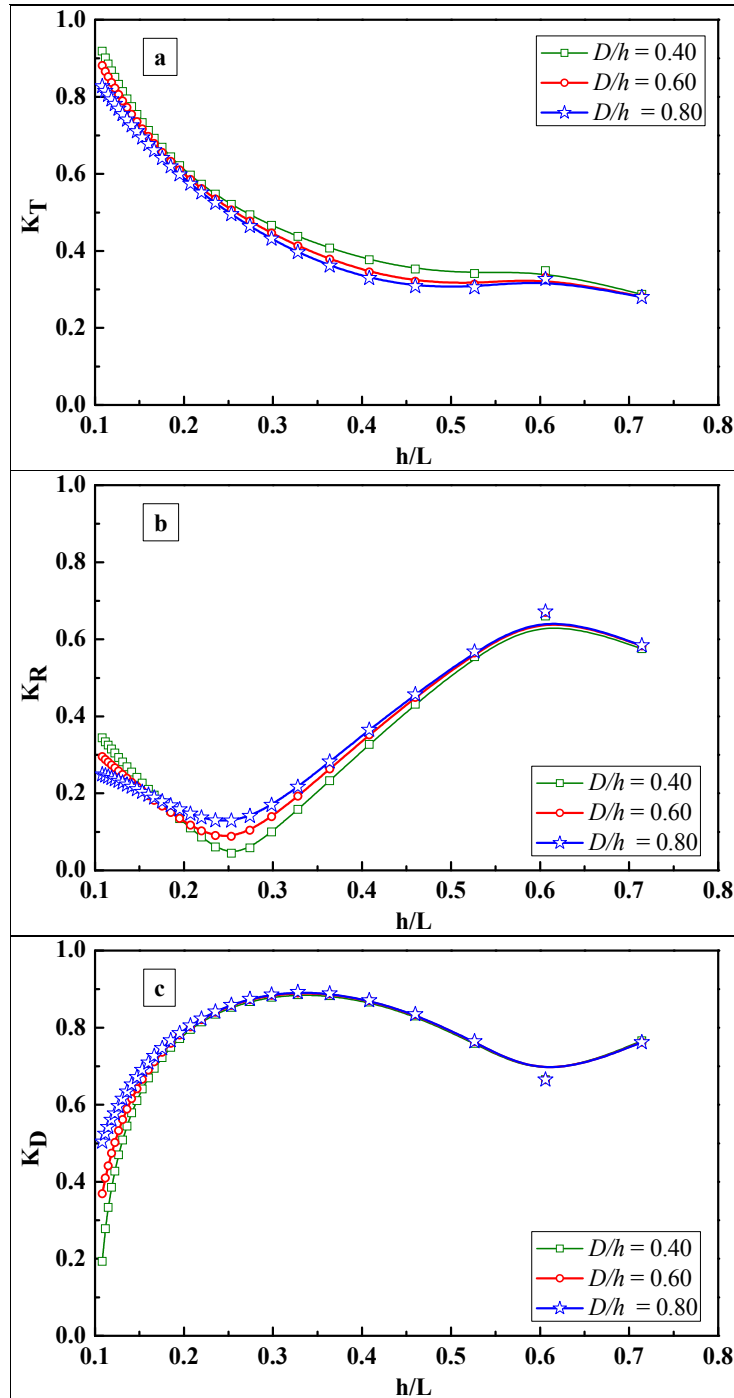


Figure 5. Effect of the equal D/h on the different hydrodynamic coefficients when $\varepsilon_{1U} = \varepsilon_{2U} = 0.3$, $\varepsilon_{1L} = \varepsilon_{2L} = 0.75$ and $2a/h = 0.8$

Further, it can be observed from Figure 6c that the energy dissipation coefficient K_D increased with increasing h/L until approximately $h/L = 0.25$ and thereafter it decreased. The effect of equal upper part porosity of the vertical walls (ε_U) was very significant after $h/L = 0.25$. This is because, up to $h/L = 0.25$, the wave energy dissipation coefficient K_D is mainly governed by transmission through the lower part of the breakwater (porosity, $\varepsilon_L = 0.75$). For higher values of h/L , the effect of upper part porosity of the walls (ε_U) becomes significant. As mentioned earlier, the wave energy is maximum closer to the SWL for higher h/L values and a major portion of this wave energy interacts with the upper part of the breakwater. Therefore, as the upper part porosity of the walls (ε_U) decreases, reflection from the seaward side wall increases and this results in a reduction in K_D .

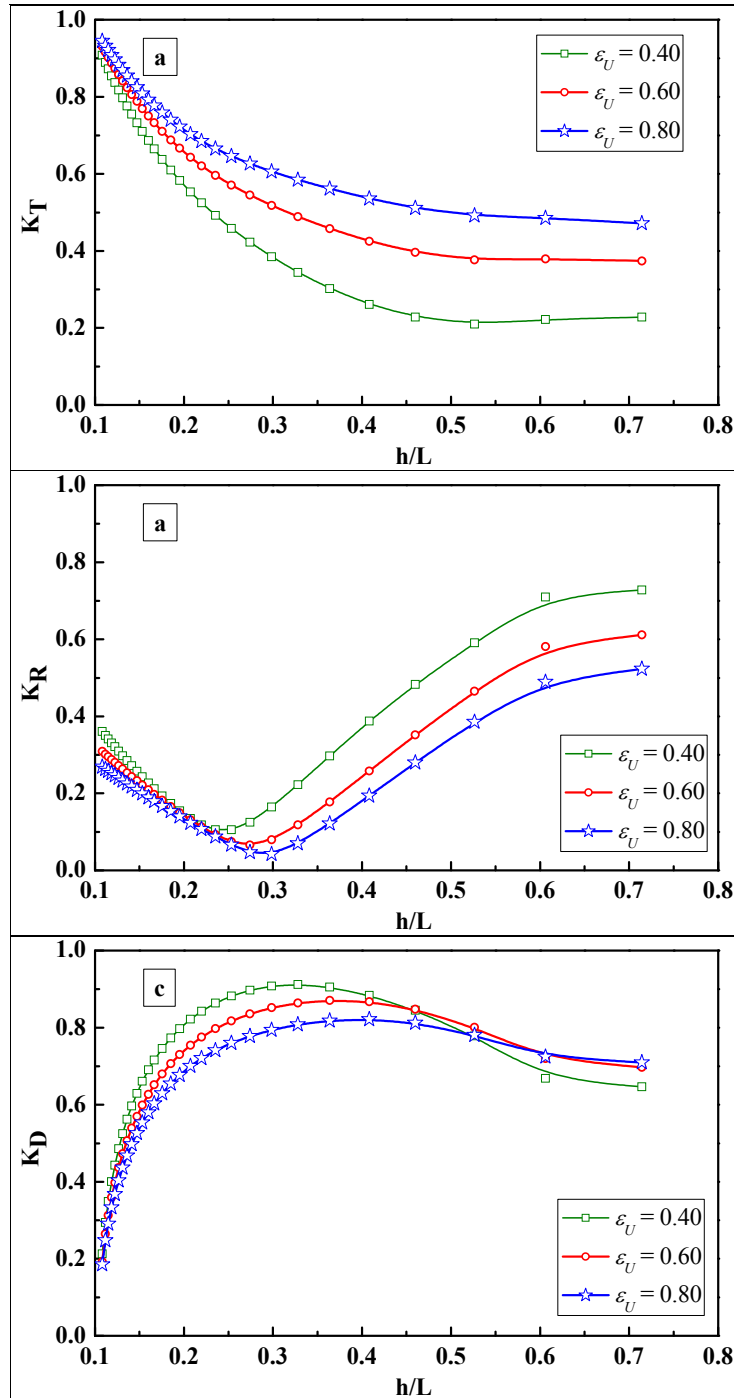


Figure 6. Effect of the equal upper part porosity of vertical walls (ϵ_U) on K_T , K_R and K_D when $D_1/h = D_2/h = 0.5$, $\epsilon_{1U} = 0.2$, $\epsilon_{1L} = \epsilon_{2L} = 0.75$ and $2a/h = 0.75$

4 CONCLUSIONS

Analytical studies were conducted on wave transmission, reflection and energy dissipation characteristics of double plate vertical porous breakwater. The salient conclusions drawn from the present study are given below.

1. In general, the coefficient of transmission (K_T) reduces significantly with the increase in relative depth of water (h/L). The K_T value decreases as the relative spacing between the breakwater walls ($2a/h$) increases. The effect of upper part submergence of both vertical walls (D/h) is not significant on the transmission coefficient of the double plate vertical porous breakwater. The value of K_T increases with increase in the upper part porosity of the vertical walls (ϵ_U) of the breakwater.
2. In general, the reflection coefficient shows an initial reduction for smaller h/L ($h/L < 0.3$), and then increases for deeper waters. The reflection coefficient K_R shows a reduction in high values of $2a/h$ and for smaller h/L (until approximately $h/L = 0.3$); for deeper waters, multiple reflections are more significant. The coefficient of reflection (K_R) is less affected by the upper part submergence of vertical walls (D/h). The

reflection coefficient for double plate vertical porous breakwater is high for vertical walls with lower upper part porosity and the effect is noticeable for higher values of h/L ($h/L > 0.3$).

3. The wave energy dissipation coefficient (K_D) generally shows an increasing trend with increasing h/L ($h/L < 0.3$), and then decreases for deeper water. The value of K_D increases up to $h/L = 0.35$ as $2a/h$ decreases and for higher values of h/L , various peaks are observed due to multiple reflections from the breakwater walls. The effect of upper part submergence of both walls of the breakwater (D/h) on K_D is not significant. The influence of upper part porosity of vertical walls (ϵ_U) on K_D is less significant for smaller h/L ($h/L < 0.2$).

REFERENCES

- Huang, Z., Li, Y. & Liu, Y. (2011). Hydraulic Performance and Wave Loadings of Perforated/Slotted Coastal Structures: A Review. *Ocean Engineering*, 38(10), 1031–1053.
- Isaacson, M., Baldwin, J., Allyn, N. & Cowdell, S. (2000). Wave Interactions with Perforated Breakwater. *Journal of Waterway Port, Coastal, and Ocean Engineering*, 126, 229–235.
- Isaacson, M., Baldwin, J., Premasiri, S. & Yang, G. (1999). Wave Interactions with Double Slotted Barriers. *Applied Ocean Research*, 21(2), 81–91.
- Jarlan, G.E. (1961). A Perforated Vertical Wall Breakwater. *Dock and Harbour Authority XII*, 486, 394–398.
- Ji, C.H. & Suh, K.D. (2010). Wave Interactions with Multiple-Row Curtainwall-Pile Breakwaters. *Coastal Engineering*, 57(5), 500–512.
- Koraim, A.S. (2011). Hydrodynamic Characteristics of Slotted Breakwaters under Regular Waves. *Journal of Marine Science and Technology*, 16(3), 331–342.
- Koraim, A.S. (2013). Hydrodynamic Efficiency of Suspended Horizontal Rows of Half Pipes Used as a New Type Breakwater. *Ocean Engineering*, 64, 1–22.
- Koraim, A. S. (2014). Hydraulic characteristics of pile-supported L-shaped bars used as a screen breakwater. *Ocean Engineering*, 83, 36–51.
- Koraim, A.S. (2015). Mathematical Study for Analyzing Caisson Breakwater Supported by Two Rows of Piles. *Ocean Engineering*, 104, 89–106.
- Koraim, A.S., Heikal, E.M. & Rageh, O.S. (2011). Hydrodynamic Characteristics of Double Permeable Breakwater under Regular Waves. *Marine Structures*, 24(4), 503–527.
- Laju, K., Sundar, V. & Sundaravadivelu, R. (2011). Hydrodynamic Characteristics of Pile Supported Skirt Breakwater Models. *Applied Ocean Research*, 33(1), 12–22.
- Neelamani, S. & Rajendran, R. (2002a). Wave Interaction with T-Type Breakwaters. *Ocean Engineering*, 29(5), 151–175.
- Neelamani, S. & Rajendran, R. (2002b). Wave interaction with \perp -Type breakwaters. *Ocean Engineering*, 29(5), 561–589.
- Rageh, O.S. & Koraim, A.S. (2010). Hydraulic Performance of Vertical Walls with Horizontal Slots Used as Breakwater. *Coastal Engineering*, 57(8), 745–756.
- Reddy, M. S. & Neelamani, S. (1992). Wave Transmission and Reflection Characteristics of a Partially Immersed Rigid Vertical Barrier. *Ocean Engineering*, 19(3), 313–325.
- Sahoo, T., Chan, A. & Chwang, A.T. (2000). Scattering of Oblique Surface Waves by Permeable Barriers. *Journal of Waterway, Port, Coastal, and Ocean Engineering*, 126, 196–205.
- Sollit, C.K. & Cross, R.H. (1972). Wave Transmission through Permeable Breakwaters. *Proceedings of the 13th Coastal Engineering Conference*, 1827–1846.

HYDRAULIC EFFICIENCY OF A FIXED FREE SURFACE H-TYPE BREAKWATER SUBJECTED TO REGULAR WAVES

HEE MIN TEH⁽¹⁾, SYED SHUJA UL HASSAN⁽²⁾ & THINAGRAN SILAVARAJ⁽³⁾

^(1,2,3) Department of Civil and Environmental Engineering, Universiti Teknologi PETRONAS, 32610 Seri Iskandar, Perak, Malaysia,
heemin.teh@utp.edu.my; shuja90@hotmail.com; thinagran@gmail.com

ABSTRACT

Design optimization of free surface breakwaters for maximum wave protection has been the research venture of many scientists. The majority of these breakwaters are designed to be good wave reflectors that may pose some undesirable sea conditions in front of the structure. This research aims at investigating hydraulic performance of a fixed free surface H-type breakwater (FSHB) exposed to regular wave action via a large-scale physical modelling. The FSHB is inherited with an exclusive feature for improved wave suppression ability through energy dissipation. A series of experiments are conducted in a wave flume to investigate wave transmission, reflection and energy dissipation characteristics of the breakwater with respect to wave steepness H/L , relative breakwater width B/L and relative breakwater draft D/d . The experimental results show that the FSHB is a good wave reflector at $0.2 < B/L < 0.3$, and an efficient energy dissipater at $B/L > 0.3$. The breakwater suppresses 50% of the incident wave heights when designed at $B/L > 0.3$. Apart from B/L , the hydraulic efficiency of the breakwater is also subject to the effect of immersion depth; however, the influence of wave steepness to the breakwater performance is rather weak.

Keywords: Free surface breakwater; wave attenuation; wave reflection; energy dissipation.

1 INTRODUCTION

Breakwaters are used to protect coastal areas from destructive wave actions. With increase in human activities along the coastal areas as well as in deeper seas, breakwaters are often used as sea defense structures in protecting the coastal and maritime facilities. Despite excellent wave suppression ability, the traditionally used rubble mound breakwaters are perceived to be environmentally destructive and less economical when constructed in deeper waters. In recent years, free surface breakwaters have been proposed in replacement of the rubble mound breakwaters in some maritime applications that do not require complete wave tranquility in the protection regions.

A free surface breakwater consists of a core body located near water surface where most of the wave energy is concentrated. The free surface breakwater can be used in fixed or floating condition. The fixed free surface breakwaters are connected to sea bottom with the help of a group of piles or jacket structures. Whereas, the floating free surface breakwaters are anchored to the sea floor using a group of mooring cables. The fixed structures are preferably used for wave protection in shallow waters, while the floating barriers are employed for wave attenuation in deeper waters. In comparison to rubble mound breakwaters, free surface breakwaters pose less interruption to water circulation, fish migration and coastal sediment transport. They are mainly used to attenuate the shorter period waves in which the period is less than 5 s. The breakwaters attenuate part of the incoming waves by reflection and/or energy dissipation. The remaining waves transmitted to the shoreward are commonly used as a measure to quantify efficiency or performance of a breakwater. Wave attenuation performance of breakwaters is often represented by the wave transmission coefficient, C_T , which is the ratio of transmitted wave height to the incident wave height.

The level of wave attenuation of fixed free surface breakwaters largely depends upon geometric properties of the structures. Many researches have been undertaken to explore design optimization of the free surface breakwaters, e.g. Günaydın and Kabdaşlı (2007), Diamantoulaki et al. (2008), Teh et al. (2011) and Ji et al. (2015), and these breakwater designs can be classified into four major types, namely solid-type, caisson-type, plate-type, and multipart-type (Teh et al., 2010). Teh (2013) reported the merits and limitations of each type of the breakwater. In the case of solid-type breakwaters, Li et al. (2005) compared rectangular and cylindrical shaped barriers and asserted that the rectangular structure was comparatively better in wave attenuation, particularly in the larger range of relative breakwater width, B/L , where B and L are breakwater width (in wave direction) and wavelength, respectively. Other solid-type breakwaters are made up of quadrant front faces, and the detailed design of the breakwater is reported by Sundar and Subbarao (2003). For caisson-type breakwaters, the typical designs include the U-shape (Günaydın and Kabdaşlı, 2004), Π -shape (Günaydın and Kabdaşlı, 2007) and semi-circular (Teh et al., 2011). The recent research also shows the potential of incorporating oscillating water columns (OWC) to the box-type free surface breakwaters so as to harness the wave energy from the open seas (He and Huang, 2016).

Apart from enhancement of wave attenuation performance, a sustainable free surface breakwater is also expected to provide improved structural stability, reduced wave reflection and environmental impacts. Teh et al. (2014) developed the H-type floating breakwater to deliver wave protection to onshore and offshore facilities. The breakwater, which was tested in floating condition under random waves, was claimed to be more hydraulically efficient, i.e. high energy dissipation and low wave reflection. The H-type floating breakwater is most suitable and more economical to be adopted in deeper waters. In shallow waters where the breakwater provides perimeter protection to the onshore facilities, the hydraulic performance may be further improved if the free surface barrier is fixed by vertical piles or jacket structures. This hypothesis is validated via physical modelling in this study. Hence, this research aims at exploring hydraulic efficiency of the fixed free surface H-type breakwater (FSHB) exposed to regular waves.

2 METHODOLOGY

2.1 Test model

The FSHB model was constructed using a scaling factor of 1:8. The test model was 500 mm wide, 1450 mm long and 250 mm high as shown in Figure 1a. The breakwater model has a pair of legs with 150 mm apart from each other, projecting 50 mm downward from the main body, and a pair of arms with 300 mm apart extending 80 mm upward. The model was made of mild steel and was painted with water-proof paint. Due to rigidity of the structure, it is anticipated that the scale effects resulted from the construction materials of the physical model on the breakwater performance was marginal. A mounting frame, as shown in Figure 1b, was custom made to allow adjustment of the breakwater position relative to the water level. Upon confirmation of the breakwater position, the model was fixated by the means of four vertical circular steel pipes firmly connected to the flume bed and the rectangular beams placed across the full width of the flume top. Model attachment to the mounting frame was done by using Ω -plates.

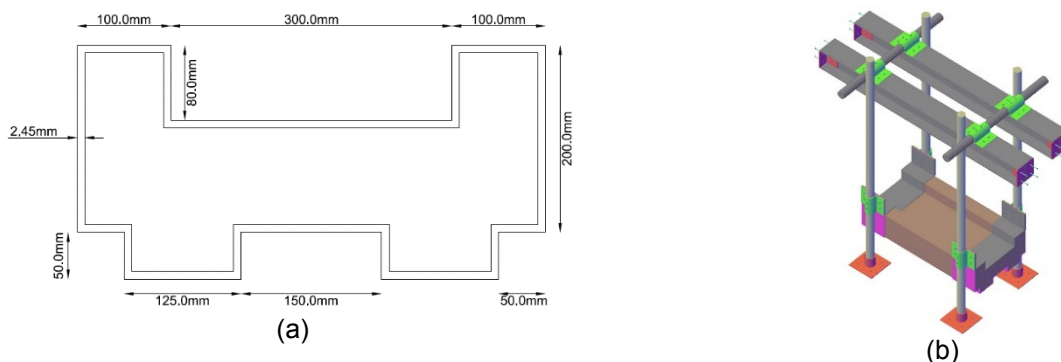


Figure 1. FSHB model: (a) Model cross-sectional dimensions; (b) Mounting frame.

2.2 Experimental setup

A series of experiments were performed in a wave flume equipped with wave generating facilities for performance assessment of the fixed FSHB. The wave flume was 25 m long, 1.5 m wide and 1.5 m high located at Offshore Engineering Laboratory of Universiti Teknologi PETRONAS, Malaysia. The flume was fitted with an active-type wave paddle fabricated by Edinburgh Design Ltd., capable of generating both random and regular waves of different characteristics, at one end. To reduce wave reflection from the other end of the wave flume, a passive type wave absorber was installed. The three-probe method proposed by Mansard and Funke (1980) was used to decompose the incident and reflected waves from the wave series recorded at both sides of the test model as shown in Figure 2. The probes at the front were for measurement incident waves and the reflected waves from the test model, and those installed at the rear were for measurement of transmitted waves and the reflected waves from the wave absorber.

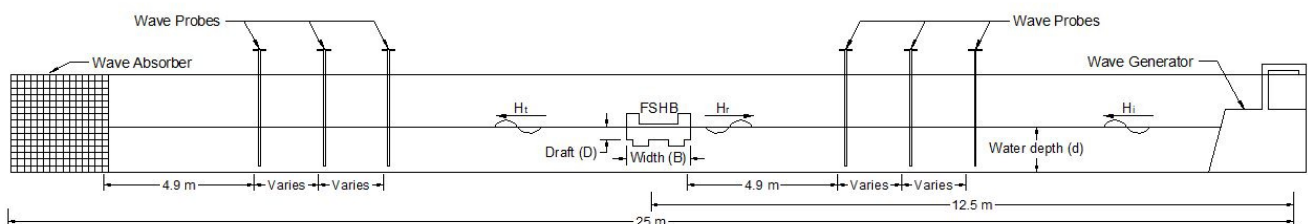


Figure 2. Side view of experimental setup.

2.3 Test conditions

The model was tested in water depth, d of 0.6 meters. To ascertain the breakwater efficiency in different tidal conditions, the immersion depths of the model, D were adjusted at 0.025 and 0.085 m from still water level. This yields the breakwater draft-to-water depth ratios, D/d of 0.0417 and 0.1417, respectively. At each specific draft, the model was tested in regular waves of wave periods ranging from 0.8 to 2.0 s with an interval of 0.1 s. The wave characteristics were subsequently represented by wave steepness parameter, H_i/L of 0.04, 0.05 and 0.06 where H_i is the average incident wave height and L is the wavelength derived from the first order wave theory. The wave steepness of 0.04, 0.05 and 0.06 indicate severity of the wave conditions where $H_i/L = 0.04$ (mild), $H_i/L = 0.05$ (moderate) and $H_i/L = 0.06$ (severe).

3 RESULTS AND DISCUSSIONS

Characterization of the hydraulic properties of the fixed FSHB was performed using several energy coefficients, namely transmission coefficient, $C_T = H_t/H_i$, reflection coefficient, $C_R = H_r/H_i$ and energy dissipation coefficient $C_L^2 = 1 - C_T^2 - C_R^2$, where H_i , H_r and H_t are incident, reflected and transmitted wave heights, respectively. These energy coefficients are correlated with the relative breakwater width, B/L and relative breakwater draft, D/d , and wave steepness, H_i/L in the form of graphical presentation as presented in the following sections.

3.1 Wave transmission coefficient

Wave transmission coefficients C_T of the fixed FSHB immersed at $D/d = 0.042$ and 0.142 and subjected to regular waves of $H_i/L = 0.04$, 0.05 and 0.06 , are presented in Figure 3. The C_T of all test cases demonstrate a rapid decrease with respect to the relative breakwater width, B/L . This signifies that the breakwater performs more efficiently in reducing wave heights when subjected to waves of smaller length relative to the full width of the structure (i.e. larger B/L values). Alternatively, increasing the width of the structure (i.e. larger B/L values) would also contribute to improvement of wave attenuation ability of the breakwater. For instance, wave dampening capability of the FSHB is expected to attain almost 90% ($C_T \approx 0.1$) at $B/L = 0.5$, i.e. the breakwater width is as long as half of the wavelength of the design incident waves, regardless of the immersion depths. When the breakwater width is comparatively small relative to the period of the incident waves (i.e. smaller B/L), the waves manage to transmit through the FSHB without much interactions with the structure, and subsequently leads to high C_T values as shown in the Figure 3. The longer waves, which are more developed and stable in nature, are likely to be restricted to an extent once the breakwater width in line with the wave direction is further increased.

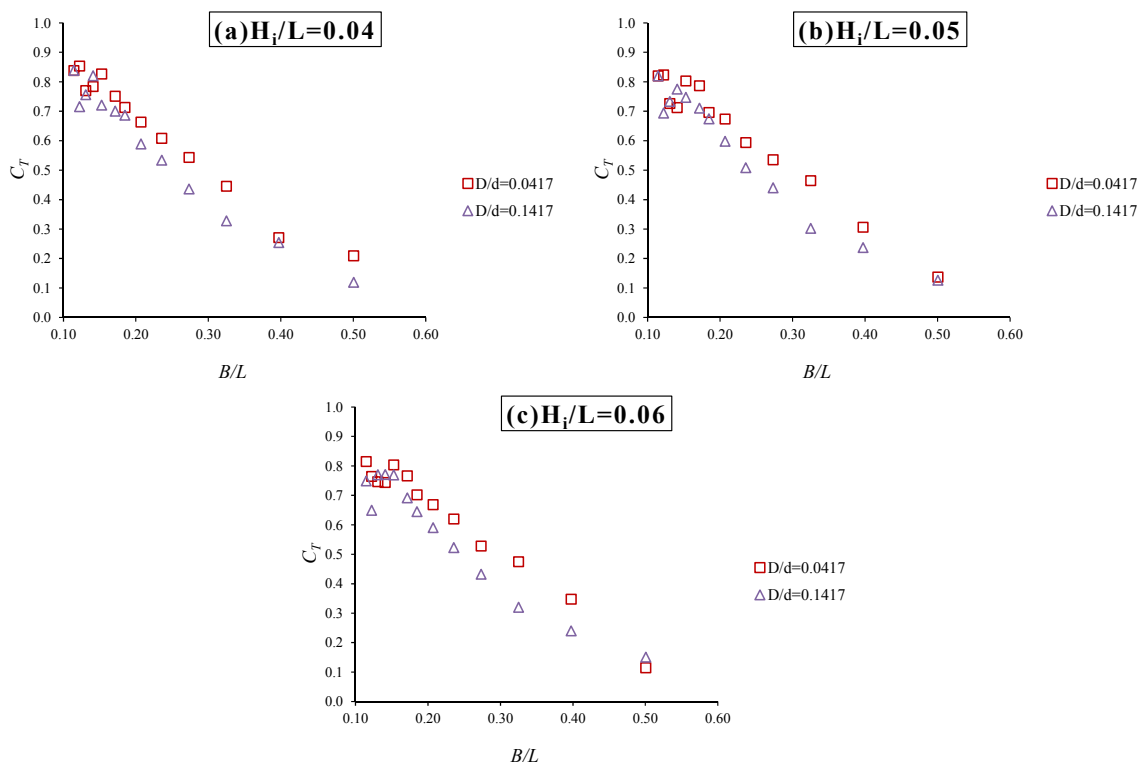


Figure 3. Transmission coefficients: (a) $H/L = 0.04$, (b) $H/L = 0.05$ and (c) $H/L = 0.06$.

The influence of breakwater draft on C_T is also clearly demonstrated in Figure 3. It is easily seen from the figure that FSHBs of higher D/d tend to produce lower C_T values in all tested wave conditions. This finding is sensible because breakwaters of larger immersion depth or draft help in withstanding the wave energy more effectively due to increased degree of interception between the waves and the structures. An increase of D/d from 0.042 to 0.142 does improve wave attenuation in an order of approximately 10%, in all test cases. Improved wave attenuation would be anticipated if D/d of the test model is further increased beyond 0.142 which has not been covered in the present experimental study.

With respect to wave steepness, the effect on C_T is found to be relatively weak. It can be seen from the Figure 3 that C_T slightly decreases with the increasing wave steepness H_i/L . This indicates that wave transmission characteristics of the FSHB is less dependent upon the wave steepness ranging from 0.04 to 0.06, in regular seas. In summary, the fixed FSHB exhibits excellent wave attenuation ability when confronted by waves of shorter periods, and the efficiency increases with the increasing immersion depth.

3.2 Wave reflection coefficient

Figure 4 presents wave reflection coefficient of the fixed FSHB of $D/d = 0.042$ and 0.142 subjected to mild, moderate and severe wave conditions. Overall, the C_R of all test cases display respective maximum values at $B/L \approx 0.25$. At $B/L = 0.25$, the FSHB exhibits partial wave reflection with a maximum C_R of 0.75 (equivalent to 56% of the incident wave in energy context) regardless of the immersion depths. This amount of wave reflection may in turn lead to some extent of wave agitation in front of the breakwater. Having said this, careful selection of B/L in design of FSHB is important in determining reflective characteristics of the breakwater. For attainment of maximum wave attenuation, the FSHB should be designed at $B/L = 0.25$ on condition that the enhanced wave activity at the front does not pose any navigation hazards. If confusing sea states in front of the breakwater is a concern, the design of breakwater at $B/L = 0.25$ should be avoided. It is worthwhile to mention that the bragging effect exhibited by the C_R of the FSHB resembles that of other types of free surface breakwater, e.g. semicircular breakwater (Teh et al., 2010).

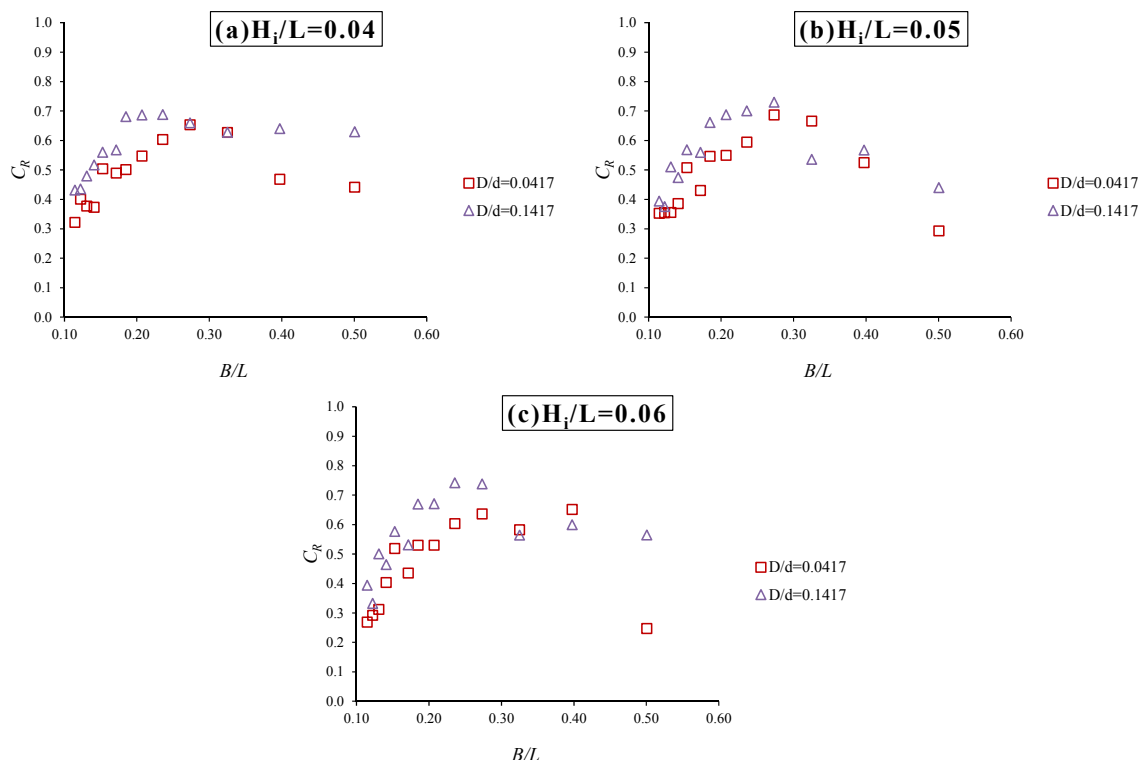


Figure 4. Reflection coefficients: (a) $H/L = 0.04$, (b) $H/L = 0.05$ and (c) $H/L = 0.06$.

The effect of D/d on C_R of the fixed FSHB is distinctive from Figure 4, i.e. the C_R data of the breakwater model with deeper immersion depth $D/d = 0.142$ are consistently higher than those of the model with $D/d = 0.042$. This is somewhat expected as the amount of wave reflection is largely dependent on frontal wetted area of the breakwater. The greater the frontal wetted area, the larger the amount of waves intercepted and subsequently reflected by the structure. Further, it is also observed from Figure 4 that wave steepness is not a strong affecting parameter to C_R for $B/L < 0.25$. The effect becomes more appreciable when the waves are limited in length scale, i.e. $B/L > 0.25$.

Despite demonstration of high wave reflection at $B/L = 0.25$, the impact is still regarded relatively small and manageable compared to that resulted by the vertical wall structures. The breakwater can be regarded as

good anti-reflection structure if it is well designed and the width is set beyond $0.2 < B/L < 0.3$. Conversely, the reflectivity ability of the FSHB can be fully optimized when designed at $B/L = 0.25$ provided that the effect of wave reflection is not an issue to the marine environment. In comparison with the floating FSHB as reported by Teh et al. (2014), the fixed FSHB has demonstrated a stronger wave reflective ability due to its rigidity during wave-structure interactions.

3.3 Energy loss coefficient

Figure 5 presents energy loss coefficient C_L^2 of the fixed FSHB exposed to different water and wave conditions. Note that C_L^2 , which is expressed in terms of energy loss relative to the incident wave energy, provides direct measurement of wave energy dissipated by the breakwater. It is evident from the figure that the C_L^2 of $D/d = 0.042$ and 0.142 drastically increases with an increase in B/L . This indicates that the energy loss induced by the breakwater increases with the decrease of wavelength. Some of the dominant wave dissipation mechanisms observed during the experiments include wave breaking, wave run-up and eddy formation at the legs. The larger the breakwater width relative to wavelength, the greater will be the amount of wave interactions with the breakwater which consequently promote dissipation of wave energy. The FSHB model is inherited with good dissipation characteristics ($C_L^2 > 0.5$) at $B/L > 0.35$. At $B/L \approx 0.5$, the C_L^2 values recorded are as high as 0.90 (90% of the incident wave energy gets dissipated). This resulted in lower C_T values at higher range of B/L as shown in Figure 3.

It can also be seen from Figure 5 that the influence of D/d on C_L^2 is almost insignificant as the data points of both $D/d = 0.042$ and 0.142 are closely related at smaller test range of B/L . At $B/L > 0.3$, it seems that the wave energy dissipation ability of the test model is affected by the change of D/d to certain extent. The effect of D/d on C_L^2 is particularly dominant at $B/L = 0.5$ and $H_i/L = 0.06$, i.e. the breakwater subjected to $D/d = 0.0417$ is highly dissipative but less reflective (see Figure 4) when exposed to short period waves, resulting in small wave transmission to its lee (see Figure 3). Similar to C_T and C_R , the C_L^2 variation of the FSHB is less affected by wave steepness. Overall, it can be deduced that the configuration of the FSHB is effective in dissipating the wave energy when exposed to smaller period waves.

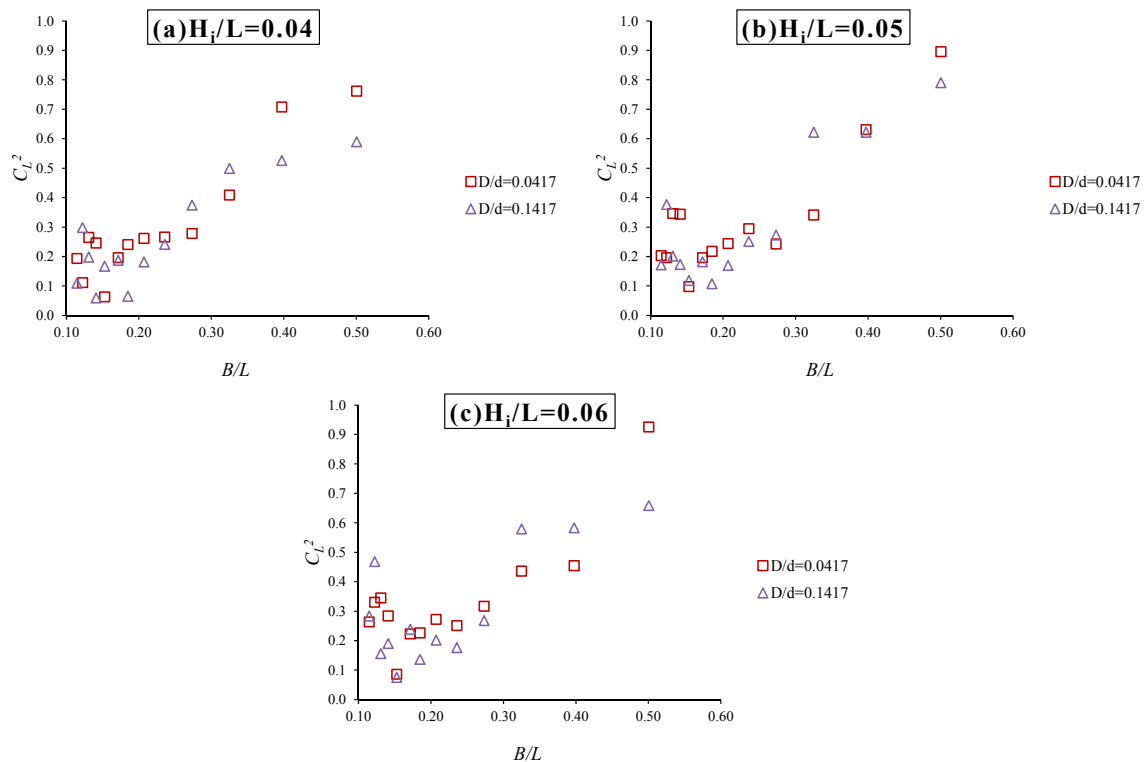


Figure 5. Energy loss coefficients: (a) $H/L = 0.04$, (b) $H/L = 0.05$ and (c) $H/L = 0.06$.

4 CONCLUSIONS

An experimental program was undertaken to investigate wave transmission, reflection and energy loss characteristics of the fixed free surface H-type breakwater (FSHB) exposed to regular waves. Within the test limits, the following conclusions can be drawn:

- Overall, the FSHB was a good wave reflector at $0.2 < B/L < 0.3$, and an efficient energy dissipater at $B/L > 0.35$.
- The FSHB exhibited excellent wave attenuation ability when confronted by waves of shorter periods, and the efficiency increases with the increasing immersion depth.

- The reflectivity ability of the FSHB can be fully optimized when designed at $B/L = 0.25$. If wave reflection is not desirable, the breakwater width should be designed beyond the range of $0.2 < B/L < 0.3$.
- Wave reflection characteristics of the FSHB increased with the increasing breakwater immersion depth at $B/L > 0.30$.
- Hydraulic efficiency of the FSHB was not governed by wave steepness.

ACKNOWLEDGEMENTS

The research is funded by *Yayasan Universiti Teknologi PETRONAS*. The authors would like to thank the laboratory technologists and Final Year Project students for their involvement in this project.

REFERENCES

- Diamantoulaki, I., Angelides, D.C. & Manolis, G.D. (2008). Performance of Pile-Restrained Flexible Floating Breakwaters. *Applied Ocean Research*, 30(4), 243-255.
- Günaydın, K. & Kabdaşlı, M. (2004). Performance of Solid and Perforated U-Type Breakwaters under Regular and Irregular Waves. *Ocean Engineering*, 31(11), 1377-1405.
- Günaydın, K. & Kabdaşlı, M. (2007). Investigation of Π -Type Breakwaters Performance under Regular and Irregular Waves. *Ocean Engineering*, 34(7), 1028-1043.
- He, F. & Huang, Z. (2016). Using an Oscillating Water Column Structure to Reduce Wave Reflection from a Vertical Wall. *Journal of Waterway, Port, Coastal, and Ocean Engineering*, 142(2), 1-10.
- Ji, C.-Y., Chen, X., Cui, J., Yuan, Z.-M. & Incecik, A. (2015). Experimental Study of a New Type of Floating Breakwater. *Ocean Engineering*, 105, 295-303.
- Li, D., Panchang, V., Tang, Z., Demirbilek, Z. & Ramsden, J. (2005). Evaluation of an Approximate Method for Incorporating Floating Docks in Harbor Wave Prediction Models. *Canadian Journal of Civil Engineering*, 32(6), 1082-1092.
- Mansard, E.P. & Funke, E. (1980). The Measurement of Incident and Reflected Spectra using a Least Squares Method. *Coastal Engineering Proceedings*, 1(17), 154-172.
- Sundar, V. & Subbarao, B. (2003). Hydrodynamic Performance Characteristics of Quadrant Front-Face Pile-Supported Breakwater. *Journal of Waterway, Port, Coastal, and Ocean Engineering*, 129(1), 22-33.
- Teh, H.M., John, K.V. & Hashim, A.M. (2014). Hydraulic Investigation of the H-Type Floating Breakwater. *MTS/IEEE OCEANS'14, TAIPEI*, 7-10 April 2014, 1-5.
- Teh, H.M., Venugopal, V. & Bruce, T. (2010). Hydrodynamic Performance of a Free Surface Semicircular Perforated Breakwater. *Coastal Engineering Proceedings*, 32(2010), 1-13.
- Teh, H.M., Venugopal, V. & Bruce, T. (2011). Hydrodynamic Characteristics of a Free-Surface Semicircular Breakwater Exposed to Irregular Waves. *Journal of Waterway, Port, Coastal, and Ocean Engineering*, 138(2), 149-163.

THREE-DIMENSIONAL SCOUR AROUND EMBEDDED SUBMARINE PIPELINE UNDER OBLIQUE WAVES

YONGZHOU CHENG⁽¹⁾, DONGWEI YANG⁽²⁾, WENSEN WANG⁽³⁾ & DIANQI LI⁽⁴⁾

^(1,2,3,4) School of Hydraulic Engineering, Changsha University of Science and Technology, Changsha, P.R. China,
(1) Key Laboratory of Water-Sediment Sciences and Water Disaster prevention of Hunan Province, Changsha, P.R. China,
chengyongzhou@163.com; yangdongwei112@foxmail.com; 764814532@qq.com; lidianqi_609901533@qq.com

ABSTRACT

Seabed near-shore is undulate, the existence of slopes changed the action characteristics of waves on pipeline and seabed, which will thus affect the scouring below pipeline. Using regular waves with an incident angle of 45° and a median particle size of 0.22 mm slope, by measuring the width and depth of the scour hole below the pipeline, scour depth and scour evolution under different wave elements and ratio of embedment depth to diameter (e/D) are investigated. The results of the experiments show that under oblique wave action, the variations of wave height and period has a clear three-dimensional distribution of scour depth along the pipeline, induced the scour depth of right side greater than the left; the scour hole evolved in two distinct stages: rapid and slack. There is a flow tunnel with front and back connected formed below the pipeline while the e/D is less than $1/4$, the existence of flow tunnel will enlarge the size of the scour hole, which may induce the pipeline to be suspended and endanger the safety of the pipeline during operation life cycle.

Keywords: Submarine pipeline; sloping seabed; oblique waves; embedment depth; scour hole.

1 INTRODUCTION

Submarine environment in the coastal zone is complicated and ever changing. The submarine pipelines under the action of wave and current can easily be suspended and thus affect the safety of the pipeline during operation stage. Many scholars have done a lot of studies on the mechanism of scour around pipeline. Gu et al. (2009) analyzed the two-dimensional local scour and three-dimensional mechanisms of scour around submarine pipelines, concluded that the most important inducing factors for submarine pipeline failure were the pipeline suspended induced by local scour, and fatigue failure caused by vortex-induced vibration. Scholars studying seabed scour around pipelines have reported that currents passing over pipelines have induced vortices to occur in both front and back of pipelines (Mao, 1986), and piping has become the main reason of scour (Chiew, 1990). Vortex development, formation and extinction around pipelines have been studied intensively (Fan et al., 2012; Muhammad and Cheng., 2010; Wen et al., 2012). Some scholars found that, under the action of unidirectional flow, evolution of local scour around submarine pipeline can be divided into rapid phase and slack phase. The rate of scour development increased with increasing current velocity, but decreased with increasing embedment depth (Zang et al., 2009a; 2009b; Wu and Chiew, 2010; 2012). By using the Froude number and Shields parameter as overturning moments, embedment depth and water depth as stabilizing moments, Wu and Chiew (2010; 2012) found that stabilizing moments reduces the rate of scour development, and stabilizing moments play a main role in slack phase; while overturning moments promotes the rate of scour development, and play a main role in rapid phase. All Froude numbers, embedment depth and water depth have a great influence on scour depth, any change in those parameters will affect the balance between stabilizing moments and overturning moments. Sumer and Fredsøe (1990; 1991) studied the effect of KC number and embedment depth on equilibrium scour depth of the pipeline, finding that tail flow was the main factor causing pipeline scour, and giving a formula which obtains the KC number, the diameter, vortex strength and the equilibrium scour depth. Pan et al. (2007) studied the evolution of local scour, and divided it into five stages of vortex formation, primary scour hole formation, the bottom of the pipeline was hollowed out, vortex formation around the pipeline, scoured slope turn into flat, scour reached equilibrium. Cheng et al. (2015; 2016a; 2016b) by changing the pipeline location and embedment depth, analyzed how location and embedment depth influence scour hole depth and the sandbar size under regular waves. Han et al. (2010a; 2010b) studied the variation of the flow fields around the pipeline, and reporting that the pressure gradient was the main factor in scour of the submarine pipeline. Yang et al. (2012a; 2012b) studied the variation of the near-bottom velocity of the submarine pipeline under the action of unidirectional flow, and obtained the calculation formula of the dynamic sediment repose angle of the scour hole on a sandy seabed.

Although local scour around submarine pipelines has been studied extensively, most of the previous investigations focused on horizontal seabed subjected to normal incident waves. Due to the fluctuating seabed near-shore, and the changeable of wave propagation angle in engineering practice, some scholars began investigating scour mechanisms around submarine pipelines on a sloping seabed, but few were concerned

with scouring under oblique wave action. The seabed slope and incident wave angle may also change wave action characteristics acting on the pipeline and on seabed erosion. We therefore investigated scour mechanism along the pipeline on a slope under the action of oblique waves. By using regular waves with an incident angle of 45° , and a seabed slope of 1:15 in inclination, we analyzed scour depth along the pipeline under different wave heights, periods and embedment depth ratios, this study can provide reference for practical engineering and numerical simulation research.

2 EXPERIMENT SETUP

Laboratory experiments were conducted in the wave basin at Changsha University of Science and Technology, the P.R., China. This basin is 40 m long, 20 m wide and 1.2 m deep. As shown in Figure 1, one end of the basin has a piston wave maker. A sloping sand bed is located near the basin's other end. The seabed slope was 10 m long, 3.5 m wide, and 1:15 in inclination. To realize wave oblique incidence, the slope toe line and the incident wave propagation direction was set at 45° . The slope frame was made of cement mortar. The sediment particle size based on geometrical-scale belongs to cohesive sediment, which is much different from non-cohesive sediment of field seabed in mechanical properties, thus can not reflect the characteristics of scour around the pipeline, so, prototype sand with medium particle size of 0.22 mm was filled in to form the slope. A steel pipe with an external diameter (D) of 48 mm was the pipeline model. Previous works (Cheng et al., 2015) have proved that sandbar formed under wave action on the near shore seabed will affect the evolution process of the pipeline; when the ratio of pipeline centre axis water depth to slope toe line water depth was 0.47, interaction between the sandbar and scour around the pipeline was the least. So, the pipe was located 3.3 m away from the slope toe and parallel to the slope toe line. In this experiment, an ADV (Nortek, Norway) controlled by multifunction control, was used to measure sand bed topography. Seabed elevation was determined by position detection based on acoustic waves from ADV (Guo et al., 2010). To reduce the lateral boundary effect, the centermost area, which was 1.2 m wide, was selected as the survey area, the initial terrain is shown in Figure 2, direction of the wave propagation was set as the positive x direction and that perpendicular to wave propagation as the positive y direction. According to the gravity similarity criterion, considering the pipeline size and distribution range of wave height and period (Chen et al., 2007), water depth of the experimental area was set to 0.35 m, and the experimental conditions are shown in Table 1.

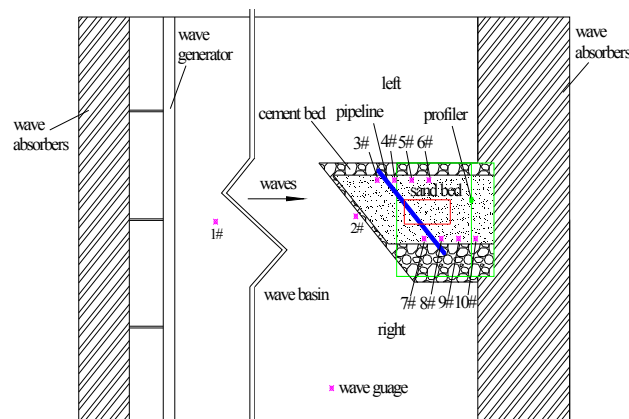


Figure 1. Experiment setup.

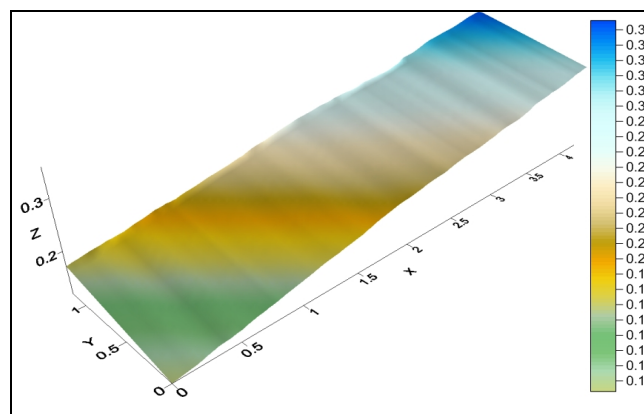


Figure 2. Initial terrain (Unit: m).

Table 1. Experimental conditions.

Case NO.	Wave height (H/cm)	period (T/s)	e/D	Case NO.	Wave height (H/cm)	period (T/s)	e/D
1	4.39	1.4	0	6	7.17	1.6	0
2	7.17	1.4	0	7	7.17	1.4	1/4
3	9.06	1.4	0	8	7.17	1.4	1/2
4	7.17	1.0	0	9	7.17	1.4	3/4
5	7.17	1.2	0				

3 RESULTS AND DISCUSSIONS

3.1 Effect of wave height variations on scour depth along the pipeline

Esin and Yalc (1999) and Cheng et al. (2016a; 2016b) investigated scour around pipeline on a slope, finding that the maximum scour depth of the pipeline on slope was not in the bottom, but in the rear of the pipeline, based on previous studies, the rear and below of the pipeline was measured as the value of the scour depth. Variations in scour depth along the pipeline on a slope with different wave height are shown in Figure 3 ($H=4.39$ cm, $H=7.17$ cm, $H=9.06$ cm). It can be found that the effects of wave height variations on scour depth along the pipeline were not stable, the scour depth along the pipeline gradually increased from left side to right and also the right-side scour depth is generally larger than the left side. The inequality of the scour depth along the pipeline was significant. When the scour depth reached equilibrium, the maximum-scour-depth formed on the right side, which has proved that the range and depth of the scour hole could not expand without limit, and there was a stable value of maximum scour depth with the influence of wave height variations (Cheng et al., 2016a; 2016b; Qin and Peng, 1995). Seabed elevation of left side is greater than the right, thus oblique wave propagated to the left side of slope first, which induced wave propagation along the coast, wave refraction and wave set-up occurred on the slope at the same time, in addition, along the direction of wave propagation, wave energy transmissibility of the left side was decreased, and the right-side wave energy transmissibility was increased by the effects of left. These reasons above aggravated the scour depth on the right side, thus the scour depth on the right was larger than the left, and the inequality of the scour depth along the pipeline was significant.

3.2 Effect of wave period variations on scour depth along the pipeline

Variations in scour depth along the pipeline on the slope with different wave periods are shown in Figure 3 ($T=1.0$ s, $T=1.2$ s, $T=1.4$ s, $T=1.6$ s). It was found that with the increasing of wave period, effects of waves on pipeline were significant; the scour depth along the pipeline increased with increasing wave period, which is different from results of wave height variations. Also, it can be found that the scour depth of right side slightly greater than the left while period was invariant. Along the pipeline, variations regulation of scour depth among the left side and right side was not significant while period variations have little effect on scour depth while comparing with wave height variations.

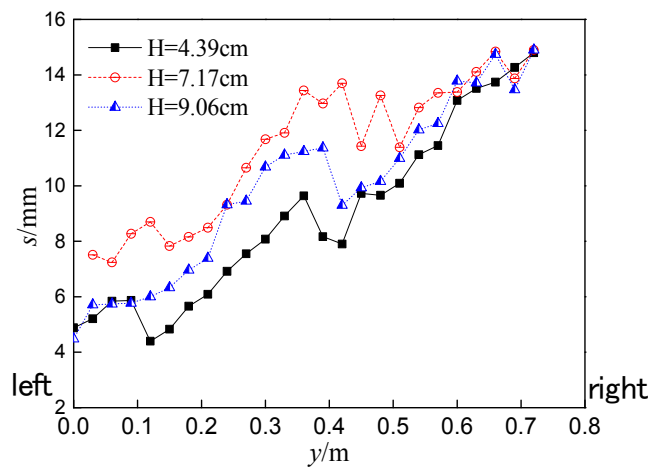


Figure 3. Wave height variations effect on scour depth.

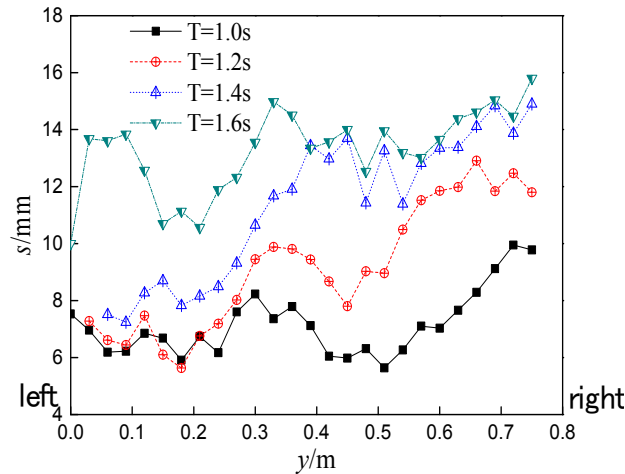


Figure 4. Wave period variations effect on scour depth.

3.3 Effect of embedment depth ratio variations on scour depth

3.3.1 Flow velocity distribution around the pipeline

The change of embedment depth ratio will induce variations of flow velocity around the pipeline on the slope, which could be a great influence on scour. Velocity around the pipeline was measured by using the ADV. As is shown in Figure 5, flow velocity variations around the pipeline with four representative embedment depth ratios ($e/D=0$, $e/D=0.25$, $e/D=0.5$, $e/D=0.75$). It can be found that the flow velocity along the pipeline was greater than the flow perpendicular to the pipeline, that's the key reason for once scour hole formed and then expanding quickly. Also, with the increasing embedment depth ratio, the effect of pipeline on waves decreased, thus flow velocity in front of the pipeline gradually increased, but the flow velocity in back side was fluctuating. When $e/D \geq 1/4$, on the back of the pipeline, with increasing embedment depth, flow velocity along the pipeline decreased, but flow velocity perpendicular to pipeline increased.

3.3.2 Seabed topography around the pipeline in the equilibrium scour state

The sand bed topography after the scour reached equilibrium with four representative embedment depths are shown in Figure 6 ($e/D=0$, $e/D=1/4$, $e/D=1/2$, $e/D=3/4$). It can be found that when $e/D \leq 1/4$, there was a large size scour hole with front and back connected formed below the pipeline, and sediment was deposited behind the pipeline; sand ripples forming at the lee side of the pipeline changed from parallel the pipeline to perpendicular to wave propagation gradually. While $e/D=1/2$ or $e/D=3/4$, a smaller scour hole could be found below the pipeline but without front and back connected, in these conditions, effects of pipeline on wave height increased significantly, the phenomenon of backwater occurred in front of pipeline, thus formed a high-water pressure area in front of the pipeline, which induced the sand bed in front of the pipeline scoured dramatically. While wave propagated to the pipeline, reflection waves induced by the existence of the pipeline appeared and then reflection waves made reversed scour occurred on the sand bed. Therefore, in front of the pipeline, there were large sand ripples formed parallel to the pipeline and small ripples perpendicular to wave propagation under the interaction of incident waves and reflected waves. While in the lee side of the pipeline, little size deposition appeared clearly, and formed a raised dune slightly.

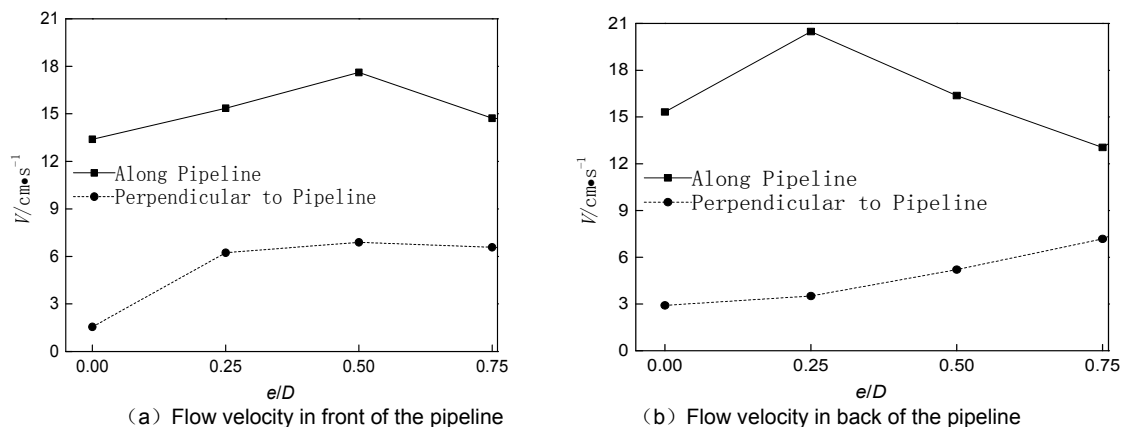


Figure 5. Flow velocity Variations around the pipeline with increasing embedment depth ratio.

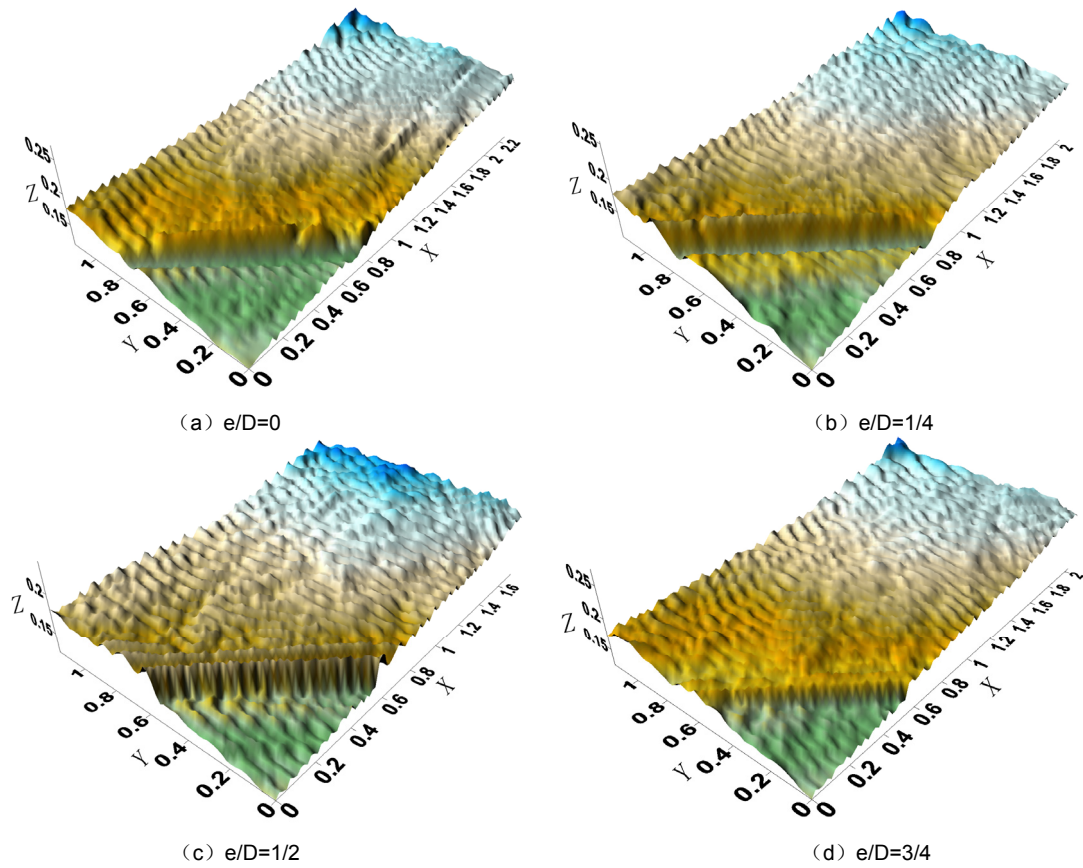


Figure 6. Scour evolution around the pipeline with variations of embedment depth ratio.

3.3.3 Effect of embedment depth ratio variations on scour depth along the pipeline

Variations in scour depth along the pipeline with different embedment depth ratio are shown in Figure 7 ($e/D=0$, $e/D=1/4$, $e/D=1/2$, $e/D=3/4$). It was found that scour depth on right side generally greater than the left, and the scour depth increased gradually from left side to right, the inequality of scour depth along the pipeline was significant in different embedment depth ratio. When $e/D=0$ or $e/D=1/4$, there was a scour hole with front and back connected formed below the pipeline, so the scour depth below the pipeline was greater than others. While $e/D=1/2$ or $e/D=3/4$, below the pipeline, seepage force caused by pressure gradient between front and back was not powerful enough induces piping, that is the reason for scour depth was little than the former. In conclusion, with increasing embedment depth ratio, the effects of pipeline on evolution of sand bed was decreased, therefore scour depth under the pipeline was decreased.

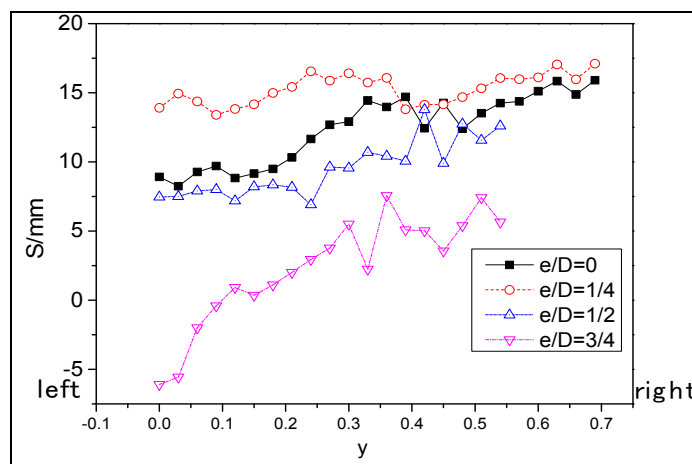
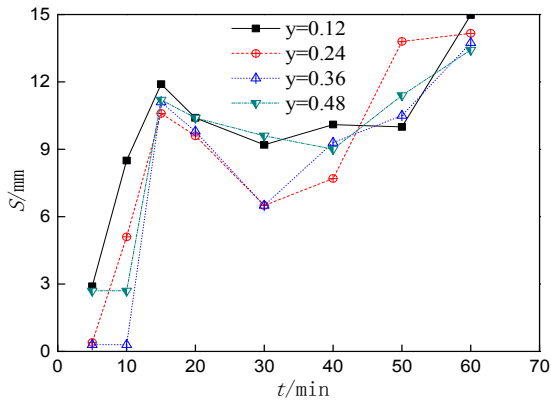


Figure 7. Scour depth along the pipeline with variations of embedment depth ratio.

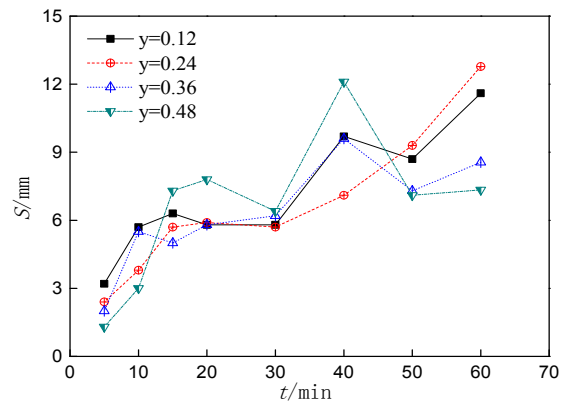
3.3.4 Scour evolution around the pipeline

After scour reached equilibrium, the three-dimensional characteristics of sand bed topography appeared significantly under oblique waves. So, it is limited to study on scour evolution process by using the scour depth of middle section or the maximum scour depth. In order to study scour evolution process around the

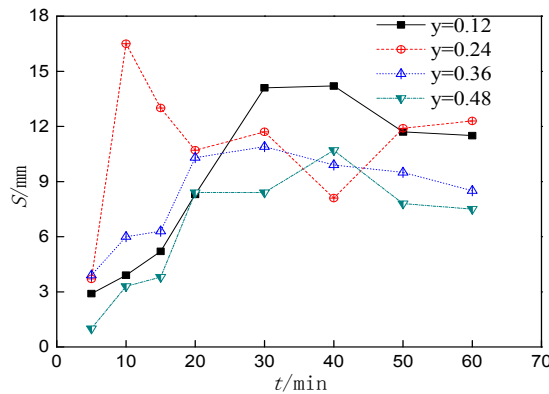
embedment pipeline, scour depth of four representative sections ($y=0.12, 0.24, 0.36, 0.48$) over time are shown in Figure 8 (a), (b) and (c). The development of scour depth when $e/D=1/4$ is shown in Figure 8 (a). It can be found that, under oblique waves, with the development of scour, there was a pressure gradient induced by backwater formed in front of the pipeline, and then water flow passing over the pipeline brought a wake vortex after separated; the wake vortex took a part of sand away below the pipeline. The scour occurred on the wake vortex areas of sand bed first, the energy of wake vortex increased with increasing exposed areas below the pipeline which will exacerbate the scour around the pipeline. At about 5 minutes, while primary scour hole appeared below the pipeline, the tiny primary scour hole expanded quickly with the piping phenomenon occurred below the pipeline. The sand below the pipeline was rolled-up by vortex, then deposited on the lee side of the pipeline, and the bottom of the pipeline was hollowed out, forming a scour hole. After 15 minutes, the scour hole formed completely and developed slowly.



(a) Scour Depth Development in Case $e/D=1/4$



(b) Scour Depth Development in Case $e/D=1/2$



(c) Scour Depth Development in Case $e/D=3/4$

Figure 8. Scour depth development in different sections over time.

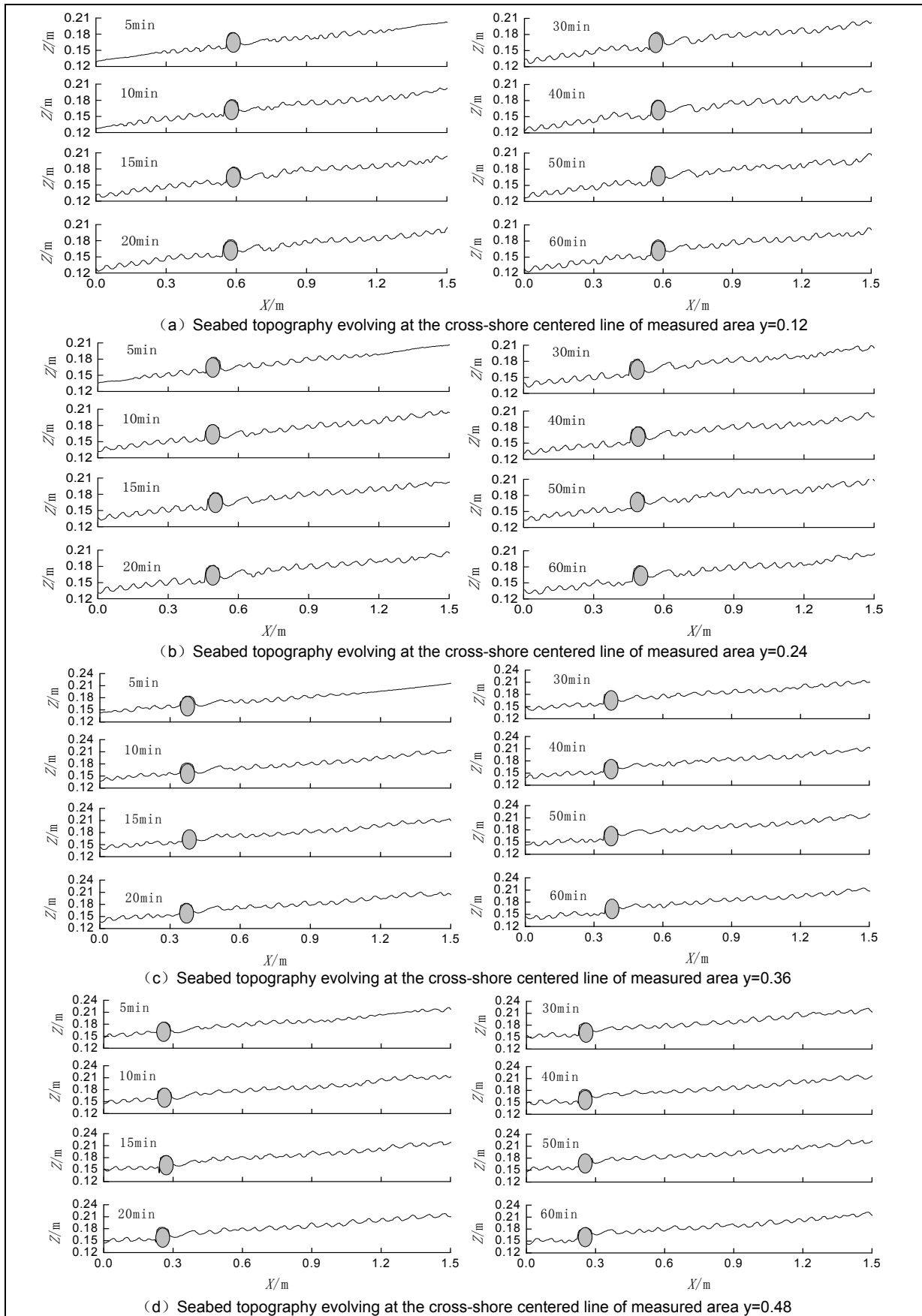


Figure 9. Sand bed profiles evolved along the cross-shore center line over time for $e/d=1/2$.

This experimental study on scour hole development over time is consistent with the research results of previous investigations (Gao et al., 2003; Voropvey et al., 2003; Myrhaug, et al., 2008). Also, it can be found that the development of scour depth under embedment pipeline could be divided into rapid and slack phases.

The critical time that the transition from the rapid phase to the slack phase occurs was between 15 and 20 minutes in this study. As is shown in Figure 8 (b) and (c), when $e/D=1/4$, scour depth development rate was much greater than $e/D=1/2$ and $e/D=3/4$ during rapid phase. By analysing the inequality of scour depth over time with different sections, the differences of scour rate between the left and right side was obvious. Scour depth development rate of section $y=0.12$ was much greater than section $y=0.48$ during rapid phase while during slack phase, scour depth development rate of section $y=0.12$ was approximately equal to section $y=0.48$. Under the wave set-up and wave refraction, scour intensity on left side was greater than right side. In summary, scour depth development rate during rapid phase of right side was much greater than left. However, during slack phase, all sections was developed in a slow rate, which illustrated that the inequality of local scour depth along the pipeline was formed during rapid phase.

In order to study scour evolution process of front and back of the pipeline, Sand bed profiles evolved along the cross-shore center line of the measured areas ($y=0.12$, $y=0.24$, $y=0.36$, $y=0.48$) over time as shown in Figure 9 (a), (b), (c) and (d) for $e/D=1/2$. It was found that the common characteristic of each section was the development rate of sand ripples on the lee side more rapidly than the sea side, which contributed to the differences of increasing scour depth between sea side and lee side. Sediment was deposited behind the pipeline, and scour hole formed in front without connected with back. Also, no piping appeared below the pipeline because of the sand bed with great thickness below the pipeline. On lee side, it can be found that deposition close to the pipeline was rose slightly, which prevented the development of scour. At about 20 minutes, deposition behind the pipeline reached equilibrium, and scour evolution before the pipeline reached equilibrium after 30 minutes.

4 CONCLUSIONS

Based on laboratory experiments, we studied the local scour depth along a pipeline on a sloping seabed under the action of oblique waves. Firstly, scour depth along the pipeline with wave height and period variations was investigated. Secondly, the evolutionary seabed scour process around the pipeline at different embedment depths ratio was investigated and then the development of scour depth in different sections over time was studied. Conclusions can be drawn as follows: (1) Under oblique waves, the scour depth along the pipeline had a clear three-dimensional distribution, wave refraction and wave set-up induced the scour depth on left side greater than right. (2) Scour depth along the pipeline was irregular, there was a constant maximum-scour-depth appeared on right side with wave height variations; scour depth increased with increasing wave period. (3) When the ratio of embedment depth to diameter (e/D) was no more than $1/4$, there was a scour hole formed below the pipeline under oblique waves action, the key reason for once scour hole formed and then expanding quickly is that the flow velocity along the pipeline was greater than the flow velocity perpendicular to the pipeline. (4) When the ratio of embedment depth to diameter (e/D) was $1/2$ or $3/4$, seepage force induced by pressure gradient between front and back was not powerful enough to induce scour hole formed below pipeline where scour occurred on sea side and deposition on lee side. Scour depth decreased with increasing embedment depth ratio. (5) Scour rate could be divided into rapid phase and slack phase. While during sour rapid phase, the scour development rate on the right side of the pipeline was much greater than left. And the inequality of scour depth along the pipeline was formed during the rapid phase.

ACKNOWLEDGEMENTS

This work was supported financially by the National Natural Science Foundation of the P. R. China (Grant Nos. 41176072 and 51679015) and the Natural Science Foundation of Hunan Province (2015JJ2006).

REFERENCES

- Chiew, Y.M. (1990). Mechanics of Local Scour around Submarine Pipelines. *Journal of Hydraulic Engineering*, 116(4), 515-529.
- Cheng, Y.Z., Yang, Q.L., Huang, X.Y. & Yi, L. (2015). Experimental Study on Scour around Submarine Pipelines Placed at Different Position of a Sloped Seabed. *Journal of Changsha University of Science and Technology*, 12(1), 55-62.
- Cheng, Y.Z., Lu, X.H., et al. (2016a). Research on Bed Sediment Composition around Submarine Pipelines under the Oblique Wave. *Advances in Water Science*, 27(5), 735-742.
- Cheng, Y.Z., Lu, X.H., et al. (2016b). The Inequality Research of Inequality 3D Scour below Submarine Pipelines under the Oblique Waves. *Acta Oceanologica Sinica*, 38(7), 126-134.
- Chen, Z.S., Li, Z.L., Feng, Y., Li, Z. & Chang, R. (2007). Kernel density estimates on distribution of wave height and period in nearshore zone. *Oceanologia et Limnologia Sinica*, 38(2), 97-103.
- Esin, C.E. & Yalc, Y.K. (1999). Scour under Submarine Pipelines in Waves in Shoaling Conditions. *Journal of waterway, port, coastal, and ocean engineering*, 125(1), 9-19.
- Fan, F.F., Ji, B., et al. (2012). Study on Hydraulic Characteristics of the Horizontal Pipeline Backflow Area. *Periodical of Ocean University of China*, 42(7-8), 173-177.
- Gao, F.P., Gu, X.Y. & Jeng, D.S. (2003). Physical Modeling of Untrenched Submarine Pipeline Instability. *Ocean Engineering*, 30(10), 1283-1304.

- Guo, R., Tong, S.C., et al. (2010). Topography Measurement Test based on the Acoustic Doppler Velocimeter. *Advances in Science and Technology of Water Resources*, 32(2), 52-54.
- Gu, F., Zhou, J., et al. (2009). Research on Mechanism of Local Scour around Submarine Pipeline. *Marine Science Bulletin*, 28(5), 110-120.
- Han, Y., Shi, B., et al. (2010a). Experimental Study on Defensive Function of Submarine Pipeline by Baffles. *Journal of Sichuan University*, 42(2), 100-106.
- Han, Y., Shi, B., Yang, L., Sun, X. & Wu, J. (2010b). Experimental Study on the Function of Flexible Spoilers in Protecting Submarine Pipeline. *International Offshore and Polar Engineering Conference*, 20, 234-239.
- Myrhaug, D., Ong, M. C. & Gjengedal, C. (2008). Scour below Marine Pipelines in Shoaling Conditions for Random Waves. *Coastal Engineering*, 55(12), 1219-1223.
- Mao, Y. (1986). The Interaction between a Pipeline and an Erodible Bed, *Ph.D. thesis. Technical University of Denmark*.
- Muhammad, S.A. & Cheng, L. (2010). A Parallel Three-Dimensional Scour to Predict Flow and Scour below the Submarine Pipeline Central. *European journal of physics*, 8(4), 604-619.
- Pan, D.Z., Wang, L.Z., et al. (2007). Experimental Study on Local Scour around Submarine Pipelines under Propulsive Waves. *The Ocean Engineering*, 25(4), 27-32.
- Qin, C.R. & Peng, Y. (1995). Washing around the Seabed Pipeline Placed Barely by Wave Action. *Harbor Engineering Technology*, 003(3), 7-12.
- Sumer, B.M. & Fredsøe, J. (1990). Scour Blow Pipelines in Waves. *Journal of Waterway, Port, Coastal, and Ocean Engineering*, 116(3), 307-323.
- Sumer, B.M. & Fredsøe, J. (1991). Onset of Scour below a Pipeline Exposed to Waves. *International Journal of Offshore and Polar Engineering*, 1(3), 189-194.
- Voropayev, S.I., Testik, F.Y. Fernando, H.J.S. & Boyer, D.L. (2003). Burial and Scour Around Short Cylinder under Progressive Shoaling Waves. *Ocean Engineering*, 30(13), 1647-1667.
- Wen, J.F., Gou, Y., et al. (2012). Numerical Analysis of Local Scour of Submarine Pipeline under Ocean Current. *The Ocean Engineering*, 30(1), 75-82.
- Wu, Y.S. & Chiew, Y.M. (2012). Three-Dimensional Scour at Submarine Pipelines. *Journal of Hydraulic Engineering*, 138(9), 788-795.
- Wu, Y.S. & Chiew, Y.M. (2010). Three-Dimensional Scour at Submarine Pipelines in Unidirectional Steady Current. *5th International Conference on Scour and Erosion*, 471-481.
- Yang, L., Shi, B. & Guo, Y. (2012). Study on Dynamic Angle of Repose for Submarine Pipeline with Spoiler on Sandy Seabed. *Journal of Petroleum Exploration and Production Technology*, 2(4), 229-236.
- Yang, L., Shi, B., Guo, Y. & Wen, X. (2012). Calculation and Experiment on Scour Depth for Submarine Pipeline with a Spoiler. *Ocean Engineering*, 55, 191-198.
- Zang, Z.P., Teng, B., Cheng, L. & Kervin, Y. (2009). Experimental Research on Propagation Velocity Of 3-D Scour of Pipelines on Sea Floor under Action of Currents. *Journal of Dalian University of Technology*, 49(1), 110.
- Zang, Z., Cheng, L., Zhao, M., Liang, D. & Teng, B. (2009). A Numerical Model for Onset of Scour Below Offshore Pipelines. *Coastal Engineering*, 56(4), 458-466.

